# OPTIMISATION OF MAGNETIC RESONANCE TECHNIQUES FOR IMAGING THE HUMAN BRAIN AT 4.7 TESLA

**KARIN SHMUELI**

Wellcome Trust High Field Magnetic Resonance Research Laboratory

Department of Medical Physics and Bioengineering

University College London
U.K.

Ph.D. Thesis

Submitted for the Degree of Doctor of Philosophy

University of London

June 2005





ProQuest LLC
789 East Eisenhower Parkway
P.O. Box 1346
Ann Arbor, MI 48106-1346

# ABSTRACT

High magnetic field strengths (4.7 Tesla) promise improved MRI quality but also pose technical challenges. The research described here aims to optimise imaging techniques to generate artifact-free human brain images.

Radio frequency (RF) $B_1$ magnetic field homogeneity is worse at high field. Progress towards reducing the effect of the inhomogeneity at 4.7 T has been made in a novel spin-echo sequence using Hyperbolic Secant (HS) RF pulses. The properties of HS pulses when used for excitation and refocusing are investigated and exploited using simulations and experiments to yield a pulse sequence in which the HS pulse refocusing is $B_1$-insensitive. This sequence has one less RF pulse than a similar commonly used technique and produces an improved slice profile compared with a previous sequence.

High resolution diffusion-weighted imaging in reasonable scan times and without severe distortion proves challenging at high magnetic field strength. A volume-selective Stimulated Echo Acquisition Mode Echo-Planar Imaging sequence developed here shows potential for overcoming these challenges. The technique is shown to give similar diffusion coefficients to standard sequences in phantoms. It is designed for application in brain regions in which the higher resolution could allow nerve fibre tracts to be followed in greater detail.

The construction of an anthropomorphic head phantom as a tool for comparing susceptibility artifact reduction techniques is described. The aim is for the phantom to accurately reproduce the magnetic environment of the brain and allow quantification of susceptibility-induced distortion and drop-out, which are worse at high field strength. The phantom is based on a water-filled plastic skull with realistic air spaces and wax to mimic soft tissues and has been used to evaluate a new technique that recovers signal in areas of drop-out in gradient-echo images. Magnetic field maps show that the field pattern in the phantom is similar to that in real brains.

# TABLE OF CONTENTS

# LIST OF FIGURES

# LIST OF TABLES

# ACKNOWLEDGEMENTS

It is a pleasure to thank the many people who have helped me throughout the last few years. I am very grateful to my supervisor Professor Roger Ordidge for giving me the opportunity to join the unique 4.7 T Lab and for sharing his ideas and wealth of MR experience. All my colleagues at the Wellcome Trust High Field MR Research Lab have been invaluable and I could not have completed this work without them. Dr Paul Kinchesh has been a caring and cheerful second supervisor. Dr David Thomas has been unfailingly patient and extremely generous with his time, knowledge and experience, not least in providing feedback on this manuscript. My thanks go to Dr Enrico De Vita for his Matlab wizardry and many stimulating discussions. I have been fortunate to be able to count on Dr Harry Parkes for every kind of practical help from photography to carrying phantoms. Thanks to Dr Maria Fernandez Seara for lunchtime chats and encouragement and to Dr David Carmichael for help with puzzling out MR concepts and advice on formatting. Professor Robert Turner has been a useful source of advice, support and interesting conversations.

My thanks also go to Dr Fernando Calamante and Dr Jacques-Donald Tournier for their helpful comments on the Diffusion Tensor Imaging Chapter. Dr Ralf Deichmann and Dr Alan Bainbridge kindly read my M. Phil transfer thesis and I am very grateful for their feedback. Dr Robin Richards helped with initial ideas and data for designing the phantom, and the staff of the UCLH Medical Physics workshop (Billy Raven, Stuart Morrison, Terry Austin and Denzil Booth) and Radiotherapy Mould Room (David Marsh and Alex Kypriotis) were indispensable during its construction. Professor Quentin Pankhurst and Dr Dimitri Hautot generously loaded my samples into their 'SQUID', and helped me analyse the data to measure magnetic susceptibilities. Thanks also to Dr Jane Utting and Dr Gaby Pell for initial Bloch simulation computer code, Dr Chloe Hutton for answering my queries about SPM and field mapping, Dr John Thornton for organising CT scans, Ros Gordon for the loan of the dodecane phantom and Dr Claudia Wheeler Kingshott for initial advice on Diffusion Weighted Imaging.

I would also like to acknowledge the financial support of the Wellcome Trust, which has not only kept me going during these years but also gave me the opportunity to travel to Japan for the 12$^{th}$ Annual Conference of the ISMRM.

Thanks to all my friends and family who have kept me (in)sane and who make it all worthwhile. The most important and heartfelt appreciation goes to my Mum and my sister Sandra for their constant support and love.

This thesis is dedicated to

My Grandmother Marta Gross

and to the memories of

My Father Gabriel Shmueli

My Grandfather Paul Gross

My 'Saba and Savta' Eliyahu and Jeanne Shmueloff

# 1 INTRODUCTION

Magnetic Resonance Imaging (MRI) is one of the most important medical imaging modalities and has become indispensable for both routine clinical diagnosis as well as *in vivo* biomedical research since its development in the second half of the last century. MRI is non-invasive, using non-ionising radiation, and images can be acquired in any orientation, these being just some of the reasons why it is so useful. It is safe (although a small population such as those with pacemakers or metallic implants are excluded from MRI studies) and provides excellent soft tissue contrast. MRI's versatility comes from the ability to use various scanning techniques to precisely manipulate the nature and level of contrast between different tissues.

There are a huge variety of endogenous contrast mechanisms in human tissues that MRI is able to exploit, including the basic contrast provided by differences in proton density and relaxation times that underpin most anatomical imaging. Other contrast mechanisms include blood flow dependent contrast, contrast enhancement by the injection of contrast agents, contrast based on transfer of magnetisation between bound and free pools of protons, contrast based on the microscopic diffusion of water molecules, contrast dependent on the level of blood oxygenation and combinations of these. Several of these contrast mechanisms have been applied to study tissue function and physiology *in vivo*. In particular the blood oxygenation level dependent (BOLD) contrast mechanism has been widely utilised in the study of human brain function with functional MRI (fMRI).

The applications of MRI vary as widely as the available contrast mechanisms and are too diverse to catalogue here, ranging from detecting brain activation in response to sad pictures with functional MRI [1] to tumour detection in toes [2]. Although this thesis is concerned with human brain imaging, it should be remembered that MRI is widely applied over the whole human body and also to scan animal models of disease for pre-clinical and drug research [3].

This thesis is concerned with imaging but the phenomenon of nuclear magnetic resonance (NMR) on which MRI is based is also widely applied for Magnetic

Resonance Spectroscopy (MRS). The MR signals in this work arise from $^{1}H$ nuclear protons, most abundant in the human body in water molecules, but MR techniques can be used to study other nuclei such as $^{31}P$, $^{13}C$ and $^{23}Na$. However, the sensitivity of MR using these nuclei is much lower than proton MR due to the low biological concentration and / or low natural abundance.

The historical development of MRI has been well-documented and described [4], [5], [6], [7] and is outlined here in the form of a time line of key discoveries and landmark events, see Table 1.

| | |
|---|---|
| **1768-1830** | Jean-Baptiste-Joseph Fourier develops the Fourier transform |
| **1857-1942** | Joseph Larmor explains the splitting of spectral lines in a magnetic field |
| **1924** | Wolfgang Pauli suggests the possibility of intrinsic nuclear angular momentum |
| **1924** | Otto Stern and Walther Gerlach observe the splitting of a beam of silver atoms in a magnetic field gradient |
| **1925** | George Eugene Uhlenbeck and Samuel A. Goudsmit introduce the concept of intrinsic electron spin |
| **1936** | Linus Pauling and Charles D. Coryell discover that the magnetic state of haemoglobin changes with its state of oxygenation. |
| **1937** | Isidor Isaac Rabi and colleagues develop molecular beam magnetic resonance by passing a beam of lithium chloride molecules through a magnetic field and then bombarding the beam with radio waves |
| **1944** | Rabi is awarded the Nobel prize for Physics "for his resonance method for recording the magnetic properties of atomic nuclei" |
| **1946** | Research groups led by Edward Purcell at Harvard University and Felix Bloch at Stanford University independently demonstrate the phenomenon known as "nuclear magnetic resonance (NMR) in condensed matter." The absorption and re-emission radiofrequency and magnetic field strength obey the relationship described by Joseph Larmor |
| **1948** | Nicolaas Bloembergen, Edward Purcell, and Robert Pound publish a paper on "nuclear magnetic relaxation" and measure longitudinal and transverse relaxation times in liquids |
| **1948** | Henry Torrey and, independently, Erwin Hahn develop pulsed NMR to replace the continuous wave methods used by Bloch and Purcell |
| **1949** | Erwin Hahn discovers the spin-echo phenomenon for nuclear magnetic resonance measurements |
| **1949-1950** | Ramsey, Knight, Dickinson, Proctor and Yu independently report the 'chemical shift' phenomenon |
| **1952** | Bloch and Purcell are awarded the Nobel Prize for Physics "for their development of new methods for nuclear magnetic precision measurements and discoveries in connection therewith" |
| **1960** | In the 1960s, Richard Ernst and Weston Anderson apply Fourier analysis to pulse signals to increase the sensitivity of nuclear magnetic resonance |
| **1963** | Alan Cormack publishes the Radon Transform image reconstruction technique used in CT |
| **1964** | Stejskal and Tanner derive and test an expression for the signal attenuation of spin echoes in the presence of diffusion and 'diffusion weighting' gradients |

| | |
|---|---|
| **1971** | Raymond Damadian publishes a *Science* paper, in which he described differences in NMR relaxation times between excised malginant tumors and normal tissues in rats |
| **1971** | Godfrey Hounsfield builds the first CT (computerized tomography) scanner, the foundation of nearly every sophisticated imaging system in use today. For this work, he shared the 1979 Nobel prize with Cormack |
| **1972** | Paul Lauterbur couples spatial localization using a magnetic field gradient to the CT scanner idea of projection-reconstruction to obtain the first magnetic resonance image (MRI) of two test tubes |
| **1974** | Peter Mansfield's group in Nottingham invents slice-selective excitation |
| **1975** | Richard Ernst's group in Zurich invents two-dimensional Fourier Transform (2DFT) imaging |
| **1976** | Peter Mansfield conceives of echo planar imaging (EPI), which increases MR imaging speeds |
| **1977** | Mansfield and his colleagues in Nottingham publish the first successful MRI of a living human body part - a finger |
| **1978** | Hugh Clow and Ian Young produce the first published human head image using MRI at 0.1 Tesla at EMI Central Research Laboratories |
| **1980** | Bill Edelstein and Jim Hutchison demonstrate the first practical 2D FT or 'spin-warp' MRI method |
| **1981** | The first commercial clinical MRI scanner is installed at the Hammersmith Hospital in London. It used a 0.15 Tesla superconducting magnet and was called 'Neptune' |
| **1986** | A 9.5 Tesla NMR spectrometer is used to obtain the first MR images of a single cell |
| **1987** | EPI is used by the Nottingham group to create the first real-time movie image of a single human cardiac cycle |
| **1987** | Charles Dumoulin perfects Magnetic Resonance Angiography |
| **1990** | Seiji Ogawa detects variations in local tissue oxygenation using blood oxygen level dependent (BOLD) contrast |
| **1990** | Moseley shows that Diffusion-weighted images highlight brain regions affected by an ischaemic event |
| **1991** | Richard Ernst wins the Nobel prize for Chemistry "for his contributions to the development of the methodology of high resolution NMR spectroscopy" |
| **1992** | Several independent studies are published using functional MRI to determine the brain's response to sensory stimulation |
| **1994** | Imaging of hyperpolarized $^{129}Xe$ gas for respiration studies is first demonstrated by researchers at the State University of New York at Stony Brook and Princeton University |
| **1994** | Investigators at the National Institutes of Health, Bethesda, Maryland outline the theoretical basis of Diffusion Tensor Imaging |
| **1996** | There are more than 10,000 MRI scanners worldwide |
| **2003** | Paul Lauterbur and Peter Mansfield awarded the Nobel Prize for Physiology or Medicine "for their discoveries concerning magnetic resonance imaging" |

**Table 1 A Time Line Illustrating Key Events in the Development of MRI**
The table is based on that found at [5]. It should be noted that these developments would not have been possible without increased computer power and speed, the development of the Fast Fourier transform, improvements in magnet design and the development of cryogenics.

## 1.1 High Field MRI – Advantages and Technical Challenges to be Overcome

The development of MRI as outlined above has been intimately linked with the increase in the magnetic field strength of the magnets that form the basis of MRI scanners. The increase in field strength has been enabled by the evolution from permanent or resistive magnets to the superconducting magnets present in all but a few clinical systems today.

In recent years more and more human magnetic resonance imaging (MRI) scanners have been introduced at higher main magnetic field strengths (from 3 to 7 Tesla (T)) than those routinely used in hospitals (1.5 T). The highest field human MRI systems at present include an 8 T whole-body system operational at the Ohio State University since 1999 and a 9.4 T system, unveiled in September 2004 at the University of Illinois at Chicago [8].

The main reason for the steady increase in field strength over the years since MRI was first invented is because the signal-to-noise ratio (SNR) increases in approximately linear proportion to the main magnetic field strength ($B_0$). This is at least the case in theory and in the absence of relaxation effects. The increased SNR can be traded-off for increased image resolution or acquisition speed. For example, if the SNR is kept constant and the field strength is increased then the measurement time can be reduced by a factor proportional to $B_0^2$ or the (isotropic) resolution can be improved by a factor proportional to $\sqrt[3]{B_0}$ [9].

A fast-growing MRI application that stands to benefit greatly from this increase in SNR is that of diffusion tensor imaging (DTI). DTI is a unique tool for visualising microstructural tissue architecture, in particular for the study of white matter diseases and brain development. Together with fibre tracking (tractography) techniques, DTI allows the investigation of neural pathways and connectivity. Since diffusion weighting gradients are applied along several directions in space to attenuate the MRI signals and generate the diffusion-weighted images that form the basis of DTI, the technique is SNR-limited. The SNR gain at higher field strengths has the potential to significantly improve the quality of DTI [8].

As well as this basic SNR advantage, further advantages of the higher field strength include the increased spectral resolution, improved fMRI contrast and increased acceleration factors possible with parallel imaging using multiple radio frequency (RF) receiver coils. The increased spectral resolution arises because the chemical shift (or frequency difference between metabolite peaks in MR spectra) is directly proportional to the external magnetic field strength.

It has been shown that parallel imaging at high field strengths benefits from the increasingly 'far-field' behaviour of the radiofrequency fields [10] and this should allow an increase in the so-called 'reduction factor' (which is equivalent to the increase in image acquisition speed in SENSE techniques) that is feasible at high field strength.

Functional MRI (fMRI) has been used extensively to give time courses and maps of cerebral activation in response to various stimuli. The primary contrast mechanism utilised in fMRI studies is the blood oxygenation level dependent or BOLD contrast. In summary this originates in the over-supply of oxygenated blood to regions of neuronal activation thereby reducing the proportion of (relatively paramagnetic) deoxyhaemoglobin and giving less susceptibility-related signal attenuation in the activated regions and in downstream blood vessels.

Many different mechanisms and factors contribute to the overall BOLD contrast including intra- and extravascular signal changes due to both static and dynamic spin dephasing, affecting both $T_2$ and $T_2^*$ in different compartments. Increasing $B_0$ acts to increase BOLD signal changes via most of these mechanisms since they are all reliant on susceptibility gradients between areas containing different amounts of deoxyhaemoglobin (which is paramagnetic compared to tissue). These susceptibility gradients increase with $B_0$ so the magnitude of the BOLD signal changes generally increases with field strength. Further advantages of performing fMRI at high field strengths include the fact that the BOLD signal changes are more highly localised to the capillaries or microvasculature rather than the larger draining veins and macrovasculature. This is partly because the $T_2$ and $T_2^*$ of venous blood decreases to such a short value at high field strengths that the signal and therefore signal changes from draining venules and veins are undetectable.

In order to exploit these advantages, however, many technical challenges have to be overcome. These challenges arise in the areas of magnet (hardware) design, radio frequency (RF) characteristics, tissue relaxation characteristics and image artifacts.

Magnet design and siting considerations at high field strengths include the fact that the magnet weight increases dramatically. The stray magnetic field increases in extent (by about 50% in going from 1.5T to 3T) requiring improved shielding technology and the cryogenic helium consumption is also increased (roughly doubled from 1.5T to 3T). These factors increase the cost of acquiring, installing and running a high field magnet.

Although there is lack of evidence for any significant (detrimental) biological effects from high static magnetic fields either in the short term (electromagnetic and magnetohydrodynamic effects on the nervous and cardiovascular systems) or long term (carcinogenic effects) some transient phenomena have been reported by subjects in high magnetic strength scanners including vertigo, magnetophosphenes or a metallic taste. Particularly relevant for clinical practice are the facts that the risk of projectiles is obviously increased with main magnetic field strength and that certain devices may no longer be MR compatible as the field strength increases. In addition the acoustic noise from gradient switching is increased because the (Lorentz) force on current-carrying wire is proportional to the main magnetic field strength.

Increased gradient performance is independent of main magnetic field strength but is particularly desirable for higher field strength systems because the $T_2$ and $T_2^*$ are short and the resolution of echo-planar type imaging sequences such as EPI and RARE / FSE is limited by the degree of signal relaxation during the echo train. Using increased gradients that can be switched at faster rates can shorten the echo trains in these sequences, provided the limits for peripheral nervous stimulation and acoustic noise levels are not exceeded.

RF field characteristics become more complicated at high field strengths and this is discussed in detail in Chapter 3. Briefly, the wavelength of the RF magnetic field ($B_1$) is lower in dielectric tissue than in free space and decreases further as $B_0$ (and therefore the frequency of $B_1$) increases, becoming more similar to the subject and coil dimensions. This results in increased interactions between the field, RF coil and subject.

In theory the RF power deposition (and related specific absorption rate (SAR)) increases quadratically with $B_0$. This restricts the number, amplitude and repetition rate of RF pulses used to excite and refocus the magnetisation in imaging pulse sequences. However in practice the restriction is not as severe as in theory since experiments have shown that the rate of increase of power deposition with $B_0$ is not as steep as predicted. For example the RF power absorbed increases by a factor of 1.8 in going from 4 T to 7 T [11] rather than the factor of 3 predicted by the theoretical square-law.

A further complication is that the homogeneity of the $B_1$ field in tissue typically worsens at higher main magnetic field strengths. The inhomogeneity affects image contrast and often results in brightening at the centre of images and is therefore sometimes described as a field-focusing effect. The effect results from the interaction between the high frequency $B_1$ field, the dielectric tissue and the RF coil on transmission and reception. The causes of $B_1$-inhomogeneity and methods for overcoming this are discussed in more detail in Chapter 3.

As well as being influenced by $B_1$ homogeneity, image contrast is also largely determined by tissue longitudinal and transverse relaxation times, $T_1$ and $T_2$ respectively. The main trends in the relaxation properties of tissues are that their longitudinal relaxation times ($T_1$) lengthen (and converge for brain grey and white matter) as $B_0$ increases and their transverse relaxation times ($T_2$ and $T_2^*$) get shorter. This means that it is more difficult to obtain conventional $T_1$- and $T_2$-weighted anatomical images with good contrast at higher field strengths.

A further challenge for high field MRI is that field offsets due to susceptibility differences between tissues are linearly proportional to $B_0$. The increase in susceptibility-induced magnetic field differences ($\Delta B_0$) is responsible for a reduction in $T_2^*$ and this is discussed in more detail in Chapter 2. Unfortunately the same increases in susceptibility-induced field gradients that increase fMRI sensitivity at high field strengths also cause artifacts in many images including those sensitive to BOLD contrast. These are known as susceptibility artifacts and manifest themselves as geometric distortion and signal drop-out in regions of susceptibility gradients such as in the vicinity of air-tissue interfaces. Susceptibility artifacts and methods for reducing them are described in more detail in Chapters 2, 4, 5 and 6.

In spite of the technical challenges, and thanks to improved imaging techniques at high $B_0$, it has been possible to acquire anatomical and functional images of very high quality compared to those acquired at lower $B_0$. Improvements range from hardware modifications (e.g. RF coil design and drive patterns [12]) through pulse sequence design (e.g. signal drop-out reduction via RF pulse design [13]) to image post-processing (e.g. geometric distortion correction [14]). The result is improved images for applications including venography, MR angiography and fMRI. It is clear that many of these challenges increase with the field strength so strategies that are applicable at 1.5 T or even 3 T may not be adequate to create the best quality images to take advantage of the increased SNR available at 4.7 T.

## 1.2 The Context and Aims of This Work

In this work the focus is on implementing and developing image acquisition methods within an exisiting hardware environment. The MR system used in this work has a main magnetic field strength of 4.7 Tesla. At the time of writing it is the highest field strength whole body magnetic resonance scanner in Europe and it has been the aim of the group at the Wellcome Trust High Field Magnetic Resonance Research Laboratory to optimise anatomical and functional imaging and MR spectroscopy at this field strength.

The scanner is a Surrey Medical Imaging Systems (SMIS) MR 5000 whole-body MR system (provided by Philips Medical Systems) and fitted with a head gradient set capable of producing maximum gradients of 36 $mT.m^{-1}$ separately in all three directions with a maximum slew rate of 182 $T.m^{-1}.s^{-1}$. (The system also contains a whole body gradient set which was not used for the work described in this thesis). All the experiments described here were carried out with a birdcage RF coil for transmission and reception of signals (coil diameter = 28cm, length = 20.9 cm, 16 rungs of width = 1cm, screen diameter = 35.6cm). In all cases where healthy volunteers were scanned this was done with the approval of the University College London Hospital Ethics Committee and informed consent was obtained.

The work described in this thesis has been part of the overall effort to compare, develop and optimise techniques for imaging the human brain *in vivo* at high field strength and in particular at 4.7 T. The focus has been on developing techniques to overcome the technical challenges of the inhomogeneous $B_1$ field and increased susceptibility artifacts

associated with the increased field strength. A substantial part of the work was devoted to implementing DTI at 4.7 T since it is such a useful tool for studying brain tissue organisation and should benefit from the increased SNR available at this field strength.

Before describing the work in detail a précis of the general MRI theory required for understanding the following chapters is presented in Chapter 2.

A technique to reduce the effect of $B_1$-inhomogeneity in images is described in Chapter 3. It involves the use of a particular shape of RF pulse (the hyperbolic secant (HS)), which has a frequency sweep as well as the standard amplitude modulation. The properties of such HS pulses when used for excitation and refocusing are investigated and exploited (using simulations and experiments) to yield a pulse sequence which gives an improved slice profile over a conventional spin-echo sequence and yields images which are less sensitive to $B_1$-inhomogeneity.

Development of a method to enable acquisition of high-resolution diffusion tensor images (DTI) at high field strength with reduced susceptibility-induced distortion is discussed in Chapter 4. The disadvantages of the conventional technique for acquiring diffusion-weighted images are demonstrated before justifying the development of a volume-selective 'STEAM-EPI' sequence for DWI. The sequence allows selection of a cuboidal region so that the imaging field of view can be decreased to enable a suitable compromise between improvements in image resolution and reduction in susceptibility-induced distortion.

Chapter 5 describes the construction of an anthropomorphic head phantom as a tool for the comparison and optimisation of the many proposed susceptibility artifact reduction techniques at this field strength. The idea is for the phantom to reproduce the magnetic environment of the brain so that images of the phantom will suffer from the same susceptibility artifacts present in real brains. This should allow different susceptibility artifact reduction techniques to be compared in the phantom so that the optimum imaging procedure can be found for each brain region. The phantom was used to optimise a technique for the reduction of signal drop-out and this is described in Chapter 6.

No research project is ever fully 'finished' and in this spirit, in Chapter 7 further work is suggested amongst the important conclusions from the work in this thesis.

# 2 GENERAL MRI THEORY

## 2.1 Nuclear Magnetism

The signal detected in MRI exists because of the magnetism of nuclei and in particular (in this thesis) hydrogen nuclei or protons. Each proton possesses a quantised spin angular momentum:

$$|\overline{p}| = \hbar\sqrt{I(I+1)}$$

**Equation 1**

where I is the half-integer or integer intrinsic nuclear spin. I = ½ for protons.

In analogy to the classical situation in which a rotating charged particle has a magnetic moment, the proton also has a (quantised) nuclear magnetic moment (μ) associated with its spin angular momentum:

$$\overline{\mu} = \gamma\overline{p}$$

**Equation 2**

Here γ is the gyromagnetic ratio. $\gamma = 2.675 \times 10^8$ rad $s^{-1}$ $T^{-1}$ for protons and is often expressed for convenience as $\gamma/2\pi = \gamma = 42.58$ MHz.$T^{-1}$. The magnetic field around each proton is similar in shape to that created by a magnetic dipole and the protons can therefore be thought of as miniature bar magnets.

## 2.2 Energy Levels

In the presence of a magnetic field $B_0$ the (previously degenerate) nuclear spins undergo Zeeman splitting into 2I + 1 energy states. The energy of each is given by

$$E = -\overline{\mu}\cdot\overline{B_0} = -\mu_z B_0$$

**Equation 3**

where $\mu_z$ is the component of the magnetic moment in the direction of the magnetic field (conventionally the z direction) and has its own quantum number $m_z$ that takes values –I,-I+1,…,I so that

$$\mu_z = \gamma\hbar m_z$$

**Equation 4**

Transitions can only occur between energy levels having $\Delta m_z = \pm 1$. This means that protons in a magnetic field will be found in two energy levels separated by

$$\Delta E = \gamma \hbar B_0$$

**Equation 5**

and transitions between the levels require quanta of this energy. Nuclear Magnetic Resonance (NMR) occurs when energy is introduced at the correct frequency:

$$\omega_0 = \gamma B_0$$

**Equation 6**

(the Larmor frequency) to stimulate transitions between the lower and upper energy states. Simplistically the lower energy state can be thought of as protons whose spins are aligned with the main magnetic field and the upper energy state can be thought of as protons with spins antiparallel to $B_0$.

## 2.3 Net Magnetisation and the Boltzmann Distribution

The (relative) populations of each energy state ($n_+$ and $n_-$) are given by the Boltzmann distribution :

$$\frac{n_+}{n_-} = \exp\left(\frac{-\Delta E}{kT}\right)$$

**Equation 7**

where k is the Boltzmann constant, T is the absolute temperature and $\Delta E$ is given by Equation 5. At 4.7 T and body temperature there will be approximately 15 more proton spins per million in the lower energy state ($n_-$) than in the upper state leading to a very weak net equilibrium magnetisation $M_0$, which explains why MRI is a relatively insensitive technique.

## 2.4 Precession and the Larmor Frequency

The behaviour of this equilibrium magnetisation can be understood using a classical vector model. In analogy to a spinning top experiencing a torque in the earth's gravitational field the magnetic moments precess around the main magnetic field axis. The precession frequency is the Larmor frequency identical to that in Equation 6. The magnetic moments are all precessing but they have random phase so that the

equilibrium magnetisation is effectively stationary along the z-axis and there is no net transverse magnetisation at equilibrium.

## 2.5 The Radio Frequency Field and Rotating Reference Frame

In order to detect some of the net magnetisation (for MRI) it is necessary to rotate it into the transverse plane. This is because the net equilibrium magnetisation is static and much smaller than the main magnetic field so it would be difficult to detect, whilst transverse magnetisation varies in time and can therefore induce a detectable voltage in a receiver coil. As stated above it is necessary to introduce energy at the Larmor frequency to induce transitions. This is in the radio frequency (RF) range for protons at MRI magnet field strengths (200MHz at 4.7T). The magnetic field used to excite transverse magnetisation is therefore known as the RF field with amplitude $B_1$. The effect of the $B_1$ field can be most easily understood in a frame of reference rotating about the main magnetic field or z-axis at the Larmor frequency.

The equation of motion for the magnetisation (M) in such a rotating frame is

$$\left(\frac{d\overline{M}}{dt}\right)_{rotating} = \gamma \overline{M} \times \left(\overline{B}_0 + \frac{\overline{\Omega}}{\gamma}\right)$$

**Equation 8**

where $\Omega$ is the angular velocity of the rotating frame and the magnetisation M behaves as if there is an effective magnetic field

$$\overline{B}_{eff} = \overline{B}_0 + \frac{\overline{\Omega}}{\gamma}$$

**Equation 9**

The precession of the magnetisation is therefore frozen if

$$\overline{\Omega} = -\gamma \overline{B}_0$$

**Equation 10**

This means that the frame most commonly used to examine the effect of the $B_1$ field rotates at this (negative) Larmor frequency.

## 2.6 Tipping Magnetisation and Flip Angles

If a circularly polarised RF field at the Larmor frequency with amplitude $B_1$ is applied perpendicular to $B_0$ it will have a fixed orientation in the rotating frame and the magnetisation will precess around it. If the $B_1$ field is applied for the correct duration $\tau$ then the net magnetisation will rotate by 90 degrees and all of the longitudinal magnetisation will be converted to measurable transverse magnetisation. Any flip angle $\alpha$ can be achieved in this way according to

$$\alpha = \int_0^{\tau} \gamma B_1(t)\, dt$$

**Equation 11**

Equation 11 can be simplified for a rectangular RF pulse (a hard pulse) of constant amplitude $B_1$:

$$\alpha = \gamma B_1 \tau$$

**Equation 12**

Both the frequency and amplitude of the RF field can be varied to manipulate the magnetisation and achieve a desired flip angle and this will be discussed in more detail in Chapter 3.

## 2.7 Specific Absorption Rate

We have seen that exciting spins for MRI requires exposure to RF pulses. These pulses deposit energy in the subject and can cause heating. For safety reasons it is therefore necessary to measure the RF exposure and this is done in terms of the specific absorption rate or SAR, defined as the total power absorbed per kilogram of tissue ($W.kg^{-1}$). An expression for the SAR can be derived if we use a circular loop model that assumes a uniform RF field over the loop area [15]. The electric field of magnitude E induced by the (sinusoidally) oscillating magnetic field of amplitude $B_1$ in the loop of radius r is given by Faraday's law:

$$E = \frac{r}{2}\left|\frac{dB}{dt}\right| = \frac{\omega_0}{2} B_1 r = \pi f B_1 r$$

**Equation 13**

where $\omega_0 = 2\pi f$ is the Larmor frequency at which the $B_1$ field is applied. The rms power deposition per unit mass or SAR is then given by

$$SAR = 0.5\,\sigma\frac{E^2}{\rho} = 0.5\frac{\sigma}{\rho}\pi^2 f^2 B_1^2 r^2 D$$

**Equation 14**

where ρ is the tissue density and D is the duty cycle or the fraction of the total scan time for which the RF pulse is on. This expression assumes a rectangular (hard) pulse shape but can be modified for different pulse envelopes. The $B_1^2$ in the expression above should then be replaced by an expression proportional to

$$\frac{\int B_1^2(t)dt}{\tau}$$

where τ is the RF pulse duration and the numerator is directly proportional to the energy associated with the RF field.

Detailed SAR calculations have been made using electromagnetic theory in more complex finite element models (FEMs) [20], [21]. At high field strengths it is particularly important to consider SAR, not only because the higher Larmor frequencies lead to higher overall SAR but also because the increasingly inhomogenous $B_1$ fields can lead to SAR 'hot spots'.

## 2.8 Relaxation Times and Mechanisms

Following a 90° RF pulse the magnetisation both continues to precess around $B_0$ but also decays and relaxes back to equilibrium. This generates a signal, in a nearby receiver coil, known as the Free Induction Decay (FID). The discussion of the fate of the magnetisation is simplified if we consider the transverse and longitudinal components independently.

The longitudinal magnetisation $M_z$ relaxes back to its equilibrium value $M_0$ via spin-lattice, longitudinal or $T_1$ relaxation. On the macroscopic scale this looks like the vector 'growing' from zero to its full magnitude of $M_0$ over time. At the microscopic level the excited protons are on average returning to the lower energy level by exchanging energy with their environment – the 'lattice'. Since transitions between the two energy levels involves the presence of fields fluctuating at the Larmor frequency the $T_1$ relaxation depends on the extent to which the molecular environment fluctuates at this frequency. For example, as a water molecule tumbles, the local dipolar field exerted by one proton

on the other varies (see Figure 1) and a component of the frequency spectrum of this motion will be at the Larmor frequency, in the transverse plane and will induce transitions between the upper and lower proton spin energy levels. Because the $T_1$ relaxation time is determined by local field fluctuations, it is affected by temperature, viscosity, molecular size and chemical exchange.

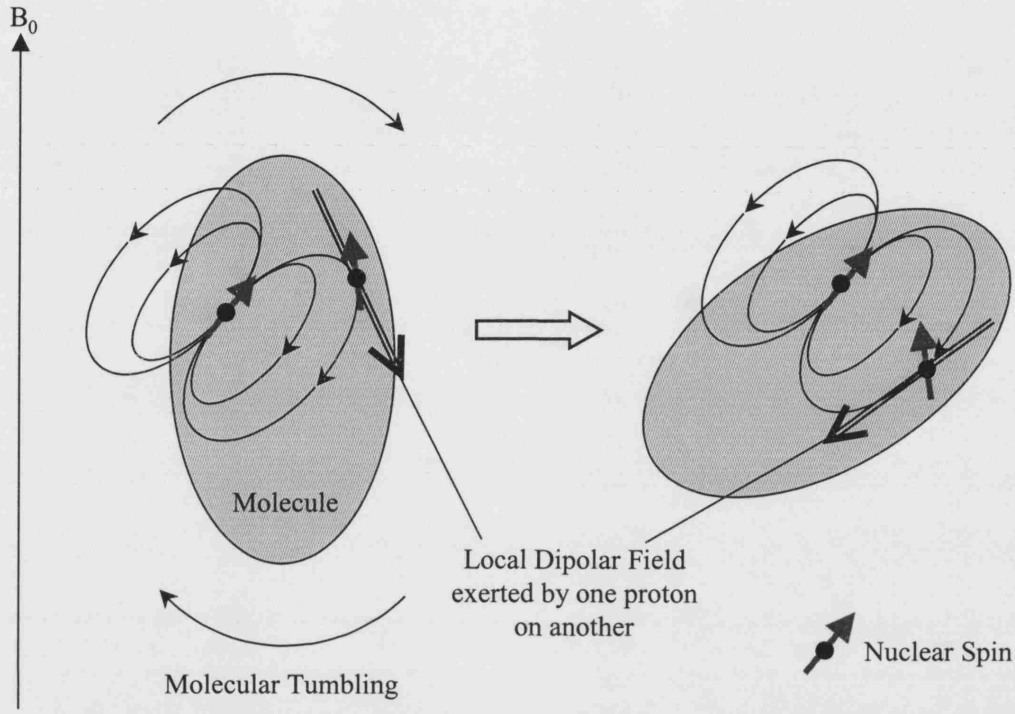


**Figure 1 The Effect of Molecular Tumbling on the Local Dipolar Field**
A schematic illustration of the modulation of the local dipolar field experienced by a nuclear spin due to molecular tumbling. As the molecule tumbles the magnitude and direction of the magnetic field exerted by one spin on the other changes.

The transverse component $M_{xy}$ decays via a process known as spin-spin, transverse or $T_2$ relaxation. Unlike $T_1$ relaxation there is no net energy transfer between the protons and their surroundings but instead a loss of phase coherence by the protons so that the resultant transverse magnetisation decays. Since $T_2$ relaxation is a net loss of magnetisation from the transverse plane it is also affected by all contributions to longitudinal $T_1$ relaxation. In addition it is affected by slowly varying (low frequency) local fields directed along the main field direction that can modulate the precessional frequency of neighbouring nuclei within an ensemble. This additional process ensures that $T_2$ is always shorter than $T_1$ in biological samples.

Transverse magnetisation is also affected by spatial inhomogeneities in the main magnetic field $B_0$ so that protons in different regions have different (Larmor) precession frequencies and the coherence of the ensemble is lost. This means that, in practice, transverse magnetisation decays with a time constant $T_2^*$ given by

$$\frac{1}{T_2^*} = \frac{1}{T_2} + \frac{1}{T_2'}$$

**Equation 15**

where $T_2'$ describes the reversible magnetic field inhomogeneity effect. The effects of main magnetic field inhomogeneities on the MR signal are discussed in more detail in sections 2.12.3 and 2.13.

## 2.9 Bloch Equations

$T_1$ relaxation can be described by the equation

$$\frac{dM_z}{dt} = \frac{M_0 - M_z}{T_1}$$

**Equation 16**

and $T_2$ relaxation can be described by

$$\frac{dM_x}{dt} = -\frac{M_x}{T_2} \quad \text{and similarly} \quad \frac{dM_y}{dt} = -\frac{M_y}{T_2}$$

**Equation 17**

where $M_x$, $M_y$ and $M_z$ are the components of the magnetisation whose equilibrium value is $M_0$.

These equations can be combined with the classical expression for the motion of the magnetisation in an external (static) magnetic field B to yield a general equation

$$\frac{d\overline{M}}{dt} = \gamma\left(\overline{M} \times \overline{B}\right) + \frac{\left(M_0 - M_z\right)\overline{k}}{T_1} - \frac{M_x\overline{i} + M_y\overline{j}}{T_2}$$

**Equation 18**

where i, j and k are the unit vectors in the x, y and z directions respectively.

## 2.10 Imaging: Slice Selection, Frequency- and Phase- Encoding

We have seen how the NMR signal can be excited by RF pulses and subsequently relaxes but MR imaging requires spatial localisation of the NMR signal. The conventional methods for spatial localisation of signal in three dimensions are slice selection, frequency encoding (FE) and phase encoding (PE). All three methods rely on the use of linear (pulsed) gradients in the main magnetic field $B_0 = B_z$:

$$G_z = \frac{dB_z}{dz}, \quad G_y = \frac{dB_z}{dy}, \quad G_x = \frac{dB_z}{dx}$$

**Equation 19**

Slice selection works by applying a frequency-selective RF pulse simultaneously with a field gradient $G_z$ in the slice thickness direction. The RF pulse amplitude is shaped in time (usually with a Sinc envelope) so that it has a particular frequency bandwidth $\Delta\omega$. The gradient $G_z$ that must be applied simultaneously with a pulse of bandwidth $\Delta\omega$ to select a slice of thickness $\Delta z$ is

$$G_z = \frac{\Delta\omega}{\gamma \Delta z}$$

**Equation 20**

The slice frequency $\omega_{rf}$ is centred on the Larmor frequency at the centre of the desired slice position (z)

$$\omega_{rf} = \omega_0 + \gamma G_z z$$

**Equation 21**

The RF pulse frequency response is given by the Fourier Transform of the amplitude-time pulse shape. For example a Sinc-shaped pulse is often used to excite a rectangular slice profile. The slice-select gradients can be applied in any direction to choose a slice in any orientation and the RF pulse amplitude must be calibrated to give the desired (e.g. 90°) flip angle within the slice. For a standard 90° (Sinc-shaped) pulse a slice-refocusing gradient must be applied after the slice-selective gradient to ensure that spins within the imaging slice are phase coherent. This is because dephasing occurs while the slice-select gradient is applied and must be rephased. The rephasing gradient area is usually half that of the slice-select gradient area (assuming the slice-select gradient is symmetric about the RF pulse time centre). However this relationship is based on the additional assumption that all the spins are tipped at the exact time centre of the RF

pulse and dephase during the remainder of the slice-select gradient pulse. This latter assumption is only accurate for the low flip angle approximation in which the spins behave in a simple linear fashion so that the flip angle is proportional to the RF pulse ($B_1$) amplitude. The Bloch equations are in fact non-linear which means that the refocusing gradient area required in practice is often slightly greater than 50% of the slice-select gradient area.

Encoding of spin position in a second (now 'in-plane' dimension) is usually achieved via frequency encoding. This relies on the direct proportionality of the Larmor frequency to the magnetic field strength (see Equation 6) so that if a magnetic field gradient is applied across an object the precession frequency of the spins will vary with position according to

$$\omega(x) = \gamma(B_0 + G_x x)$$

**Equation 22**

The signal variation with position (i.e. a profile of the object in the frequency-encoding – usually called 'read' – direction) can be decoded from the total time-varying signal measured while the gradient is on if the signal amplitude at each frequency can be obtained. Fourier transformation is a method designed to analyse the frequency components present in a signal and so is ideally suited to obtain the profile.

Phase encoding is usually used for spatial encoding in the third dimension. As for frequency encoding, phase-encoding gradients alter the Larmor frequency of spins at different positions. However the phase encoding gradients are pulsed for a short time and the signal is acquired after they have been switched off and a position-dependent phase shift has accumulated

$$\phi(y) = \gamma(B_0 + G_y y)\tau$$

**Equation 23**

where $\tau$ is the duration of the phase-encoding gradient. Each value of the PE gradient therefore results in a particular set of phase shifts across the object, each of which is sensitive to a particular spatial frequency. This means that to build up a representation of all the spatial frequencies in an object, it is necessary to repeat signal acquisition over a range of different PE gradient values.

## 2.11 The Fourier Transform and K-space

Neglecting relaxation effects, the effect of the frequency and phase encoding gradients on the demodulated signal δs from an element of an excited slice is given by

$$\delta s(t) = \rho(x,y).\exp(i\phi_{FE}(x,t)).\exp(i\phi_{PE}(y,t)).\,dx\,dy$$

**Equation 24**

where ρ(x,y) is the spin density, $\phi_{FE}(x,t)$ is the accumulated phase change up to time t due to the FE gradient and $\phi_{PE}(y,t)$ is the accumulated phase change up to time t due to the PE gradient. The accumulated phases are given by

$$\phi_{FE}(x,t) = \gamma x \int_0^t G_x(t')dt' \quad \text{and} \quad \phi_{PE}(y,t) = \gamma y \int_0^t G_y(t')dt'$$

**Equation 25**

and the total signal from the slice is obtained by integrating δs over x and y to obtain

$$S(t) = \iint \rho(x,y).\exp\left(i\gamma x \int_0^t G_x(t')dt'\right).\exp\left(i\gamma y \int_0^t G_y(t')dt'\right) dx\,dy$$

**Equation 26**

If we define

$$k_x(t) = \gamma \int_0^t G_x(t')dt' \quad \text{and} \quad k_y(t) = \gamma \int_0^t G_y(t')dt'$$

**Equation 27**

then the signal can be written

$$S(k_x,k_y) = \iint \rho(x,y).\exp(i\,(k_x x + k_y y))dx\,dy$$

**Equation 28**

which is the inverse (2D) Fourier transform (FT) of the spin density. Therefore the 2D FT of the encoded signal yields a representation of the spin density in 2D i.e. an image. Position (x, y) and spatial frequency ($k_x$, $k_y$) constitute a FT pair and the Fourier equivalent of image space (or real space) is then k-space.

Since the image and k-space are a Fourier pair, several useful relationships can be deduced between the spacing and extents of sample points in either domain. For example the image resolution is determined by the extent of points out into k-space. This can be understood qualitatively since the central point in k-space is acquired with

no net gradient encoding and therefore contains no spatial information about the signal (low spatial frequency) whilst points farther out in k-space represent information about smaller structures (high spatial frequencies). It follows that the further samples extend in k-space, the more information there is about higher spatial frequencies and the smaller the details that can be detected in the image i.e. the higher the image resolution. Conversely, the spacing between points in k-space determines the spatial extent of the image or the 'field-of-view' (FOV).

These Fourier relationships between k-space, resolution and FOV can be expressed mathematically. For example the image FOV in the PE direction is inversely related to the k-space separation between points in the PE direction $\Delta k_{PE}$ (see Figure 2) via:

$$FOV_{PE} = \frac{2\pi}{\Delta k_{PE}}$$

**Equation 29**

so if there are $N_{PE}$ lines collected then the image resolution in the PE direction $\Delta y$ is given by

$$\Delta y = \frac{FOV_{PE}}{N_{PE}} = \frac{2\pi}{N_{PE}\,\Delta k_{PE}}$$

**Equation 30**

i.e. $\Delta y$ is inversely related to the k-space extent in the PE direction. Similar relationships hold for the FE direction.

Another way of thinking about k-space is as the raw data matrix in which the encoded MR signals are stored. There are several ways of traversing k-space and filling it with samples of MR data. For the conventional 2DFT experiment described above, k-space is filled one line of $k_{PE}$ at a time as shown in Figure 2. This means that the experiment needs to be repeated for each PE line or step. Single-shot imaging methods are those in which the whole of k-space is traversed following a single slice excitation pulse and are therefore usually more rapid than conventional 2DFT experiments. Echo-planar imaging (EPI) is a widely used single-shot method.

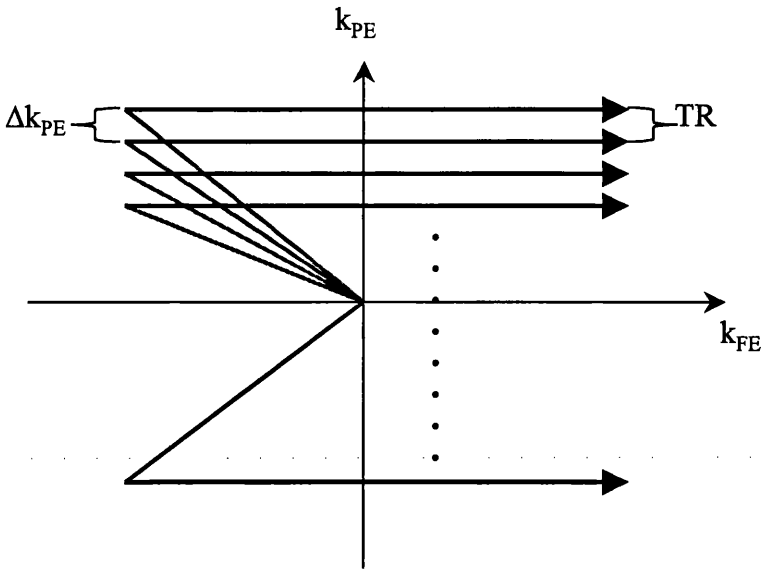


**Figure 2 K-Space**
The filling of k-space in a standard 2DFT MR experiment. The initial displacement from the centre of k-space (grey lines) prior to the acquisition of each line is achieved by applying 'dephase' gradients along the phase-encoding and readout directions. The data are collected in the presence of the readout or frequency encoding gradient and the signal is reformed in the TR period after each line is acquired. The process is repeated with a different initial ($k_{PE}$) displacement until k-space has been filled to the required extent and density.

# 2.12 Echo Planar Imaging

## 2.12.1 K-Space Trajectory

EPI is a method that addresses the challenge of filling k-space rapidly enough in 'one shot' following a single excitation, before the signal has decayed away. There are several possible paths through k-space or k-space trajectories and the one used in the experiments described in this thesis is shown in Figure 3B. It is a 'blipped' k-space trajectory in which short gradient pulses (blips) are used on the PE gradient axis to move up a line in k-space. Early versions of EPI sequences used constant PE gradients but this lead to a 'raster' type k-space trajectory that required regridding in the PE direction.

## 2.12.2 EPI Imaging Sequence

Using Equation 27 and Equation 28 above it is possible to deduce the sequence of gradients that will result in the EPI trajectory shown. Such a time-sequence of gradient pulses (with the RF pulses required for excitation) is known as an imaging pulse

sequence and is commonly illustrated as a schematic diagram plotting the gradients along three directions and the RF pulses against time. The EPI pulse sequence that corresponds to Figure 3B is shown in Figure 3A.

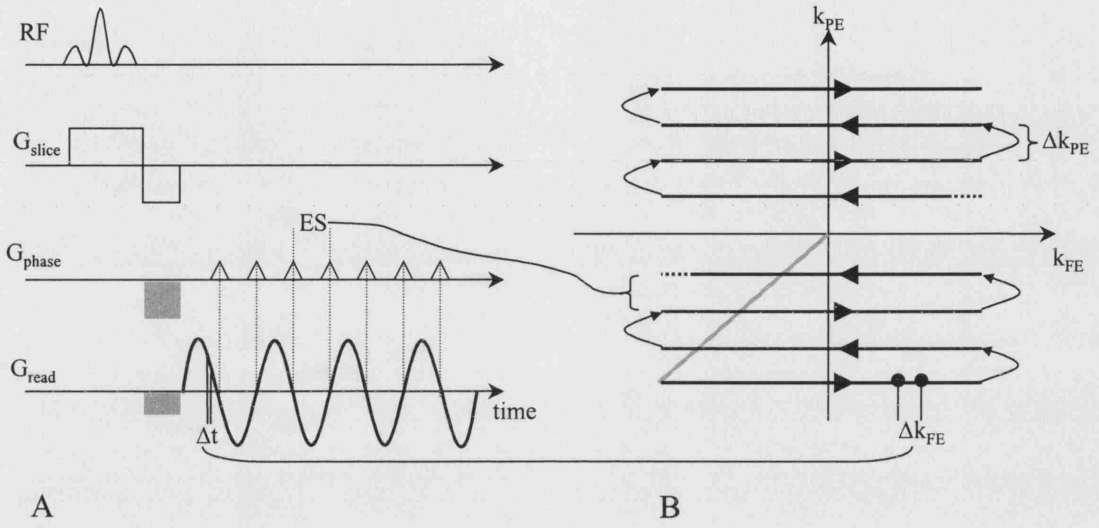


**Figure 3 EPI Sequence and K-Space Trajectory**
Schematic diagrams of the Echo-Planar Imaging (EPI) sequence **A** and k-space trajectory **B**. The grey line in **B** shows the displacement brought about by the 'dephase' gradients shown in grey in **A**. The thick black lines in both figures show the sinusoidal readout or frequency-encoding gradient. The thin curved arrows in **B** correspond to the triangular 'blipped' phase-encode gradients in **A**. Note that there are usually many more lines of k-space (~64/128) collected in a standard EPI sequence but only a few are shown here for clarity. The effective time between phase encode lines is now ES, which is much longer than the sample period Δt in the readout direction, giving EPI a much smaller bandwidth in the PE than in the FE direction, and making EPI vulnerable to artifacts in this direction as discussed in section 2.12.3.2.

As can be seen in Figure 3, reversing the polarity of the readout gradients reverses the direction of k-space traversal in the read direction for alternate lines. This demonstrates that every other echo must be time-reversed prior to 2DFT image reconstruction.

When sinusoidal read gradients are used, as was the case in all EPI experiments in this thesis, the readout sample rate ($1/\Delta t$) can be varied to ensure that the gradient-time integral (proportional to $\Delta k_{FE}$ see Equation 27) is equal between each sample point. This is done in order that the data samples are regularly spaced on a Cartesian (square or rectilinear) grid in k-space to allow straightforward image reconstruction by inverse Fourier transformation. Alternatively a constant sampling rate may be used, followed by

interpolation (or regridding) in k-space to place points on a regular grid before performing the inverse (2D) FT. The latter, constant sampling rate method was employed for all the EPI acquisitions in this work. For example in a 64 x 64 standard EPI acquisition, for each PE line, 100 points were acquired in the read direction, evenly spaced in time and these data were then interpolated to 64 points evenly spaced in k-space before the inverse FT was performed.

The Fourier relationships described in Equation 29 and Equation 30 above between the resolution and the FOV are the same for the EPI sequence.

## 2.12.3 Image Artifacts in EPI

EPI is particularly vulnerable to artifacts (in the PE direction) for two reasons. One is the necessary time reversal of alternate echoes and the second is the relatively long total data acquisition time and consequent narrow bandwidth per pixel in the PE direction.

### *2.12.3.1 Nyquist Ghosting*

Any difference between alternate lines in k-space will lead to a ghost image shifted by $FOV_{PE}/2$. This is called the Nyquist or N/2 ghost. Differences between alternate lines can arise from any imperfection in the signal because the signals from every second line must be reflected in time before placing them in k-space. Sources of signal imperfections that lead to ghosting include eddy currents and the low-pass filtering in the RF receive system.

The simplest effect of eddy currents is to cause a time delay between the current in the coil and the gradient as well as a gradient amplitude reduction. Figure 4 illustrates how such a time shift causes ghosting. It is therefore possible to mitigate ghosting caused in this way by adjusting the analog-digital converter (ADC) data acquisition timing so that it is exactly in phase with the resultant gradient. Residual ghosting will remain if there is a variable time shift across the FOV caused by any asymmetry in the eddy currents (or the structures in which they occur) with respect to the gradient-producing currents.

A further mechanism by which eddy currents cause N/2 ghosting is by their asymmetry, which causes $B_0$ modulation. Such asymmetry can arise from misalignment of the

gradients and the structures in which the eddy currents occur such as the magnet shield. This means that the eddy currents produce a $B_0$ field which changes from line to line with the polarity of the read gradient and leads to phase differences between odd and even lines which then produce N/2 ghosts.

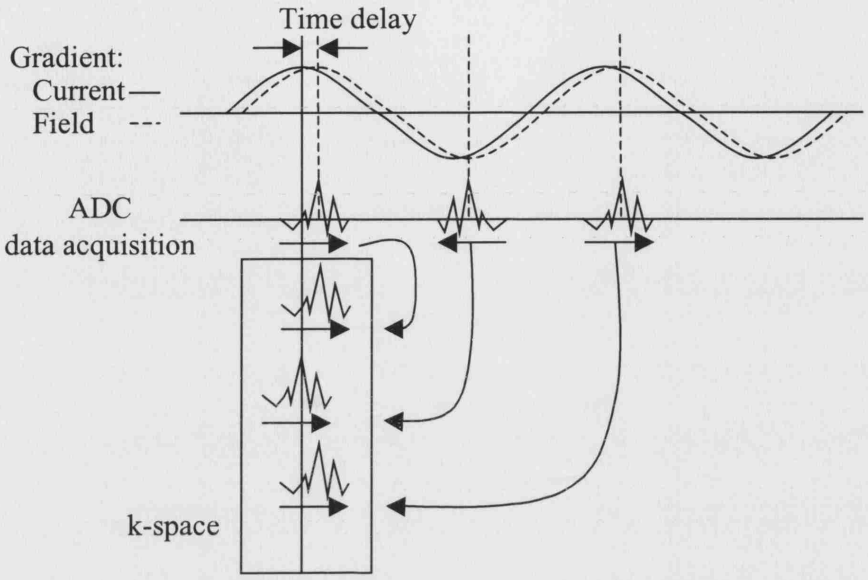


**Figure 4 Eddy Currents as a Cause of Nyquist Ghosting**
The figure illustrates a misalignment of gradient and ADC timing because of a time delay due to eddy currents. Every second echo must be time-reversed before putting it into k-space so the time delay leads to a zig-zag pattern of echoes in k-space and therefore ghost artifacts.

Low-pass filtering of the MR signal is necessary to reduce noise with a frequency greater than the sampling rate. Applying such low-pass filters can cause a time delay in the signal, which causes ghosting in a similar way to the delay resulting from eddy currents (see Figure 4). Again, ghosting due to the time shift can be reduced by adjustment of ADC timing.

#### 2.12.3.1.1 Methods for Nyquist Ghost Reduction

Hardware modifications that should minimise ghosting include ensuring gradient stability and minimal eddy currents. We have already seen that timing delays can be introduced to ensure that the sampling train is exactly coincident with the gradient waveform and such delays (μs) were introduced in all EPI sequences in this work. Alternative methods to mitigate N/2 ghosts include using calibration or reference scans to correct the EPI data. The principle is to collect non-phase-encoded navigator echoes and use them to correct the phase and time shifts between the odd and even EPI echoes.

The latter (time shifting) is equivalent to aligning the PE lines in Figure 4. It is possible to acquire either a full reference calibration scan in which the same number of navigator echoes is collected as the number of PE lines that form the image. Alternatively two to three navigator echoes can be acquired and used to correct the whole raw data matrix. In this work full reference calibration scans were acquired and used to correct the EPI data.

### *2.12.3.2 Artifacts Due to the Low PE Bandwidth per Pixel*

As illustrated in Figure 3 the time (ES) between points in the PE direction is longer than the sampling period ($\Delta t$) in the read (FE) direction by a factor approximately equal to the number of points in the readout direction ($N_{FE}$). The total bandwidth in each direction is given by the inverse of the corresponding acquisition time per point. Therefore the bandwidth per pixel ($BW_{pixel}$) in each direction is this inverse divided by the number of points in each direction. In this way

$$BW_{pixel-FE} = \frac{1}{N_{FE}.\Delta t} \approx \frac{1}{ES}$$

**Equation 31**

$$BW_{pixel-PE} = \frac{1}{N_{PE}.ES}$$

**Equation 32**

We can therefore see that the bandwidth per pixel in the PE direction is much smaller than in the FE direction and this is the main cause of several artifacts described below.

#### 2.12.3.2.1 Chemical Shift Artifacts

When protons are in different chemical environments (such as in fat or water molecules) they have different resonant frequencies due to the changes in the orbital motion of electrons which act to reduce the main magnetic field experienced by the nuclear protons. The screened field is expressed as

$$B = B_0(1-\sigma)$$

**Equation 33**

where $\sigma$ is a shielding constant and is approximately 3.3 ppm for fat relative to water. Fat protons therefore have a resonant frequency lower than water protons and this chemical shift results in a displacement of the fat signal relative to the water signal. The shift $\Delta$PE (in number of image pixels) can be calculated using:

$$\Delta_{PE} = \frac{\gamma \sigma B_0}{BW_{pixel-PE}} = \gamma \sigma B_0 N_{PE} ES$$

**Equation 34**

which gives nearly 17 pixels fat-water shift for a 64 PE-line EPI with ES = 400μs at 4.7T. It is obvious from Equation 34 that this artifact worsens at higher main magnetic field strength $B_0$. The corresponding shift in the FE direction is sub-pixel since it is less by a factor $N_{PE}$.

#### 2.12.3.2.2 Geometric Distortion

Other artifacts arising due to the low $BW_{pixel-PE}$ are geometric distortions. These are one type of susceptibility artifact arising due to differences in magnetic susceptibility $\chi$ between different tissues, which cause spatial variation in the magnetic field (see Equation 38) and this is discussed in greater detail in section 2.13. The other types of susceptibility artifacts are discussed in section 2.12.3.3.

Magnetic field inhomogeneities, for example at the boundary between air and soft tissue with a susceptibility difference $\Delta\chi$, cause local geometric distortion (d in mm)

$$d = \frac{\Delta\chi B_0}{G} = \gamma \Delta\chi B_0 N_{PE} ES \Delta y$$

**Equation 35**

In this equation G is the constant PE gradient amplitude that would provide the same $\Delta k_{PE}$ as the blipped PE gradients. This distortion is worse for higher $B_0$ and can be reduced by increasing the amplitude of the phase-encoding gradient blips (equivalent to increasing G) or reducing the number of PE lines or the echo spacing ES. However these sequence modifications will change the k-space sampling leading to changes in image FOV and resolution (see Equation 29 and Equation 30). As the image is stretched or compressed by the geometric distortion there is a corresponding variation in image intensity because the intensity is proportional to the volume of tissue it represents.

### *2.12.3.3 Signal Drop-Out and $T_2^*$ Blurring*

It is possible to decompose the effects of local susceptibility gradients on EPI into through-plane and in-plane components. The in–plane gradients are primarily responsible for the geometric distortion described in section 2.12.3.2.2 but can cause

signal drop-out if they are extremely large as explained below. However, through-plane gradients mainly cause image intensity loss and alteration of $T_2^*$ relaxation characteristics.

If an in-plane local susceptibility gradient is strong enough with respect to the phase encoding gradient, the echo may form so early or late that it is pushed outside the EPI acquisition window. In this case there is total loss of signal known as drop-out. Because the data reconstruction is performed with the ideal TE taken as the centre of k-space, any temporal shift in the echo due to in-plane susceptibility gradients leads to a phase shift upon Fourier transformation and therefore to phase dispersion across the voxel and signal reduction.

Drop-out can also occur when the through-plane susceptibility gradient across a voxel is sufficient to cause total dephasing of the spins within that voxel before they are sampled so that there is no net signal from the voxel. In general, through-plane susceptibility gradients cause spin dephasing and thus an image intensity loss, which depends on the magnitude of the susceptibility gradient, the slice thickness and the echo time.

The signal in EPI also depends on $T_2^*$ (see Equation 15). The fact that the ideal EPI signal is multiplied by the $T_2^*$ signal decay envelope leads to image blurring (pixel broadening) and signal reduction. Blurring can be understood using the FT convolution theorem which means that multiplying the time or k-space signal by a decay function is equivalent to convolving the transformed image data with a point spread function (PSF) given by the FT of the decay function. The signal reduction can be understood to arise from field inhomogeneities caused by susceptibility and other effects since:

$$\frac{1}{T_2'} \approx \gamma \Delta B$$

**Equation 36**

so there is rapid dephasing in regions of inhomogeneity leading to signal loss and image blurring.

## 2.13 A General Framework for Understanding the Effects of Static Magnetic Field Inhomogeneities on the MR Signal

First of all it is useful to note that main magnetic field inhomogeneities $\Delta B_0$ are often caused by the presence of objects or structures of different magnetic susceptibilities $\chi$. In the simplest case for linear materials in which the magnetisation M is proportional to the H field:

$$M = \chi H$$

**Equation 37**

and the magnetic field B is also dependent on the susceptibility

$$B = (1 + \chi)\mu_0 H$$

**Equation 38**

where $\mu_0$ is the permeability of free space.

Most tissues in the body are weakly diamagnetic, having susceptibilities similar to water (~ -9 ppm). The change in B or the inhomogeneity $\Delta B_0$ between different tissues is in general a function of the difference in susceptibility between the two tissues $\Delta\chi$:

$$\Delta B_0 = f(\Delta\chi) \propto B_0$$

**Equation 39**

The exact form of the function will vary depending on the geometry of the regions and there is not always a simple analytical solution. The size of the inhomogeneities increases with both $\Delta\chi$ and the external main magnetic field $B_0$. This means that field inhomogeneities, and therefore susceptibility artifacts, are worse at higher field strengths.

When examining the effect on the MRI signal of these main magnetic field inhomogeneities, caused primarily by susceptibility differences, it is assumed that the inhomogeneities are static. It is useful to divide the inhomogeneities and their effects into different regimes.

One classification is based on the relative importance of two processes of which the first is the accumulation of different spin phases through a sample due to the different local

frequencies experienced by different spins. This is reversible (on application of a spin refocusing RF $\pi$ pulse). The second is irreversible signal loss due to molecular diffusion causing a loss of phase memory. If spins are dephased due to field inhomogeneities before molecular diffusion can average out their phases then they are in the so-called *static dephasing* regime. However if the converse is true and diffusion and flow affect the signal before it is dephased by static inhomogeneities this is described as the *motional-narrowing* regime. This classification is mostly applied to the mesoscopic regime discussed below.

A second classification is based on the relative sizes of the magnetic field inhomogeneities with respect to the image voxels. Changes in magnetic field over atomic or molecular distances are *microscopic* and fluctuating microscopic field inhomogeneities lead to the irreversible $T_2$ decay described in section 2.8. The *mesoscopic* regime is one in which the field inhomogeneities are much smaller than the image voxel size but also much bigger than the atomic or molecular scale. Hence $1/T_2'$ (see Equation 36) is a relaxation rate constant due to static mesoscopic magnetic field inhomogeneity effects which are not altered by imaging gradients. This regime is the one in which susceptibility-based contrast changes occur due to red blood cells in capillary networks, paramagnetic contrast agents and bone trabeculae amongst others. An extensive study of dephasing in this regime has been carried out by Yablonskiy and Haacke [16] and applied in a phantom study [17].

If the size of the inhomogeneity is greater than or similar to the voxel dimensions this is described as the *macroscopic* regime. In this regime the signal decay no longer follows the exponential form and depends on voxel size and imaging gradients. This is the regime in which undesirable susceptibility image artifacts occur, for example because of air sinuses inside the head. The detailed effects of inhomogeneities in this regime on gradient-echo images are discussed in Reichenbach et al [18] and by Haacke et al in Chapter 20 of their book [19].

# 3 Radio-Frequency Pulse Sequence Development for Reduction of $B_1$-Inhomogeneity

## 3.1 Background and Specific Theory

### 3.1.1 $B_1$ Inhomogeneity at High Field Strength

There have been many observations (see Figure 5) and numerical calculations demonstrating that the radio frequency $B_1$ field in the human head is increasingly inhomogeneous at higher field strengths. Computational simulations include those at 63, 175, 200 and 300 MHz by Collins et al [20] and those at 1.5, 3 and 6 T by Jin et al [21]. Investigators who have compared experimental observations with numerical calculations include Alecci et al at 3 T [22], Vaughan et al at 4 T and 7 T [11] and Ibrahim et al at 8 T [23].

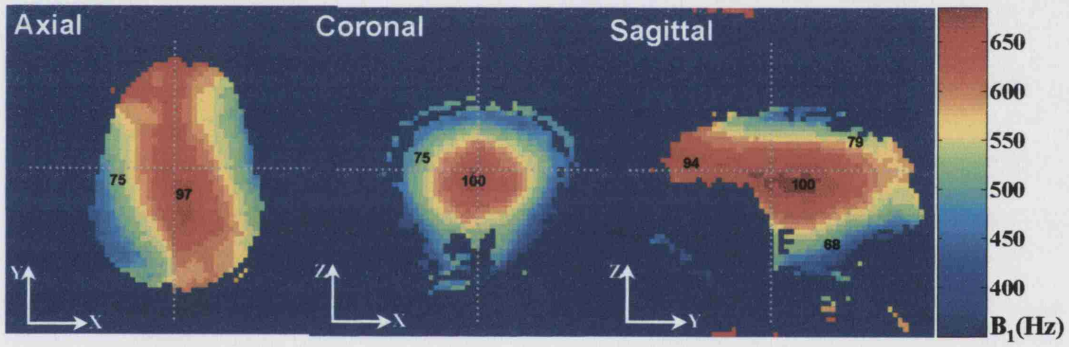


**Figure 5 $B_1$ Maps of a Human Head**
$B_1$ maps of Axial, Coronal and Sagittal slices through a human head at 4.7 T. The $B_1$ mapping method used ($B_1$ amplitude scale in Hz) was based on acquisition of a set of SE-EPI images acquired using hard RF pulses with a range of different durations. The $B_1$ mapping method is described in detail in De Vita [7]

At high main magnetic ($B_0$) field strengths RF fields interact more strongly with human tissues. This is because the RF operational frequency (equal to the Larmor frequency) increases with field strength (see Equation 6) and the wavelength in the sample** becomes comparable to the head/body size and RF coil dimensions, so that interactions between the tissue and the RF coil become increasingly important.

---

** From this point forward when the term 'sample' is used it should be taken mean the object, phantom or area of the body under MRI investigation.

The RF-sample (electrodynamic) interactions that contribute to $B_1$-inhomogeneity, as shown in Figure 5, can be understood as a combination of both conductivity-dependent RF penetration or attenuation effects and permittivity-dependent dielectric or standing wave effects. The former arise because eddy currents are induced in the conductive human tissues and at high frequencies these cause so much attenuation of the $B_1$ field that its penetration becomes limited to a 'skin depth'. The skin depth for a uniform sample is given by

$$\delta = \sqrt{\frac{2}{\mu_r \mu_0 \omega \sigma}}$$

**Equation 40**

where $\omega$ is the $B_1$ frequency, $\mu_r$ and $\mu_0$ are the relative and free space permeabilities respectively and $\sigma$ is the conductivity [24]. Röschmann [25] derived effective RF penetration depths in the human body from experimental resonance frequency shift data and calculated that the effective penetration depth drops from 17cm at 85MHz to 7cm at 220 MHz.

The dielectric or standing wave effects occur because, as described, the effective (permittivity-dependent) wavelength in the sample becomes comparable to or smaller than the dimension of the human body. For example the wavelength for a circularly polarized RF standing wave in a cylinder is given by

$$\lambda = \frac{2\pi}{\omega \sqrt{\frac{1}{2}\varepsilon_r \varepsilon_0 \mu_r \mu_0 \left(1 + \sqrt{1 + \frac{1}{\rho^2 \varepsilon_r^2 \varepsilon_0^2 \omega^2}}\right)}}$$

**Equation 41**

where $\omega$ is the frequency of the magnetic field, $\varepsilon_r$ and $\varepsilon_0$ are respectively the relative and free space permittivities, $\mu_r$ and $\mu_0$ the respective permeabilities and $\rho$ is the resistivity of the medium [24]. These wavelength effects cause the phase and amplitude of the $B_1$ field to vary substantially with position and $B_1$ is often strongest at the centre of the sample prompting Hoult [26] to call this inherent $B_1$ inhomogeneity the 'field focusing' effect.

A special case of standing wave or field focusing effects is 'dielectric resonance' when the diameter of the sample is equal to an integral number of RF wavelengths. Hoult [26]

writes that resonance only occurs when this is true 'to a considerable accuracy'. Röschmann [27] refers to this as the $B_1$-eigenfield arising from the solution of Maxwell's equations but observes that central enhancement of $B_1$ occurs even at off-resonance conditions.

This observation serves to emphasise the distinction between dielectric resonance and central brightening or field focusing. Collins [28] demonstrates that central brightening can be observed even in a case where dielectric resonance gives a central magnetic field minimum. He concludes that central brightening is a result of multiple current sources and wavelength effects in the sample causing constructive interference at the centre rather than a resonance effect. Kangarlu [29] also observed that the presence of significant conductivity suppressed dielectric resonances in water (saline) phantoms, where the dominant effect was then coupling between source and phantom. Similarly Yang [30] concludes that dielectric resonances cannot be sustained in the head because of the strong decay of the RF electromagnetic waves caused by sample resistance and that the inhomogeneous $B_1$ fields are a result of the interference pattern of decaying travelling waves in a given sample-coil configuration (plus near field contributions).

It should also be borne in mind that the RF wavelength will also become comparable to the length of the coil elements at high frequencies leading to a standing wave pattern of currents along the coil axis which can produce significant $B_1$ inhomogeneity along the coil axis [22]. So we can see that $B_1$ inhomogeneity depends on the interaction of a variety of factors including operating frequency, coil size, sample size and dielectric and conductive properties of the sample. It is the strong interactions between the RF coil (and in particular the excitation sources [12]) and the sample that dominate at high field, leading to non-uniform current distributions on the RF coil struts and therefore inhomogeneous $B_1$ fields.

#### *3.1.1.1 The Effects of $B_1$ Inhomogeneity*

Transmit $B_1$ inhomogeneity will cause flip angles to vary with location giving spatially dependent sensitivity and SNR and non-uniform image contrast that does not depend solely on tissue properties. This can result in image non-uniformity or a spatial dependence of apparent metabolite concentrations in MR spectra [31]. The spatial variation of flip angle also makes pulse calibration more difficult.

Non-uniform images may cause problems for brain-segmentation algorithms based on (image-wide) tissue contrast thresholds. The validity of the statistical analyses used to produce statistical parametric maps of brain activation in fMRI may also be compromised when image sensitivity varies through the brain volume

All these drawbacks of $B_1$-inhomogeneity make it desirable to overcome the problem and there are several methods that have been proposed to do this which will be described in the next section. The methods discussed here are 'at source' acquisition-based corrections rather than image post-processing solutions.

### *3.1.1.2 Approaches for Improving $B_1$ Homogeneity*

In this section examples of previous approaches to the problem are discussed with their advantages and disadvantages.

#### 3.1.1.2.1 Hardware modifications

Several approaches have been made to mitigate the effects of $B_1$ inhomogeneity in high field imaging. One method involves the placement of dielectric loading materials with a high dielectric constant or permittivity (i.e. water bags) between the coil and sample to manipulate the $B_1$ field distribution and therefore improve the MR image intensity distribution [32].

It is also possible to design and drive coils for optimised $B_1$ uniformity [12], [33]. For example Ibrahim showed that four-port drive of birdcage RF coil at 200MHz increased $B_1^+$ homogeneity to 52% compared with 37% for quadrature excitation. Optimisation of the phases between the excitation sources increased the homogeneity further to 63% [34]. Similarly for a TEM resonator operating at 8T he found that the $B_1$ inhomogeneity could be minimised when all 24 ports were driven with optimised variable phases and magnitudes [12].

Failing optimised coil design and excitation, active transmit power modulation for each axial slice has been demonstrated to reduce the $B_1$ variation along the z-axis [35]. However this method is unable to remove inhomogeneities in the x-y plane.

#### 3.1.1.2.2 RF pulse design approaches

It is possible to compensate for $B_1$ variation along two directions (simultaneously) as shown by Deichmann [36] for MP-RAGE structural imaging. He uses two RF pulses applied in orthogonal directions with each having an excitation profile calculated to compensate for the quadratic $B_1$-variation observed in each direction.

Saekho [37] extends $B_1$ compensation to all three dimensions by using 3D Tailored RF pulses. The approach uses the inverse of inhomogeneous brain images to design a two-shot RF and gradient combination to remove $B_1$-inhomogeneity in a 10 cm-thick slab that is subsequently acquired using a conventional low flip angle gradient-echo imaging sequence.

A simpler approach that aims to correct $B_1$-non-uniformity in a single slice is the sequence of composite excitation pulses proposed by Thesen [38]. Here the conventional $90_x$ pulse prior to gradient-echo EPI acquisition is followed by a $90_y$ pulse with 90° phase offset so that spins that have not reached or overshot the transverse plane are excited into it whilst the spins that were excited to the y-axis are locked along the axis.

Many approaches to reducing $B_1$-inhomogeneity are based on RF pulses that achieve a specified flip angle, leaving the magnetisation in a desired orientation with a degree of independence on the $B_1$ amplitude. In most cases the pulses do not just have an amplitude 'envelope' over a single (Larmor) carrier frequency but are also frequency- (or equivalently phase-) modulated, meaning that the carrier frequency is also varied (or swept) during the pulse.

##### 3.1.1.2.2.1 HS Pulses for Inversion

Perhaps the most well-known and simplest of these $B_1$-insenstive pulses is the adiabatic hyperbolic secant pulse for slice-selective inversion [39, 40, 41].

The Hyperbolic secant (HS) pulse can be expressed in several forms [42] (see Figure 6):

Complex function: $$B_1(t) = B_{1max}(\mathrm{sech}(\beta t))^{1+i\mu}$$

**Equation 42**

Amplitude modulated AM function: $B_1(t) = B_{1max}\text{sech}(\beta t)$

**Equation 43**

Frequency modulated FM function: $\Delta\omega(t) = \omega_{RF} - \omega_L = -\mu\beta \tanh(\beta t)$

**Equation 44**

where $\Delta\omega(t)$ is the frequency offset of the $\omega_{RF}$ $B_1$ field from the central Larmor frequency $\omega_L$ at a particular position (rad.s$^{-1}$), $\beta$ is a real constant (rad.s$^{-1}$) and $\mu$ is a real constant. The complex function (Equation 42) is a complete description of the pulse, which is alternatively described by the AM and FM functions together (Equation 43 and Equation 44). The frequency modulation can also be understood as the differential of a phase modulation function.

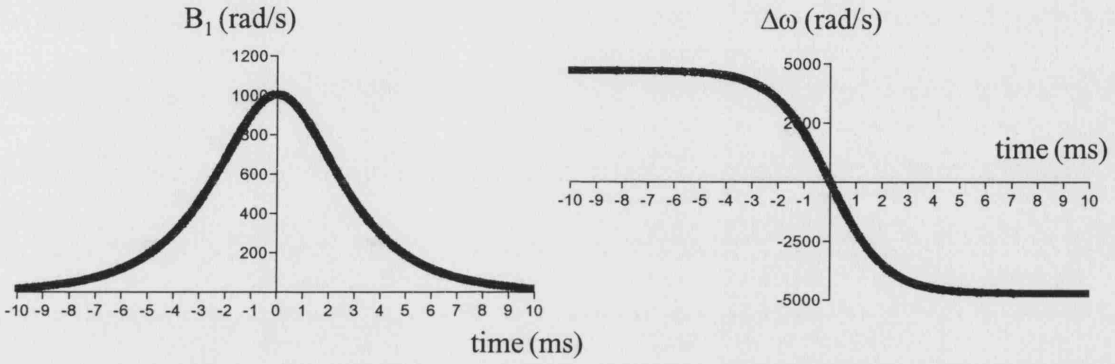


**Figure 6 Amplitude and Frequency of the Hyperbolic Secant Pulse**
The amplitude ($B_1$) and frequency ($\Delta\omega$) modulation functions for the Hyperbolic Secant Radio Frequency Pulse.

The mechanism by which these pulses result in inversion of magnetisation can be understood with the help of the 'frequency-modulated frame' ($\omega_{RF}$ frame), which rotates at the instantaneous frequency of the $B_1$ field $\omega_{RF}$ so that the $B_1$ orientation is stationary in this frame during an adiabatic HS pulse. If $\omega_{RF}$ differs from $\omega_L$ there will be a net longitudinal magnetic field $\Delta B_{0HS}$ in the $\omega_{RF}$ frame equal to

$$\Delta B_{0HS} = \frac{-\Delta\omega(t)}{\gamma} = \frac{\omega_L - \omega_{RF}}{\gamma}$$

**Equation 45**

The effective magnetic field in the $\omega_{RF}$ frame $B_{eff}$ is then the vector sum of $\Delta B_{0HS}$ and $B_1$

$$\left|B_{eff}\right| = \sqrt{\Delta B_{0HS}^2 + B_1^2}$$

**Equation 46**

and is at an angle $\alpha$ from the z'axis where

$$\tan(\alpha) = \frac{B_1}{\Delta B_{0HS}}$$

**Equation 47**

Figure 7 illustrates the trajectory of $B_{eff}$ in the $\omega_{RF}$ frame during the HS pulse.

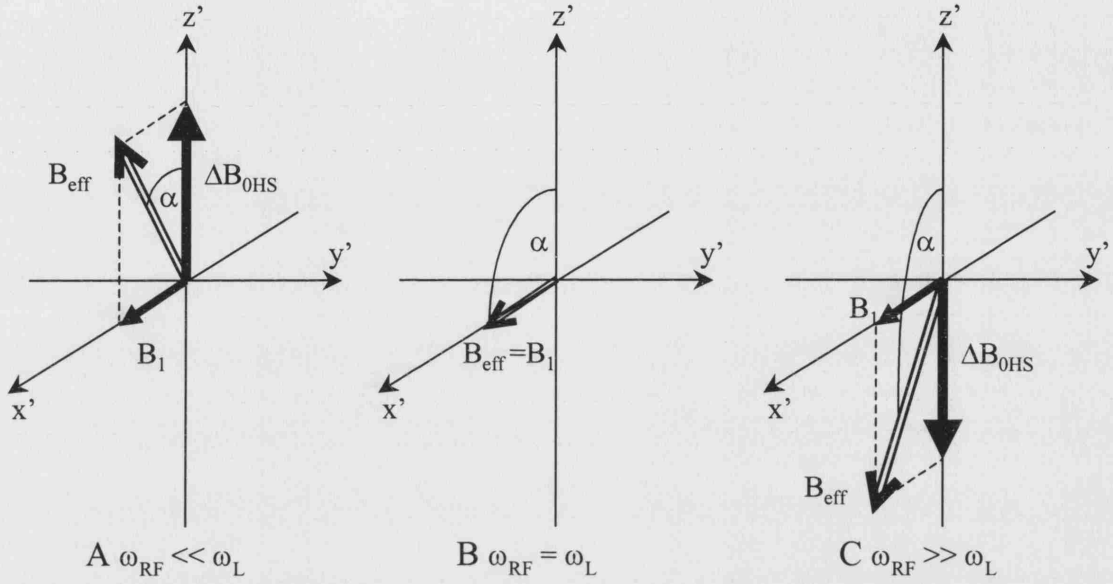


**Figure 7 Trajectory of the Effective Field in the Frequency Modulated Frame During the Hyperbolic Secant Inversion Pulse**
A schematic diagram illustrating the trajectory of the effective field $B_{eff}$ and its components in the frequency-modulated $\omega_{RF}$ frame during the Hyperbolic Secant Inversion pulse. The three conditions or time points correspond to the instantaneous radio frequency $\omega_{RF}$ being **A** far below the resonant frequency $\omega_L$, **B** at resonance, and **C** far above resonance.

Assuming $\omega_{RF} << \omega_L$ at first, meaning that the pulse starts far below resonance, $\Delta B_{0HS}$ is large relative to $B_1$ and $B_{eff}$ starts almost parallel to the z' axis of the $\omega_{RF}$ frame. As $|\Delta\omega(t)|$ decreases $B_{eff}$ rotates towards the transverse plane (in which it lies when $\omega_{RF} = \omega_L$) and as $\Delta\omega(t)$ changes sign $B_{eff}$ rotates further until it comes to its final orientation almost parallel to -z' when $\omega_{RF} >> \omega_L$.

To understand what happens to the magnetisation during the pulse it is useful to introduce a further frame of reference known as the second rotating frame or the doubly rotating frame of reference ($\omega_{eff}$ frame) in which $B_{eff}$ is stationary (see Figure 8).

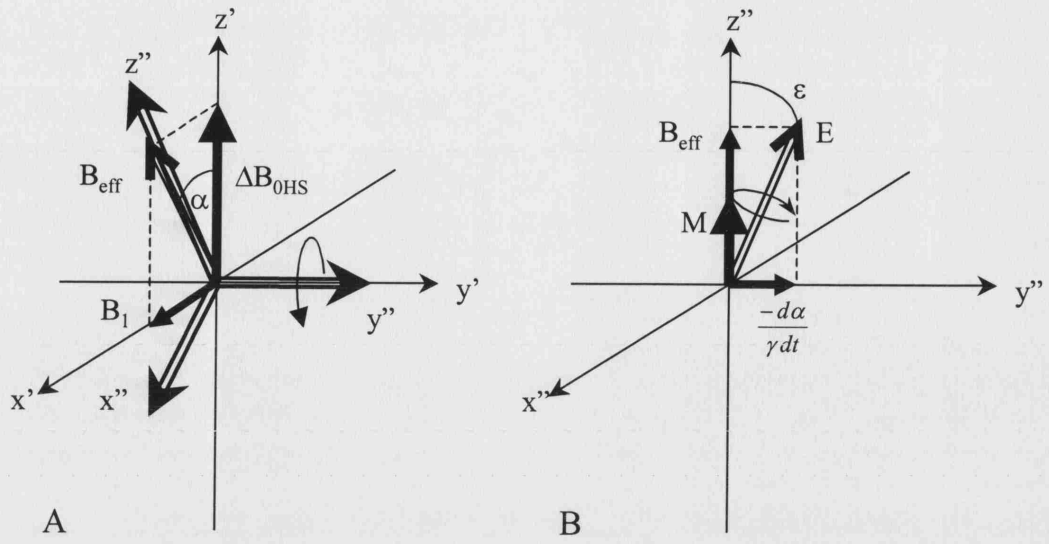


**Figure 8 Frames of Reference for the Hyperbolic Secant Pulse**
Diagrams to illustrate the effective field and its components in two frames of reference for a Hyperbolic Secant pulse. **A** Relationship between the $\omega_{RF}$ frame (x', y', z') and the $\omega_{eff}$ frame (x", y", z"). **B** Components of the resultant field E and evolution of the magnetisation vector M in the $\omega_{eff}$ frame.

During the HS pulse the $\omega_{eff}$ frame rotates about the $\omega_{RF}$ frame with angular velocity $\frac{d\alpha}{dt}$ so that there is a fictitious or effective magnetic field in the $\omega_{eff}$ frame equal to $\frac{-d\alpha}{\gamma dt}$ similarly to $\Delta B_{0HS}$ in the $\omega_{RF}$ frame. In the same way as for $B_{eff}$ the resultant field in this frame E(t) will then be the vector sum of $B_{eff}$ and $\frac{-d\alpha}{\gamma dt}$ and the magnetisation will precess about E on a cone of angle ε. If $\frac{-d\alpha}{\gamma dt}$ is small compared to $B_{eff}$, ε will be small and the magnetisation will always remain within an angle 2ε from E ≈ $B_{eff}$ . This means that the magnetisation will follow the motion of $B_{eff}$ in the $\omega_{RF}$ frame if

$$\left|\frac{d\alpha}{\gamma dt}\right| << \left|B_{eff}\right|$$

**Equation 48**

throughout the pulse and this is known as the adiabatic condition. A pulse is adiabatic if this condition is satisfied, and for the adiabatic HS inversion pulse described, the initial z-magnetisation is inverted because it is initially almost collinear with $B_{eff}$ which rotates by π in the $\omega_{RF}$ frame. Similarly magnetisation that is initially perpendicular to $B_{eff}$ should remain so (to within ± ε) when the adiabatic condition is satisfied [43].

Two transformations of the magnetisation are well defined for such adiabatic 'rapid-passage' pulses: adiabatic full passage (AFP) (inversion) and adiabatic half-passage (AHP) (excitation). An adiabatic half-passage (AHP) is equivalent to running only half of the full HS pulse (i.e. from t = -T/2 to t = 0 in Figure 6 where T is the full pulse duration). An AHP can only result in slice-selective excitation for a single isochromat because the time at which ($B_{eff}$ and therefore) the magnetisation reaches the transverse plane varies with the magnitude of the offset $\Delta\omega(t)$ and the pulse amplitude $B_{1max}$.

*3.1.1.2.2.1.1 Off-resonance spins and frequency-selectivity:*

In the presence of off-resonance spins

$$\Delta B_{0HS} = \frac{-\Delta\omega(t)}{\gamma} + \frac{\Omega}{\gamma} = \frac{\mu\beta}{\gamma}\tanh(\beta t) + \frac{\Omega}{\gamma}$$

**Equation 49**

where $\Omega$ is the resonance offset ($rad.s^{-1}$) which may be caused by a slice-selective gradient

$$\Omega = \gamma G_z z$$

**Equation 50**

This can be written as

$$\gamma\Delta B_{0HS} = \mu\beta f_{\omega}(t) + \Omega$$

**Equation 51**

where $f_{\omega}(t)$ is a driving function that goes between ±1 during the pulse and means that at the beginning and end of the pulse

$$\gamma B_{eff} = \Omega \pm \mu\beta$$

**Equation 52**

From this equation and in Figure 9 we can see that the $B_{eff}$ trajectory defines an inversion provided that $|\Omega| < |\mu\beta|$ (as deduced by Conolly from his sweep diagram analysis[44]). This means that adiabatic HS pulses are inherently frequency-selective (or slice-selective in the presence of a slice-select gradient) and the bandwidth over which the pulse inverts is related not to the amplitude but to the frequency sweep via

$$BW(Hz) = \frac{\mu\beta}{\pi}$$

**Equation 53**

Typical values of μ and β are, respectively, 1-10 and thousands of rad.s$^{-1}$.

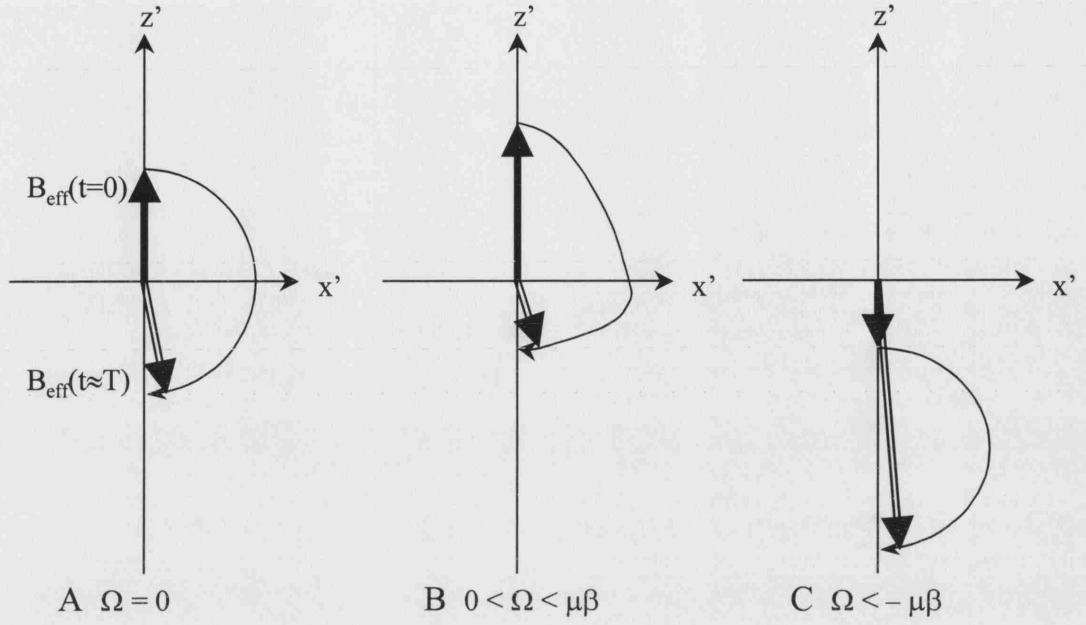


**Figure 9 Sweep Diagrams at Different Resonance Offsets for the Hyperbolic Secant Inversion Pulse**

Sweep diagrams illustrating the trajectory of the effective field $B_{eff}$ during the Hyperbolic Secant pulse for different frequency offsets in the new $\omega_{RF}$ frame. The solid vector represents $B_{eff}$ at the beginning of the pulse and the other vector represents $B_{eff}$ near the end of the pulse (t~T). The thin line shows the trajectory traced by the tip of the $B_{eff}$ vector. In **A** there is no offset. In **B** there is a positive frequency offset $\Omega<\mu\beta$ so the magnetisation will still be inverted. In **C** there is a negative offset of greater magnitude than the frequency modulation so that the magnetisation is not inverted and this is effectively outside the inversion slice.

*3.1.1.2.2.1.2 Practical issues encountered when implementing these pulses:*

For a given bandwidth μ determines how 'sharp' the slice is, with higher values of μ yielding squarer inversion profiles. The slice inversion profile is also affected by the level at which the pulse is 'cut-off', usually given as the amplitude (as a percentage of the maximum) at which the pulse starts or ends, and conventionally set such that sech(βT/2) ~ 0.01 [39], [45]. Thus the cut-off will be affected by the pulse duration (T) as well as by μ and β, so that inversion profiles will be degraded as $B_{1max}$ values increase if the pulse duration is not increased accordingly. However de Graaf and Nicolay [46] suggest removing the cut-off from the pulses to improve inversion profiles, but this may require a corresponding increase in $B_{1max}$ to ensure that adiabaticity is maintained.

Adiabatic HS pulses are often termed '$B_1$-insensitive' because the inversion is insensitive to increases in $B_{1max}$ beyond the threshold needed to satisfy the adiabatic

condition. Again this can be understood from the sweep diagram (Figure 9) since increases in $B_1$ only stretch the trajectories of $B_{eff}$ in the x direction but do not change the net angular trajectory. Silver et al [40] give this critical amplitude threshold as

$$B_{1\max} \geq 0.4\frac{\mu\beta}{\pi}$$

**Equation 54**

and state that as $B_{1max}$ is increased the profile of the inversion remains unaffected.

### 3.1.1.2.2.2 Spin-Echo Sequence with Refocusing by Two HS Pulses [47]

Although the HS pulse is most commonly used for inversion, a pair of HS pulses has been used for refocusing in spin-echo sequences [47] (see Figure 17). As stated above, magnetisation that is initially perpendicular to $B_{eff}$ should remain so and this is the basis of the use of the adiabatic HS pulse for refocusing. However the perpendicular spins precess about the $B_{eff}$ field at the Larmor frequency (i.e. $\gamma B_{eff}$) and therefore accumulate an additional phase given by:

$$\left|\phi(B_{1\max}, z)\right| = \gamma \int_{-T/2}^{T/2} \left\| B_{eff}(B_{1\max}, z, t) \right\| dt$$

**Equation 55**

where T is the pulse duration and z is the slice-selection direction. The quadratic z-dependence of this phase originates in the z-dependent offset (see Equation 46, Equation 49 and Equation 50). This phase is quadratic in z and a second identical HS pulse is therefore used for refocusing in order to compensate the quadratic phase resulting from the first. The effect of the second identical HS 180° pulse is to reverse the quadratic phase distribution resulting from the first HS 180° pulse and to add its own quadratic phase distribution of the same magnitude. The positive and negative quadratic phase distributions cancel leaving no net spatial phase variation.

Since two (high power) HS pulses are required for refocusing, only the second echo has no net phase. This extends the minimum spin-echo sequence length and means that the sequence has quite a high specific absorption rate (SAR) (see section 2.7).

### 3.1.1.2.2.3 Spin-echo sequence with Linearly Frequency-Modulated Pulses [48], [49]

An alternative spin-echo sequence to Conolly's uses linearly frequency-modulated pulses (LFM) pulses based on a linear frequency sweep for both refocusing and excitation [48], [49].

The LFM pulse is given by

$$B_1(t) = B_{1max} \exp\left(i\pi a t^2\right)$$

**Equation 56**

where $B_{1max}$ is the maximum amplitude and ***a*** is a constant sweep velocity ($s^{-2}$). In practice this LFM pulse has constant amplitude and varying phase, but it must be multiplied by a suitable 'windowing' function. Kunz [48], [49] applies a windowing function with Gaussian edges to give a desired frequency bandwidth by Fourier transforming $B_1(t)$ into the frequency domain, windowing and then inverse transforming the windowed function back into the time domain.

Since these pulses are frequency-modulated they have similarities with the HS pulse described above: Figure 10 and Figure 11 show how the LFM pulse can be visualised as either frequency- or phase-modulated. Once windowed these pulses are selective over a bandwidth given by the extent of the frequency sweep

$$BW(Hz) = aT$$

**Equation 57**

where T is the pulse duration.

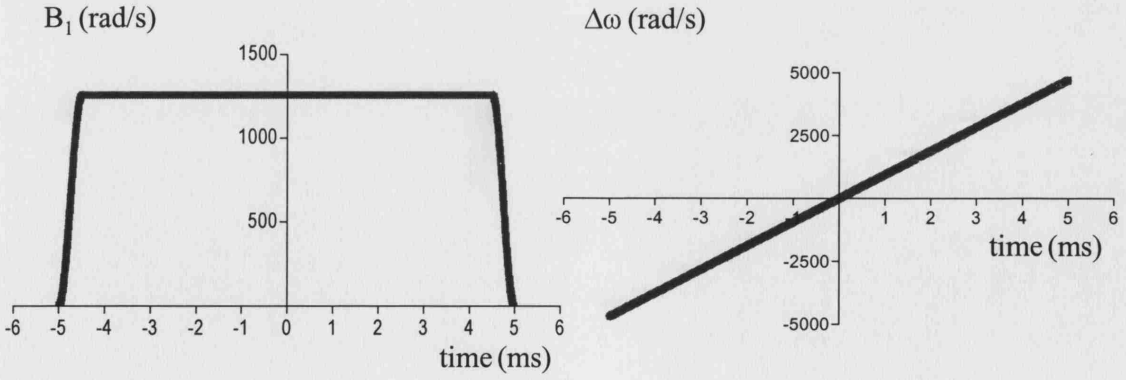


**Figure 10 Amplitude and Frequency of the Linearly Frequency Modulated Pulse**
The amplitude ($B_1$) and frequency ($\Delta\omega$) modulation functions for the Linearly Frequency-Modulated Radio Frequency Pulse.

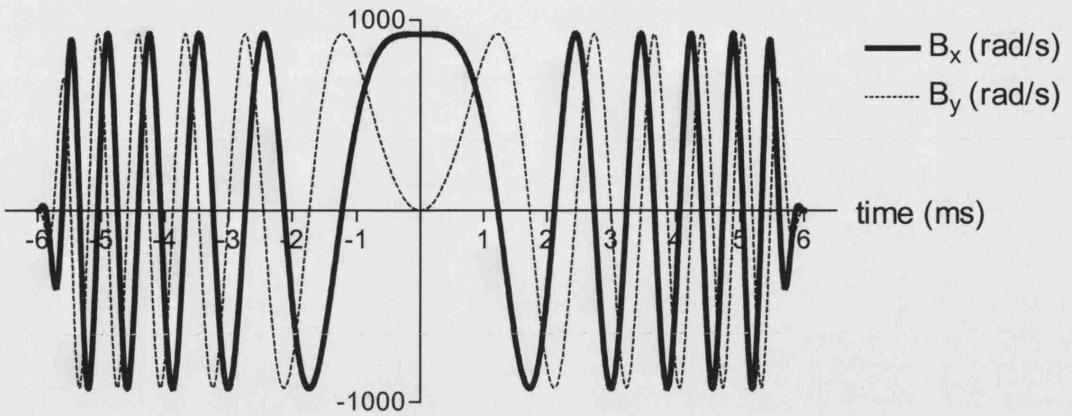


**Figure 11 Real and Imaginary Components of the Linearly Frequency Modulated Pulse**
The (time-windowed) $B_1$ field components ($B_x$ and $B_y$) for the Linearly Frequency-Modulated (LFM) Radio Frequency Pulse. The varying time lag between $B_x$ and $B_y$ demonstrates that the LFM pulse can be viewed as a phase-modulated pulse.

Similarly to the HS pulses these LFM pulses can be used for both refocusing and excitation and generate a quadratic phase [50] perpendicular to the selected slice. The spatial variation of quadratic phase follows a simple relationship

$$\phi = \frac{2\pi\nu^2}{a}$$

**Equation 58**

where

$$\nu = \gamma G_z z$$

**Equation 59**

when the pulse is used for refocusing, and half of this phase variation when it is used for excitation.

In Kunz's implementation of the spin-echo sequence the excitation and refocusing pulses are applied with identical slice-select gradients. This means that for the quadratic phases to compensate each other the sweep rate (***a***) of the 180° pulse must be twice that of the 90° pulse. For equal bandwidths (and slice thicknesses) for both pulses it is then necessary to apply the 180° pulse for half the duration of the 90° pulse.

An advantage of this method over the double-HS refocusing sequence is that it has one less pulse in total, leading to less power deposition (SAR) Unlike the double-HS

method, only odd echoes can be acquired as only these will have no net phase across them. This has the advantage that the sequence is shorter since the first echo can be used.

A potential disadvantage of the sequence is that an LFM $\pi$ pulse can have as much as twice the SAR of an amplitude-modulated pulse of the same BW and flip angle. However LFM pulses require a lower peak power than the corresponding amplitude-modulated pulses. One other disadvantage of this sequence is that the phase compensation may vary with the RF field variations because the excitation pulse is non-adiabatic.

The main disadvantage of using LFM pulses is that they are not fully adiabatic. Unlike adiabatic HS pulses the LFM pulses do not have an adiabatic threshold above which they retain their adiabaticity (or inversion profile) when $B_{1max}$ is increased. In fact Pipe [50] states that the condition

$$B_{1max} \leq BW/200\gamma$$

**Equation 60**

is required to ensure that the RF is swept from far above to far below resonance for every spin and to give a parabolic phase profile. Furthermore, as $B_{1max}$ exceeds this condition the flip angle is not stable but becomes a very complicated function of the RF parameters until

$$B_{1max} >> BW/\gamma$$

**Equation 61**

by which point the pulse resembles a conventional square (hard) RF pulse of amplitude $B_{1max}$.

The HS pulse is more truly adiabatic at all times than the LFM pulse and should therefore give a better slice profile. This is because at the beginning and end of the LFM pulse's linear frequency sweep (in the $\omega_{RF}$ frame), $B_{eff}$ does not approach the longitudinal axis. This means that the sweep is less than 180°, the magnetisation is not collinear with $B_{eff}$ (the adiabatic condition is not properly satisfied) and isochromats near the extremes of the sweep are not inverted / refocused. In contrast, at the beginning and end of the HS pulse, $B_1$ smoothly increases from or approaches zero so that $B_{eff}$ is

approximately collinear with the magnetisation and the adiabatic condition is satisfied at all times leading to a better inversion slice profile.

#### 3.1.1.2.2.4 Adiabatic Plane Rotation Pulses

The adiabatic pulses (AHP and AFP) discussed so far are not plane-rotation pulses, meaning that they do not rotate all the magnetisation vectors with arbitrary orientations about a single rotation axis by a uniform rotation angle.

The adiabatic plane rotation pulses are composites constructed from AFP, AHP (and inverse AHP) segments, often with phase shifts in $B_{eff}$ between them. The two principles on which the pulses are based are that the transformation on any magnetisation vector must be an identity transformation in the $\omega_{eff}$ frame meaning that the net rotation in the $\omega_{eff}$ frame at the end of the pulse must be zero. In addition the $\omega_{eff}$ frame must undergo the desired rotation relative to the $\omega_{RF}$ frame during the pulse [51].

A host of $B_1$-insensitive refocusing (BIREF) pulses were proposed by Ugurbil et al [52] but none show both complete phase compensation and slice-selectivity. Conolly [44] gives a more detailed critique of these BIREF pulses.

The most useful general purpose plane rotation pulse, capable of producing any desired flip angle, is the BIR-4 pulse [53], [54] shown in Figure 12. BIR-4 produces complete outer volume suppression and is therefore only suitable for single voxel localisation in spectroscopy or single slice imaging [55]. Norris [56] claims that "although the bandwidth of BIR-4 is acceptably broad, the edges of the profile are not sufficiently sharp to make it usable for slice-selective excitation".

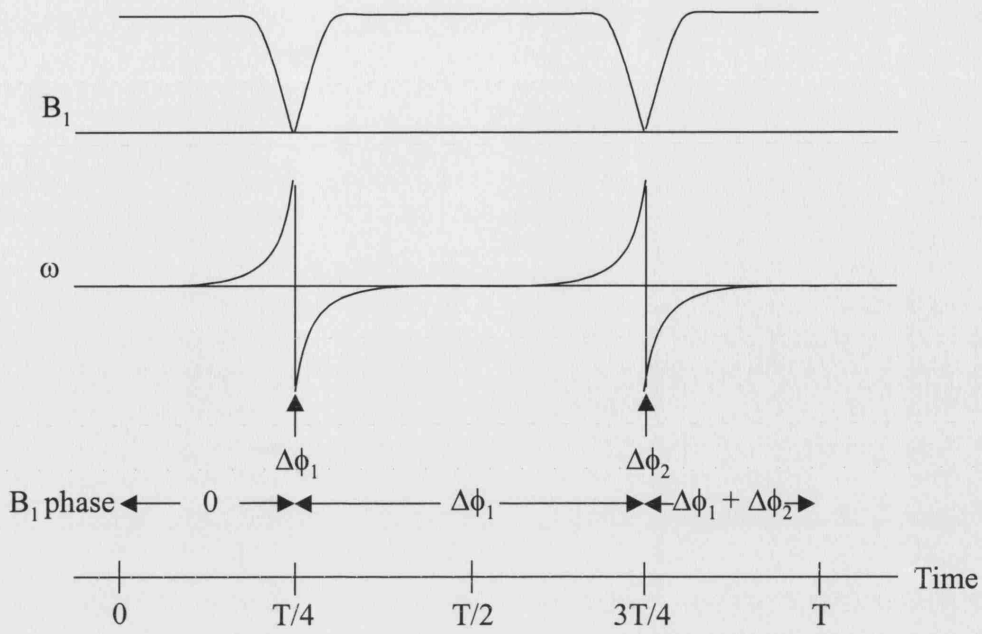


**Figure 12 The BIR-4 Pulse**
A schematic graph of the BIR-4 pulse. It can be thought of as four adiabatic half passage (AHP) segments (with two time-reversed) or alternatively an AHP followed by an adiabatic full passage (AFP) and a time-reversed AHP. Arbitrary flip angles can be selected by choosing the phase jumps $\Delta\phi$.

De Graaf and Nicolay [55, 57] have combined the principles of BIR-4 with simultaneous RF and gradient modulation to develop an adiabatic slice-selective pulse (BISS-8) which can produce plane rotations without affecting the out-of-slice magnetisation. However the average power of BISS-8 is 55 times higher than an equivalent Sinc excitation pulse, making it unsuitable for human imaging with volume RF coils within SAR limits. Such pulses are also demanding on the gradient hardware since high gradient slew rates are required

## 3.2 Aim of This Work

The aim of this work was to investigate whether HS pulses could be used for both excitation and refocusing in the spin-echo sequence. It was suggested that the true adiabaticity of the HS refocusing pulse may lead to better $B_1$ insensitivity than so far achieved with the LFM pulses. The phase dependence of the HS excitation pulse needed to be investigated to see if quadratic phase compensation would be possible by choice of appropriate pulse parameters. A potential advantage of such a sequence over that using a refocusing HS pulse pair would be the lower SAR associated with having one

less RF pulse and the ability to use the first echo and thus achieve a shorter minimum TE.

The HS excitation pulse is still a 'full passage' meaning that the full frequency sweep and pulse is played out. However the excitation pulse has its amplitude reduced to give a 90° excitation and is therefore non-adiabatic. This means that a degree of $B_1$ inhomogeneity is expected to remain, which may affect image uniformity.

The proposed method aims to reduce transmit $B_1$ inhomogeneity (by RF pulse sequence design) but some image non-uniformity is expected to remain due to RF receive coil inhomogeneity.

# 3.3 Initial Sequence Development

## 3.3.1 Methods

### *3.3.1.1 Simulations*

The phase resulting from using the HS pulse for refocusing could be predicted using Conolly's expression above, but since there was no analytic expression available** for the phase resulting from the HS excitation pulse, simulation programmes were written to predict it.

The simulations were based on the fact that the vector form of the Bloch equations can be broken down into three rotations for an elemental spin magnetisation at a particular (z) position [58]. The elemental spin magnetisation is treated as its three ($\delta M_x$, $\delta M_y$, $\delta M_z$) components. $T_1$ and $T_2$ relaxation are initially neglected which leaves the cross-product part of the Bloch equation (Equation 18 section 2.9) in which the magnetisation precesses about the effective magnetic field. The physical picture is similar to that described for adiabatic pulses in the frequency $\omega_{RF}$ frame as in Figure 8 above and in Figure 13. The effect of the applied $B_1$ field on an element of magnetisation at a position (z) can be described by three rotations – this is equivalent to Euler's rotation

** At the time of experimentation there was no expression available but recently Park and Garwood [59] have published an expression for the phase resulting from an HS excitation pulse (See Equation 62)

theorem (which states that any rotation may be described in terms of three rotations through three Euler angles). The three rotations in this case are :

i. first a negative rotation about y' through $\alpha$ to bring $B_{eff}$ along the z'' axis (i.e. a transformation into the $\omega_{eff}$ frame)

ii. then a rotation through an angle $\phi = \omega_{eff} T$ where T is the duration of the selective pulse and $\omega_{eff}$ is given by Equation 46. In these simulations the process is broken up into several time points of duration dt so that the rotation becomes lots of small rotations through $\delta\phi = \omega_{eff} dt$

iii. and finally a positive rotation about y'' through $\alpha$ to take z'' back to z' or transform the magnetisation back into the $\omega_{RF}$ frame.

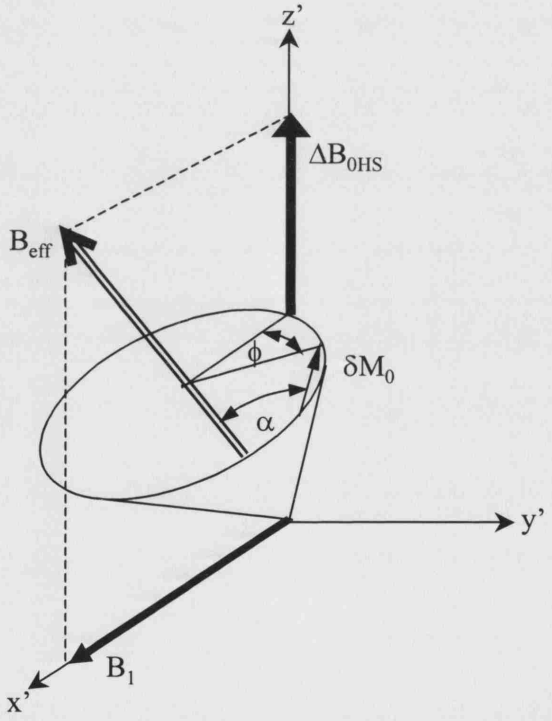


**Figure 13 Precession of Magnetisation in Rotating Reference Frames**[58]
The precession of an element of magnetisation $\delta M_0$ in the rotating reference frame $\omega_{RF}$. Rotation through $\alpha$ about y' brings the $\omega_{RF}$ frame into the tilted or second $\omega_{eff}$ rotating frame where the second rotation through angle $\phi$ about $B_{eff}$ is made.

The main structure of the programme is to set up the $B_1$ waveform as an array over time. The effective field at every z-position is then calculated at each time point and the rotations described above are carried out for the magnetisation element at each z-position for the first time point. The resultant orientation of the elemental magnetisations is fed in as the starting point for the next time point at which the

effective field is again calculated and the rotations are performed. The process is repeated for each time point until the end of the pulse.

The simulations were written in the C programming language and some were later translated into Matlab (*Matlab, The MathWorks Inc.*) scripts and functions.

The input parameters fed into the simulations are given below with typical values:
The number of time points for each RF pulse: 1000 or 2000
The number of spatial isochromats or z-positions: 1000 or 2000
$B_{1max}$ : a range of values ($rad.s^{-1}$) for pulse calibration
Field of view: 10-20 mm – this corresponds to the total bandwidth of interest
Pulse duration: 5-20 ms
Slice thickness: 3-5 mm
For LFM pulses $a$: 75,000-667,000 $rad.s^{-2}$ and the BW(Hz) was calculated using Equation 57.
For HS pulses BW: 1000-4000 Hz
For HS pulses $\mu$: 2-10 and $\beta$ was calculated using Equation 53 above

The LFM pulses had some windowing applied. However, unlike Kunz's method described above and more similarly to Pipe [50] (who uses a linear ramp in the time domain), the smoothing was carried out directly in the time domain by multiplying the first and last 50-100 time points of the $B_1$ waveform by quarter-cosines.

Outputs from the simulation programmes include the magnetisation over the field of view ($M_x(z)$, $M_y(z)$ and $M_z(z)$), which allowed the calculation of the slice profile and the phase of the transverse magnetisation. For the simulations $B_{1max}$ needed to be adjusted until the required flip angle was obtained in a process equivalent to pulse calibration on the real system. For the HS180° pulses a module was added to calculate the phase by integration of $B_{eff}$ over time according to Connolly's Equation 55 above.

The results of the simulations were analysed. The standard deviation and range of the transverse magnetisation's phase were calculated within the central 75% of the nominal slice width. The central 75% was chosen as the region over which to calculate these statistics since the phase can fluctuate substantially in the slice edges and measures such as the phase range can become meaningless. A quadratic polynomial $\phi(z) = A + Bz + Cz^2$ was fitted *(GraphPad Prism, GraphPad Software, Inc.)* to the phase inside the slice to examine the quadratic phase coefficient C.

Since these simulations calculate the effect of the pulses being applied in the presence of slice-selective gradients, gradient refocusing was simulated after all 90° excitation pulses. In the first instance this was carried out simply by calculating the effective field and applying the rotations in the absence of $B_1$ and for half the excitation pulse duration. An option was added by which the refocusing gradient could be run for a few extra time points in order to compensate for the non-linearity of the spin system just as is possible on the MRI scanner.

Recently Park and Garwood [59] published an analytically derived expression for the phase of spins after the application of a HS full-passage pulse when scaled down for excitation. By following the analysis proposed by Pipe [50] for LFM pulses, they found that the phase of a spin isochromat at position $z$ (through the slice) could be written as:

$$\phi = \mu.\ln\left(\frac{\frac{\mu\beta}{2\pi}\operatorname{sech}\left(\frac{\beta T}{2}\right)}{\sqrt{\left(\frac{\mu\beta}{2\pi}\right)^2-(\gamma G_z z)^2}}\right)-\frac{\pi\gamma G_z z}{\beta}.\ln\left(\frac{\frac{\mu\beta}{2\pi}+\gamma G_z z}{\frac{\mu\beta}{2\pi}-\gamma G_z z}\right)+\pi T\gamma G_z z+\frac{\pi}{2}$$

**Equation 62**

where the symbols have the same meaning as defined previously for adiabatic pulses. The third term in the equation above cancels with the phase due to refocusing with the same slice-select gradient $G_z$ for a time equal to half the pulse duration T.

#### 3.3.1.1.1 Simulation Results: the Basis for Quadratic Phase Compensation

It was found in pulse simulations that a HS pulse calibrated for $\pi/2$ excitation had a quadratic phase variation of half that produced when the same shaped pulse is used for refocusing. This is exemplified in Figure 14 and Figure 15. The quadratic phase coefficient from the 90° excitation pulse in Figure 14 is -2.463 rad.mm$^{-2}$ and the coefficient when the same pulse is used for refocusing is 4.926 rad.mm$^{-2}$, which is exactly double the 90° phase coefficient. The refocusing quadratic phase coefficient predicted by numerically integrating Conolly's expression in Equation 55 was 4.894 rad.mm$^{-2}$. This is in good agreement with the value from the Bloch rotation simulations. The quadratic phase coefficient found from a fit to the phase from excitation using Park's expression in Equation 62 was -2.447 rad.mm$^{-2}$, which also agrees with the coefficient from the Bloch rotation simulation.

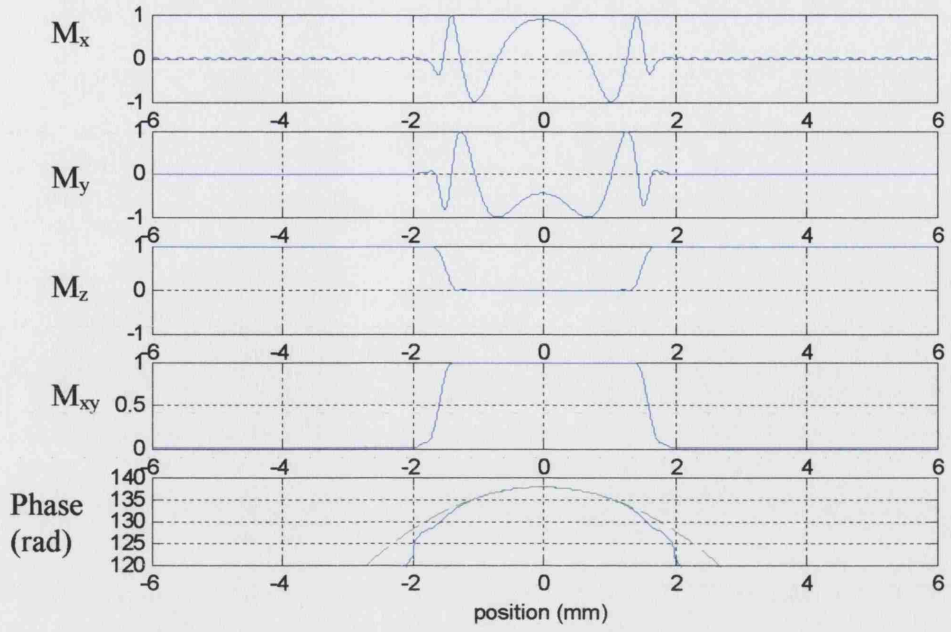


**Figure 14 Simulation Results for a 90° HS Excitation Pulse with $\mu$ =10**
The quadratic phase is clearly visible in the lowest graph. The quadratic phase coefficient from the fit over the central 75% of the nominal slice thickness ( fit line = green dashed) was -2.463 rad.mm$^{-2}$. The simulation parameters were: HS pulse BW = 1.5kHz, $\mu$ = 10, $T_p$ = 20ms, $B_{1max}$ = 160Hz, slice thickness = 3mm, 2000 time points and 2000 points in space across a 12mm field of view.

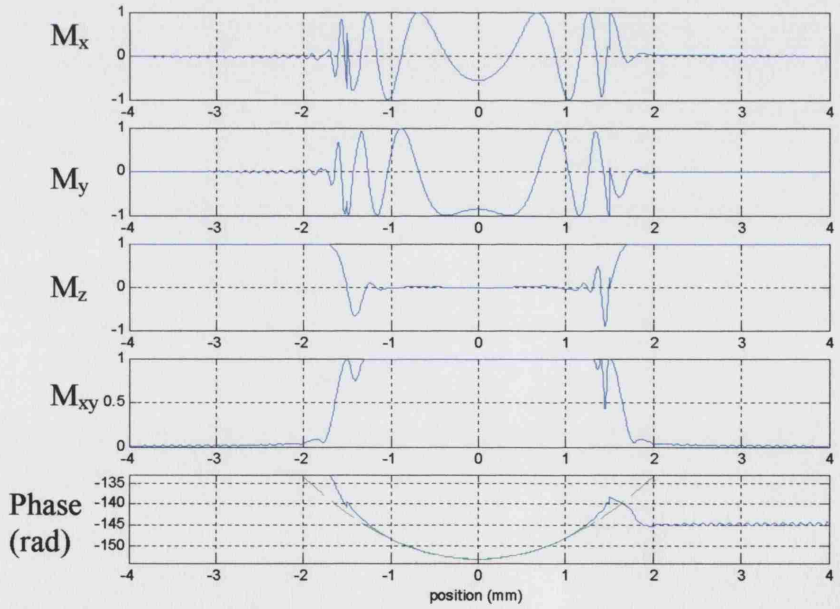


**Figure 15 Simulation Results for a 180° HS Refocusing Pulse with $\mu$ = 10**
The pulse parameters are identical to those in Figure 14 except for $B_{1max}$ = 600Hz. The pulse was applied to refocus a perfect 'top hat' of transverse magnetisation. The quadratic phase coefficient from the fit over the central 75% of the nominal slice thickness (fit line = green dashed) was 4.926 rad.mm$^{-2}$. The rest of the simulation parameters were identical to those in Figure 14.

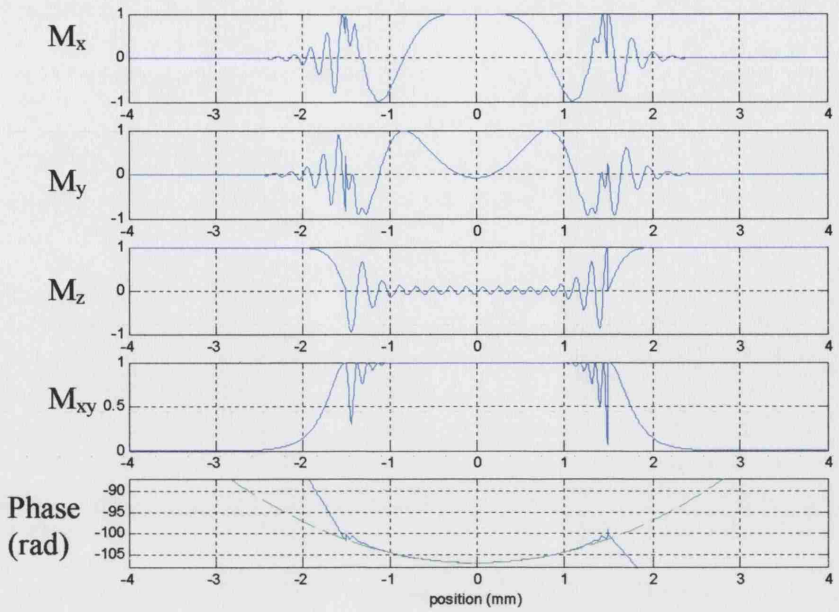


**Figure 16 Simulation Results for a 180° HS Refocusing Pulse with $\mu = 5$**
Simulation results for a 180° HS refocusing pulse. The pulse parameters are identical to those in Figure 15 except for $\mu = 5$. The pulse was applied to refocus a perfect 'top hat' of transverse magnetisation. The quadratic phase coefficient from the fit over the central 75% of the nominal slice thickness (fit line = green dashed) was 2.516 rad.mm$^{-2}$. The rest of the simulation parameters were identical to those in Figure 15.

It was also observed that, in analogy with the LFM pulses, halving the maximum sweep rate of the HS $\pi/2$ excitation pulse caused the quadratic phase to match that of the HS refocusing pulse (of the same bandwidth). This is demonstrated by comparing the quadratic phase coefficients of the pulses in Figure 14 and Figure 16. The $\mu$=10 90° HS excitation pulse has a quadratic phase coefficient of 2.463 rad.mm$^{-2}$ whilst the $\mu$=5 180° HS refocusing pulse has a quadratic phase coefficient of 2.516 rad.mm$^{-2}$.

Quadratic phase compensation was therefore achieved by designing pulses with the same duration and bandwidth but with $\beta$ for the HS $\pi/2$ excitation pulse half that of the HS refocusing pulse: $\beta_{90°} = \beta_{180°}/2$ and $\mu_{90°} = 2\mu_{180°}$.

The effect of $\mu$ on the pulses is demonstrated by comparing Figure 15 and Figure 16. The refocusing slice profile from the pulse with $\mu$=5 in Figure 16 is poorer than that from the pulse with $\mu$=10 in Figure 15.

### 3.3.1.2 Experiments

Experiments were carried out on a 10 cm diameter spherical (plastic) phantom doped with $CuSO_4$ ($T_1$ = 286 ms and $T_2$ = 151 ms).

The Bloch rotation simulations described above were used to predict quadratic phase coefficients and flip angle variation with peak RF amplitude for a variety of LFM and HS pulses including those used in the experiments.

For the experiments all RF pulses were digitised with 2000 time points and had a slice thickness of 3 mm. Sinc pulses were the standard ones used in most SMIS sequences and had 5 lobes and a bandwidth of 1.5 kHz. HS and LFM pulses also had a bandwidth of 1.5 kHz. HS pulse duration was 20ms with $\mu_{90°} = 10$, $\mu_{180°} = 5$. LFM pulses had $a_{90°}$ = 75 kHz.s$^{-1}$, $a_{180°}$ = 150 kHz.s$^{-1}$ and durations of 20 ms and 10 ms respectively to ensure identical bandwidths. As described for the simulations, the $B_1$ amplitude of the LFM pulses was windowed by a temporal window consisting of quarter-cosines multiplying the first and last 100 time points of the 2000.

For HS and LFM pulse calibration, $M_z$ profiles were collected at a range of RF transmit amplitudes. The spin-echo sequence for collecting the profiles consisted of the slice-selective pulse to be calibrated followed by spoiler gradients. This was followed by a spin-echo acquisition with a wider slice and read gradients on the same axis so that a 1D profile would be obtained on 1D Fourier transformation (FT). The sequence had the following parameters: TR / TE = 2000 / 75 ms, 12 mm FOV, 256 points, 16.7 kHz spectral width.

Flip angles ($\alpha$) were calculated using the relationship

$$M_z = M_0.\cos(\alpha)$$

**Equation 63**

where $M_z$ is the signal in the centre of the slice and $M_0$ can be approximated by the signal in the region unexcited by the initial pulse. The amplitude setting (%) required for excitation or inversion by each pulse was noted.

The RF amplitude was approximately calibrated by applying a hard pulse with a range of durations and noting the RF amplitude setting (%) required for a 90° pulse excitation at each duration.

For both the calibrated excitation and refocusing HS and LFM pulses a phase profile was collected using a spin-echo sequence in which the other pulse was a non-selective Sinc-shaped pulse. For example, to obtain the phase profile of the HS90° pulse, a SE sequence with a slice-selective HS90° pulse and a non-selective Sinc-180° pulse was acquired. Measured quadratic phase coefficients, from fits of the central 75% of these phase profiles, were used to predict any residual quadratic phase in the HS and LFM spin-echo slice profiles. The spin-echo phase profile sequence parameters were the same as for pulse calibration except for TR / TE = 1000 / 140 ms.

Spin-echo slice profiles were collected using the four sequences shown in Figure 17: a standard Sinc90°-Sinc180° pulse combination, the proposed HS90°-HS180° pulse combination, Kunz's LFM90°- LFM180° spin-echo and Conolly's Sinc90°- HS180°-HS180° sequence. The spin-echo profiles were collected with the same parameters as the individual pulse phase profiles.

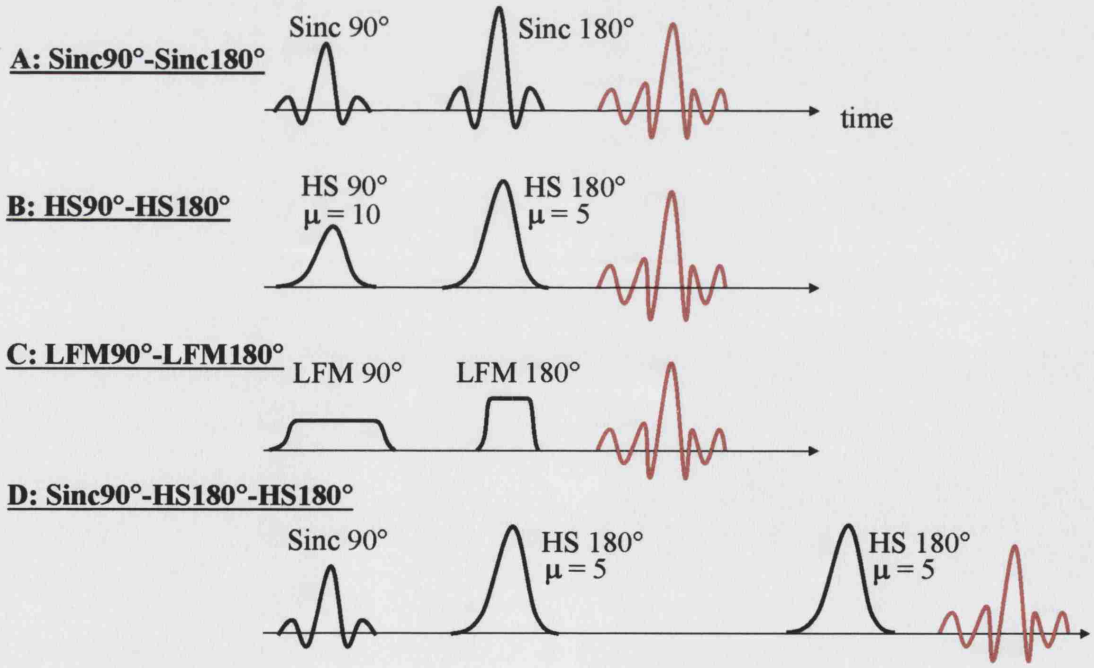


**Figure 17 The Spin-Echo RF Pulse Sequences Used in This Work**
**A** shows the Sinc90°-Sinc180° sequence, **B** shows the HS90°-HS180° sequence, **C** shows the LFM90°-LFM180° sequence and **D** shows the Sinc90°-HS180°-HS180° sequence. The RF amplitude is shown in black and the echoes are shown in red.

The resulting slice profiles were analysed: the phases were fitted to give residual quadratic phase coefficients (over the central 75% of the slice thickness) and the magnitudes were used to calculate the FWHM and slice sharpness as defined in Equation 64 and Figure 18. The sharpness of a perfectly rectangular slice profile would be 100% according to this definition and a triangular slice profile would have a sharpness of 0%.

$$Sharpness(\%) = 100 \times \left(1 - \frac{E_1 + E_2}{2FWHM}\right)$$

**Equation 64**

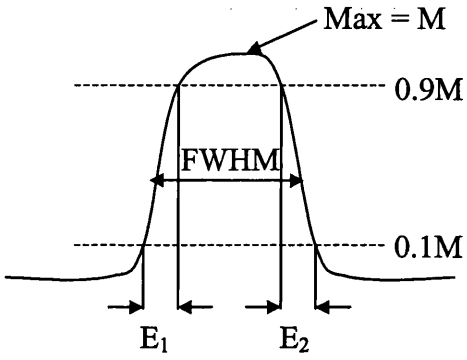


**Figure 18 Schematic Diagram to Illustrate the Sharpness Calculation**

## 3.3.2 Results

### *3.3.2.1 Pulse Calibration Curves*

Figure 19 and Figure 20 below show calibration curves for the HS and LFM pulses used in the subsequent experiments.

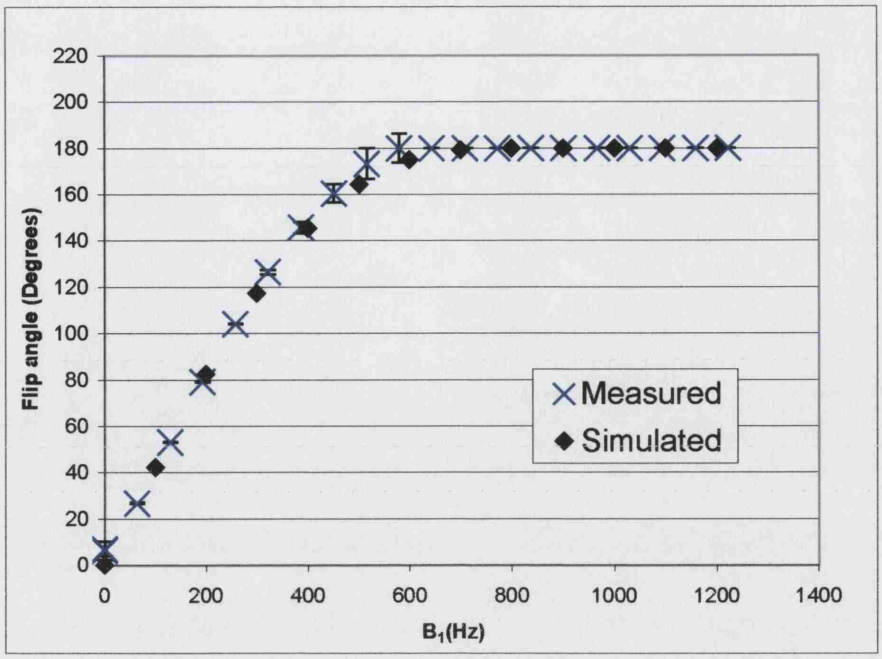


**Figure 19 HS Refocusing Pulse Calibration Data**
Simulated and measured pulse calibration data for the HS refocusing pulse with parameters: $\mu = 5$, BW = 1.5 kHz, $T_p = 20$ ms, slice thickness = 3 mm. The error bars were calculated from the difference between the flip angle measured using the mean of the central 5% of the slice profile for $M_z$ (Equation 63) and the flip angle measured using the mean of the central 75% of the slice profile for $M_z$.

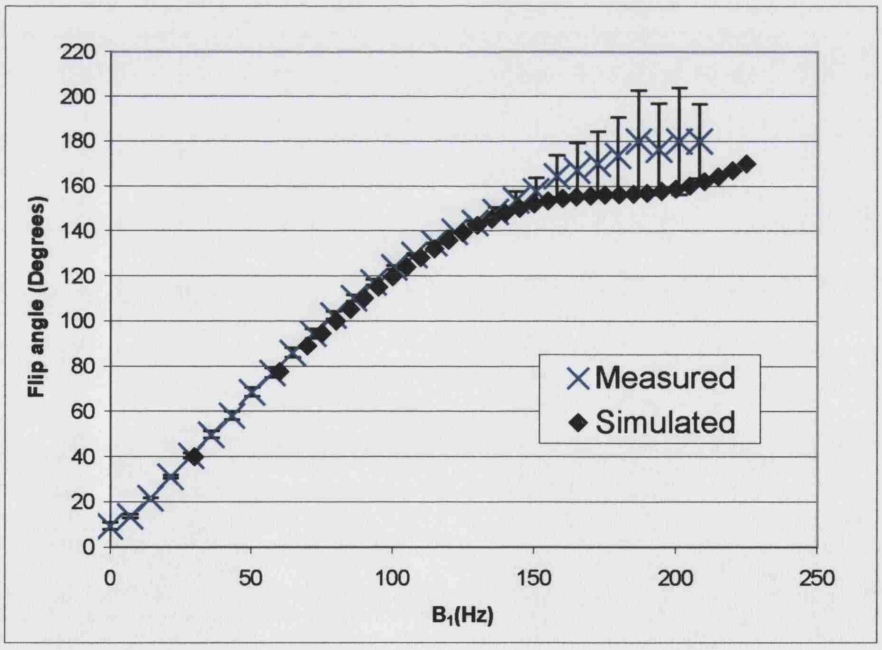


**Figure 20 LFM Excitation Pulse Calibration Data**
Simulated and measured pulse calibration data for the LFM excitation pulse with parameters: $a_{90°} = 75$ kHz.s$^{-1}$, T = 20 ms, BW = 1.5 kHz. The error bars were calculated from the difference between the flip angle measured using the mean of the central 5% of the slice profile for $M_z$ (Equation 63) and the flip angle measured using the mean of the central 75% of the slice profile for $M_z$. The large error bars at high pulse amplitudes therefore reflect the highly non-uniform slice profile at these high amplitudes.

### 3.3.2.2 Predicted and Measured Quadratic Phase Coefficients

Figure 21 below shows the quadratic phase profiles along the slice-select direction (z) measured for each of the HS and LFM pulses. The corresponding quadratic phase coefficients (rad.mm$^{-2}$) are compared with simulated coefficients in Table 2.

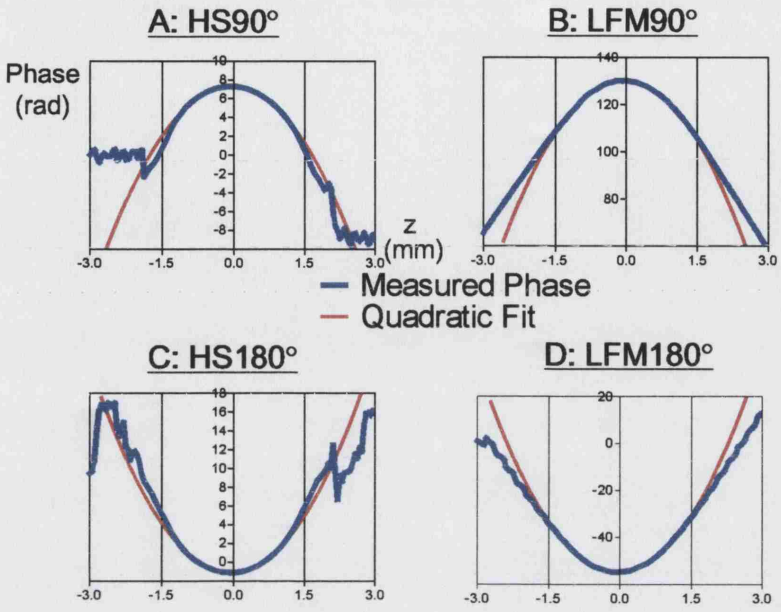


**Figure 21 Quadratic Phase Profiles for the HS and LFM Pulses**
Quadratic phase profiles and quadratic best-fit curves along the slice-select direction (z) measured for each of the HS and LFM pulses.

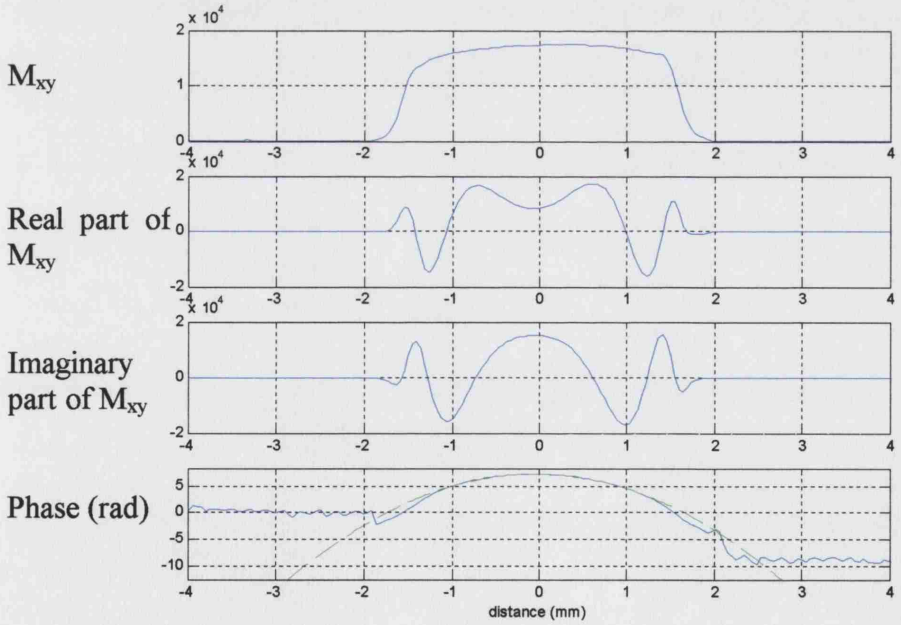


**Figure 22 Slice Profiles for the HS 90° Pulse**
The (phase-corrected) slice profiles are shown for the 90° HS pulse. The phase profile is the same as that in Figure 21A with the fitted quadratic shown in dashed green. These profiles can be compared with the simulated profiles in Figure 14.

| | | Quadratic Phase Coefficient ($rad.mm^{-2}$) | |
|---|---|---|---|
| | Flip Angle (°) | HS pulse | LFM pulse |
| Measured | 90 | -2.499 ± 0.029 | -10.6 ± 0.09 |
| | 180 | 2.523 ± 0.029 | 10.16 ± 0.08 |
| Simulated | 90 | -2.46 | -10.45 |
| | 180 | 2.52 | 10.15 |

**Table 2 Measured and Simulated Quadratic Phase Coefficients**
Measured and simulated quadratic phase coefficients ($rad.mm^{-2}$) for the phase profiles shown in Figure 21.

### 3.3.2.3 Slice Profiles

Figure 23 shows slice profiles measured for each spin-echo sequence shown in Figure 17.

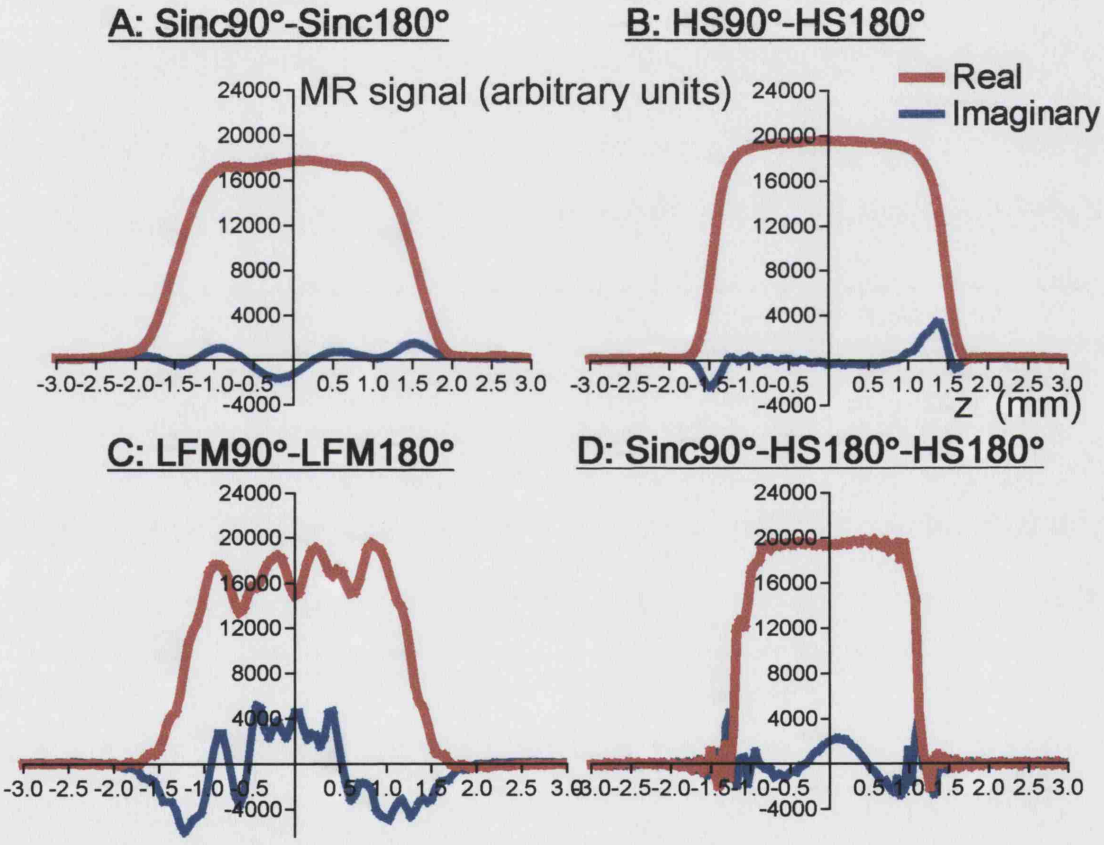


**Figure 23 Slice Profiles for the Spin-Echo Pulse Sequences**
Real and imaginary slice profiles measured for each of the spin-echo sequences shown in Figure 17.

Statistics describing the slice profiles shown in Figure 23 are given in Table 3 and Table 4.

| Profile | A | B | C | D |
|---|---|---|---|---|
| FWHM (mm) | 3.05 | 3.00 | 2.58 | 2.34 |
| Slice Sharpness (%) | 77.34 | 87.50 | 77.34 | 93.75 |
| Standard Deviation of Phase (in 100% FWHM) (°) | 3.2 | 5.1 | 15.2 | 4.1 |
| Phase Range (in 75% FWHM) (°) | 8.9 | 4.1 | 33.2 | 15.2 |
| Average signal magnitude (in 75% FWHM) x$10^3$ a.u. | 17.2 | 19.3 | 16.8 | 18.6 |

**Table 3 Slice Profile Statistics for the Spin-Echo Pulse Sequences**
The full-width-half-maximum (FWHM) and slice sharpness (as defined in Figure 18) are given for each of the sequences shown in Figure 17 with the slice profiles shown in Figure 23. The nominal slice thickness was 3mm. The Range and Standard Deviation of the phase are also given as is the average signal magnitude for each of the sequences.

| Profile | B | C |
|---|---|---|
| Measured residual quadratic phase coefficient (rad.$mm^{-2}$) | 0.0358 ± 0.0009 | -0.408 ± 0.09 |
| Predicted residual quadratic phase coefficient (rad.$mm^{-2}$) | 0.024 ± 0.041 | -0.44 ± 0.12 |

**Table 4 Measured and Predicted Residual Quadratic Phase Coefficients**
Measured and predicted residual quadratic phase coefficients for the HS90°-HS180° and LFM90°-LFM180° sequences shown in Figure 17B and Figure 17C with slice profiles shown in Figure 23B and Figure 23C respectively.

## 3.3.3 Discussion and Conclusions

Figure 19 and Figure 20 show that the measured pulse calibration curves were very close to the simulated curves for both LFM and HS pulses suggesting that the Bloch rotation simulations are useful for predicting the real pulse behaviour. Figure 19 clearly shows the adiabatic region for the HS pulse where the flip angle becomes independent of the $B_1$ amplitude. This region is not evident for the LFM pulses for which the increasing error bars as the pulse amplitude increases demonstrate the deterioration of the LFM slice profile at these high amplitudes.

Further evidence for the applicability of the Bloch rotation simulations is the similarity of the simulated and measured magnetisation and phase profiles in Figure 14 and Figure 22 respectively. The strong similarity of the profiles in these figures also implies that the non-selective Sinc pulse used for refocusing the magnetisation when collecting the profile has a negligible influence.

In addition Table 2 shows that the simulated and measured quadratic phase coefficients for both LFM and HS pulses agree. The table shows that halving $\mu$ for the HS180° pulse gives a quadratic phase coefficient similar to that for the HS90° pulse so that combining

pulses with these parameters in the spin-echo sequence should result in a negligible residual quadratic phase. Similarly the results reproduce Kunz's finding that an LFM90° pulse with half the sweep rate $a$ of a LFM180° pulse with the same bandwidth has a very similar quadratic phase coefficient.

Figure 23 shows that almost complete phase compensation was achieved in the HS90°-HS180° spin-echo sequence as demonstrated by the small residual quadratic phase coefficient in Table 4. The sequence behaved as predicted and gave a sharp slice profile and an accurate slice width. The double HS refocusing sequence gave a sharper slice but with a width significantly narrower than the nominal width. Such degradation of slice edges is common in sequences where several RF pulses are used because the slight errors in slice profile are cumulative. The HS90°-HS180° sequence has the advantage of a 10% improvement in slice sharpness over the standard Sinc SE sequence without the degradation in slice width caused by the double HS pulse.

The level of phase dispersion (standard deviation over 100% FWHM in Table 3) in the HS90°-HS180° spin-echo profile is similar to that in the other spin-echo profiles (except the LFM value). However the phase range in the central 75% of FWHM is the lowest of all the profiles. This shows that the quadratic phase compensation works well in this sequence and that any phase deviation is mostly at the slice edges. The reason that the phase may deviate near the slice edges is because this is where $|\Omega| \approx |\mu\beta|$ (see Equation 52) so the refocusing by the HS180° pulse may be imperfect leaving the spins with a range of phases in the transverse plane.

The poorest slice profile results from the LFM90°-LFM180° sequence. It has the greatest level of phase dispersion probably due to a small residual quadratic phase variation arising from incomplete phase compensation by the two pulses which have slightly different quadratic phase coefficients (see Table 2). There may be potential for further improvement of the phase profile by optimisation of pulse parameters. For example the $a$ and T of the pulses could be adjusted slightly in an attempt to improve the quadratic phase matching. The in-slice signal oscillation is likely to result from the time windowing of the pulse. Again there may be potential to optimise the windowing method (e.g. window in the Fourier domain) and windowing function. Windowing in

the frequency domain might also be expected to improve the slice sharpness. However the profiles from these pulses are unlikely to be as smooth and sharp as those from the HS90°-HS180° sequence.

The magnitude profiles have similar in-slice mean values (Table 3) implying that all the sequences should yield equivalent in-slice signal (at least in regions where the $B_1$ is close to the 90° and 180° pulse calibration values).

## 3.4 HS Pulse Parameter Variation - Profiles

After having demonstrated that the newly developed HS-SE sequence works and produces satisfactory slice profiles, the next stage was to investigate how the quadratic phase coefficients of the individual HS pulses vary with the pulse parameters. The results would be useful to aid pulse design for future experiments and could inform the optimal choice of pulse parameters for matching the quadratic phase coefficients of the HS90° and HS180° pulses.

Firstly the HS pulse bandwidth was fixed because the bandwidth limits the minimum slice thickness for a given set of scanner gradient coils. Here the bandwidths were fixed at 4 kHz and 1.5 kHz giving minimum slice thicknesses of 2.58 mm and 0.97 mm for this scanner's maximum head gradient strength of 1552 $Hz.mm^{-1}$. It was then decided to vary the pulse $\mu$ value, since this is the parameter that determines both the sharpness of the individual slice profiles [39] and the pulse duration required for a given bandwidth and cut-off level.

The variation of the HS180° pulse quadratic phase coefficient with pulse amplitude or $B_{1max}$ was also investigated since this will affect the overall robustness of the HS90°-HS180° sequence to $B_1$ inhomogeneity.

### 3.4.1 Methods

To look at the quadratic phase coefficient variation with $\mu$, a set of pulses were designed with the following parameters: BW = 4 kHz, $T_p$ = 8.8 ms and $\mu$ varying from 6-8.5 in steps of 0.5 for the refocusing pulses and $\mu$ varying from 15 to 19 in steps of 1 for the

excitation pulses. Individual RF pulse profiles were collected as described in section 3.3.1.2 for each of these pulses. The quadratic phase coefficients emerged from fits of the profile phases (as described in section 3.3.1.2). A Matlab (*Matlab, The MathWorks Inc.*) script was written to calculate and fit the phase predicted using Park's expression in Equation 62 for the excitation pulses and the resulting quadratic phase coefficients were compared with those measured. Similarly, Conolly's expression (Equation 55) was used to simulate the quadratic phase coefficients expected from the refocusing pulses.

To investigate any variation of the HS180° pulse quadratic phase coefficient with $B_{1max}$, slice phase profiles were collected using the method described in section 3.3.1.2 over a range of pulse amplitude settings. The phantom was a 10cm diameter spherical (plastic) phantom filled with water doped with $MnCl_2$ ($T_1$ / $T_2$ = 1100 / 86 ms). As before, quadratic phase coefficients were obtained from fits of the phase profiles. The pulse parameters were the same as those used to acquire the slice profiles in section 3.3.1.2 i.e. $\mu = 5$, bandwidth = 1.5 kHz, T = 20 ms and a slice thickness of 3 mm.

Again the RF amplitude was approximately calibrated by applying a hard pulse with a range of durations and noting the RF amplitude setting (%) required for a 90° pulse excitation at each duration. This time the resulting graph was processed to yield information about the degree of linearity of the RF amplifier. Once the calibration graph had been plotted, a linear fit of the lowest few pulse amplitudes was used to convert the x-axis (measured RF amplitude setting for a 90° pulse) into a nominal $B_1$(Hz), assuming ideal linear performance of the RF amplifier. The calculated $B_1$(Hz) for a 90° pulse (see Equation 12) was then plotted against this nominal $B_1$(Hz) and best-fit quartic and quadratic polynomials were calculated.

If the amplifier had ideal (linear) behaviour then the HS pulse shape would not be distorted in any way. However in practice, most amplifiers have non-linear behaviour, which would be expected to lead to a 'compressed' HS pulse shape. To investigate the effect of the amplifier performance on HS pulse shape and quadratic phase profiles, the best-fit polynomials (of $B_1$ output against $B_1$ input see Figure 27) were then used to convert the 'ideal' HS pulse amplitude shape into a more realistic (compressed) shape to be fed into the Bloch rotation simulations. The simulations were used to generate phase

profiles and quadratic phase coefficients over a similar range of $B_{1max}$ values for comparison with the measured data.

It should be noted that gradient spoiling was applied around the HS180° pulse and that the equivalent of this spoiling was achieved in the Bloch rotation simulations by phase reversal of the 90° excitation pulse and then averaging the two profiles

Slice profiles from the HS90°-HS180° sequence were then collected over the same range of HS180° amplitudes with a fixed HS90° ($\mu$=10) amplitude. These profiles were analysed in the same way as the slice profiles in section 3.3.1.2 to investigate the robustness of the SE sequence to changes in HS180° amplitude.

## 3.4.2 Results

Figure 24 and Figure 25 show the variation of quadratic phase coefficients with the pulse $\mu$.

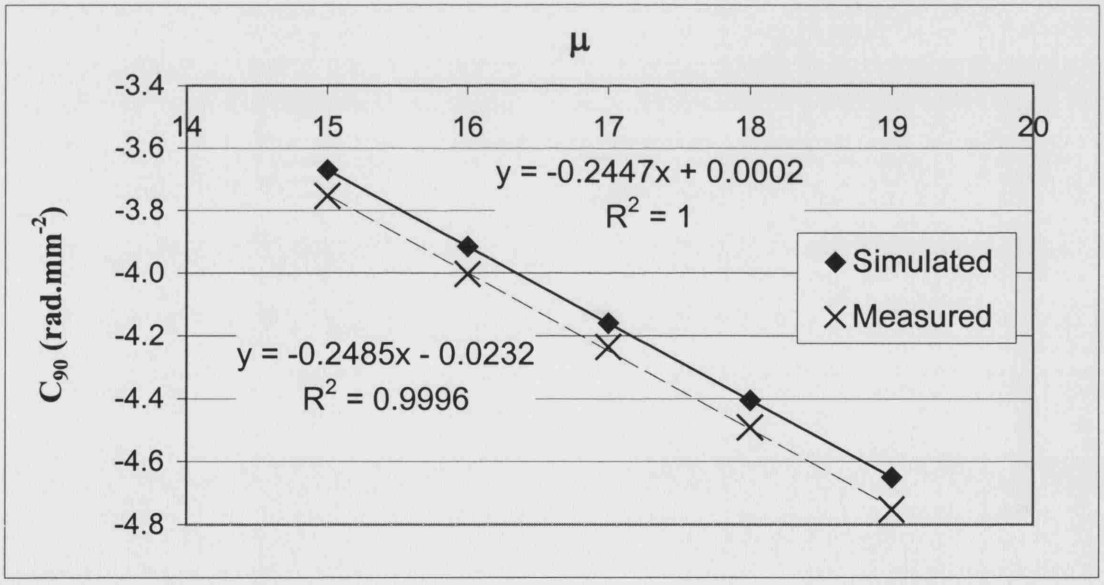


**Figure 24 Variation of Measured and Simulated Quadratic Phase Coefficient with Excitation Pulse $\mu$**
The simulated values were calculated using Equation 62. The equations on the graph are those of the best-fit lines.

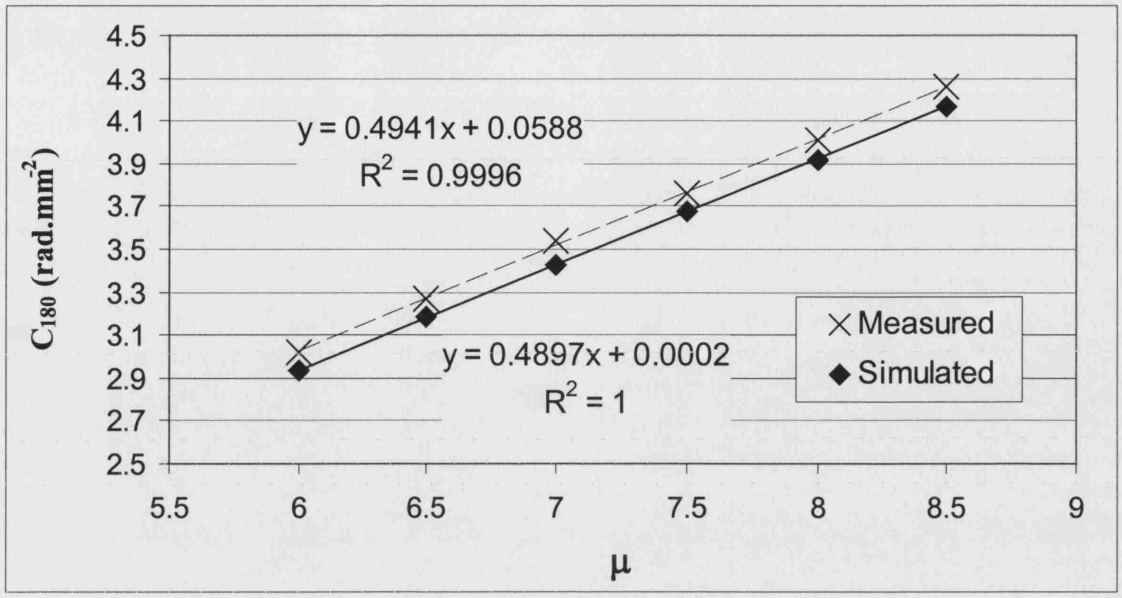


**Figure 25 Variation of Measured and Simulated Quadratic Phase Coefficient with Refocusing Pulse μ**

The simulated values were calculated using Equation 55. The equations on the graph are those of the best-fit lines.

The hard pulse calibration curves are shown in Figure 26 and Figure 27.

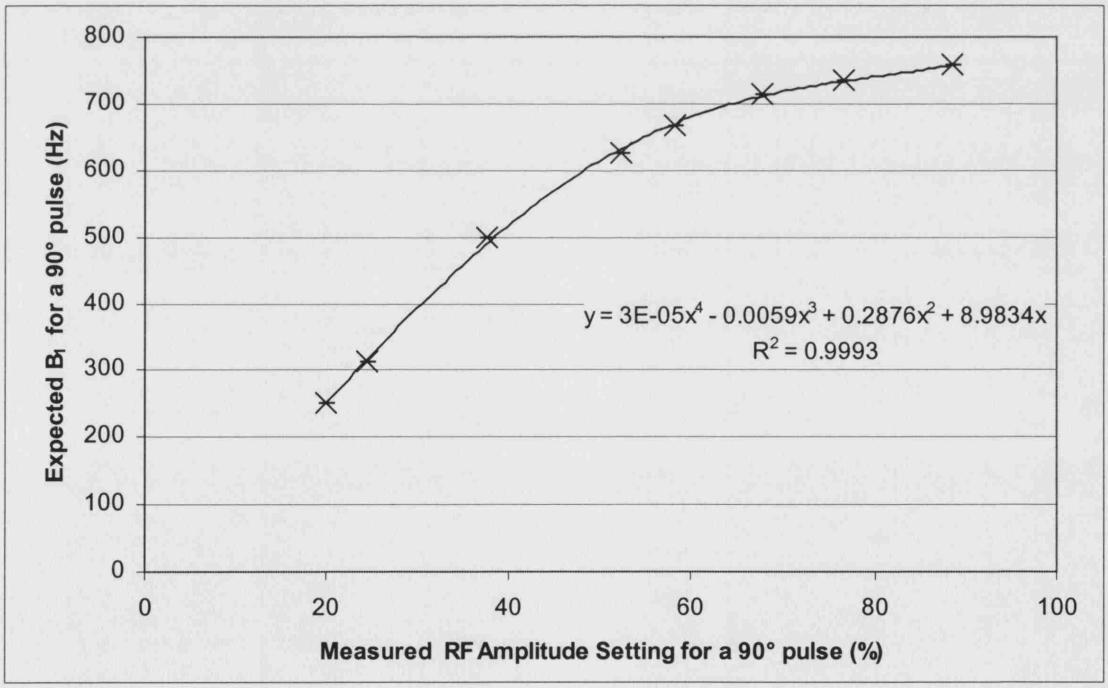


**Figure 26 Hard 90° Pulse Calibration Curve Showing RF Amplifier Non-Linearity**

The RF amplitude scanner setting required to achieve a 90° pulse, for a variety of hard pulse durations, is plotted (on the x-axis) against the expected $B_1$ required for a 90° pulse from a hard pulse of each duration (on the y-axis).

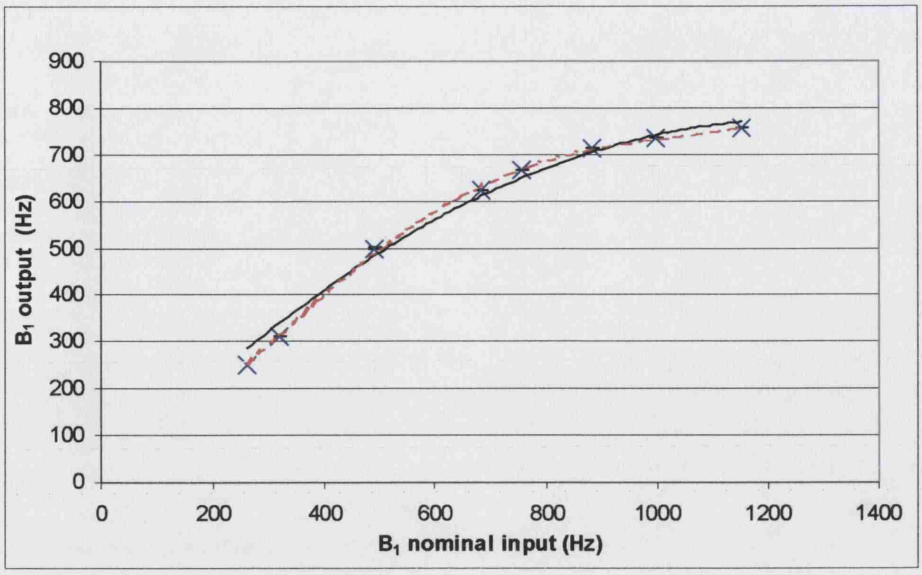


**Figure 27 RF Amplifier Non-Linearity**
The same curve as shown in Figure 26 but with the x-axis converted to a nominal $B_1$ power assuming ideal linear RF amplifier behaviour. A quadratic fit to the data is shown as the (black) solid line and a quartic fit as the (red) dashed line.

The effect of the RF amplifier non-linearity on the HS pulse shape is illustrated in Figure 28.

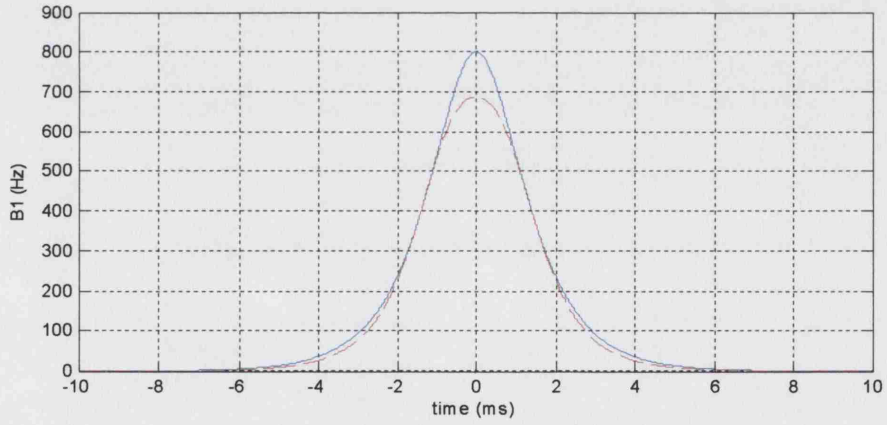


**Figure 28 The Effect of RF Amplifier Non-Linearity on HS Pulse Shape**
HS180° pulse amplitude converted using the RF calibration curve in Figure 27. The (blue) solid curve is the ideal 'sech' shape fed into the RF amplifier. The (red) dashed curve shows the compressed shape output by the RF amplifier when $B_{1max}$ (nominal) = 800Hz. The compressed pulse is an example of that fed into the Bloch rotation simulations to generate a set of quadratic phase coefficients at increasing pulse powers.

The measured and simulated quadratic phase coefficients for the HS180° pulse at increasing pulse amplitudes are shown in Figure 29. The measured and predicted residual quadratic phase coefficients in the HS90°-HS180° sequence are shown in Figure 30.

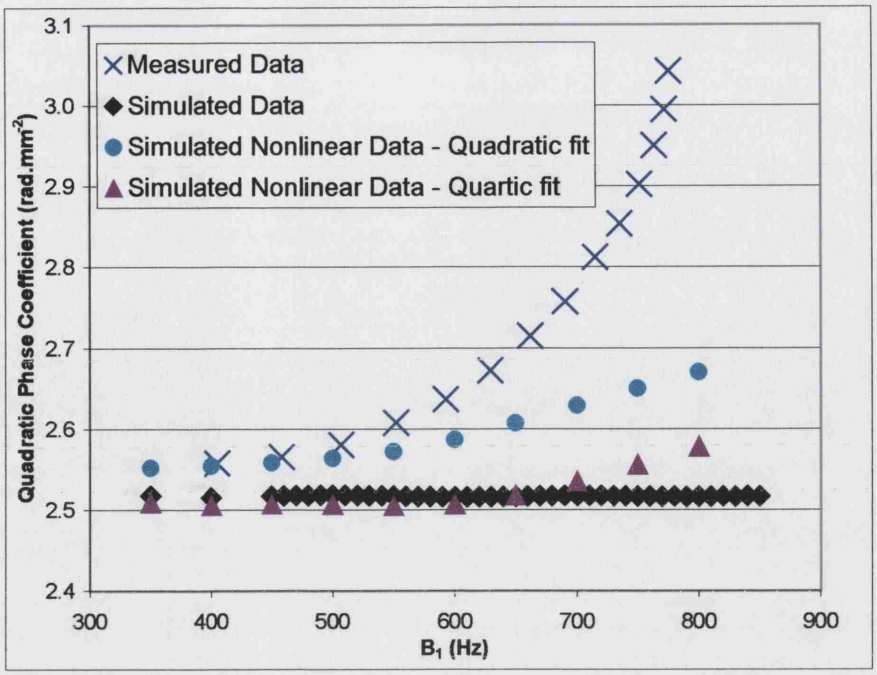


**Figure 29 Variation of the HS180° Quadratic Phase Coefficient with Pulse Amplitude**

Both the measured values and those simulated using the Bloch rotation simulations are shown. The simulated data (circles) were generated from HS pulse shapes converted using the quadratic fit (solid line) to the RF amplifier non-linearity curve in Figure 27. The simulated data (triangles) were generated using the quartic fit (dashed line) in Figure 27 to compress the HS pulse shapes fed into the Bloch rotation simulations.

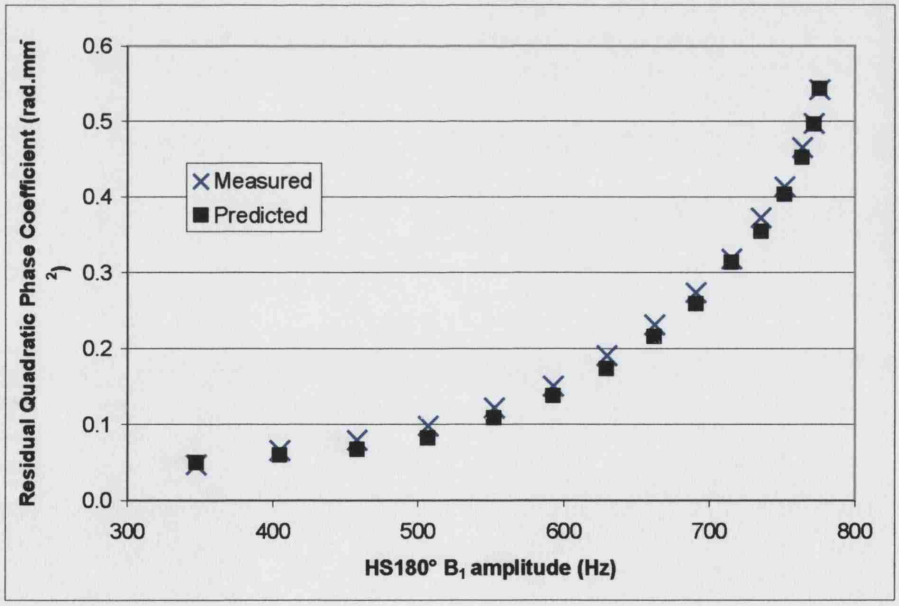


**Figure 30 Variation of Residual Quadratic Phase Coefficient in the HS90°-HS180° Sequence with HS180° Pulse Amplitude**

The 'predicted' residual quadratic phase coefficients were calculated by adding the coefficients measured for the HS180° pulse (see Figure 29) to that measured previously for the HS90° pulse i.e. –2.499 rad.mm$^{-2}$ (see Table 2).

The measured HS90°-HS180° signal magnitude at different HS180° amplitudes is shown in Figure 31.

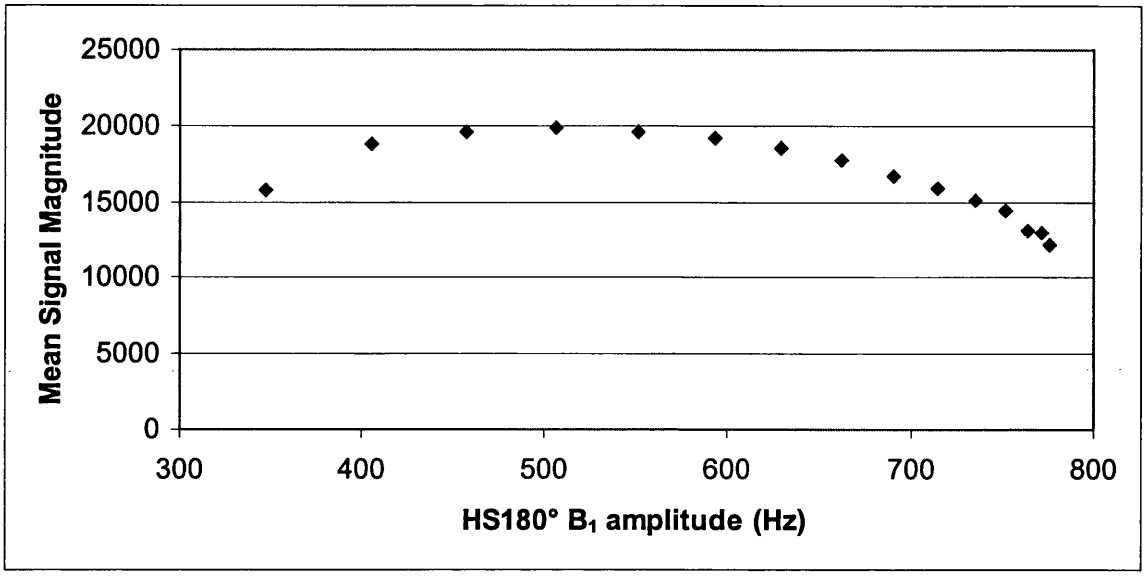


**Figure 31 Variation of Signal Magnitude in the HS90°-HS180° Sequence with HS180° Pulse Amplitude.**
The signal in this graph is the mean of the magnitude slice profile over 75% of the nominal slice thickness.

## 3.4.3 Discussion

From Figure 24 and Figure 25 it seems that the measured and simulated quadratic phase coefficients broadly agree, validating the accuracy and utility of both Park's expression (Equation 62) to predict the phase from a HS excitation pulse and Conolly's expression (Equation 55) for the phase from a HS refocusing pulse. Usefully, the relationship between the quadratic phase coefficients and $\mu$ is linear in both cases so that pulse design for perfect quadratic phase cancellation should be simple to achieve.

When increasing $\mu$ values for a fixed pulse bandwidth and pulse duration, the cut-off value ($B_1(t = 0$ and $t = T_p)$) will increase and this could adversely affect slice profiles. (As an example of the effects of high cut-off values see the ripples in $M_z$ in Figure 16). In fact this problem can be circumvented by subtracting this cut-off or baseline from the entire set of $B_1$ values as suggested by De Graaf and Nicolay [46]. This should not only reduce 'ripple' inside the slice but should also allow shorter pulse durations as well as ensuring adiabaticity at the start and end of the pulses. However care must be taken that the (now reduced) $B_{1max}$ remains over the adiabatic threshold to maintain adiabaticity throughout the pulse.

The RF calibration curve in Figure 26 demonstrates that the RF amplifier behaves in a non-linear fashion, with increasing amplitude settings resulting in a lower $B_1$ output from the amplifier than expected in the ideal linear case. When one of the fits from Figure 27 is used to convert the HS180° amplitude curve into the actual output $B_1$ curve, the result (shown in Figure 28) is that the sech or HS shape is compressed. From Figure 27 and Figure 28 we can conclude that, as pulse amplitudes increase, the RF amplifier non-linearity results in a more and more compressed HS pulse shape.

As the pulse amplitude increases, Figure 29 illustrates that the measured HS180° quadratic phase coefficient diverges increasingly from the approximately constant simulated value. However, when the Bloch simulations include the effect of the RF amplifier non-linearity, the simulated quadratic phase coefficients are no longer invariant with increasing pulse amplitude. Instead they also start to increase with increasing pulse amplitudes as a reflection of the increasingly compressed HS pulse shape. Neither the simulated coefficients based on the quartic fit nor those based on the quadratic fit agree exactly with the measured coefficients. However, taking the RF amplifier non-linearity into account does make the simulated coefficients behave more like the measured values. In addition, the exact variation of the simulated quadratic phase coefficients seems to be sensitive to the exact form of the RF non-linearity curve (whether quartic or quadratic). Both these facts suggest that the increase in quadratic phase coefficient with pulse amplitude is caused, at least in part, by the compression of the HS pulses due to the non-linear performance of the RF amplifier at high pulse amplitudes.

Since the HS180° quadratic phase coefficient varies with increasing pulse amplitude, it follows that the residual quadratic phase in the HS90°-HS180° sequence will be affected. This is indeed observed in Figure 30 where the residual quadratic phase coefficient in the SE sequence is found to mirror closely the increase with HS180° pulse amplitude of the HS180° quadratic phase coefficient. In the SE sequence, the increasing residual quadratic phase coefficient with increasing HS180° amplitude might be expected to result in a decrease in signal because of the spread in phase through the voxel in the slice direction. This signal decrease with increasing HS180° amplitude is observed in practice (see Figure 31). The signal at the lowest amplitudes is not maximal probably because the HS refocusing pulse is not a fully 180° pulse at these amplitudes.

This suggests that the HS180° amplitude should be chosen carefully for maximum signal amplitude but even an amplitude of approximately 500Hz will still result in a slight residual quadratic phase coefficient of about 0.1 rad.mm$^{-2}$.

The results in section 3.4.2 have therefore demonstrated that in practice, the HS90°-HS180° sequence is not as robust to $B_1$ variations as expected from theoretical considerations such as the adiabaticity of the HS180° pulse. Instead, at higher $B_1$ amplitudes, the RF amplifier non-linearity leads to compression of the HS180° pulse shapes leading to a greater residual quadratic phase coefficient and a concomitant reduction in signal intensity. It is not clear whether the compression of the HS180° pulse at high amplitudes is sufficient to interfere with its adiabaticity.

## 3.5 HS Pulse Parameter Variation - Images

The experiments to this point have involved the acquisition of slice profiles but the sequence was originally intended to improve image uniformity. It was therefore necessary to investigate the effect on images of the observed residual quadratic phase and signal variations with increasing HS180° pulse amplitude.

### 3.5.1 Methods

Images were acquired with the HS90°-HS180° sequence with the HS90° pulse amplitude fixed at the calibrated value and the HS180° pulse amplitude varying over a range similar to that in the profile experiments in section 3.4. The HS pulses were the standard 1.5 kHz pulses with parameters as in section 3.3.1.2. The standard 2DFT SE imaging sequence parameters were TR / TE = 1500 / 82 ms, 192 x 192 mm FOV, 64 x 128 PE x read matrix, 33.3 kHz spectral width. The mean signal in a region of interest (ROI) comprising most of the phantom was plotted against the HS180° pulse amplitude.

This experiment was performed both in the $MnCl_2$-doped water phantom and in a ~20 cm diameter sphere filled with Silicone Oil. This was an attempt to allow separation of the effect of a spatially varying $B_1$ from the effect of experimentally varying the pulse amplitude $B_1$. A silicone oil-filled phantom ($T_1$ / $T_2$ = 1041 / 244 ms) was chosen because silicone oil has a much lower dielectric constant [60] than water resulting in a

much more homogenous $B_1$ field than the $MnCl_2$-doped water phantom (see theory section 3.1.1). To verify this and characterise the $B_1$ variation in the phantoms, $B_1$ maps were acquired of both phantoms using the $B_1$ mapping method of De Vita [61].

As before, $B_1$ was approximately calibrated by recording the amplitude setting required for 90° excitation by hard pulses of a range of durations

## 3.5.2 Results

Graphs of the variation in image signal with HS180° $B_{1max}$ are presented in Figure 32 and Figure 33.

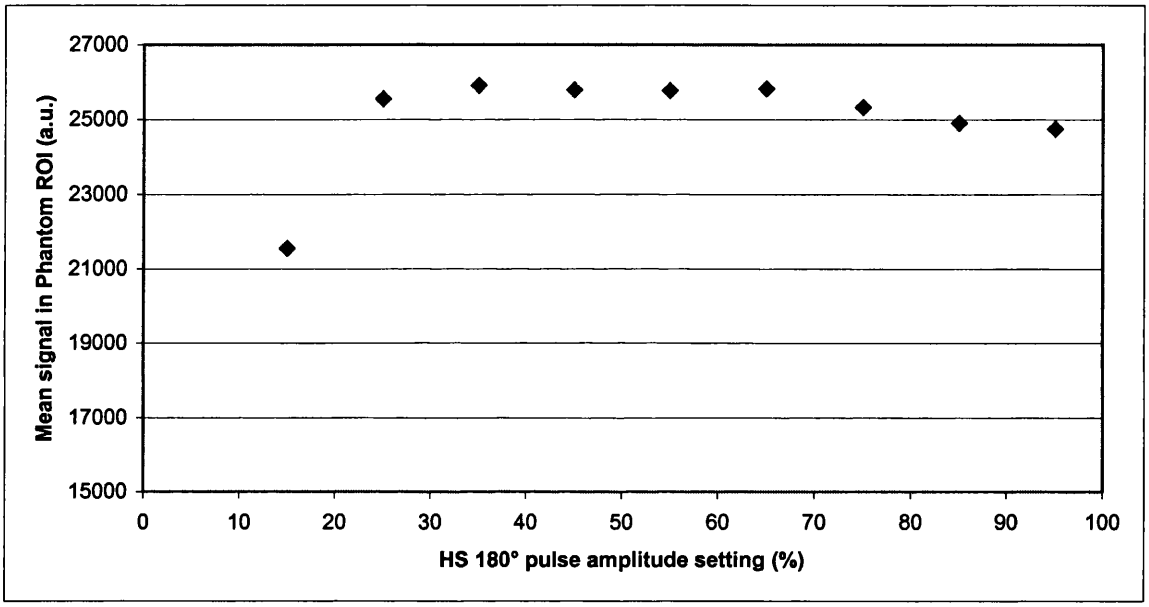


**Figure 32 HS90°-HS180° Signal Variation with HS180° Pulse Amplitude**
The signal was the mean signal in a ROI covering most of the $MnCl_2$-doped water phantom.

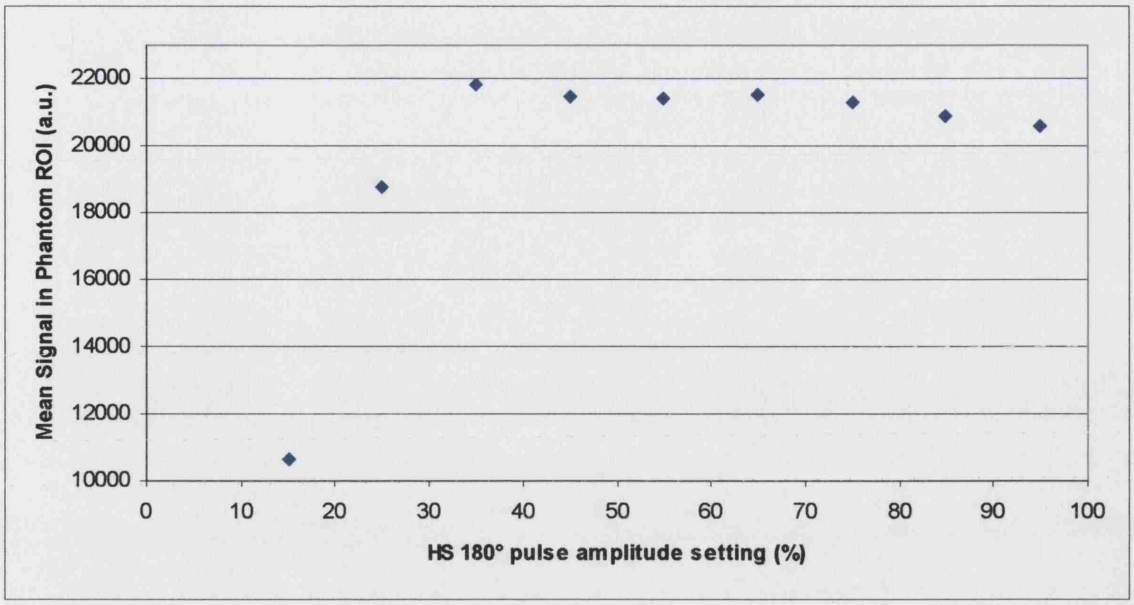


**Figure 33 HS90°-HS180° Signal Variation with HS180° Pulse Amplitude**
The signal was the mean signal in a ROI covering most of the silicone oil-filled phantom.

$B_1$ maps for both phantoms are shown in Figures Figure 34 and Figure 35.

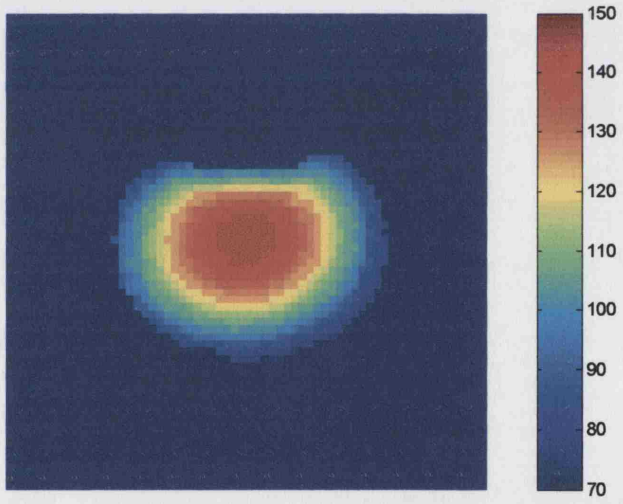


**Figure 34 A $B_1$ Map of the $MnCl_2$-Doped Water Phantom**
The map was acquired using the method developed by De Vita [61]. The right-hand scale is the $B_1$ expressed as a percentage of the nominal $B_1$ value according to the hard pulse calibration (500 Hz).

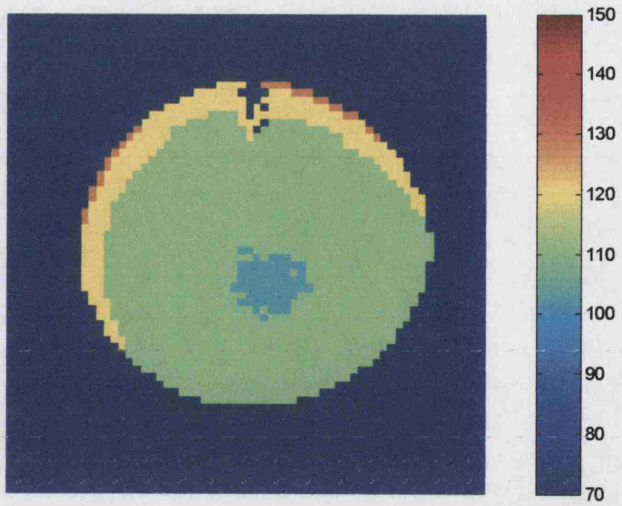


**Figure 35 A $B_1$ map of the Silicone Oil phantom.**
The map was acquired using the method developed by De Vita [61]. The right-hand scale is the $B_1$ expressed as a percentage of the nominal $B_1$ value according to the hard pulse calibration (211 Hz).

## 3.5.3 Analysis

Phase images of the $MnCl_2$-doped water phantom and Silicone Oil phantom at different HS180° pulse amplitudes are shown in Figure 36 and Figure 37 respectively.

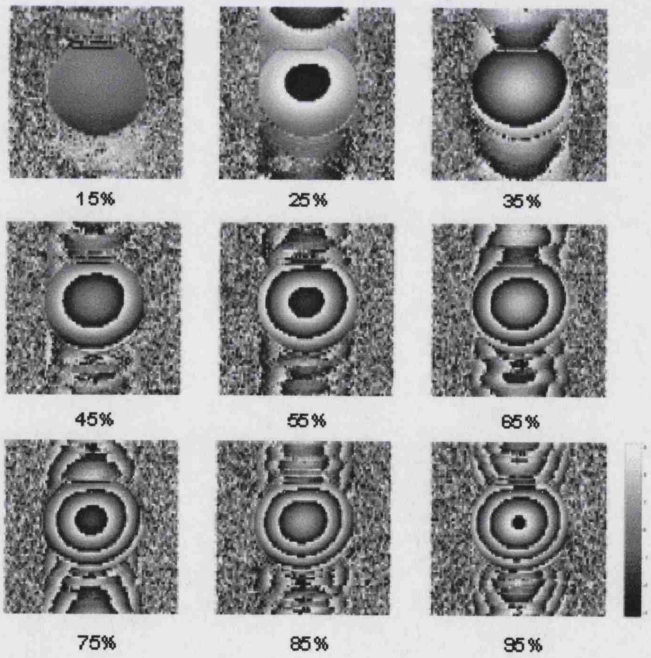


**Figure 36 HS90°-HS180° Phase Images of the $MnCl_2$-Doped Water Phantom**
The percentages are scanner amplitude settings for the HS180° pulse.

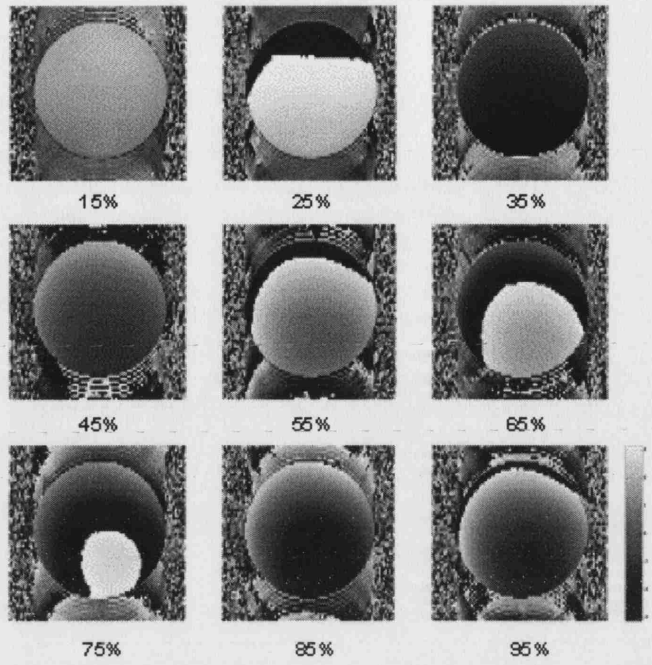


**Figure 37 HS90°-HS180° Phase Images of the Silicone Oil-Filled Sphere**
The percentages are scanner amplitude settings for the HS180° pulse.

As illustrated in Figure 36, a significant phase variation was observed across the images of the $MnCl_2$-doped water phantom. Images of the silicone oil phantom (Figure 37) did not show as much phase variation but in both cases the phase distribution had a similar spatial pattern to the $B_1$ map. It therefore seemed likely that the phase distribution was linked to the $B_1$ distribution. Conolly's expression (Equation 55) shows that the phase due to the HS180° refocusing pulse will indeed depend on the pulse $B_1$. To establish whether the phase variation observed in the water phantom was just that predicted by Conolly's expression, the phase offset expected from the HS180° pulse used here was calculated for the image with the greatest phase variation (and the highest HS180° pulse power). In other words, Conolly's expression was used to calculate the phase at each point within the $B_1$ map. Before this could be done the HS180° amplitude was estimated from the hard pulse calibration curve and the $B_1$ map (acquired for a 500 Hz amplitude hard pulse) was linearly scaled so that it matched this HS180° maximum $B_1$. The final calculated phase was offset by a fixed amount so that its maximum matched the measured phase maximum. To compare the measured and simulated phase images and profiles, the measured phase image was unwrapped using FSL Prelude software [62].

Measured and Simulated phase images and profiles are shown in Figure 38.

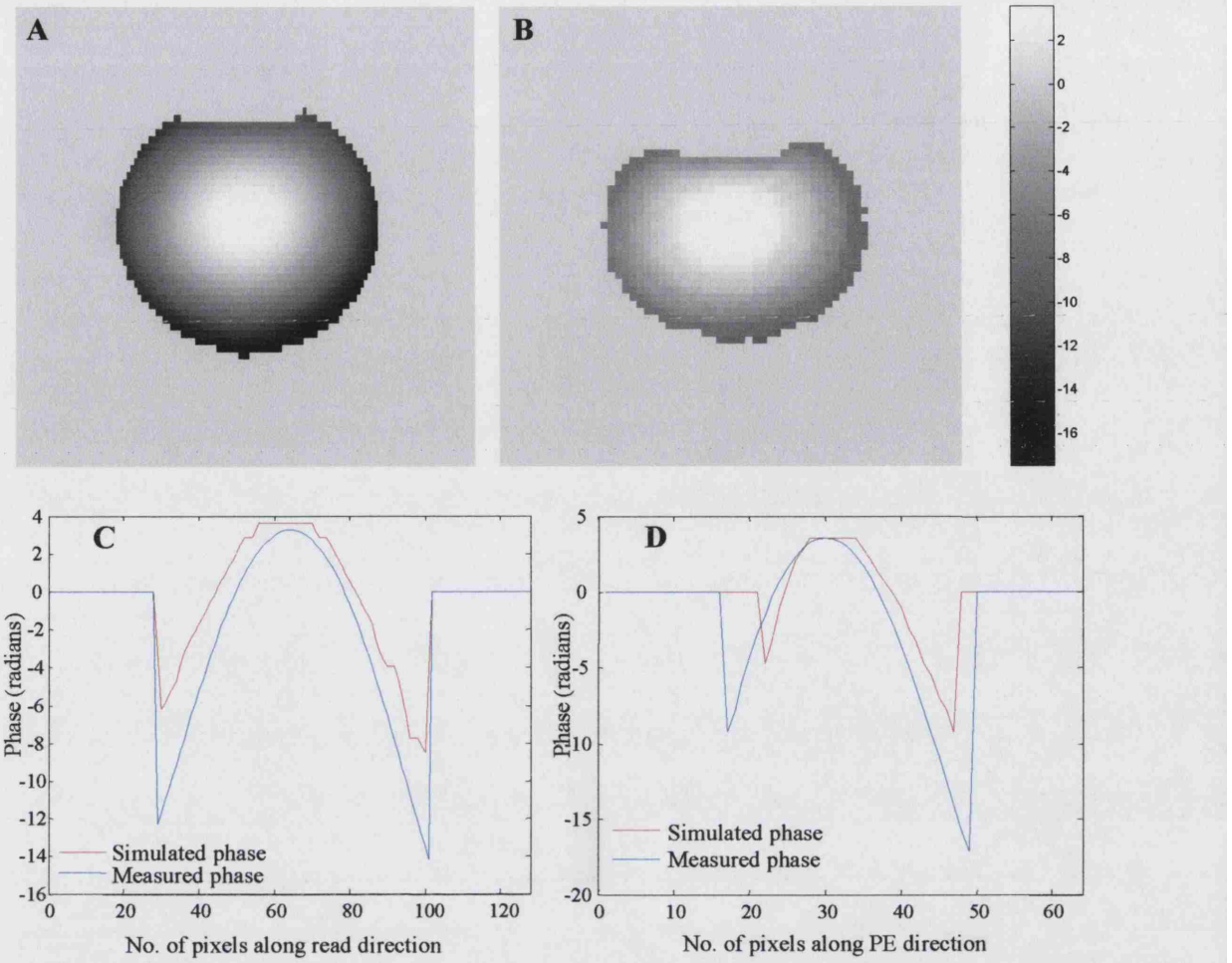


**Figure 38 Measured and Simulated Phases for the HS90°-HS180° Image with the Largest HS180° Pulse Power**

**A**: Measured phase image (unwrapped). **B**: Phase simulated from scaled $B_1$ map (Figure 34) using Conolly's expression (Equation 55). **C**: Horizontal profiles along the centre of the both measured and simulated phase images in the read direction. **D**: Vertical profiles along the centre of the both measured and simulated phase images in the PE direction.

## 3.5.4 Discussion

The signal in images acquired with the HS90°-HS180° sequence (see Figure 32 and Figure 33) varied with HS180° pulse amplitude in a similar fashion to the signal in image profiles (over a similar range of pulse amplitudes) (see Figure 31). At the lowest HS180° amplitudes the refocusing pulse has a flip angle much closer to 90° than 180°, so that it has only a small refocusing component and results in a much lower SE signal. At higher HS180° amplitudes the signal decreases slightly due to an increased residual quadratic phase coefficient resulting from RF amplifier non-linearity. The signal decrease is less than 6% of the maximum signal for both phantoms so the image signal

seems fairly robust to HS180° $B_1$ variations despite the increased residual quadratic phase coefficient in the presence of RF amplifier non-linearity.

As expected, the $B_1$ maps for the water and oil-filled phantoms (Figure 34 and Figure 35) are very different with the water-filled phantom showing strong $B_1$ inhomogeneity or field focusing effects. The range of $B_1$ values in the water-filled sphere is not dissimilar to the range found in the human head (see Figure 5).

Figure 38 demonstrates that the phase variation observed in the water-filled phantom reflects the $B_1$ distribution within it, as predicted by Conolly. The predicted phase image is a slightly different shape to the measured phase image and does not contain the largest negative phases observed at the edges of the sphere. This is because the $B_1$ map used to predict the phases was based on SE-EPI images that contain geometric distortions (as described in sections 2.12.3.2.2 and 4.2).

The large phase variation across the water-filled sphere might be expected to cause in-plane intravoxel dephasing resulting in a decreased signal. However the slight signal decrease at high HS180° amplitudes (Figure 32 and Figure 33) is similar in magnitude for both the water and oil-filled phantoms despite the very slight phase variation across the silicone oil phantom. This is good evidence that the in-plane phase variation is not causing any additional signal decrease in the water-filled phantom and does not affect the $B_1$-sensitivity of the signal from this sequence. The phase variation is, however, manifest as a smearing out of the signal in k-space (see Figure 39) and is simply a result of spin isochromats being refocused by the HS180° pulse at slightly different times depending on the particular $B_1$ at each position. This can be understood using sweep diagrams (Figure 9): the greater the $B_1$, the larger the $B_{eff}$ sweep, the later the spin isochromat arrives in the transverse plane and the more phase offset it will possess.

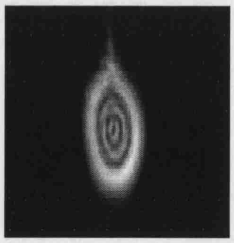

**Figure 39 K-space from an HS90°-HS180° Image of the $MnCl_2$-Doped Water Phantom**
The image was acquired with maximal HS180° amplitude. The pattern is elongated in the vertical PE direction because the matrix size was rectangular (64 x 128 PE x read).

It should be noted that, unlike the phase in the HS90°-HS180° image (see Figure 36), the phase in the Sinc90°-Sinc180° and Sinc90°-HS180°- HS180° images was constant. Even though the HS180° pulses in the latter sequence both create a $B_1$-dependent phase as predicted by Conolly, the phases from the two HS refocusing pulses cancel so that there is no net phase remaining in the image. Some phase variation was observed in the LFM90°-LFM180° image, with a pattern similar to the $B_1$ distribution, but was much less than in the HS90°-HS180° image.

## 3.6 Image Uniformity Evaluation

Now that the behaviour of slice profiles and images with varying HS parameters has been investigated, it is possible to address the original aim of using the HS-SE sequence to improve image uniformity. The next section is devoted to looking at whether the four sequences reduce image sensitivity to $B_1$ inhomogeneity. It still remains to determine which sequence gives the most uniform image, which RF pulse amplitudes are required for the most uniform image from each sequence, and how the image uniformity varies with $B_1$ (pulse amplitude) for each sequence. It was therefore necessary to investigate the behaviour of images acquired using the four SE sequences (see Figure 17). The following imaging experiments aimed to shed light on these issues.

### 3.6.1 Initial Approach

The initial simple approach to determining which sequence gives the most uniform image was to run the four sequences with the pulses at their calibrated values and measure the uniformity of each of the four images. Images of the $MnCl_2$-doped water phantom were acquired using the spin-echo sequences in Figure 17 with the RF pulses

at their calibrated values. The HS180° amplitude was chosen to be sufficiently above the value required for inversion to try to ensure that the pulse would be above the adiabatic threshold. However the amplitude was not set too high so that the residual quadratic phase coefficient would be minimised to prevent signal loss as in Figure 32 and Figure 33. The standard pulse parameters were used as in section 3.3.1.2. Sequence parameters were TR / TE = 1500 / 82 ms, 128 x 128 mm FOV, 64 x 64 PE x read matrix, 33.3 kHz spectral width.

Image histograms (with 50 bins) were plotted and used to calculate a measure of image uniformity. The measure selected was the percentage of voxels within the object having image intensities within ± 10% of the histogram mode. This is similar to the uniformity measure recommended by the Institute of Physics and Engineering in Medicine [63].

Figure 40 shows the images and corresponding histograms taken with the four sequences. The uniformity (%) and relative signal in each image are given in Table 5.

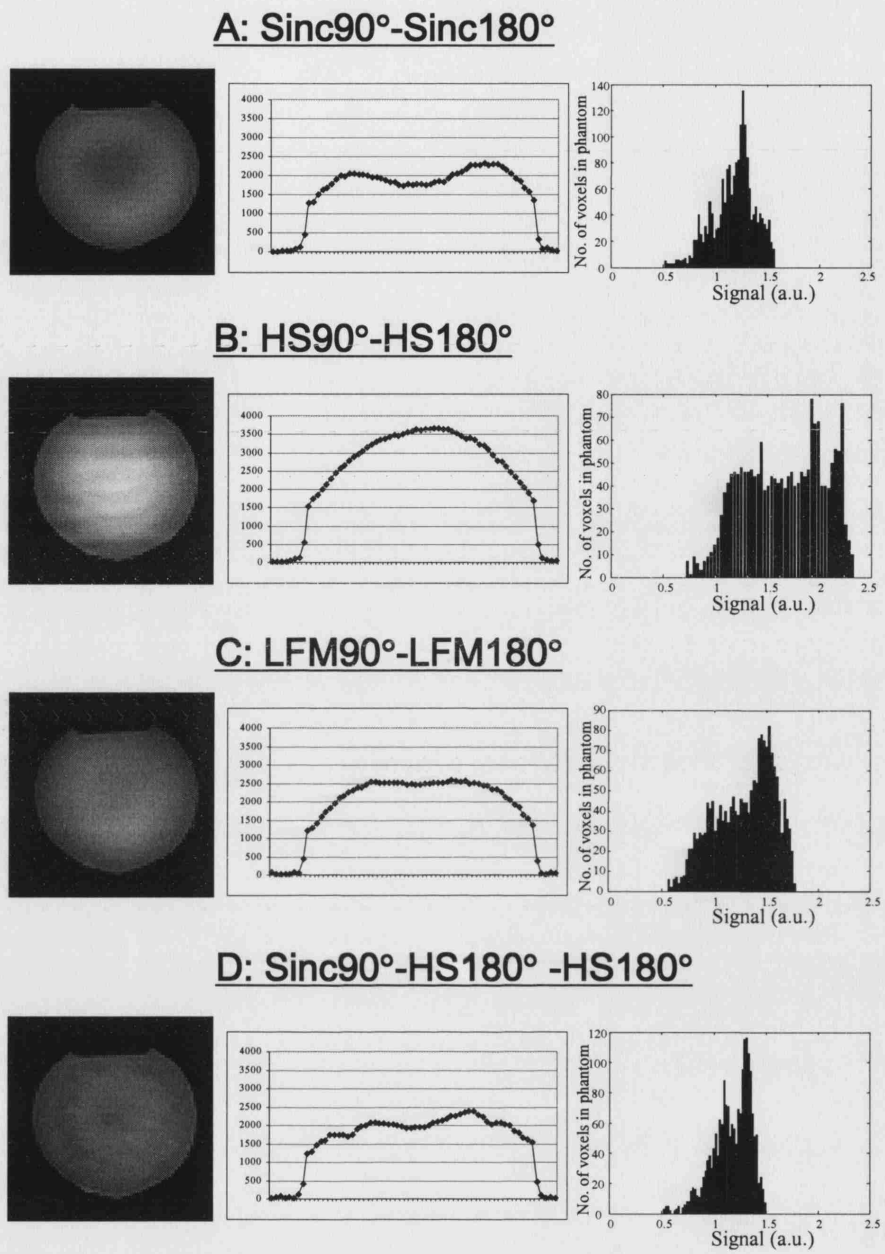


**Figure 40 SE Images Taken with the Four SE Sequences**
In the left-hand column are the images, all scaled to the same intensity scale. In the central column are horizontal image signal intensity profiles taken through the centre of the images on the left. In the right-hand column are histograms corresponding to the voxels inside the phantom in each image.

| Image | A | B | C | D |
|---|---|---|---|---|
| Sequence | Sinc SE | HS-SE | LFM-SE | Sinc-HS-HS |
| Uniformity (%) | 49.1 | 31.8 | 41.6 | 51.2 |
| Mean Signal (a.u.) | 16368 | 23968 | 18632 | 16304 |

**Table 5 Image Uniformity and Mean Signal**
The uniformity (% of voxels that are within ±10% of the histogram mode value) is given for each of the images in Figure 40. The mean signal in a region of interest covering most of the phantom is also given for comparison.

From this simplistic approach we could conclude that, for images acquired at the 'calibrated' pulse values, the Sinc90°-HS180°-HS180° sequence gives the most uniform image (see Figure 40 and Table 5). It appears from the table that the HS90°-HS180° sequence gives the least uniform image of all the sequences. This sequence also gives the most signal of all probably due to the wide and sharp slice profile compared with the other sequences (see Figure 23). This means that the HS90°-HS180° sequence has the largest integral under the slice profile and therefore the greatest signal.

There is a central dark region in the conventional SE image in Figure 40A probably due to 'overtipping' when the excitation flip angle exceeds 90° where $B_1$ is higher than the calibrated excitation value. This may be exacerbated in the SE sequence because the variation in $B_1$ will also lead to errors in the refocusing flip-angle which could further reduce signal. The HS90°-HS180° image lacks this central dark region, however it has a rounded image profile with poorer overall uniformity than the conventional image. The rounded profile shows that this sequence still retains some sensitivity to $B_1$ probably due to the remaining variation of the HS90° pulse flip-angle with $B_1$. However the lack of a central dark region may result from the relative insensitivity to $B_1$ of the signal from the HS refocusing pulse.

## 3.6.2 Methods

We have seen in sections 3.4 and 3.5 that the residual quadratic phase coefficient and signal vary unexpectedly with the amplitude of the HS180° pulse in the HS90°-HS180° sequence. This means that the uniformity may vary with pulse amplitude as well. For this reason it is inadequate to conclude which sequence gives the most uniform image from a set of images taken at a single pulse amplitude setting. For all the sequences it is likely that the image uniformity will vary with pulse amplitudes and this should be investigated before attempting to answer the question of "which pulse amplitudes are required for the most uniform image from each sequence?". Only with this information will it be possible to properly optimise each sequence and evaluate which gives the most uniform image.

It would be too time-consuming to investigate the entire parameter space created by varying both 90° and 180° pulse amplitudes independently through all possible values,

therefore it was decided to fix the pulse amplitude ratio to that for the 'calibrated' pulse values and multiply both pulse amplitudes by the same factor (between 0.5 and 1.5). This also mimics what happens at different locations within a phantom containing a range of $B_1$ values. For example at the centre of the $MnCl_2$-doped water phantom, the $B_1$ map shows a region of high $B_1$ where both pulses of a SE sequence would be expected to reach amplitudes higher than the nominal or calibrated values. The initial experiment was therefore extended by acquiring images using each of the four SE sequences with pulse amplitude multiplication factors varying in steps of 0.1 between 0.5 and 1.5. For each image, the histogram was again calculated and a measure of image uniformity was obtained in the way described previously in section 3.6.1.

In addition, for two of the sequences (HS90°-HS180° and LFM90°-LFM180°), the 90° pulse amplitude was fixed at the calibrated value and images were acquired with the 'calibrated' 180° pulse amplitude multiplied by a range of factors between 0.5 and 1.5. This allowed investigation of the effect on the image uniformity of the 180° pulse only.

## 3.6.3 Results

The approximate hard pulse calibration was used to translate the scanner pulse amplitude settings into approximate $B_1$ values and the resulting parameter space probed by the experiments is shown in Figure 41.

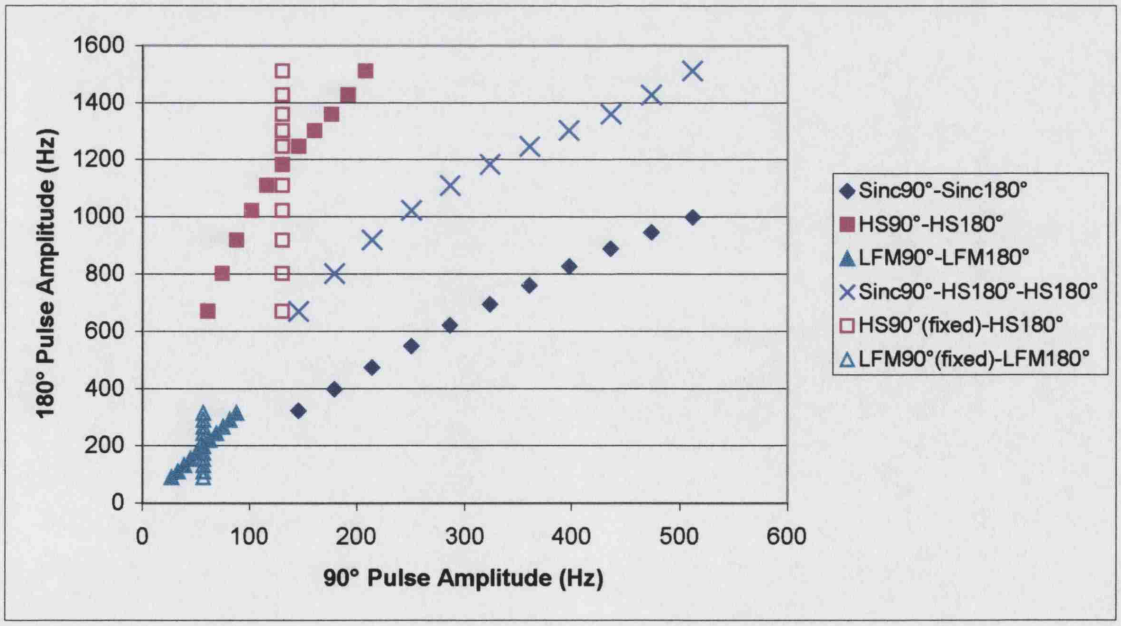


**Figure 41 The $B_1$-Space Probed by the Series of Experiments in this Section**

The variation of the mean signal in a region of interest covering most of the phantom is shown in Figure 42.

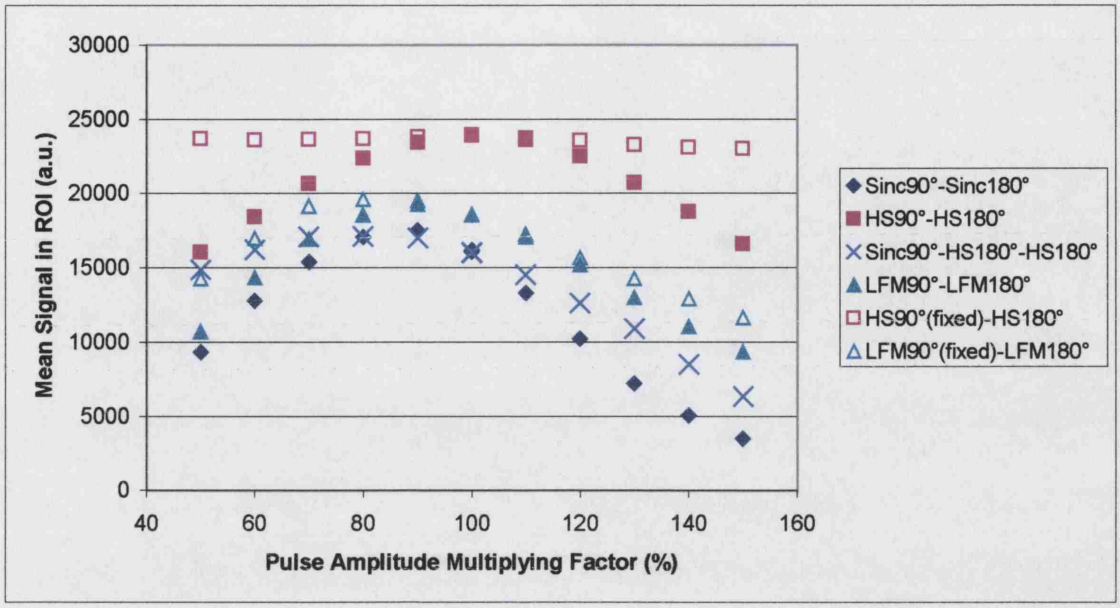


**Figure 42 The Signal Variation with Pulse Amplitude Factor for All Four SE Sequences**
The signal plotted is the mean inside a region of interest comprising most of the phantom.

Figure 43 shows the uniformity calculated for each image. Table 6 summarises the maximum uniformities and variation of uniformity over the range of pulse amplitude factors.

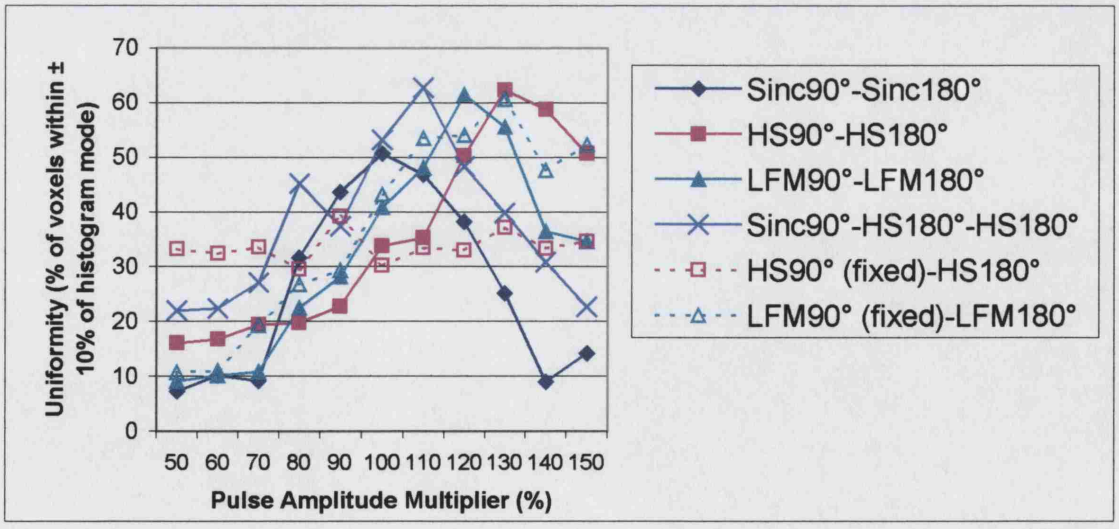


**Figure 43 Uniformity Measured with Each Sequence over a Range of Amplitude Factors**
The uniformity measure used was the percentage of voxels having intensities within ± 10% of the histogram mode.

| Sequence: | Sinc90°-Sinc180° | HS90°-HS180° | LFM90°-LFM180° | Sinc90°-HS180°-HS180° | HS90° (fixed)-HS180° | LFM90° (fixed)-LFM180° |
|---|---|---|---|---|---|---|
| Pulse multiplier for max. uniformity(%) | 100 | 130 | 120 | 110 | 90 | 130 |
| Maximum uniformity (%) | 50.7 | 62.3 | 61.5 | 62.8 | 39.3 | 60.6 |
| Mean uniformity (%) | 26.0 | 35.1 | 32.6 | 37.5 | 33.7 | 37.2 |
| Standard Deviation (%) | 16.9 | 17.6 | 18.3 | 13.8 | 2.7 | 18.3 |

**Table 6 A Summary of the Uniformity for Each of the Four SE Sequences**
The uniformity measure used was the percentage of voxels having intensities within ± 10% of the histogram mode.

## 3.6.4 Discussion

As we can see from Figure 41, the experiments here have not sampled the entire $B_1$ parameter space so the conclusions made here will not be exhaustive. However the region of $B_1$ covered surrounds the 'calibrated' values and is similar to the range of $B_1$ found in the water phantom used here (see Figure 34). A crude indication of the robustness of each sequence to $B_1$ variation is given by the variation of the overall image signal with the pulse amplitude factor (Figure 42). Perhaps the most striking (and reassuring) result from this graph is that changing the HS180° pulse amplitude while fixing the HS90° amplitude hardly affects the overall signal when compared with changing both pulse powers. This highlights the difference between the HS90° and HS180° pulses, namely that the former is not adiabatic whilst the latter is. It also means that the subtle effects observed when changing the HS180° pulse amplitude in sections 3.4 and 3.5 become insignificant when compared to the gross signal changes resulting from changing both the excitation and refocusing pulse amplitudes. Here we are in the relatively flat region of the curves in Figure 32 and Figure 33 where the HS180° pulse is giving the signal magnitude performance we expect from an adiabatic refocusing pulse.

It is clear from Figure 42 that the signal variation from the LFM90°-LFM180° sequence is largely independent of whether the 90° pulse is varied or fixed. This means that, in contrast to the HS180° pulse, the refocusing LFM180° pulse is not behaving adiabatically and is contributing as much (if not more than) the LFM90° pulse to the observed signal variation.

The standard Sinc SE sequence seems to show the most signal variation suggesting that it is the most sensitive to $B_1$ variations as expected. The HS90°-HS180°, LFM90°-LFM180° and Sinc90°-HS180°-HS180° sequences show similar levels of signal variation suggesting that they have similar levels of robustness to $B_1$ variation. It is necessary to look at the other results to distinguish between the performance of these sequences.

Figure 43 and Table 6 allow progress towards addressing the outstanding issues of how the image uniformity varies with $B_1$ (pulse amplitude) for each sequence, which RF pulse amplitudes are required for the most uniform image from each sequence, and which sequence gives the most uniform image.

All the sequences show significant variation of image uniformity with pulse amplitude factor. An exception is the HS90°-HS180° sequence with fixed HS90° pulse amplitude, which shows a roughly constant uniformity. This follows from the fact that the refocusing pulse is adiabatic as discussed above. For all the other sequences, a maximum uniformity is reached at some point within the range investigated here. It is interesting to note that only the standard Sinc SE sequence has its maximum uniformity at the calibrated pulse values. The other sequences all reach maximum uniformity at pulse amplitude multipliers greater than 100% and this may be because, at a nominal excitation pulse amplitude slightly greater than the calibrated value, the spatial $B_1$ distribution in the phantom is such that the flip angles are closer to 90° in more of the phantom and therefore the signal is more similar across the phantom making the image more uniform.

Again, the LFM90°-LFM180° sequence shows similar uniformity variation independent of whether the 90° pulse amplitude is fixed or varied. In fact, both the LFM90°-LFM180° and HS90°-HS180° sequences show a similar pattern of uniformity variation with pulse amplitude, which may reflect the similar mode of operation of these sequences.

Now that the variation of uniformity with $B_1$ has been elucidated and we can note the RF pulse amplitudes required for the most uniform image from each sequence (Table

6), it is possible to make a conclusion about which sequence gives the most uniform image. Clearly the standard Sinc SE gives the least uniform images. Again it seems that the other three sequences have similar maximum uniformities of around 60% (at least within the parameter space covered here).

It must be borne in mind that the result of the HS90°-HS180° sequence is not expected to be completely uniform since the HS90° pulse is not $B_1$-insensitive and any intrinsic coil receive inhomogeneity will also contribute to the image. Any residual image inhomogeneity could be removed from the images by scaling [35] based on the acquired $B_1$ maps.

### 3.6.5 Analysis

Since, from the results so far, it is not possible to distinguish between the performance of the three sequences (HS90°-HS180°, LFM90°-LFM180° and Sinc90°-HS180°-HS180°) in terms of uniformity and robustness to $B_1$ variation, it was decided to undertake further analysis of the images.

It is desirable that the signal in each voxel from a particular sequence should remain relatively constant, independent of the pulse amplitudes and if this is the case, that sequence can then be said to be robust to $B_1$ variations. In order to assess this robustness a map of the signal range in each voxel (for the whole range of pulse amplitude factors) was made for each sequence. An ideal map would show a zero signal range throughout the phantom. Since the $B_1$ is also known to vary spatially, a histogram of each map was also prepared to allow assessment of how the signal range varied across the phantom. The resulting maps and histograms are shown in Figure 44.

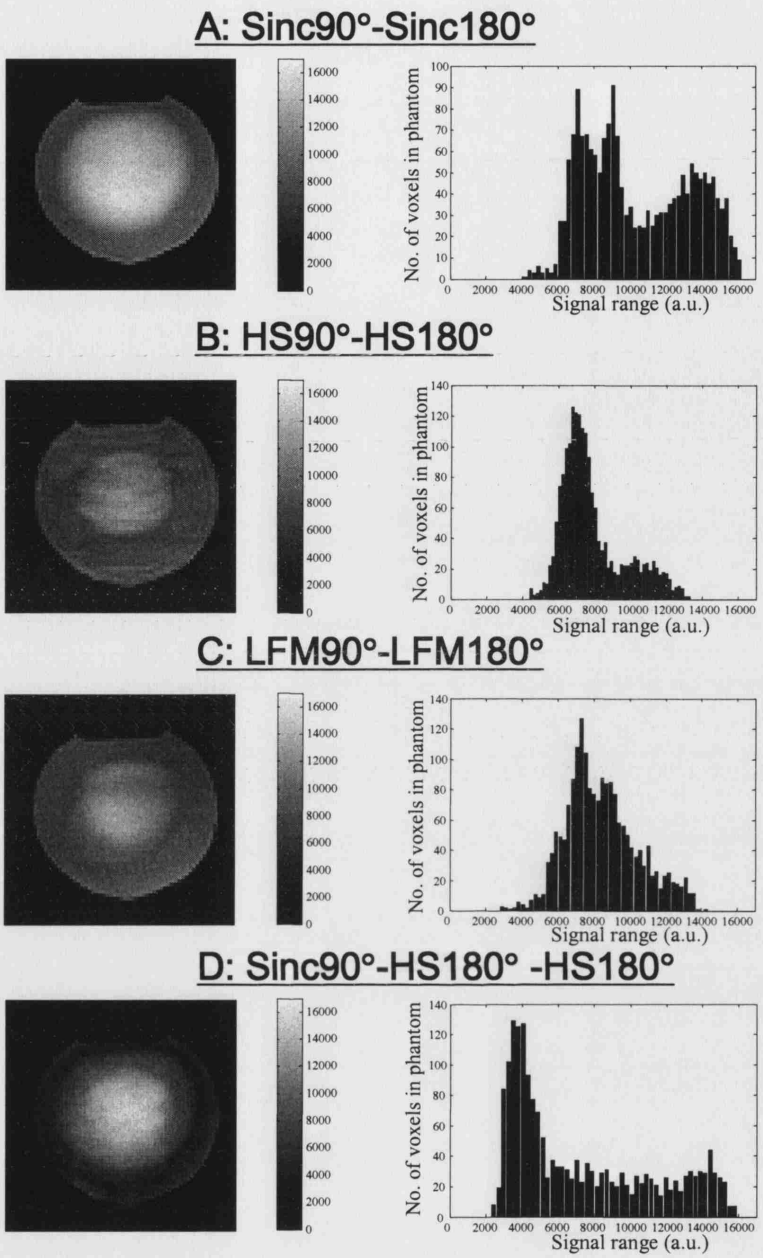


**Figure 44 Maps of Signal Range over Pulse Amplitude Multipliers from 0.5-1.5**
The maps are all scaled between 0 and 16000 arbitrary signal units. On the right-hand side are corresponding histograms.

As stated, the ideal map would be dark everywhere in the phantom. All the maps in Figure 44 reflect the $B_1$ distribution mapped in Figure 34 to some extent. It is clear that the worst sequence in terms of signal range is the standard SE sequence. The map is bright for this sequence showing that many voxels have a large signal range and corroborating previous results demonstrating that this sequence is not robust to changes in $B_1$. The map for the Sinc90°-HS180°-HS180° sequence has a very dark outer band, which shows that this sequence performs the best in this outer region of the phantom. However there is a bright central region which experiences very large signal ranges. The

HS90°-HS180° sequence has a more homogenous signal range map (narrower histogram) clustered mostly around relatively low ranges (a low histogram mode). This suggests that this sequence is more robust throughout the phantom to changes in pulse amplitude although there is still a slightly brighter central region in the map where the signal range is larger. The LFM90°-LFM180° map shows similar, if slightly poorer, behaviour. The histogram is not as narrow with more voxels having larger signal ranges showing that this sequence's robustness to changes in pulse amplitude is not as good as the HS90°-HS180° sequence.

The reason for the bright central region in the Sinc90°-HS180°-HS180° map is likely to be because the $B_1$ in the centre of the water-filled phantom reached levels sufficient to yield flip angles close to 180° for the Sinc pulse at the highest pulse amplitude multiplying factors. In this central region the signal from the Sinc 'excitation' pulse would then have reached values close to zero, resulting in a very large signal range over the whole range of pulse amplitudes and a bright region in the signal range map. The same behaviour of the signal from the Sinc90° pulse explains the bright region in the Sinc90°-Sinc180° map. The region in the HS90°-HS180° map is not as bright as that in the Sinc90°-HS180°-HS180° map because the approach to 180° flip angles and zero signal as $B_1$ increases is slower (see calibration curve Figure 19) compared with the Sinc pulse so even high pulse amplitude multipliers at the centre of the water phantom do not reach signal levels as low as those reached by the Sinc90° in similar conditions.

## 3.7 SAR Considerations

A final factor to consider when comparing the practical applicability of the four sequences is their specific absorption rate or SAR. The theory behind the calculation of SAR is given in section 2.7. Here we use the fact that, for a given object

$$SAR \propto \frac{\int B_1^2(t)dt}{T_p}.D$$

**Equation 65**

where $D = T_p/TR$ is the duty cycle or fraction of the total scan time for which the RF pulse is on. If we assume that all the sequences will be applied with the same TR, the relative SAR for each sequence will simply be proportional to the integral of $B_1^2(t)$ dt for all the pulses.

This integral was calculated for all four sequences, using the standard pulse parameters and calibrated pulse $B_{1max}$ values in Hz shown in Figure 41. The relative SAR for each sequence (a.u.) was found to be 1000 for the Sinc90°-Sinc180° sequence, 7795 for the HS90°-HS180° sequence, 1169 for the LFM90°-LFM180° sequence and 15,395 for the Sinc90°-HS180°-HS180° sequence.

It is clear from these figures that the SAR of the HS90°-HS180° is slightly less than half that of the Sinc90°-HS180°-HS180° sequence, which is as expected since it has one less RF refocusing pulse.

## 3.8 Conclusions and Further Work

It has been demonstrated that HS full passage pulses can be used for both excitation and refocusing in a SE sequence. The principle of quadratic phase compensation was investigated and exploited in the HS90°-HS180° sequence. Slice profiles from each of the four sequences investigated show that the LFM90°-LFM180° gives the poorest profile with the greatest phase variation. The HS90°-HS180° also gives a 10% sharper slice than the conventional Sinc SE sequence without the slice thickness degradation caused by using two HS refocusing pulses.

Further measurements of a series of HS90° and HS180° pulse quadratic phase coefficients agreed with values predicted using the analytical expressions of Park [59] and Conolly et al [64] respectively. A linear relationship was found between the quadratic phase coefficient and the pulse $\mu$ (for a fixed bandwidth and pulse duration) for both excitation and refocusing pulses and this could prove useful in designing pulses to ensure quadratic phase compensation in future HS90°-HS180° sequences.

When investigating the effects of increasing the HS180° amplitude, RF amplifier non-linearity was found to compress the HS180° pulse shapes at high amplitudes leading to an unexpected increase in the HS180° quadratic phase coefficient and a consequent increase in the residual quadratic phase coefficient in the HS90°-HS180° sequence. This increase in the residual quadratic phase coefficient was found to cause a small decrease in the signal from this sequence at high amplitudes in both profiles and images.

An additional phenomenon observed for the HS90°-HS180° sequence was the phase variation present due to the range of $B_1$ values in the water-filled phantom. This phase was demonstrated to be that predicted by Conolly [64] and was only significant in the water-filled phantom (but not in an oil-filled phantom) since it contained an appreciable $B_1$ inhomogeneity. This spatial phase variation within the phantom did not cause any signal reduction but was only manifest as a smearing of the signal in k-space. This phase variation was not present in Sinc90°-HS180°-HS180° images since the two refocusing pulses compensate each other's phase exactly. For this reason this sequence is not expected to suffer from RF amplifier non-linearity in the same way as the HS90°-HS180° sequence.

A simplistic approach to comparing the uniformity of images acquired using the four different sequences by looking at a single set of images acquired with 'calibrated' pulse values was found to be inconclusive. When pulse amplitude factors were varied, a fuller set of images was obtained from which limited conclusions could be drawn. Plots of the overall image signal for the HS90°-HS180° and LFM90°-LFM180° with fixed excitation pulse amplitudes and varying refocusing pulse amplitudes demonstrated unambiguously the advantage of the adiabatic HS180° over the non-adiabatic LFM180° pulse. It also became clear that the subtle effects of RF amplifier non-linearity on the HS90°-HS180° signal were negligible compared with the gross signal changes observed when changing both excitation and refocusing pulse amplitudes simultaneously.

Image uniformities were found to vary significantly with pulse amplitude multiplier for all the sequences since none of them are fully adiabatic. The standard Sinc-SE sequence had a lower maximum image uniformity than the other sequences, showing that the others all go some way towards reducing the effect of $B_1$ inhomogeneity in images. The maximum uniformity of the other sequences was similar so further analysis was necessary to differentiate between the sequences in terms of their robustness to $B_1$ inhomogeneity.

Signal range maps again demonstrated that the standard Sinc-SE sequence was the most sensitive to $B_1$ variations. The least robust of the other sequences seemed to be the LFM90°-LFM180° sequence which showed a reasonable signal range over the set of

pulse amplitude multipliers throughout the water-filled phantom. The Sinc90°-HS180°-HS180° sequence was extremely robust to $B_1$ changes in one region of the phantom but not in the centre of the phantom, largely due to variations in the signal excited by the Sinc90° pulse with pulse amplitude multiplier. The signal range map for the HS90°-HS180° sequence seemed the most uniform, the sequence achieving relatively low signal ranges fairly consistently throughout the phantom.

From these considerations it is clear that the best of these four sequences in terms of image uniformity and robustness to $B_1$ inhomogeneity are the HS90°-HS180° and the Sinc90°-HS180°-HS180° sequence. An advantage of the HS90°-HS180° sequence over the Sinc90°-HS180°-HS180° sequence is that it is shorter, using one less RF pulse and having a lower associated SAR. Obviously the SAR of these two sequences is greater than the others because they use relatively high-amplitude HS180° pulses.

It therefore seems that the HS90°-HS180° sequence performs the best of the sequences investigated here when uniformity, sensitivity to $B_1$ inhomogeneity and SAR are all considered. Unfortunately some image non-uniformity remains due to the non-adiabatic HS90° pulse and the RF coil receive inhomogeneity. This residual non-uniformity could be removed from images by scaling on reconstruction [35] according to acquired $B_1$ maps and the measured behaviour of the HS excitation pulse at different maximum $B_1$ amplitudes.

Ideally the sequence performance would be investigated *in vivo*. This technique could be compared with some of the other methods for reduction of $B_1$ inhomogeneity described in section 3.1.1.2. It would be interesting to see how it functions in a multislice mode. Potential applications include using these pulses for SE-EPI sequences that are often used for diffusion-weighted imaging (see Chapter 4) or occasionally for functional imaging studies.

# 4 TOWARDS HIGH RESOLUTION DIFFUSION TENSOR IMAGING WITH REDUCED DISTORTION AT HIGH FIELD STRENGTH

## 4.1 Background Theory of Diffusion Tensor Imaging

Diffusion weighted imaging (DWI) is MRI that is sensitive to the diffusion (random Brownian motion) of water molecules. The basic method for making NMR signals sensitive to the diffusion of water molecules is to apply gradients in the manner of Stejskal and Tanner [65], [66] as illustrated in Figure 45.

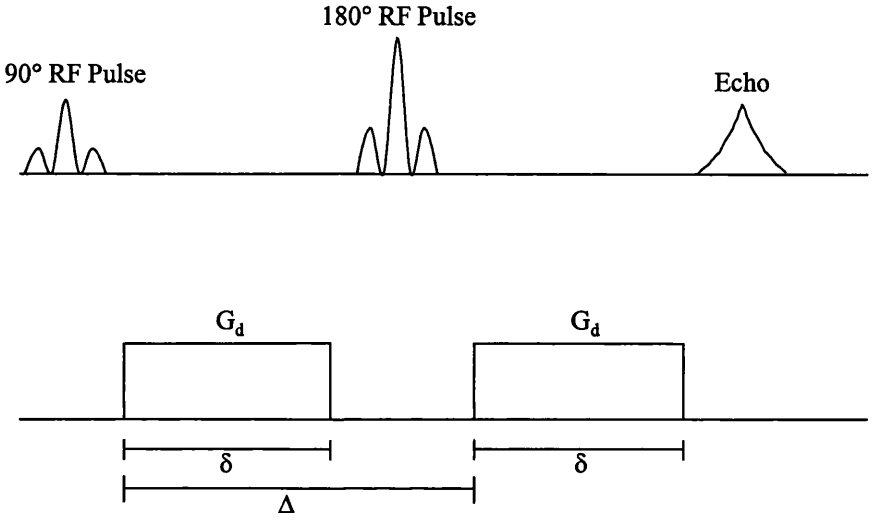


**Figure 45 The Conventional Stejskal-Tanner Sequence for Diffusion Weighting**

The result is a signal that depends on the net amount of diffusion that takes place between and during the gradients. The signal is attenuated by diffusion because the random nature of the motion causes spins to lose their phase coherence. It has been shown [65] that the signal S measured using the sequence in Figure 45 is given by

$$S = S_0 e^{-bD}$$

**Equation 66**

where $S_0$ is the signal that would be measured in the spin-echo sequence in the absence of the diffusion-sensitising gradients. D is the diffusion coefficient of the water in the sample in the direction of the diffusion sensitising gradients and b is a (scalar) parameter determined by the gradient sequence properties. Using the symbols in Figure 45, for the Stejskal-Tanner sequence b is defined as [65]

$$b = (\gamma G_d \delta)^2 \left( \Delta - \frac{\delta}{3} \right)$$

**Equation 67**

Images collected using the scheme shown in Figure 45 (or similar sequences) are known as diffusion weighted (DW) images and it is usual to estimate an apparent diffusion coefficient (ADC) from several such images collected at different b values. This is normally done by fitting the measured signal plotted against the calculated b value to an exponential decay (Equation 66) or equivalently by linear regression of a plot of ln(diffusion weighted signal) against b value. The gradient of the best-fit line gives an estimate of the ADC.

So far our description of diffusion-weighted imaging has been one-dimensional, assuming that the DW gradients are applied in one direction only, giving a single scalar ADC. In some tissues, such as in most areas of brain grey matter, this single ADC is sufficient to characterise the diffusion characteristics since they are largely independent of the orientation of the tissue (i.e. diffusion is isotropic). However in other tissues such as brain white matter or skeletal or cardiac muscle, the measured diffusivity is known to depend on the tissue orientation and no single ADC can fully characterise diffusion in these anisotropic tissues. Because diffusion is a three-dimensional anisotropic process, it is better described by a symmetric tensor containing six independent terms:

$$\overline{\overline{D}} = \begin{bmatrix} D_{xx} & D_{xy} & D_{xz} \\ D_{xy} & D_{yy} & D_{yz} \\ D_{xz} & D_{yz} & D_{zz} \end{bmatrix}$$

**Equation 68**

Where $D_{xx}$, $D_{yy}$ and $D_{zz}$ are the ADCs that would be obtained using only the x, y or z gradients respectively and the off-diagonal elements reflect the coupling or correlation between (diffusional) random molecular displacements and gradients in orthogonal directions [67], [68], [69].

It follows that any measured ADC will depend on the anisotropic subject orientation with respect to the gradients. A common approach to eliminate this directional dependence of the ADC measurement is to make three independent measurements and calculate a scalar invariant quantity known as the average ADC or bulk mean diffusivity [70] ($D_{av}$) which is related to the Trace of the diffusion tensor:

$$D_{av} = \frac{1}{3} Trace(\overline{\overline{D}}) = \frac{1}{3}\left(D_{xx} + D_{yy} + D_{zz}\right) = \frac{1}{3}\left(\lambda_1 + \lambda_2 + \lambda_3\right)$$

**Equation 69**

where $\lambda_1$, $\lambda_2$ and $\lambda_3$ are the eigenvalues of the tensor (see discussion below).

This bulk mean diffusivity can be measured by applying diffusion weighting gradients along the x, y and z axes in separate experiments and then averaging the ADC from each of the experiments (the so-called three-shot approach). Alternatively several gradient pulse sequences have been proposed to make the measurement in a single shot [71], [72]. Both the resulting maps of $D_{av}$ or Trace(D) and the underlying 'trace-weighted' or 'isotropically-weighted' images have been clinically useful in the diagnosis and assessment of acute ischaemic stroke [73] particularly because $D_{av}$ and Trace(D) seem very uniform in normal brain parenchyma [69] so that any diseased regions are conspicuous.

ADCs and $D_{av}$ can be clinically useful but in order to quantitate diffusion anisotropy it is necessary to measure the whole diffusion tensor. All the elements of the tensor can be estimated by applying diffusion weighting gradients in several different directions. The symmetry of the tensor (i.e. $D_{xy} = D_{yx}$ etc) can be exploited so that, at a minimum, seven independent measurements would be required: one for each of the six independent tensor elements and one (often a non-weighted b=0 image) to estimate $S_0$. This type of imaging experiment is called diffusion tensor imaging (DTI) and instead of a single scalar b-value (Equation 67) a symmetric b-matrix is defined in order to relate the effective diffusion tensor to the measured echo [70]:

$$\ln\left(\frac{S}{S_0}\right) = -\sum_{i=1}^{3}\sum_{j=1}^{3} b_{ij} D_{ij}$$

**Equation 70**

where $b_{ij}$ are the elements of the b-matrix and $D_{ij}$ are the elements of the diffusion tensor and S and $S_0$ are the echo magnitudes of the DW and non-DW signals respectively. In analogy with the diffusion tensor, the b-matrix has diagonal and off-diagonal elements, the former describing all interactions between diffusion and imaging gradients along the same axis and the off-diagonal elements coupling imaging and diffusion gradients in orthogonal directions. Each DWI and its corresponding b-matrix are then used to estimate the diffusion tensor by inverting Equation 70.

We have seen that the elements of the diffusion tensor depend on the orientation of the anisotropic structures of interest with respect to the gradient axes. However it is possible to calculate rotationally invariant quantities from the tensor (elements) that are intrinsic to the tissue such as the Trace (Equation 69). For example the tensor can be summarised by its three eigenvectors and eigenvalues that describe the axes of a diffusion ellipsoid (see Figure 46) and define a local 'fibre' frame of reference. The lengths of the axes of the diffusion ellipsoid are the eigenvalues $\lambda_1$, $\lambda_2$ and $\lambda_3$ first encountered in Equation 69 and correspond to the principal diffusion coefficients measured along the intrinsic coordinate directions in the voxel. A widely used measure of anisotropy is based on these eigenvalues and is known as the Fractional Anisotropy (FA):

$$FA = \frac{\sqrt{(\lambda_1 - \lambda_2)^2 + (\lambda_2 - \lambda_3)^2 + (\lambda_3 - \lambda_1)^2}}{\sqrt{2(\lambda_1^2 + \lambda_2^2 + \lambda_3^2)}}$$

**Equation 71**

The FA, one of several anisotropy indices, measures the fraction of the 'magnitude' of the diffusion tensor that can be ascribed to anisotropic diffusion [74].

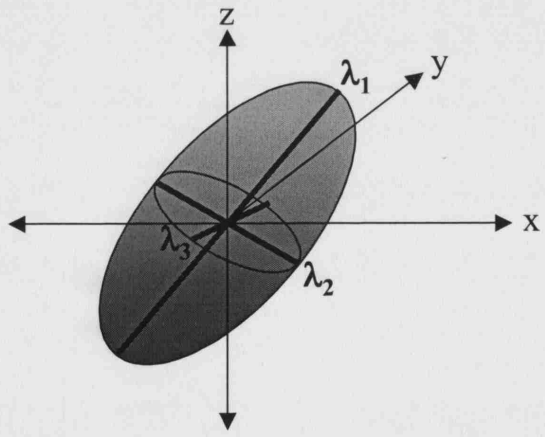


**Figure 46 The Diffusion Ellipsoid**
The axes of the ellipsoid (bold) lie along the eigenvectors of the diffusion tensor in the voxel under consideration and their lengths are equal to the tensor eigenvalues $\lambda_1$, $\lambda_2$ and $\lambda_3$ of which $\lambda_1$ is the greatest and is the diffusivity along the principal axis or major eigenvector.

Even though the determinants of water diffusion in tissues are still not fully understood, it is clear that tissue microstructure and architecture can substantially influence diffusivity [75]. For example, the idea that, in ordered fibrous tissues, the eigenvector associated with the largest eigenvalue in a voxel is parallel to the local fibre orientation,

has been applied in the white matter of the brain. Since it is easier for water molecules to diffuse along axons, it is reasonable that the principal axis of diffusion lies along nerve fibres. Water molecules diffusing in the direction perpendicular to the fibres encounter barriers such as the axonal membranes and myelin sheaths.

The local fibre directions or orientational properties of the diffusion tensor field can be displayed on a voxel-by-voxel basis in several ways. These display techniques include displaying the diffusion ellipsoid (Figure 46) for each voxel, direction field mapping in which the local fibre direction is displayed as a vector in each voxel and colour mapping in which colour is used to denote the local fibre direction in anisotropic voxels [70], [74] (see Figure 58).

There are many applications of DTI [76], [74] including the study of ischaemic brain injury, brain white matter diseases such as multiple sclerosis, Alzheimer's disease, brain development and aging as well as different areas of the body such as the spinal cord. A further application that has been a topic of much recent research is that of fibre tracking or tractography in the brain [77]. This is a method for reconstructing and following the trajectories of axonal fibre tracts in the brain and may give insights into white matter connectivity and anatomy. There are many tractography algorithms or fibre reconstruction techniques but they are generally based on the assumption that the principal diffusion axis in a voxel aligns with a single local fibre orientation and on tracing the principal axis or eigenvector of diffusion from voxel to neighbouring voxel in three dimensions. In reality, voxels are likely to contain contributions from several tissues (different white matter tracts, CSF and grey matter etc) and the signal to noise may be limited, both of these factors making it difficult to define a clear principal axis inside the MRI voxel and thereby limiting tractography.

Despite these limitations, DTI-based tractography has been qualitatively validated in humans and animals [77]. It has also been usefully applied to studying white matter anatomy and reorganisation in disease or following stroke [73] and has recently been combined with functional activation to look at the connections between activated brain regions [78] as well intraoperatively to neurosurgery [79], [80].

## 4.2 Using The DW-SE-EPI Sequence for DTI

One of the most commonly used sequences for DTI is the diffusion weighted spin-echo echo planar imaging (DW-SE-EPI) sequence. To assess its performance at high field strengths, and as a starting point for development of new techniques, the sequence was implemented on the 4.7 T system and images of volunteers were acquired. The aim was to investigate what could be achieved with this basic sequence in a first attempt (to the best of our knowledge) at human brain DTI *in vivo* at this field strength.

### 4.2.1 Methods

Single shot DW-SE-EPI images of a volunteer were acquired with no cardiac gating. EPI imaging parameters were TR = 12 s, TE = 81 ms (the minimum possible for the DW gradients and EPI readout selected), matrix size = 64 x 64 (100 read points), bandwidth = 250 kHz (4 μs per point), FOV = 192 mm, 50 slices to give whole brain coverage, slice thickness = 3 mm, slice centre-centre separation = 3 mm with interleaved slice acquisition order, yielding a final image resolution of 3 x 3 x 3 mm. The slice-select gradient for the 180° refocusing pulse was extended by 1 ms either side of the RF pulse to act as a crusher gradient for any magnetisation excited by the 180° pulse. This gradient was not included in the b-factor calculation but is relatively small in amplitude and will therefore provide negligible diffusion weighting. Cross-terms (resulting from interactions between diffusion and imaging gradients) were not included in the calculation of the b-matrix. Images were acquired in the transverse orientation with vertical phase encoding. One DTI acquisition was made with PE in the anterior-posterior (A-P) direction and another with PE in the opposite P-A direction. A single non-diffusion-weighted non-phase-encoded reference scan was acquired first to allow reduction of Nyquist ghost artifacts in the subsequently acquired images (see section 2.12.3.1.1).

Fat suppression was performed prior to exciting every slice to mitigate the chemical shift artifact (see section 2.12.3.2.1). The suppression module consisted of a single Gaussian fat-frequency-selective (non-slice-selective) presaturation pulse offset from the resonant (water) frequency by –661 Hz (corresponding to the fat shift of 3.3 ppm) followed by gradient spoilers. A non-diffusion-weighted image volume was acquired without fat suppression to investigate the effectiveness of the saturation pulse in removing the fat signal.

Diffusion weighting was applied using gradients placed either side of the 180° refocusing pulse as in Figure 45 with $\delta$ = 20.35 ms and $\Delta$ = 38.18 ms. Gradient amplitudes were set to give a resultant gradient magnitude of 90% of the system maximum resulting in a b-factor of 1,001 s.mm$^{-2}$. This diffusion weighting was applied in 20 directions based on the standard sequence used routinely for DTI at 1.5T at Great Ormond Street Hospital (GOSH) [81]. The 20 directions, evenly distributed throughout space, had been obtained using the electrostatic repulsion model proposed by Jones et al [68, 82] and are listed in Table 7 and illustrated in Figure 47. Three b=0 images were also collected to give an approximately optimal ratio of DW measurements to non-DW measurements [68, 82] giving a total of 24 acquisitions per slice (the 20 DW and 3 non-DW images as well as the non-DW non-PE reference scan for Nyquist ghost correction). The total acquisition time for a single DTI dataset was therefore just under 5 minutes.

| Direction | Read Gradient | Phase Gradient | Slice Gradient |
|---|---|---|---|
| 1 | 0 | 0 | 0 |
| 2 | 1000 | 0 | 0 |
| 3 | 336 | 942 | 0 |
| 4 | -405 | 606 | -685 |
| 5 | 825 | -513 | 236 |
| 6 | 6 | -363 | -932 |
| 7 | -811 | -287 | -510 |
| 8 | 852 | -320 | -414 |
| 9 | -240 | 959 | -149 |
| 10 | 835 | 272 | -478 |
| 11 | 9 | -904 | -427 |
| 12 | 0 | 0 | 0 |
| 13 | -63 | -812 | 580 |
| 14 | -269 | -390 | 881 |
| 15 | -422 | -624 | -658 |
| 16 | -601 | 779 | 177 |
| 17 | -516 | 86 | 852 |
| 18 | -790 | -607 | -87 |
| 19 | 728 | -181 | 661 |
| 20 | 265 | -96 | 959 |
| 21 | -561 | -701 | 440 |
| 22 | -405 | 631 | 662 |
| 23 | 0 | 0 | 0 |

**Table 7 The 23 Diffusion Weighting Gradient Directions**
The 20 equally-spaced DW gradient directions that result from using the electrostatic repulsion algorithm [68, 82] and the three b=0 repeats are listed in the order in which they were applied in the DW-SE-EPI experiment. The gradient values are normalised such that the gradient magnitude = 1000 for every direction.

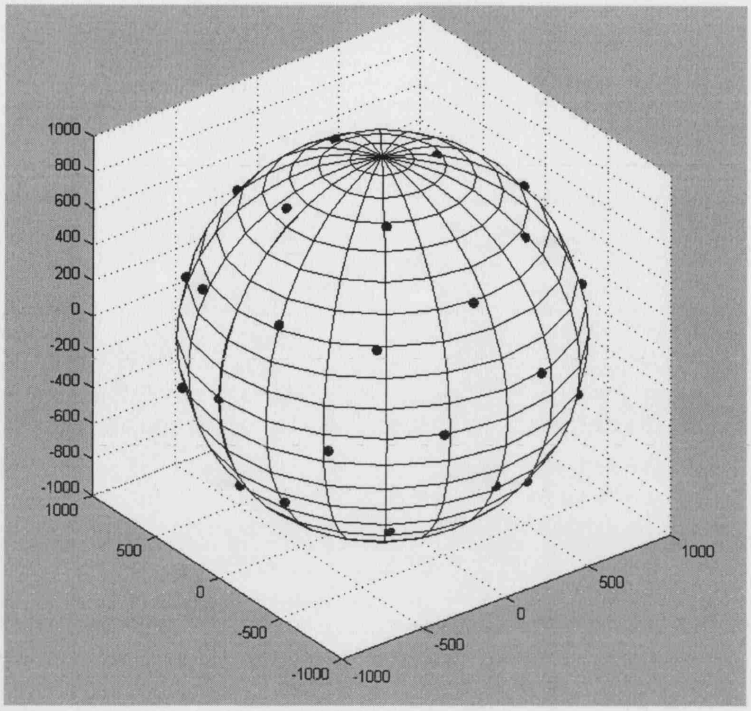


**Figure 47 The Diffusion Weighting Gradient Directions on a Sphere**
An opaque sphere with dots on its surface showing the 20 equally spaced DW gradient directions that result from using the electrostatic repulsion algorithm [68] see Table 7. Both positive and negative ends of the gradient direction vectors are shown.

Structural images were also acquired for anatomical reference and to allow assessment of the geometric distortion in the EPI images. The sequence used was a magnetisation-prepared (MDEFT) 3D-FLASH technique that had been previously optimised [83] to provide rapid, high-resolution structural acquisitions similar to those that accompany fMRI acquisitions on the 4.7 T scanner. Image parameters were the same as those described in Thomas et al [83].

The EPI images were reconstructed using the SMIS system reconstruction software. The Nyquist ghost removal (see section 2.12.3.1.1) used all the echoes from the non-phase-encoded reference scan to correct the phase of all the PE lines. This was found to reduce the ghosting level further than using only the central three echoes of the reference scan. Sampling delays were corrected for and the read data were interpolated from 100 raw data points to 64 equally spaced points in k-space. The raw data were filtered in both the read and PE dimensions using a Hanning filter applied to the first and last 12.5% of the data as is standard in the SMIS reconstruction software to reduce Gibbs ringing artifacts.

EPI images may be differently distorted for different diffusion gradient directions because of the effects of eddy currents in different directions (and this may cause errors in calculating the diffusion tensor). To investigate whether there was a substantial contribution to image distortions from eddy currents that varied with the different DW gradient directions, image subtractions were performed in which the image from one DW direction was subtracted from images in all the other DW directions. Image subtraction was performed for a few slices from several different directions.

In addition, to avoid the confounding effect of image differences due to tissue diffusion anisotropy, eddy current induced distortions were evaluated in the same way using an oil-filled bottle phantom. Transverse images were acquired both without diffusion weighting and with DW gradients applied in the positive and negative read, phase and slice directions separately. The EPI parameters were the same as for the head images except for TR = 2 s, TE = 102 ms, $\delta$ = 30 ms and $\Delta$ = 51.53 ms. In the case of the oil the non-DW image could be subtracted from images in the other DW directions since oil has a negligible diffusion coefficient [84].

Before processing the images to obtain an estimate of the diffusion tensor, the images were masked using a threshold-based mask created on an image with no diffusion weighting. To obtain the diffusion tensor, the b-matrix was inverted (using a method based on singular value decomposition in Matlab) and multiplied by the log of the signal. Maps of the trace of the tensor were created (and these will be directly proportional to the 'bulk mean diffusivity' in Equation 69). Regions of interest were drawn manually (Matlab) on (34) slices in areas of white and grey matter and in areas of CSF where these were clearly separated. ROI statistics such as the mean and standard deviation of the trace in each region were collected.

The fractional anisotropy (Equation 71) was also calculated and displayed. Finally the principal eigenvectors were calculated for the tensor in each voxel (using singular value decomposition) and a colour map of the directional pattern of the principal eigenvector was created by assigning the x (L-R) components a red colour, the y (A-P) components a green colour and the z (H-F) components a blue colour, each in proportion to their magnitude. The colour map was multiplied by the fractional anisotropy map to give increasing weight to the more anisotropic voxels.

Some of the DW images appeared extremely artifacted, containing bright and dark stripes in a variety of orientations. The striping was found to occur in only one DW direction (direction 7 Table 7) for the dataset presented here. Images from this DW gradient direction were therefore excluded from the analysis used for obtaining the diffusion tensor. To investigate the cause of the artifacts, the raw (k-space) data for the artifacted images was inspected and found to contain large signal 'spikes'. An example is shown in Figure 48. In a phantom DTI dataset acquired with the same parameters, 'spiking' and artifacts were observed in DW directions 7 and 18 (see Table 7) and in a later human DTI dataset spiking was observed in four DW directions 2, 5, 7 and 18 (see Table 7).

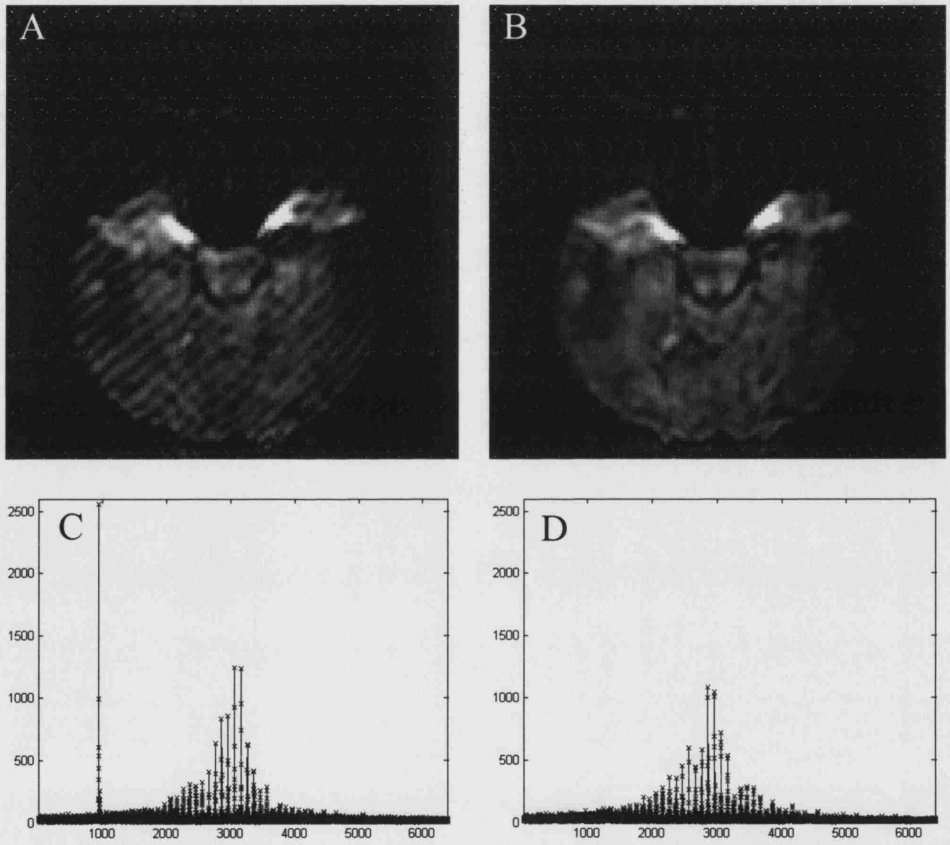


**Figure 48 The Effect of a Data Spike in the Image**
The artifacted image **A** and corresponding raw k-space data with a large 'spike' **C** is shown for diffusion-weighted direction 7 (see Table 7). For comparison, an image of the same slice for the next DW direction (direction 8 in Table 7) **B** with the corresponding raw k-space data **D** is included.

## 4.2.2 Results

Figure 49 shows some undistorted structural images compared with SE-EPI images acquired as part of the DTI experiment. Distortions are clearly visible in the EPI images.

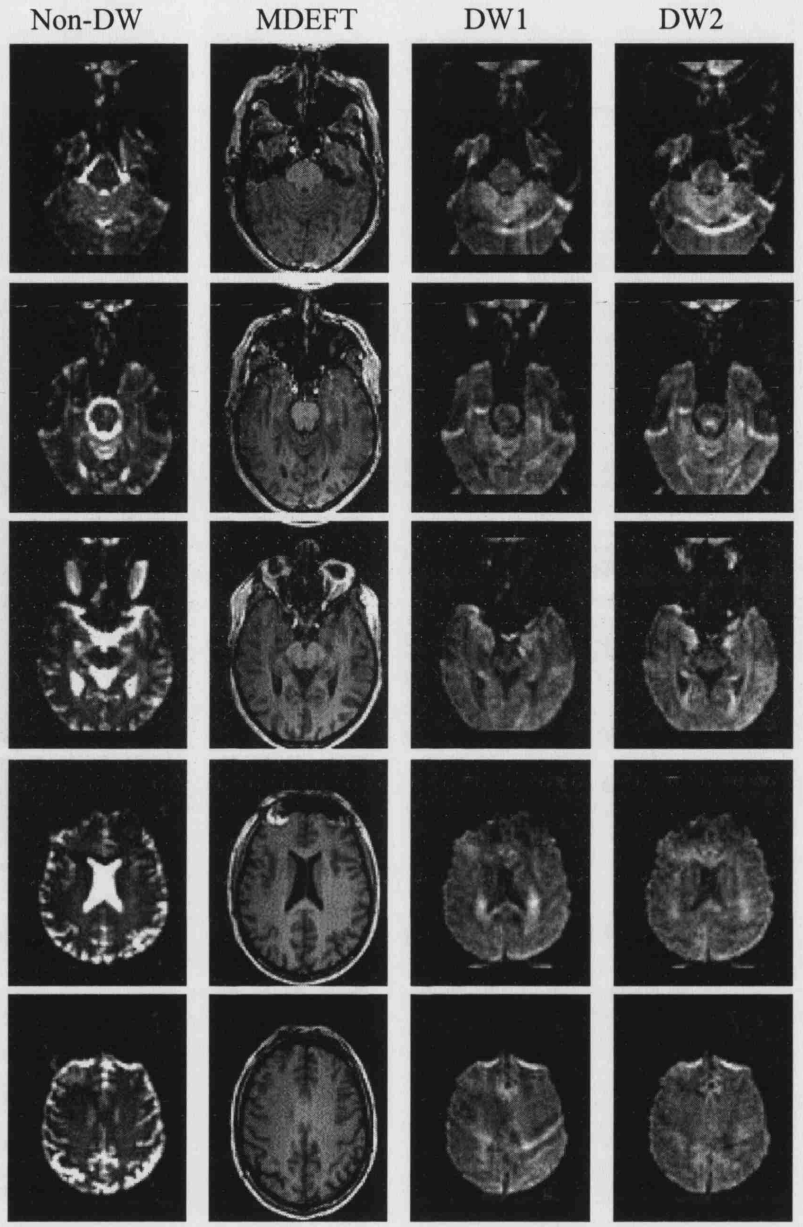


**Figure 49 Distortions in SE-EPI Images Relative to MDEFT Images**
Five transverse slices of the same subject are shown from scans taken with non-diffusion-weighted SE-EPI (direction 1 in Table 7) (**Non DW**), the MDEFT structural sequence described in the text (**MDEFT**), a DW-SE-EPI sequence with b = 1,001 s.mm$^{-2}$ in direction 4 in Table 7 (**DW1**), the same DW-SE-EPI sequence and b-value but with DW gradients in direction 6 in Table 7 (**DW2**). Phase encoding was in the vertical A-P direction with positive polarity. The EPI images here were coregistered to the MDEFT image and resliced using SPM2 [85] so that equivalent slices could be compared.

Figure 50 shows the effect of the fat suppression module used here on the non-DW SE-EPI images. The chemical shift artifact from the subcutaneous fat is not obvious in the fat-suppressed images.

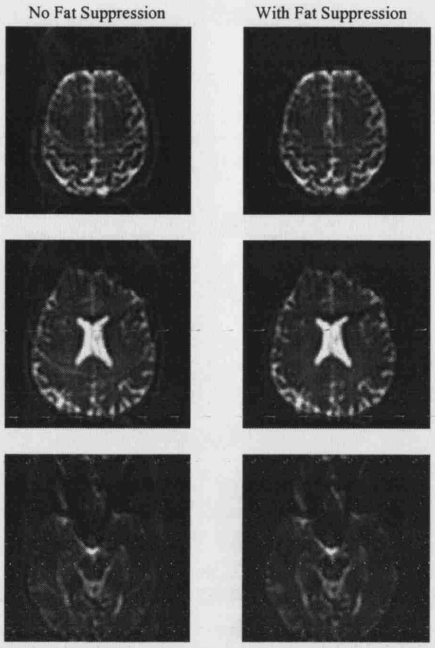


**Figure 50 The Effect of Fat Suppression on Non Diffusion-Weighted SE-EPI Images**
Three slices of non-DW EPI images of the same subject are shown with (Right-hand column) and without (Left-hand column) a fat-selective pre-saturation pulse followed by gradient spoiling to suppress the fat signal and the chemical shift artifact. Phase encoding was in the vertical A-P direction with positive polarity.

The effect of the PE gradient polarity on the chemical shift artifact and the fat-suppressed DW-SE-EPI images is illustrated in Figure 51. The subcutaneous fat is shifted in opposite directions in the images acquired with opposite PE gradient polarity. In some cases the fat is shifted outside the FOV but is aliased back in, forming a chemical shift artifact at an unexpected image location.

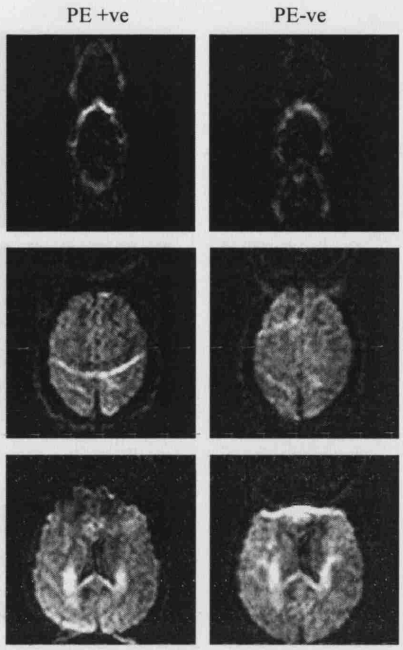


**Figure 51 The Effect of PE Polarity on Fat-Suppressed DW-SE-EPI images**
The left-hand column has PE gradients in the 'positive' direction whilst the right-hand column was acquired with the PE gradients in the opposite polarity so that k-space was traversed in the other direction.

The image subtractions for each gradient direction acquired with the oil phantom are shown in Figure 52. In the ideal case (no eddy-current-induced geometric distortions) there would be no difference between the DW and non-DW images and the subtracted images would be expected to contain only noise. Eddy-current-induced image shifts or shears would cause image differences especially visible at the edges of the phantom.

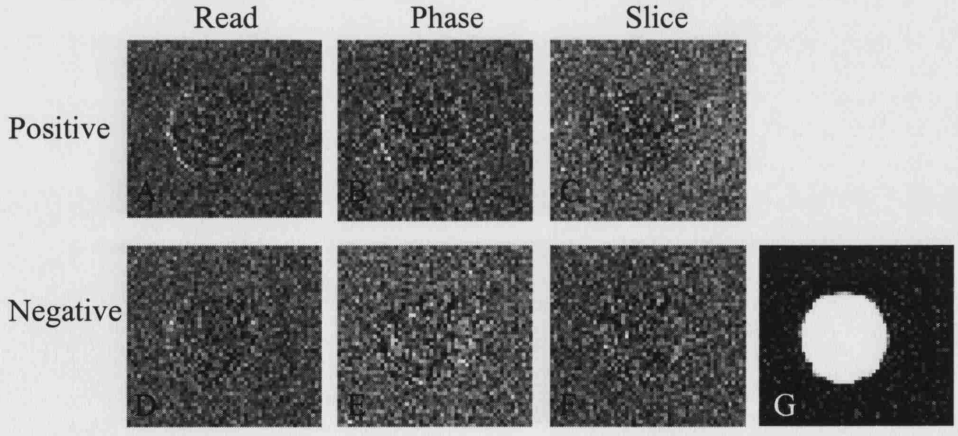


**Figure 52 DW Image Subtractions with an Oil Phantom**
The non-DW image of the phantom (**G**) was subtracted from DW images with gradients in the read, phase and slice directions to yield the subtracted images **A**,**B** and **C** (positive gradients) and **D**, **E** and **F** (negative gradients) respectively.

Examples of image subtractions carried out to investigate the eddy-current induced distortions are shown in Figure 53 and Figure 54. In the absence of eddy-current-induced geometric distortions, the only differences arising in the subtracted images should be due to diffusion anisotropy. Eddy-current-induced image shifts or shears would cause image differences especially visible at the edges of the brain.

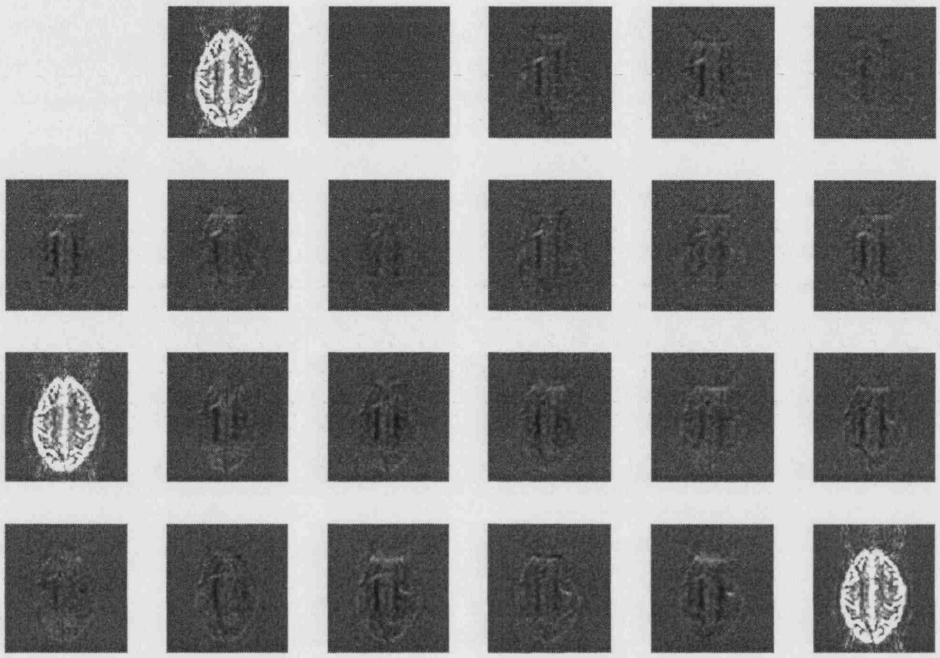

**Figure 53 DTI Image Subtractions for the Second DW Gradient Direction**
A single image slice is shown for each direction. The second direction (see Table 7) appears blank because this was the image subtracted from all the others. The three bright images correspond to the non-diffusion-weighted images, which have different contrast to the DW images. The signal differences inside the brain appear to arise mainly from diffusion anisotropy in areas of white matter.

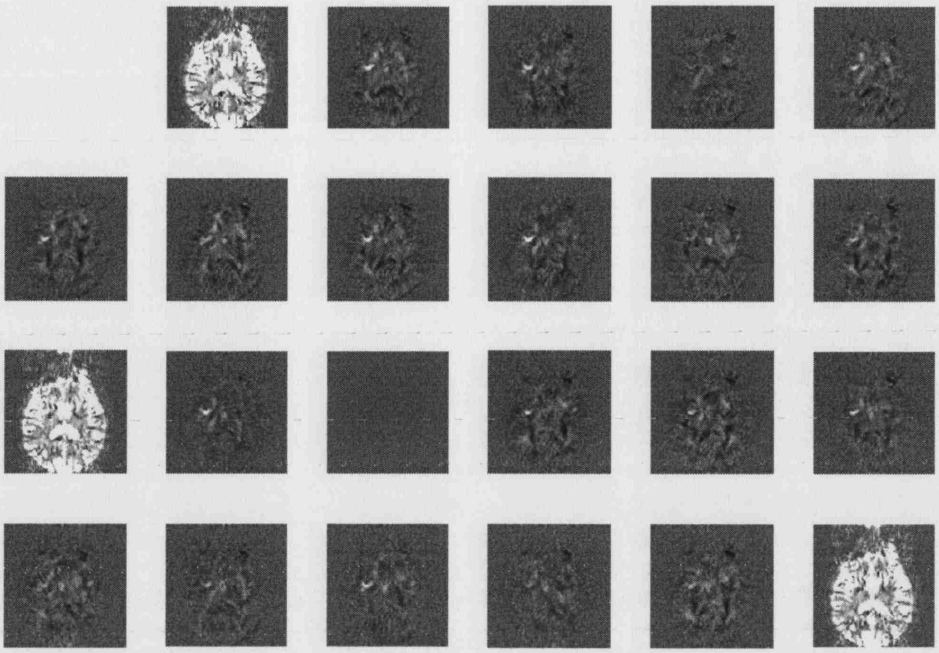

**Figure 54 DTI Image Subtractions for the Fourteenth DW Gradient Direction**
A single image slice is shown for each direction. The fourteenth direction (see Table 7) appears blank because this was the image subtracted from all the others. The three bright images correspond to the non-diffusion-weighted images, which have different contrast to the DW images. The signal differences inside the brain appear to arise mainly from diffusion anisotropy in areas of white matter.

Maps of the Trace of the diffusion tensor are shown in Figure 55 for the whole brain. The CSF appears bright, since it has a higher diffusion coefficient than tissue. There is not much contrast visible in the brain parenchyma. The maps show evidence of strong susceptibility-induced distortions.

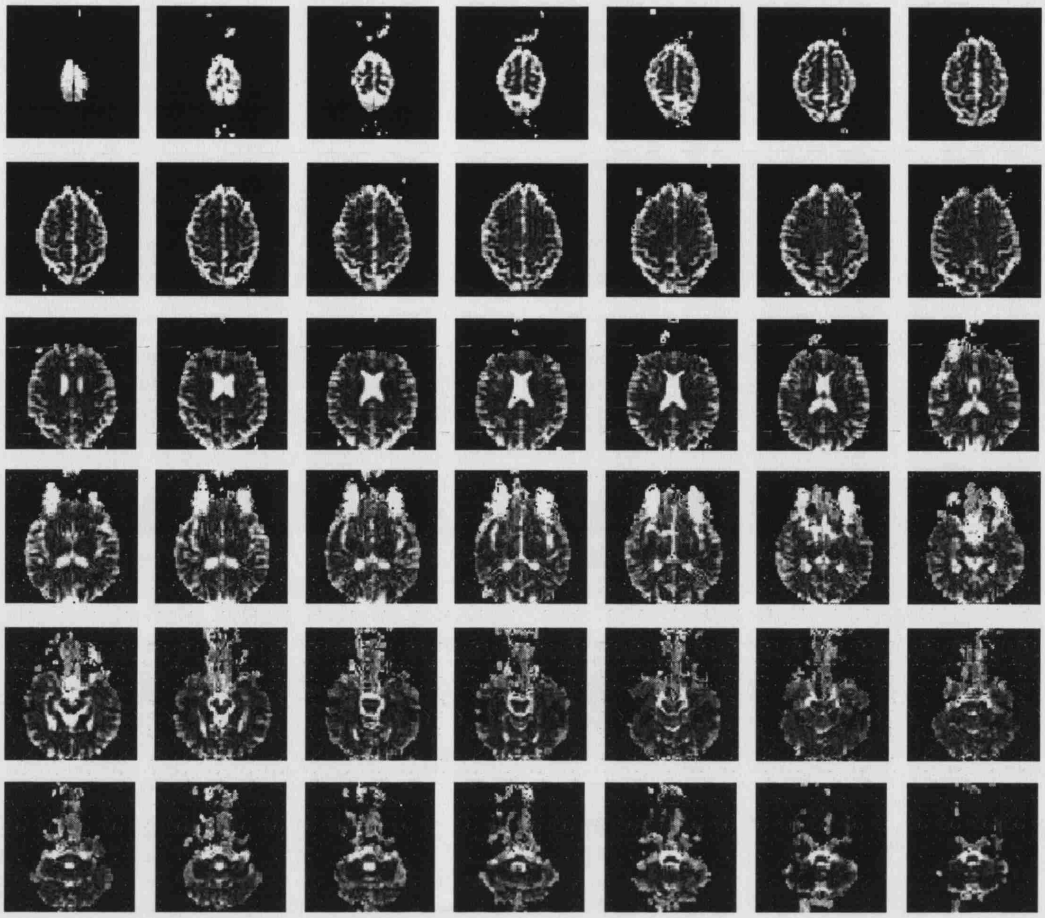

**Figure 55 Maps of the Trace of the Diffusion Tensor**
42 transverse slices covering the brain are shown in descending order from the top left to the bottom right. The images are scaled from a trace of 0 (black) to 7.5 x $10^{-3}$ $mm^2s^{-1}$ (white). The base images had been acquired with PE in the negative polarity in the vertical direction.

The ROIs used to obtain estimates of the mean trace in areas of CSF and areas of brain grey and white matter are illustrated in Figure 56.

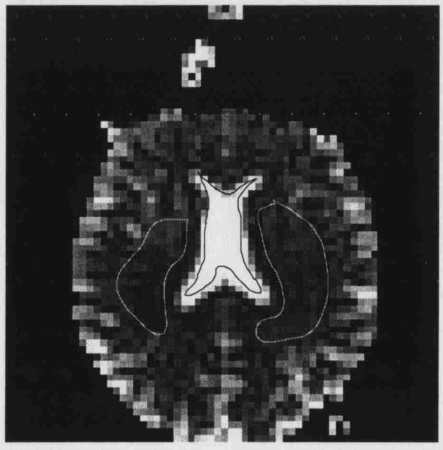

**Figure 56 Regions of Interest on a Trace map**
Typical regions of interest covering CSF in the ventricles (central ROI) and areas of primarily grey and white matter (left and right ROIs) are shown.

The mean of the ROI mean trace in all the grey and white matter ROIs (Figure 56) was $2.1 \pm 0.22 \times 10^{-3}$ $mm^2s^{-1}$ and the mean of the ROI mean trace in all the CSF ROIs (Figure 56) was $9.0 \pm 0.85 \times 10^{-3}$ $mm^2s^{-1}$.

Maps of the fractional anisotropy are shown in Figure 57 for the whole brain for the same dataset as in Figure 55. These show much more structure in the brain tissue than the trace maps in Figure 55. Bright areas in fractional anisotropy maps usually correspond to areas of white matter.

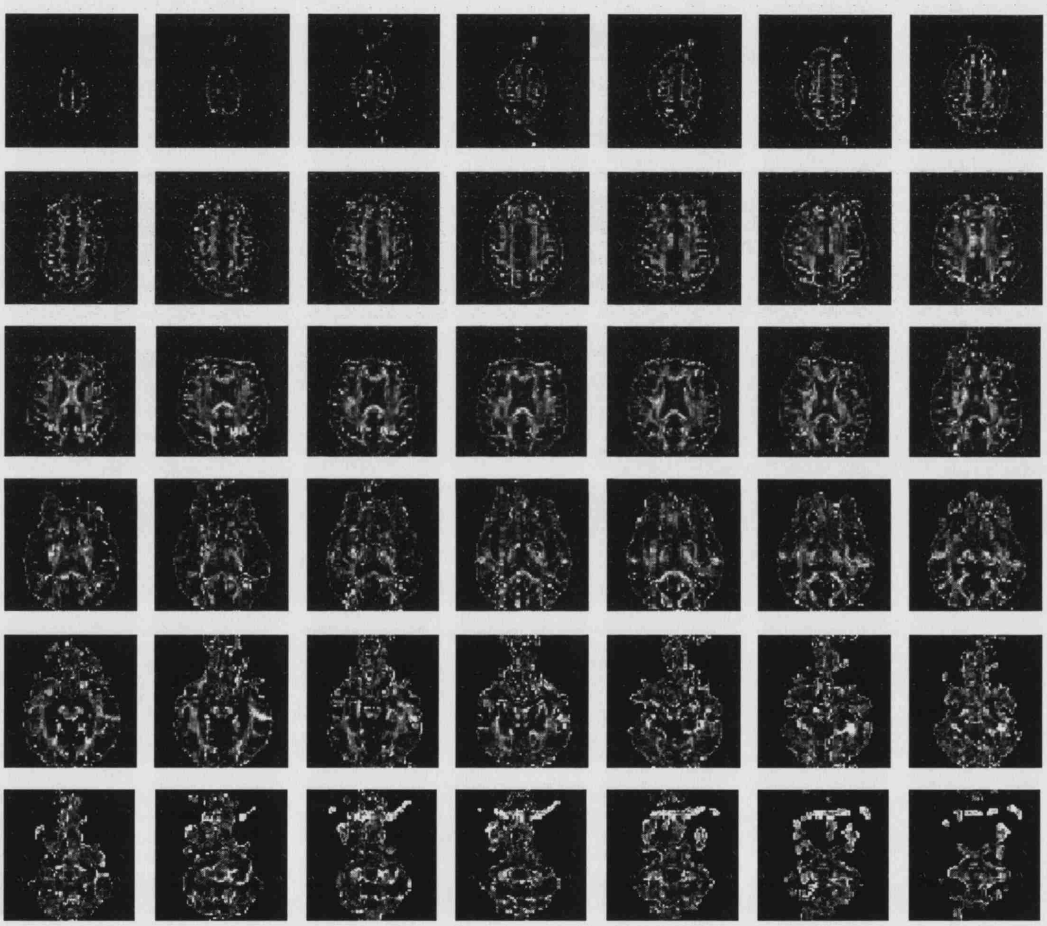

**Figure 57 Maps of the Fractional Anisotropy**
42 transverse slices covering the brain are shown in descending order from the top left to the bottom right. The images are scaled from a fractional anisotropy of 0 (black) to 1 (white) and are the same slices as shown in Figure 55.

Colour maps of the directional pattern of the diffusion tensor are shown in Figure 58 for the same dataset as in Figure 55 and Figure 57. Such maps are often useful for distinguishing white matter fibre tracts [86].

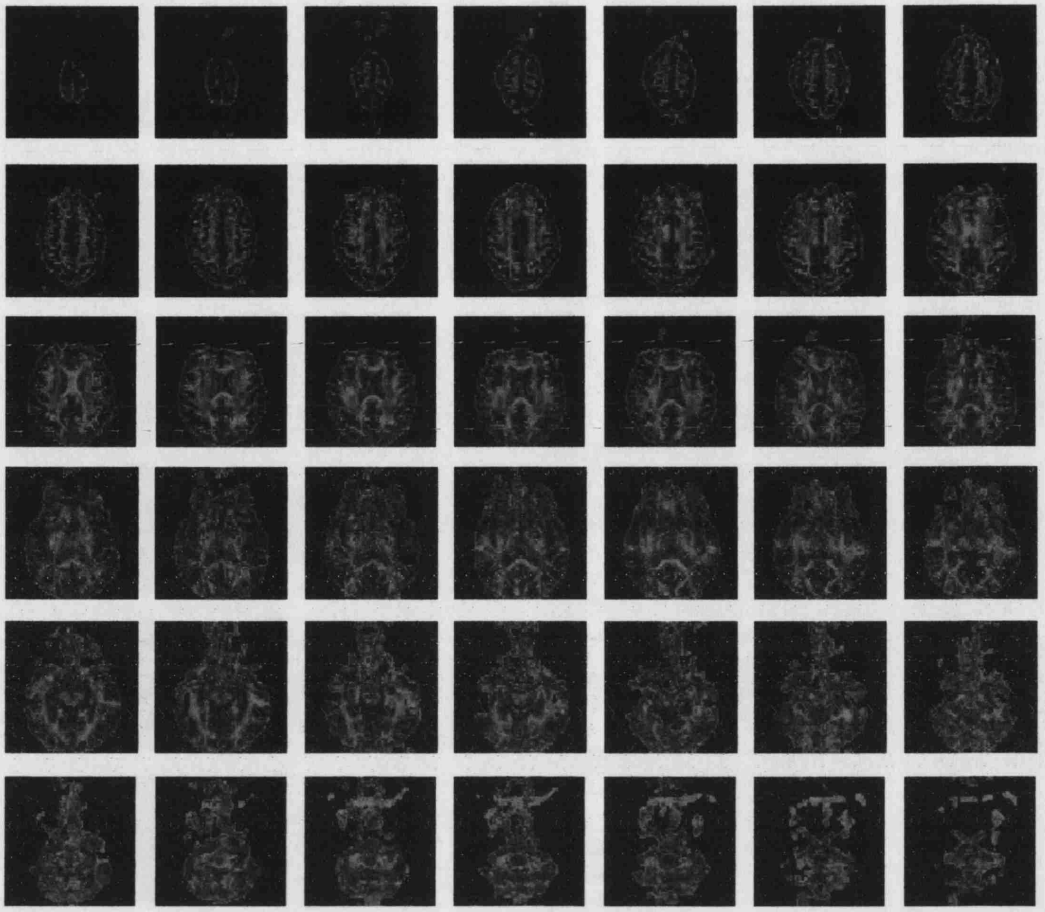

**Figure 58 Colour Maps Representing the Directional Pattern of the Diffusion Tensor**
42 transverse slices covering the brain are shown in descending order from the top left to the bottom right. Red corresponds to L-R diffusion eigenvectors, green corresponds to A-P diffusion eigenvectors and blue corresponds to H-F eigenvectors. The colour map was multiplied by the fractional anisotropy map in Figure 57 to give increasing weight to the anisotropic voxels. The slices shown are the same as those in Figure 55 and Figure 57.

## 4.2.3 Discussion

The striping caused by the 'spike' is obvious in Figure 48. Suggestions as to the cause of the spurious signal include vibrations of the gradient power cables that carry current from the gradient amplifiers to the gradient coils due to Lorentz forces. Vibrations may have caused the cables to temporarily disconnect, resulting in a sudden voltage across the connection and noise that could be picked up by the RF receive system.

A potential post-processing solution to the spiking could be to excise 'spikes' (detected for example by a nearest neighbour comparison between individual echoes or PE lines) from the raw data and interpolate between uncorrupted surrounding data points. Such a

strategy would fail to correct for spikes of similar magnitude to the real data. Spiking became more and more severe over a period of several months, affecting more DW directions. A hardware solution to the problem involved improving the connection between the gradient cables and gradient coils but a further improvement could be made by physically securing the cables to restrict their movement and reduce the likelihood of disconnection.

It is clear from comparing both the non-DW and DW SE-EPI images with the undistorted MDEFT structural images that there is extensive geometric distortion present in the SE-EPI data. From Equation 72 in section 4.3.2 it is clear that susceptibility-induced geometric distortion is worse at higher field strengths so the severe distortions are to be expected. The distortion is manifested as a stretching or compression of signal in the A–P direction since this is the direction of the phase encoding. Areas where the distortion is particularly severe are those close to the air spaces where there are main magnetic field variations due to the difference in susceptibility between air and soft tissue (see Chapter 5). For example, the areas adjacent to the auditory canals and mastoid air cells in the lowest slices in Figure 49 are markedly distorted in the A-P direction and the stretching and compression of signal is so severe that it results in intensity variations that are visible as dark and bright areas respectively. The distortion associated with the nasopharyngeal air spaces is particularly evident in the misshapen signal from the eyes in the non-DW SE-EPI image. The frontal sinus results in stretching of signal in some slices and compression in others.

It is clear from the Figure 49 that some areas of the brain are so severely distorted that it is impossible to obtain useful DTI data from these. In some regions the signal is stretched or shifted away, leaving behind only noise so there is insufficient signal to allow calculation of diffusion coefficients. Conversely, distortion may lead to signal from a large area being compressed into an artifactually bright region in which the measured ADC will be some combination of the actual diffusion coefficients of the different tissues in the area from which the signal originated.

Figure 50 shows that the fat suppression module appears to reduce the signal and chemical shift artifact from the subcutaneous fat around the skull. However there is still some residual fat signal visible in the fat-suppressed images, suggesting that the method

of fat suppression employed here is not sufficient. The inadequacy of the fat suppression is much more evident in the lower-SNR DW images in Figure 51. The direction of the chemical shift depends on the PE direction with 'positive' PE polarity resulting in a P→A shift of the fat signal and 'negative' PE causing an A→P shift. It seems that the positive PE polarity is less useful since the fat signal from the back of the head is shifted forward into the brain where it forms a bright curve. Future studies in this orientation should use the negative PE polarity but it would also be advisable to implement a more efficient fat suppression technique. An alternative fat suppression method which could be investigated is binomial fat suppression [87] (in which hard pulses are applied with their amplitudes in the ratio given by a binomial distribution and with phases cycled and interpulse delays such that the fat magnetisation is excited prior to gradient spoiling whilst the water magnetisation returns to the z axis).

The subtracted images in Figure 52 seem to contain mostly noise (except for a hint of a very fine bright rim in Figure 52A) demonstrating that there are no substantial visible eddy-current induced distortions from each (positive and negative) main gradient direction. This suggests that the gradient pre-emphasis was set up such that any eddy currents from the ramps of the diffusion gradients were reduced to an unobtrusive level.

There do not seem to be significant image shifts or distortions in the subtracted images in Figure 53 and Figure 54, which suggests that there are no severe eddy-current-induced distortions in the acquired DW images. The signal differences inside the brain appear to arise mainly from diffusion anisotropy. A further source of differences in the images could be patient motion but this seems to have been minimal, especially considering that the DW images were not coregistered or otherwise motion corrected prior to subtraction. There is a slight brightening in the anterior or posterior edges of some of the images in Figure 53. This may imply some slight eddy-current induced distortion or patient motion but the changes seem to be of the order of a voxel. Further evidence for some slight eddy-current induced distortions or patient motion is the thin bright rim visible around some of the FA images in Figure 57 and colour maps in Figure 58. Again this rim is of the order of a voxel or less.

There are many acquisition [88], [89] and post-processing [90], [91] methods to reduce the effects of eddy currents in DWI which could be applied in future but these were not pursued

since the distortions due to eddy currents were minimal, especially when compared with the susceptibility-induced geometric distortions.

It is important to note that Nyquist ghost correction was achieved in this study by acquiring a single non-PE reference scan (see section 2.12.3.1.1) prior to the rest of the experiment. This strategy seems to have removed most of the ghosting but has not been entirely efficient, particularly in the lower slices of the brain where the ghosting seems more obvious (Figure 55, Figure 57 and Figure 58). It is not an ideal strategy since the patient may move between acquisitions of different DW directions, so that the initial reference scan may no longer be applicable. In addition the eddy currents for different DW gradient directions may differ and cause the level of ghosting to vary with the DW direction. In future non-PE reference scans (or at least three echoes) could be collected prior to acquiring each DW direction volume (or even before each slice). For example, the group at GOSH collect 3 echoes before every slice using a low-flip-angle RF pulse followed by 3 gradient reversals [81].

The trace maps in Figure 55 were compared visually with some DTI data obtained at 1.5T [81] and shared the bright appearance of the CSF and fairly homogeneous appearance of the brain grey and white matter. There are some areas in the maps in Figure 55, particularly around the auditory air spaces, where the signal is so low that it is below the mask threshold. This is because of distortion and leads to voids in the trace, FA and colour maps in the temporal lobes of the brain. In contrast the signals from the eyes are bright and distorted into an elongated shape in the trace maps.

The trace maps were found to contain a few voxels with negative trace values. Negative components of the diffusion tensor are physically impossible but can arise from the calculations used to obtain the tensor if the signal in the non-diffusion-weighted image is less than that in the DW image. This may occur if a voxel has such a low SNR that the signal approaches the noise level and a random noise fluctuation causes it to have a lower signal value in the non-DW image than in the DW image. Many of the voxels with negative trace values appeared in the poorly suppressed fat signal and this can be explained by the very low ADC of fat (~ 1-2 x $10^{-5}$ $mm^2s^{-1}$) [92] compared with other tissues. In the absence of noise the fat signal would, therefore, be expected to be similar in both the DW and non-DW images, so a noise fluctuation could easily result in a

lower signal in the non-DW image and, therefore, an apparently negative diffusion coefficient.

Despite the obvious distortions and the few negative values in the trace maps, the ROI analysis based on manually drawn regions such as those shown in Figure 56 yielded results consistent with those found in the DWI literature. For example Chun et al [93] used a single-shot trace-weighted EPI sequence to obtain mean diffusivities (= Trace(D)/3) of $3.02 \pm 0.22 \times 10^{-3}$ $mm^2.s^{-1}$ for ventricle CSF, $0.70 \pm 0.03 \times 10^{-3}$ $mm^2.s^{-1}$ for white matter and $0.81 \pm 0.02 \times 10^{-3}$ $mm^2.s^{-1}$ for (cortical) grey matter and Pierpaoli et al found a Trace of $\sim 2.1 \times 10^{-3}$ $mm^2.s^{-1}$ within normal brain parenchyma [69]. These are in good agreement with the values obtained here.

The fractional anisotropy maps in Figure 57 do appear to highlight areas corresponding to white matter anatomy such as the corpus callosum and inferior longitudinal fasciculi. However the maps do appear relatively noisy with bright, highly anisotropic voxels appearing outside areas of white matter and the bright rim discussed previously. Some of the bright 'anisotropic' areas are artifactual, for example the bright rim in the lowest slices corresponds to the aliased, chemically shifted fat signal from the back of the head. Perhaps some of the 'noise' in these images could be reduced if several averages were acquired to boost the overall SNR of the DWIs. The effects of susceptibility-induced distortion are again manifest in these images.

The colour maps in Figure 58 show some directional patterns that match those seen in other DTI studies [94], [86]. For example there are the bright red (L-R) fibres of the corpus callosum (genu and splenium as well) and the green (A-P) fibres of the inferior longitudinal fasciculus as well as the blue (H-F) regions in upper slices corresponding to the superior corona radiata. Similar noise, distortion, ghosting and chemical shift artifacts appear in these images as in the FA maps.

In conclusion, single shot DW-SE-EPI, one of the most straightforward methods for DTI, has been implemented on the 4.7 T system as an initial attempt at a DTI experiment. The base images are severely distorted as expected and these distortions are therefore manifest in the tensor-derived maps such as the trace, FA and colour maps. Despite the lack of any form of motion or eddy current correction schemes, any image-

to-image shifts or distortions appear to be of the order of a voxel or less. Trace values correspond to those in the DWI literature and some familiar structures appear in the FA and colour maps. This basic acquisition could be refined in future by acquiring several averages, acquiring non-phase-encoded reference data for Nyquist ghost removal prior to every DW direction and by using cardiac gating. In addition, the b-value and number of directions could be optimised for the particular SNR at 4.7 T using the approach of Jones et al [68].

## 4.3 Development of a DTI Technique at High Field Strength

### 4.3.1 Requirements for a High Field DTI sequence

As demonstrated by the experiment above, at high magnetic fields the commonly used diffusion-weighted imaging technique of single shot spin-echo EPI suffers from severe susceptibility-induced geometric distortion. This means that whole-brain DTI images suffer from inaccuracies due to artifacts in some regions. As well as the base diffusion weighted images, Trace, FA and colour maps being distorted as observed here, fibre tracking in such DTI data may not be possible in distorted regions or could result in distorted or inaccurate fibre tracts [95], [96].

There are post-processing strategies for 'undistorting' or unwarping images if $B_0$ field maps are acquired [97] (see Chapter 5). However such field-map-based corrections have been shown to produce incorrect redistribution of DW image intensities, causing the wrong FA values to be assigned to some regions and other artifactual results [98]. An alternative is to collect images with both positive and negative traversal of k-space in the PE direction [99] and it has been shown that both base images and tractography results [95] are affected by the correction. This correction method does seem to produce tracts that are consistent with those found at lower field strengths (with less distortion) but the data is not conclusive since validation is difficult because of a lack of a 'gold standard'. For these reasons it is desirable to reduce the vulnerability of DTI acquisition sequences to distortion at high field.

High field strengths seem to be disadvantageous for DTI in terms of geometric distortion but DTI is a SNR-starved method so any increases in SNR, for example by going to higher field strengths, are desirable to improve the base images and thereby

any tensor estimates or derived quantities (such as the FA or trace). Furthermore, it may be possible to exploit the higher SNR potentially available at higher field strengths to increase the resolution of DTI.

Higher resolution DTI is desirable for several reasons, primarily because it reduces partial volume effects between different tissue types or fibre types. It has been demonstrated that apparent partial volume effects in white matter decrease significantly when smaller voxels are used [100]. Reduction of partial volume effects lead to more accurate estimates of FA particularly in areas where fibres cross at large angles [101] where increased resolution reduces the amount of directional averaging. In addition, partial volume effects limit fibre tracking or tractography [77] since it is dependent on accurate estimation of the orientation of the diffusion tensor within each voxel, which requires optimal SNR while retaining the highest possible spatial resolution [91]. Tournier et al [102] found that partial volume effects have a detrimental effect on fibre tracking algorithms when the background is anisotropic and when tracking narrow fibres. Similarly Conturo et al [103] conclude that the spatial resolution affects the ability to track small and complexly arranged fibre bundles. There is also evidence that DTI at high resolution, for reduction of partial volume effects, is needed to improve the correlation between diffusion parameters (volume fractions of diffusion compartments) and known cell volume fraction [104].

As well as high resolution, isotropic resolution is desirable since it allows data to be reformatted and viewed in any arbitrary orientation [91]. In addition, the use of non-isotropic voxels in DTI causes an anisotropic SNR distribution that may introduce a directional error in fibre tracking algorithms [105].

Any high field DTI sequence should ideally have not only minimal distortion and high resolution, it should also be insensitive to motion artifacts and fast enough to allow acquisition of DWI images with sufficient SNR and quality to perform DTI in a reasonable scan time. Other desirable features for any high field imaging sequence include insensitivity to $B_1$ inhomogeneity and an SAR within the recommended safe limits.

The aim in this work was therefore to develop a high resolution DTI technique applicable at 4.7 T that has reduced distortion and fulfils as far as possible the other requirements described above.

### 4.3.2 The Search for a High Resolution DTI Sequence for use at High Field Strength

There is a huge diversity of sequences that have been developed for DTI of the human brain. It is from this multiplicity that the sequences best suited for application to high field strength DTI must be selected. In order to evaluate which sequence is likely to fulfil the requirements outlined in section 4.3.1 it is necessary to understand the advantages and disadvantages of the different types of DWI sequence.

It is often possible to classify DTI sequences both by their diffusion weighting (DW) preparation and by their acquisition method. For example the single-shot SE-EPI sequence used in section 4.2 has SE diffusion preparation and EPI readout. Sometimes the diffusion preparation and read-out are not separable as in some SSFP sequences [106] in which a single diffusion-weighting gradient is inserted into the (otherwise) balanced SSFP acquisition. Another sequence which has the diffusion preparation intertwined with the acquisition is Delalande's echo-shifted EPI sequence [107].

Examples of types of DW preparation modules include spin-echo [65], stimulated echo [108], driven equilibrium (DW-DE) [109], [110] and the recently suggested hyperecho [111].

Examples of acquisition sequences that have been used for DWI and may be applicable for DTI include SSFP [106], [109], TurboFLASH [112], [110], EPI [91], line scan imaging [113], radial k-space acquisitions such as PROPELLER [114], [115], FSE methods [116], [117] and spiral imaging [118]. For EPI and FSE methods both single-shot [91] and multi-shot [119] acquisitions have been used.

It will be clear from this far-from-exhaustive list that it is difficult to pick out the best-suited sequences for this application since there are so many possible combinations of DW preparations with acquisition sequences. It is important to evaluate any candidate sequence as a whole since its SNR, scan time, resolution, distortion, and other properties will be a function of both DW preparation and readout.

We have seen the performance of single-shot DW-SE-EPI for DTI at 4.7 T (section 4.2) and it is worth noting that, despite its vulnerability to off-resonance effects and limited resolution due to $T_2$* decay, this technique is robust to motion since it is often fast enough that physiologic motion can be 'frozen out' and any phase error due to bulk motion is equal in each PE step and therefore does not affect the image quality in a magnitude reconstruction.

However it is clear that susceptibility-induced distortion is one of the major obstacles to be overcome if SE-EPI is to be applicable for DTI at high field strength. As a first step towards reducing distortion it is instructive to look closely at how it arises. As we can see from Equation 72 and Equation 73 the geometric distortion d (in the PE direction) in EPI is inversely proportional to the bandwidth per pixel in the PE direction $BW_{pixel\text{-}PE}$ :

$$d = \frac{\Delta\chi.B_0}{G} = \gamma.\Delta\chi.B_0.ES.N_{PE}.\Delta y$$

**Equation 72**

(for definitions of the terms in these equations see section 2.12.3.2)

$$BW_{pixel-PE} = \frac{1}{N_{PE}.ES}$$

**Equation 73**

$$\Delta x = \frac{FOV_{FE}}{N_{FE}} = \frac{1}{N_{FE}.\Delta k_{FE}}$$

**Equation 74**

From Equation 72 and Equation 74 we can see that achieving increased resolution and reduced distortion are mutually incompatible for conventional whole-brain single-shot SE-EPI. For example, if we wish to increase the FE resolution (corresponds to decreasing $\Delta x$ in Equation 74) by increasing the number of read sample points $N_{FE}$ (but maintaining the sampling time per point and thereby the total read bandwidth) then the echo spacing ES ($\approx N_{FE}.\Delta t$) (see Figure 3 section 2.12.2) would increase and Equation 72 shows that the geometric distortion artifacts in the PE direction would increase correspondingly.

There is an alternative way of reducing distortion, which can be understood via Equation 72. This would be to reduce the number of phase encoding steps in the phase

encode direction ($N_{PE}$). If the resolution ($\Delta y$) is to be maintained, this would cause a decrease in the $FOV_{PE}$, which would normally lead to aliasing (image wrap-around). However there is a way of decreasing $N_{PE}$ (and thereby distortion), maintaining resolution and reaching the full $FOV_{PE}$. This is by acquiring the full k-space using several acquisitions, each with its own RF excitation pulse, and is known as multi-shot or segmented EPI. The k-space is filled as illustrated in Figure 59, for example, before conventional 2D-FT reconstruction. The result is that the number of phase encode lines per 'shot' is reduced for the same k-space extent so that G in Equation 72 is increased, leading to reduced distortion while maintaining image resolution. There is no aliasing because the lines from other shots 'fill the gaps' to keep $\Delta k_{PE}$ and therefore the final $FOV_{PE}$ the same as in an equivalent single-shot acquisition.

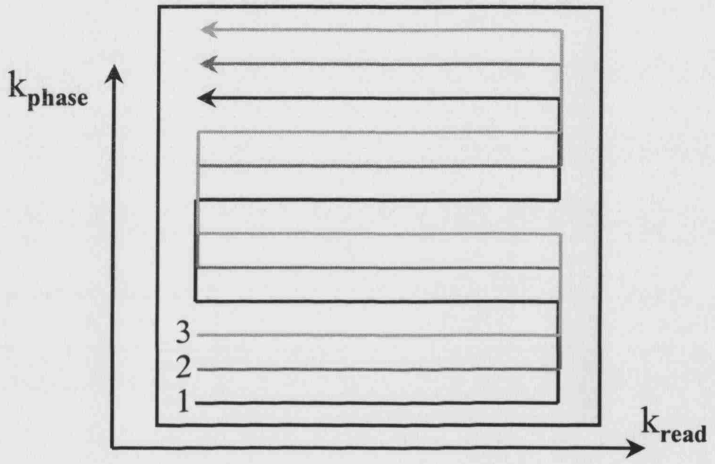


**Figure 59 A Schematic Diagram to Illustrate Multi-Shot EPI**
Here the full k-space is filled by three shots (numbered) each with its own excitation.

At first glance multi-shot EPI seems like a good solution to simultaneously improve resolution and reduce EPI distortion for DWI. However with multi-shot DWI *in vivo* there are the additional problems of both patient motion between the different shots and differing patient motion during the diffusion-sensitising gradients for each shot. The latter leads to shifts in k-space and therefore different phases for each shot so that, when the shots are combined in the final reconstruction, severe ghosting artifacts may arise due to the different offsets between adjacent lines in k-space [120]. Several methods as outlined by Norris and Bammer in their reviews [121], [122] have been described to mitigate these artifacts, of which perhaps the most widely applied is the acquisition of navigator echoes [123] to correct the phase of each shot. Navigator echoes are additional non-phase-encoded echoes acquired either before or after the imaging echoes. This approach may lengthen DWI acquisitions, particularly if 2D navigators are acquired [120] as is often

necessary for DTI. Even 2D navigators cannot correct for through-plane or non-rigid-body (pulsatile) motion and therefore work best in conjunction with cardiac gating or triggering since most of this pulsatile motion is found in the first few hundred milliseconds of the cardiac cycle [122]. Acquisition with triggering lengthens the total acquisition time and means that the available time is less efficiently utilised. Despite these disadvantages multi-shot EPI has been successfully applied to DTI [119, 124, 125, 105].

An alternative method to ensure that the information from two shots can be used to form a single image without being corrupted by motion artifacts is a reduced $FOV_{PE}$ approach using saturation pulses [126]. In this technique, instead of combining multi-shot EPI data in k-space, it is combined in image space after magnitude reconstruction. This means that the phase information is discarded so that motion-related ghosting is absent. In this method aliasing in each half-FOV image is prevented by pre-saturating alternate halves of the FOV using RF pre-pulses. The two main drawbacks of this technique are that the SNR in the half-FOV images is reduced by a factor of $\sqrt{2}$ compared to the SNR per unit time achieved by standard multi-shot EPI images with the same final FOV. In addition, achieving uniform saturation may be problematic in the case of non-uniform $B_1$ as found at 4.7 T.

This technique is one of several reduced-FOV methods. We have already seen (Equation 72) that decreasing the $FOV_{PE}$ is effective for reducing distortion while maintaining image resolution. An alternative reduced-FOV EPI technique is that of zonally-magnified oblique multislice (ZOOM) EPI [127, 128, 129]. ZOOM-EPI is a variant of single-shot SE-EPI in which the slice-selective 180° refocusing RF pulse is applied obliquely to the 90° excitation pulse in order to excite an inner volume (and thereby allow EPI $FOV_{PE}$ reduction). It has the disadvantage that multiple slices must be separated by a significant distance that depends on the angle between the slab refocused by the oblique 180° pulse and the slice excited by the 90° pulse. This may preclude acquisition of a high-resolution 3D multislice volume in a reasonable scan time. Since separate, spatially-interleaved acquisitions would be required for the contiguous slices necessary for fibre tracking in three dimensions, motion could occur between interleaves causing discontinuities between slices that could lead to errors in fibre tracking.

At this point it is important to mention the application of parallel imaging via sensitivity encoding (SENSE) [130] to DWI / DTI acquisition methods. SENSE has been combined with single-shot DW-EPI acquisitions [131], [132], [133] to reduce distortion and increase resolution by effectively reducing the $FOV_{PE}$. A recent example of the combination of SENSE with single-shot SE-EPI for DTI at 3T [131] reached a resolution of 0.8 x 0.8 x 3 mm. SNR was also improved, partly due to shorter TE enabled by a shorter echo train. Such TE-related SNR improvement may also apply to multi-shot SE-EPI sequences (See Table 9). This SENSE technique therefore shows promise for fulfilling the requirements for a high field strength, high resolution, DTI sequence. However SENSE requires specialised hardware that is not available in all MRI systems. Unfortunately the SENSE coil under development for our system [134] was not fully functional for application to DTI at the time of experimentation. Once the coil is completely optimised it would be advantageous to apply SENSE in addition to any techniques developed for high field DTI to further reduce distortion artifacts.

So far, the discussion has focused mainly on EPI-based methods. Other potentially high-resolution DTI acquisition sequences that have been proposed to overcome the distortion associated with EPI and are possible candidates for use at high field strength will be described below.

A rapid, high-SNR sequence using DW-DE preparation and multishot 3D-SSFP acquisition [109] has achieved a DTI resolution of 0.78 x 0.78 x 1.6 mm at 1.5 T. 3D-SSFP is relatively free from the susceptibility and off-resonance artifacts that plague EPI. However despite these advantages and no requirement for navigator echoes, the sequence has a number of disadvantages that may preclude its application to DTI at high field strength. Instead of navigator echoes to remove the phase error due to motion and eddy currents, the sequence relies on repeating data acquisition with the final preparation (90°) pulse 90° out of phase from the first acquisition. The two acquisitions are then combined using the square root of the sum of the squares (SRSS) of the magnitude data but this technique only works if the phase error is consistent throughout the acquisition. This means that motion-related artifacts can still occur if there are vibrations due to the DW gradients or other sources of noncyclic coherent motion. There is a contribution to the signal from non-DW magnetisation that recovers by $T_1$-relaxation during the readout echo train and causes signal intensities to deviate from

true diffusion curves for the high b values (> 700 $s.mm^{-2}$) ordinarily required for DTI. This '$T_1$ contamination' can be minimised by lengthening the repetition time between echo trains but this would increase the total time required for a 3D acquisition, making accurate DTI acquisitions prohibitively long. In fact, it may be necessary to increase the interpulse interval for such an SSFP sequence at high field strength to remain within SAR limits [135], leading to even longer total imaging times.

A single-shot sequence that is also gradient-echo-based but has been used to achieve a resolution of 2 x 1 x 6 mm at 2 T is that proposed by Nolte et al [136] (see Figure 61). Instead of the DW-DE preparation used by Jeong et al, this sequence uses SE-based DW preparation that is included in an overall STEAM signal preparation module and is followed by a single-shot TurboFLASH acquisition.

The sequence has several advantages that make it suitable for DTI at high field strengths. Like SSFP, TurboFLASH is a low flip-angle, short-TE, GE-based acquisition that is insensitive to the EPI artifacts and has a low SAR relative to fast spin-echo (FSE) techniques. Being a rapid, single-shot technique eliminates the need for any navigator echo acquisition or other motion correction technique. In fact the inclusion of TE spoiler gradients make this technique particularly robust to motion but at the cost of approximately half the available SNR since a stimulated echo is selected (see section 4.3.3 below). An advantage of the DW-SE preparation being completely decoupled from the STEAM-FLASH readout module is that the influence of gradient cross terms is minimised in the calculation of diffusion weighting b-factors. A potential disadvantage of using this technique to achieve high-resolution images is that the intrinsic resolution is limited by the flip angle due to $T_1$ signal-attenuation during the readout period. This may be less of an issue at higher field strengths since $T_1$ relaxation times tend to increase leading to an improvement of this resolution limit. $B_1$ inhomogeneity at high field strengths could lead to different flip angles across the brain and therefore different resolution limits (PSFs) in different regions of the same image.

An alternative acquisition technique that has recently been applied to high resolution DTI at high field strengths [96] is that based on the PROPELLER acquisition method. PROPELLER [114] stands for Periodically Rotated Overlapping ParalleL Lines with Enhanced Reconstruction and is a radial multi-shot FSE technique with inherent 2D

navigator information in each FSE echo train or 'blade'. Figure 60 illustrates how the k-space is filled in a PROPELLER experiment. Being an FSE technique, it provides far greater immunity against geometric distortion and other off-resonance artifacts than EPI or any of the gradient-echo-based sequences discussed so far. The radial nature of the sequence means that any residual artifacts are expressed more benignly as radial blurring rather than the PE ghosting that occurs with standard Cartesian acquisitions. Using FSE for DWI acquisition has proved to be a particular challenge since, due to motion in patients *in vivo*, the DW signal is unlikely to be exactly in phase (or antiphase) with the multiple refocusing pulses, thereby violating the Carr-Purcell Meiboom-Gill (CPMG) condition and leading to signal loss via destructive interference between the many stimulated and spin echo pathways that contribute to the signal. Several solutions have been proposed to overcome this problem although some result in significant signal loss [137], [138], [139], [140], [117]. PROPELLER relies on a special case of the solution proposed by Bastin and Le Roux [116] which is to phase cycle the refocusing pulses in a quadratic scheme such that (almost) full signal is maintained throughout the FSE echo train. PROPELLER is also advantageous because it is self-navigating meaning that a separate acquisition for each shot is not required to collect the 2D navigator information.

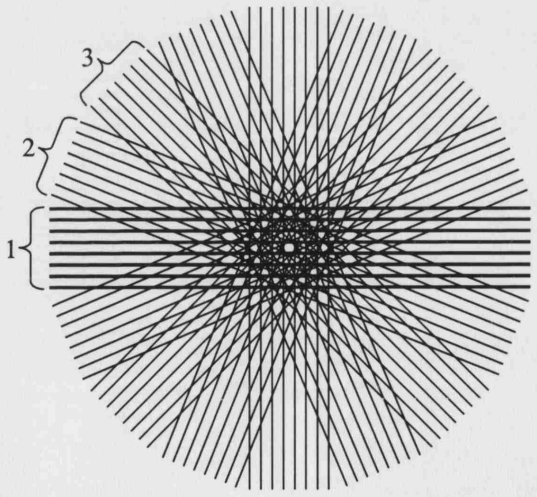


**Figure 60 PROPELLER K-space trajectory**
This is a schematic diagram to illustrate the k-space trajectory for the PROPELLER sequence [114]. The bold lines indicate the area ('blade') of k-space covered by one echo train in a FSE experiment. The trajectory within a blade is similar to that in an EPI experiment (see Figure 3 section 2.12.2). In subsequent TRs (e.g. 1, 2 and 3) the blade is rotated to measure the remaining parts of k-space while resampling the centre of k-space each time.

Despite these advantages, there are several obstacles that need to be overcome before using PROPELLER at high field strength. One of these is that the high SAR of the technique, due to the use of multiple refocusing pulses, could severely limit the speed of the acquisition [141]. The SAR has been reduced [142] by using a FSE-EPI (GRASE-type) hybrid sequence known as Turboprop [143] in which three gradient echoes are collected for each spin echo. This reduces the number of refocusing RF pulses required and thus the SAR but may also introduce some small sensitivity to susceptibility artifacts. The VERSE algorithm [47] has been used to further reduce the SAR by reshaping the refocusing pulses to decrease their peak power. With these improvements the reduced-SAR Turboprop sequence has yielded brain DTI images at 3T with a resolution of 1.25 x 1.25 x 5 mm. It is not clear whether these sequence changes mitigate the additional high-field challenge of $B_1$ inhomogeneity. Non-SAR-reduced DW-PROPELLER images at 3T [141] contained artifacts due to $B_1$ inhomogeneity because the stability of the FSE echo train is compromised for refocusing pulses less than 160° [144]. It is possible that the reduction in the number of refocusing pulses in the Turboprop sequence means that the $B_1$ inhomogeneity may not cause such severe signal instability but this needs further investigation.

It is also important to note several practical points regarding the application of the PROPELLER sequence. Not only does it require sophisticated phase cycling (tailored to the particular echo train length) and image-space phase correction using the 2D navigator information from each blade, a final correction is imposed in the reconstruction just prior to image formation. This correction is needed because (as discussed above) there are some motion-related phase errors that cannot be corrected using the navigator information. Such errors are minimised by assigning a smaller weighting to blades containing motion-corrupted data and this is known as correlation weighting.

It is therefore clear that PROPELLER requires complicated reconstruction software as well as a relatively sophisticated sequence programme especially for the SAR-reduced implementation. There is also some evidence that the PROPELLER technique is relatively time-consuming compared with single-shot SE-EPI [96] especially if the EPI acquisition time is further reduced with SENSE [145], [146] although the scan time could be reduced if PROPELLER is combined with parallel imaging [147]. Because it is time-

consuming, potentially sensitive to $B_1$-inhomogeneities and requires complicated reconstruction it was decided not to implement PROPELLER for high resolution DTI at 4.7 T.

Finally, a recently developed technique based on a multishot variable-density spiral acquisition [118] is showing promise for high-resolution DTI at high field strength. Spiral acquisitions are less sensitive to off-resonant artifacts and any residual effects are manifested as radial blurring rather than geometric distortion. Like the PROPELLER sequence this acquisition is self-navigating, meaning that no extra navigator echoes need to be acquired. This is achieved by having an increased sampling density at the centre of each k-space spiral so that the centre of k-space can be used for 2D image-based phase correction. As well as image-based phase correction, the image reconstruction needs to include re-gridding of the spiral data to a Cartesian k-space before Fourier transforming. The sequence has been applied with DW-SE preparation at 1.5T to achieve DTI with a resolution of 0.47 x 0.47 x 8 mm [118]. Despite the high in-plane resolution, the large slice thickness may preclude accurate fibre tracking. As for all multi-shot techniques, misregistration due to gross patient motion between shots / spiral interleaves still remains a potential problem. As with PROPELLER, this technique is relatively time-consuming.

After having evaluated several approaches that may be applicable to high resolution DTI at high field strength, it was decided to develop a technique with some of the best aspects of the methods outlined above to try and achieve high isotropic resolution with minimal distortion using the 4.7 T system. A single-shot technique was favoured for simplicity of acquisition and reconstruction as well as robustness to motion artifacts. It was felt that a reduced-FOV EPI technique would be a good solution to achieve high-resolution, high-SNR, rapid DW images with reduced distortion.

As we have seen, whole brain DTI has been optimised at lower field strengths, which also have less distortion, but a reduced FOV approach at 4.7 T could complement whole brain DTI data acquired at a lower field by utilising the higher field strength and higher SNR to achieve higher resolution, enabling an investigator to focus in on an area of interest. For example, one could envisage doing a whole brain study on a 1.5T scanner and then using a reduced FOV technique on the 4.7 T system to focus in on regions in

which pathology, lesions, crossing fibres or fibre tracts of interest have been previously identified. Cortical U-fibres [148], [96], the pons and fibre tracts in the vicinity of tumours [149] are examples of areas that could benefit from the reduced partial volume effect that comes with higher resolution.

In order to excite only the reduced FOV and include DW sensitisation, an appropriate sequence preparation module needed to be developed. A DW-SE module with STEAM preparation, similar to that of Nolte et al [136] described above, was chosen to select a cuboid, as described in the next section. The sequence shares many of the advantages of the Nolte sequence described above but has an EPI-based acquisition.

### 4.3.3 Development of the Volume Selective DW-STEAM-EPI Technique

In this section the development of the volume selective DW-STEAM-EPI is described from a historical perspective, starting from similar pre-existing sequences that form the components on which the new sequence is based. The advantages and disadvantages of the volume selective DW-STEAM-EPI in relation to these 'predecessor' sequences are discussed.

Stimulated echo acquisition mode (STEAM) was originally developed to select a volume of interest for localised NMR spectroscopy. The technique was first used for diffusion weighted imaging by Merboldt and Frahm et al [108]. It was later combined with the 'FLASH' or low flip-angle gradient-echo acquisition for rapid (non-diffusion-weighted) imaging [150] (and this has recently been made even faster by using a Half-Fourier approach [151]). A rapid diffusion-weighted version 'Diffusion Weighted High Speed STEAM MRI' was implemented by Merboldt et al [152], [153]. This DW High Speed STEAM MRI technique (which I will call DW-STEAM-FLASH) consists of the imaging sequence

$$90° - TE/2 - 90° - TM - [\alpha° - TE/2\ (STE)]_n$$

**Equation 75**

where 90° and $\alpha°$ are the RF pulses, TE is the echo time, TM is the mixing time, STE is the stimulated echo and the final bracket is repeated n times where n is the number of

phase encode lines. The diffusion weighting gradients are applied with one lobe during each of the TE/2 periods.

The advantages of this DW-STEAM-FLASH technique include its speed and concomitant minimisation of motion problems as well as its relative robustness to susceptibility artifacts when compared with standard whole brain SE-EPI. During the mixing time TM between the second and third RF pulses there is predominantly longitudinal rather than transverse relaxation. This STEAM diffusion preparation is advantageous over SE diffusion preparation when $T_1 >> T_2$ as in most biological tissues and especially at high field strengths because the magnetisation can be 'stored' along the z-axis for longer than in the transverse plane. The separation of the diffusion weighting gradients by the long TM can give long $\Delta$ times so that high b-values can be achieved without the need for high gradient amplitudes and restricted diffusion can more easily be measured [154].

The main disadvantage of all techniques that use STEAM preparation instead of standard spin-echo diffusion preparation is that the diffusion weighted signal here is purely a stimulated echo. This means there is a factor of two penalty in signal compared with a pure spin-echo occurring at the same time (neglecting signal weightings due to $T_1$ and $T_2$ relaxation). In addition there is a need for gradient spoilers or crusher pulses to dephase unwanted coherences and prevent them from contributing to the signal that is read out [155]. The DW-STEAM-FLASH technique described above will have even lower SNR because it uses a low flip angle ($\alpha$).

A further disadvantage of the DW-STEAM-FLASH technique includes the fact that the second diffusion weighting gradient occurs inside the phase encode loop so that $\Delta$, and therefore the b value for diffusion weighting, increase with the mixing time (TM) so that each phase-encode line has a slightly different diffusion weighting leading to image blurring and degradation of diffusion information. Two sequences that include modifications to overcome this problem are that of Nolte et al [136] and Yongbi et al [156]. Nolte et al (see Figure 61) replace the first 90° pulse in the conventional sequence by a SE diffusion preparation module and Yongbi et al use very high gradients (not normally available on a whole body MRI scanner) to put bipolar diffusion weighting gradients between the first two 90° pulses of the STEAM sequence.

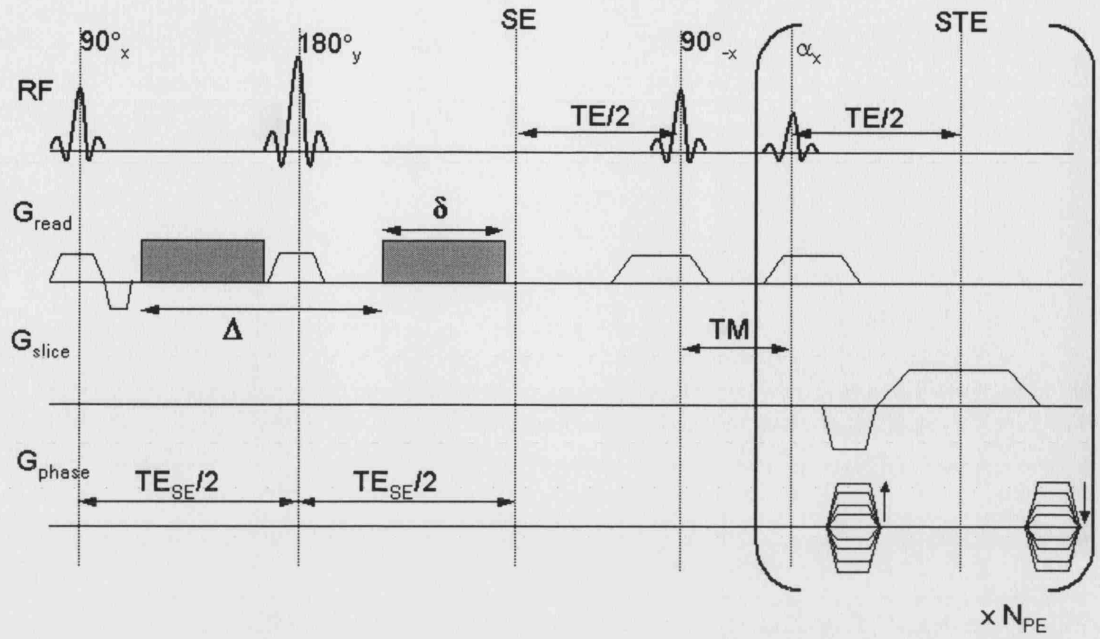


**Figure 61 Nolte et al's DW-STEAM Low Flip-Angle Gradient-Echo Sequence**
SE and STE denote where the spin-echo and stimulated echo occur respectively[136]. The bracketed part of the sequence is repeated once for every phase-encode line.

Despite the robustness of the low flip-angle gradient-echo-based techniques described so far to susceptibility artifacts, the focus here is on an EPI-based technique. This is not only because EPI has a much greater SNR than TurboFLASH (see section 4.3.4) but also in order to take advantage of the trade-off between increased resolution and reduced geometric distortion that can be made if the EPI FOV is reduced (as explained in section 4.3.2 above). This FOV reduction is achieved by using the RF pulses in the sequence's diffusion preparation module to select a cuboid. All the techniques described so far have used non-selective RF pulses during the diffusion preparation or pulses that are slice-selective along the same direction so that they all select the same slice.

The first use of STEAM preparation with EPI was demonstrated by Turner et al [157]. In that work the sequence was not used (initially) for diffusion weighting although the authors do state (as an advantage of STEAM localisation over the PRESS technique) that heavy diffusion weighting may be applied while the echo time is kept short (see Figure 62). Despite this it seems that the method has not found widespread use. In cases where it has been used [158], [159], [160] the first two 90° RF pulses during the diffusion preparation were again either non-slice-selective or selective along the same slice as the final 'imaging' 90° pulse as shown in Figure 62, and the whole sequence including the DW-SE preparation is repeated for each slice.

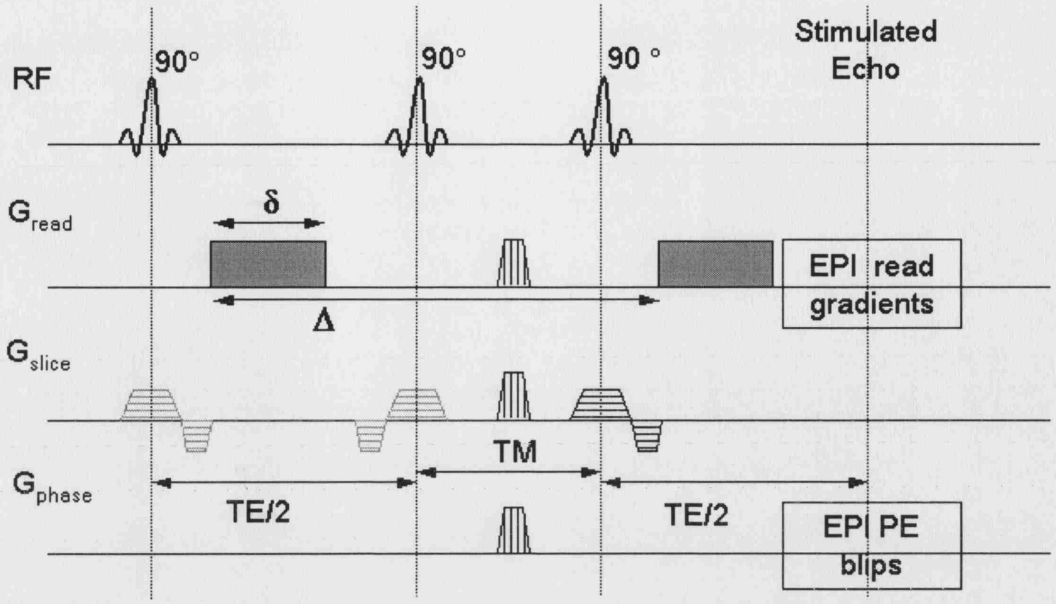


**Figure 62 The Conventional DW-STEAM-EPI Sequence**
The first two 90° pulses are either non-slice-selective or selective along the same axis as the imaging slice-selective pulse [158], [159], [160]. The whole sequence is repeated for each slice. Slice-select gradient pulses have horizontal stripes. TM crusher gradients have vertical stripes.

If this conventional DW-STEAM-EPI sequence were to be implemented in a volume selective multislice mode (see Figure 63) then it would still suffer from the same main disadvantage as the DW-STEAM-FLASH technique above i.e. the second diffusion weighting gradient occurs inside the slice loop so that Δ and therefore the b-value for diffusion weighting increase with slice number and TM.

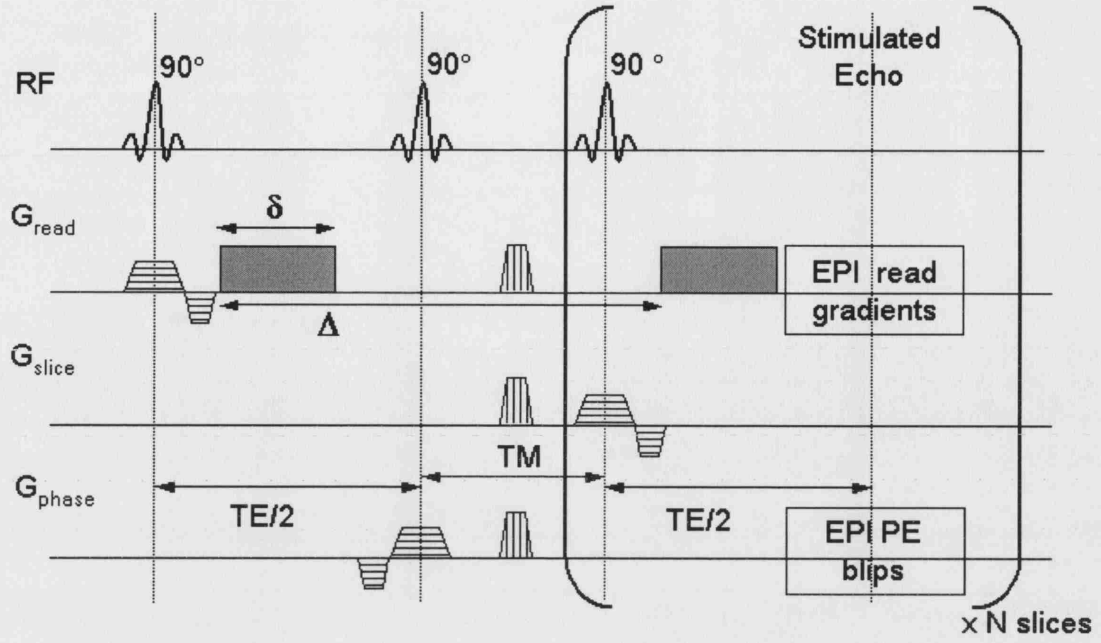


**Figure 63 A Volume-Selective Version of the Conventional DW-STEAM-EPI Sequence**

Now the first two 90° pulses select a column of spins and the final (repeated) 90° pulse selects each slice. The second diffusion-weighting gradient is inside the slice loop. Slice/slab-select gradient pulses have horizontal stripes. TM crusher gradients have vertical stripes.

In the volume selective technique proposed here (see Figure 64) (called the volume selective DW-STEAM-EPI technique from here onwards) the first 90° pulse in the conventional DW-STEAM-EPI is replaced by a SE diffusion preparation module (as in Nolte et al). This overcomes the problem of the b-value varying with slice and a further advantage of the DW-SE preparation being completely decoupled from the STEAM-FLASH readout module is that the influence of gradient cross terms is minimised in the calculation of diffusion weighting b-factors. This sequence preparation also allows a faster slice acquisition rate since the minimum STEAM TE is only limited by the EPI readout module and does not need to include the diffusion gradient duration. In addition, the preparatory RF pulses now select a column of spins to enable a reduced EPI $FOV_{PE}$, leading to reduced distortion via larger PE gradient blips. For this reduced $FOV_{PE}$ it is possible to increase $N_{PE}$ and reduce $\Delta y$ in order to progress towards both increased resolution and reduced distortion.

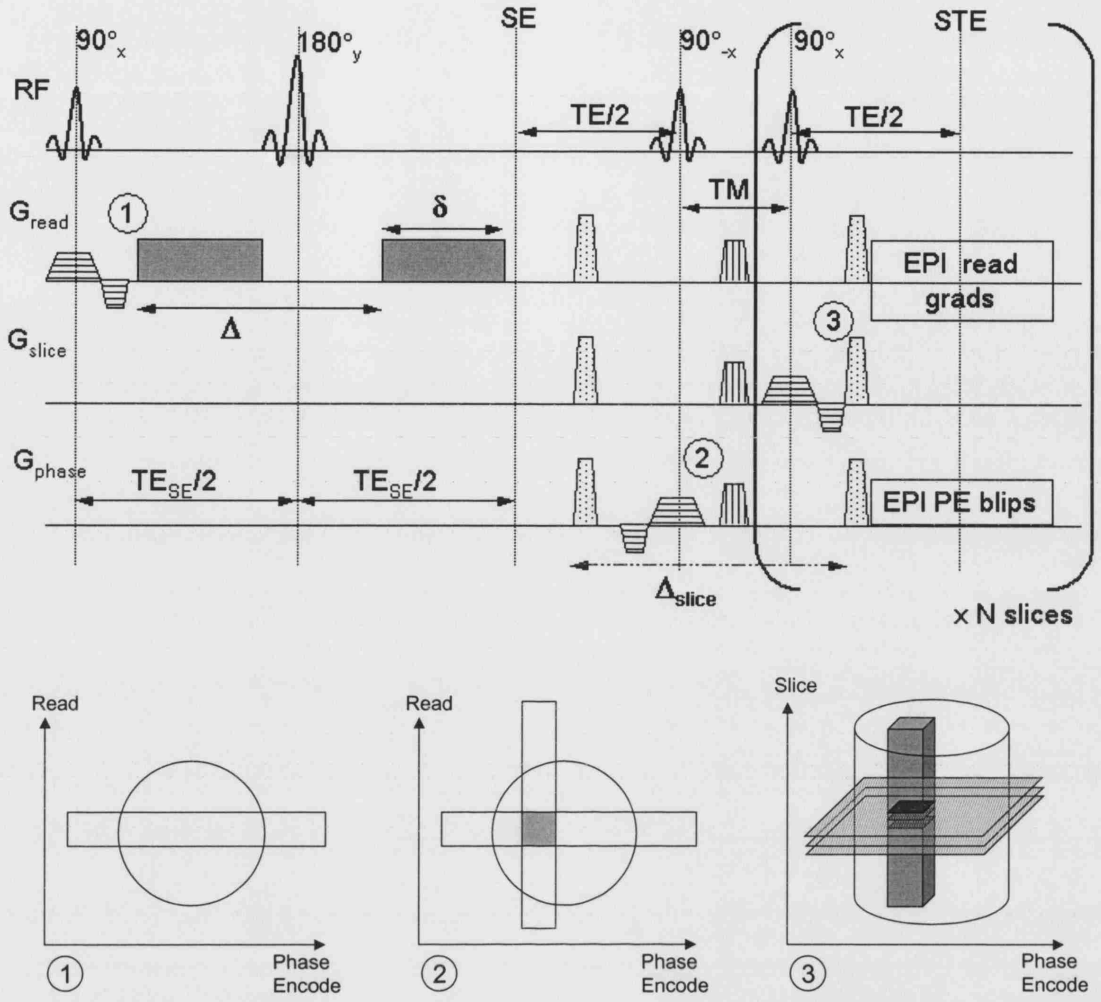


**Figure 64 The Volume-selective DW-STEAM-EPI Sequence and Cuboid Selection**
At the top is a schematic diagram of the Volume-selective DW-STEAM-EPI sequence developed in this work. Below are diagrams to illustrate the effect of the sequence on a cylindrical object at time points (1) (2) and (3). Here the first 90° pulse of the conventional DW-STEAM-EPI sequence has been replaced by a 90°-180° SE DW preparation module so that there is no longer a diffusion weighting gradient inside the slice loop. Slice/slab-selective gradient pulses have horizontal stripes. TM crusher gradients have vertical stripes. TE spoiler gradients are spotted. The first 90° pulse selects a slab in one dimension (1) (here it is the read direction). It is followed by a non-selective 180° pulse in the SE diffusion preparation module, which contains standard Stejskal-Tanner diffusion weighting gradients. After the point at which the SE forms, the TE spoiler gradients are played out on all axes to fully dephase the signal. The second 90° pulse then selects a slab orthogonal to the first (along the phase encode direction here) so that a column of spins is stored along the z-axis (2). During the mixing time TM the spins are stored along the z-axis. Then comes the final 'imaging' or slice-select 90° pulse which selects a slice (3), bringing signal from the z-axis within a cubic region into the transverse plane ready for readout. This is followed by the second set of TE spoilers identical to the first and finally by an EPI readout. The final section of the sequence from the 90° pulse onwards is repeated for each slice leaving a stack of images through a cuboidal volume of interest (3).

An additional advantage of this sequence is that the diffusion weighting gradients only have to be applied once for the whole set of slices within the selected cuboid. In this way it may be possible to acquire a whole volume faster than with other single-shot diffusion-weighted techniques since it is not necessary to apply the DW preparation before every slice. This may result in less stress on the gradient system particularly at high b-values that require large diffusion gradient amplitudes. This is investigated further in the duty cycle calculations in section 4.3.4.2.4.

The TE spoiler gradient (Figure 64), applied just before the tip-up 90° pulse and rewound prior to each acquisition, dephases the unprepared longitudinal magnetisation and therefore prevents any longitudinal magnetisation that has recovered during TM from contributing signal to the image. It also adds motion insensitivity to the sequence (at the cost of a loss in sensitivity of half the magnetization by selecting only the stimulated echo coherence pathway) because it completely dephases the DW-prepared transverse magnetisation prior to its being returned to the longitudinal axis. This makes the experiment completely independent of phase (unlike the DW-DE method of Jeong) and therefore to any movement [121]. This TE spoiling is also applied in Nolte's sequence (Figure 61) by extending the slice select gradients of the last two pulses (90° and α°) and omitting their refocusing lobes. The DW-STEAM-EPI technique should be much more robust to motion than any of the 'true' 3-D acquisition techniques as these rely on phase accuracy to allow phase encoding over two dimensions.

## 4.3.4 Quantitative Comparison of Candidate Sequences

Now that several sequences for high-resolution DTI at high field strength have been qualitatively assessed with respect to their potential ability to achieve high resolution with minimal distortion, and a new volume-selective sequence has been proposed, it is necessary to embark on a more quantitative comparison. This section aims to compare several candidate sequences in a quantitative fashion to determine whether they fulfil the requirements set out in section 4.3.1. In this way the relative advantages and disadvantages of the newly developed technique can be assessed.

### *4.3.4.1 Sequences*

The sequences to be compared with the new volume selective DW-STEAM-EPI sequence include one of its precursors, Nolte's high speed STEAM sequence [136] and a

range of DW-SE-EPI sequences. Single shot EPI was included for reference since it is still such a commonly-used technique and so that the results of any calculations could be referred back to the results of section 4.2. Multi-shot EPI was included since it also allows a trade-off between resolution and SNR in a similar way to the reduced FOV technique developed here and has shown promise for high field strength DTI [124]. Several investigators [131], [119] have used partial (half) Fourier [161] acquisitions to improve image resolution at the expense of SNR so it was decided to investigate the effect of this modification on some of the sequences.

### *4.3.4.2 Methods*

The quantities calculated for each sequence were based on the desired criteria outlined in section 4.3.1, namely the resolution, geometric distortion, SNR and minimum imaging time. The SNR was then combined with the voxel volume and minimum imaging time to give a measure of the SNR efficiency per unit volume. Described here are the assumptions in the calculation of each of these quantities for each sequence. A transverse image orientation was assumed with phase encoding along the anterior to posterior (A-P) direction and frequency encoding along the left to right (L-R) dimension. Phase encoding is conventionally done in the A-P direction in transverse images so that the symmetry of distortions matches the overall brain symmetry.

#### 4.3.4.2.1 Resolution and FOV

Since there were so many interrelated imaging factors, it was decided to fix the resolution before comparing the sequences. This is because achieving a high resolution was the ultimate aim and it would be useful to see how this constrained each of the different sequences. A resolution of 1 x 1 x 1 mm (or as close as possible within the constraints of the system) was chosen as the baseline for comparison since this is higher than has been achieved so far. Liu et al [118] claim that they produced the highest resolution reported so far for *in vivo* DTI in humans, reaching a voxel size of 0.47 x 0.47 x 8 mm at 1.5 T. A 1 x 1 x1 mm voxel would have a smaller volume and therefore less overall partial volume effect.

As stated, some sequences would be incapable of reaching this high resolution due to the system limitations such as the maximum gradient strength. For example all the EPI-based sequences could only reach a minimum read FOV of 161 mm or 129 mm for a

maximum read gradient ($G_{read}^{max}$) of 1552 Hz.mm$^{-1}$ (or 36.5 mT.m$^{-1}$). This follows from Equation 76 (see section 2.11).

$$FOV_{FE}^{min} = \frac{2\pi}{\Delta k_{FE}} = \frac{1}{\gamma G_{read}^{max} \Delta t}$$

**Equation 76**

In order to properly assess EPI, two values for $FOV_{FE}^{min}$ were used because there were two implementations of EPI: a 200 kHz version with a sample time ($\Delta t$) of 5 μs per point and a 250 kHz version with a sample time of 4 μs per point. Incidentally 4 μs per point is the shortest time per point achievable within slew rate constraints for 200-point EPI with sinusoidal maximum-strength read gradients. For a reasonable read matrix size of 200 time points, interpolated to 128 k-space data points, these minimum $FOV_{FE}^{min}$ values lead to optimum resolutions of 1.26 mm and 1.01 mm respectively. It is worth bearing in mind that for SE-EPI in the transverse orientation with read along the L-R direction, the minimum read FOV should not be smaller than the minimum L-R object extent to avoid aliasing. This means that the 129 mm FOV, and therefore the highest resolution, may only be achievable for a proportion of the population, for instance in paediatric applications. The 161 mm FOV is likely to be more achievable in practice although using a 4 μs sampling time may put more stress on the gradients as they will have to switch at a greater rate. This discussion highlights a further advantage of the volume-selective STEAM-EPI technique over the SE-EPI technique. The former allows selection of a slab in the read direction that is smaller than the minimum EPI FOV thereby avoiding aliasing even when the L-R extent of the brain is greater than 129 or 161 mm.

For blipped EPI-based sequences, rather than being limited by the maximum gradient value, the minimum phase-encode $FOV_{PE}$ is instead limited by the maximum slew rate possible because the phase encode gradient 'blips' are applied for such a short time. The gradient system we have is capable of reaching the maximum gradient strength in a ramp time of 200 μs giving a maximum achievable slew rate of 182 T.m$^{-1}$.s$^{-1}$ for a gradient along one axis. If this maximum slew rate were applied for the 50μs ramp time of the PE blip gradients, the resulting dB/dt would be well within the normal operating mode dB/dt limit (164.2 Ts$^{-1}$ for a 50 μs ramp time) [4, 7] to prevent peripheral nervous stimulation. This means that during the 50 μs ramp time of the blip gradient ($\Delta t_{blip}$), the maximum gradient that can be reached at maximum slew rate is 9.1 mT.m$^{-1}$ or 388

Hz.mm$^{-1}$. If this $G_{blip}^{max}$ value is then substituted into Equation 77, the minimum achievable $FOV_{PE}$ is 52 mm.

$$FOV_{PE}^{min} = \frac{2\pi}{\Delta k_{PE}} = \frac{1}{\gamma G_{blip}^{max} \Delta t_{blip}}$$

**Equation 77**

This limit was applicable to the reduced-FOV volume-selective STEAM-EPI technique but a $FOV_{PE}$ of 64 mm was used in the calculations (for a 1 mm PE resolution with $N_{PE}$ = 64) to avoid using the maximum slew rates. Obviously if this minimum $FOV_{PE}$ were used in practice for the (non-volume-selective) SE-EPI sequences, the images would be severely aliased. For this reason the calculations for the SE-EPI sequences were based on the minimum $FOV_{PE}$ needed to cover the maximum A-P extent of the brain. Based on experience with MDEFT structural acquisitions in this laboratory (see section 4.2), the minimum usable $FOV_{PE}$ was set at 176 mm, giving a minimum resolution of 1.375 mm for a total of 128 PE steps.

#### 4.3.4.2.2 Geometric Distortion

To calculate the relative geometric distortion likely to occur in each of the EPI-based sequences, Equation 72 was used.

In the case of multi-shot acquisitions the effective $FOV_{PE}$ for the calculation was taken to be equal to the full $FOV_{PE}$ divided by the total number of shots. This is explained in section 4.3.2 above. In the partial Fourier case, the spacing between adjacent PE lines in k-space is the same as in the full Fourier acquisition so the distortion was calculated as for a full Fourier acquisition.

It is worth reiterating that there is no benefit, in terms of geometric distortion, associated with reducing the read FOV to its minimum value for a fixed number of data points and echo spacing. This is because the bandwidth in this direction is much greater than in the PE direction and therefore distortion artifacts in the read direction are negligible.

The Nolte sequence will have no distortion in the PE direction since, unlike EPI, in the FLASH-based readout every line has signal from a new RF excitation. The relative

distortion in the read direction can be calculated from the read gradient and is negligible.

#### 4.3.4.2.3 SNR

One of the most important quantities is the SNR. This depends on both the basic imaging sequence and on the preparation module although here the diffusion weighting itself is neglected and the non-DW SNR is calculated. The SNR was therefore calculated using the following formula:

$$SNR \propto \frac{F_{sequence}.\Delta x.\Delta y.\Delta z.\sqrt{N_{av}.N_{FE}.N_{PE}}}{\sqrt{BW}}$$

**Equation 78**

where $\Delta x$, $\Delta y$ and $\Delta z$ are the voxel dimensions in each of the read, phase encode and slice thickness directions. In the calculations here the slice thickness $\Delta z$ was assumed to be 1 mm for all sequences. $F_{sequence}$ is a sequence-dependent relaxation factor that includes the effects of both the DW-preparation module and relaxation during the readout module. $N_{av}$ is the number of image averages, which was taken as 1 for these calculations. $N_{FE}$ and $N_{PE}$ are the number of points in the frequency- and phase-encode directions respectively. BW is the total acquisition bandwidth, defined as the inverse of the sampling period.

For the partial Fourier acquisitions, $N_{PE}$ was not simply half the number for the full Fourier acquisition but included a few extra lines to be collected before reaching the centre of k-space. It is usually necessary to acquire over half of k-space to correct for any asymmetry or phase errors in the data and allow the absent half of the raw k-space data to be synthesised correctly [161].

Described here are the sequence-dependent relaxation factors $F_{sequence}$ used in the SNR calculations. The SE-EPI value only depends on the $T_2$ relaxation during the SE echo time $TE_{SE}$:

$$F_{SE-EPI} = e^{-\frac{TE_{SE}}{T_2}}$$

**Equation 79**

The relaxation factor for Nolte's sequence contains a factor of ½ for the stimulated echo. There is also the $T_2$ relaxation during the SE echo time $TE_{SE}$, the $T_1$ relaxation

during the mixing time TM and the $T_2$ relaxation that occurs during both halves of the stimulated echo time TE:

$$F_{Nolte-STEAM} = \frac{1}{2} e^{-\frac{TE_{SE}}{T_2}} . e^{-\frac{TM}{T_1}} . e^{-\frac{TE}{T_2}} . \sin\alpha$$

**Equation 80**

The sinα factor arises because the sequence uses a low flip-angle α and there is no signal relaxation factor across the phase-encoding steps to be taken into account because the sequence has centric phase encoding. Since the SNR is primarily determined by the centre of k-space, which is acquired after the first α pulse, the relevant factor is simply the transverse component of the magnetisation rotated through α i.e. sinα.

The sequence factor for the first slice in the volume selective DW-STEAM-EPI sequence is identical to that for Nolte's sequence except for the sinα factor since the 90° pulse is assumed to give perfect signal excitation:

$$F_{STEAM-EPI}^{slice1} = \frac{1}{2} e^{-\frac{TE_{SE}}{T_2}} . e^{-\frac{TM}{T_1}} . e^{-\frac{TE}{T_2}}$$

**Equation 81**

where TM is the mixing time for the first slice (see Figure 64). However for subsequent slices the effect of the $T_1$ relaxation during the increasing TM needs to be added. The 'slice decay' factor also includes the effect of diffusion weighting by the TE spoiler pulses (of resultant gradient amplitude G) across the diffusion time $\Delta_{slice}$ (see Figure 64) that increases with slice number as well:

$$F_{STEAM-EPI}^{decay} = e^{-\gamma^2 \delta^2 G^2 \left(\Delta_{slice}(slice) - \frac{\delta}{3}\right) D} . e^{-\frac{\Delta TM(slice)}{T_1}}$$

**Equation 82**

where ΔTM(slice) is the TM for a particular slice minus the first slice TM. D in Equation 82 is the diffusion coefficient applicable to the tissue of interest and corresponds to the component of the diffusion tensor along the resultant direction of the TE spoiler gradients. This decay factor is equivalent to an exponential decay with a time constant:

$$\frac{1}{\tau_{decay}} = \frac{1}{T_1} + (\gamma G \delta)^2 . D$$

**Equation 83**

This means that the overall relaxation factor in the volume selective DW-STEAM-EPI sequence is slice-dependent and can be calculated for a given slice using:

$$F_{STEAM-EPI} = F^{slice1}_{STEAM-EPI} \times F^{decay}_{STEAM-EPI}$$

**Equation 84**

It should be noted that the signal in Nolte's sequence will decay with a factor similar to $F^{decay}$ for the STEAM-EPI sequence but in Nolte's sequence the decay occurs over the phase encoding steps rather than over the slices. Because Nolte's sequence uses centric phase encoding this decay factor will not affect the SNR. However it will affect the resulting images because the roughly exponential signal decay through k-space (decaying with both positive and negative $k_{PE}$ from a maximum at $k_{PE} = 0$) will lead to image blurring (see Equation 85 and discussion below) since the image point-spread function (PSF) is equivalent to the Fourier transform of the k-space signal envelope. The decay here is not expected to be as severe as in the STEAM-EPI sequence because the inter-PE-step time is much shorter than the inter-slice time in the STEAM-EPI sequence.

From Equation 80, Equation 81 and Equation 82 above it is clear that several sequence parameters as well as $T_1$ and $T_2$ must be determined in order to calculate the sequence-dependent SNR factors for each sequence. For example the $T_1$ and $T_2$ values used (1043 ms and 50 ms) were based on literature values of brain white matter $T_1$ and $T_2$ at 4 T [162]. The minimum $TE_{SE}$ time for all the sequences will obviously be restricted by the required diffusion weighting (since the b-value depends on TE via $\Delta$ and $\delta$ (see Equation 67)) and in the SE-EPI sequences by the EPI readout time as well. It was assumed for the calculations here that a b-factor of ~1,000 s.mm$^{-2}$ was to be applied. This is not necessarily the optimal value for a given number of measurements [68] but is an approximate value based on the values (1048 s.mm$^{-2}$) used by Jones et al in their optimised tensor sequence [68]. It had been found previously (see section 4.2 above) that a $\delta$ = 20 ms resulted in a b-factor of 1,000 s.mm$^{-2}$ for DW gradients at 90% of their maximum value on a single axis with maximum time efficiency (minimum $TE_{SE}$) in a SE DW preparation module for a single-shot SE-EPI sequence. Since all of the sequences used here had SE-based DW-preparation, it was assumed for simplicity that $\delta$ = 20 ms for calculating minimum $TE_{SE}$. In fact using $\delta$ = 20 ms will result in slightly different b-values for identical DW gradient strengths in the different sequences due to the different value of TE and therefore $\Delta$ for each sequence. Other standard sequence

parameters such as RF pulse, gradient refocusing pulse and gradient spoiler durations (as well as EPI half-echo-train-lengths for SE-EPI) were included in the minimum $TE_{SE}$ calculations.

For partial Fourier SE-EPI acquisitions the 'time to echo' was less than for full Fourier acquisitions since only a few lines need to be collected before reaching the centre of k-space at $TE_{SE}$.

The minimum TE for the STEAM sequences included time for the RF excitation, slice refocusing, TE spoiler and read and phase dephase pulses. For the STEAM-EPI sequence $TE_{min}$ is dominated by half the EPI readout time but in the Nolte sequence the $TE_{min}$ is much shorter since it has to include half the read gradient duration for only one k-space line.

To limit the complexity of the calculations and comparisons, the effect of $F_{decay}$ on the SNR of every slice was not included. Instead the decay factor was estimated for the $10^{th}$ slice of each of the STEAM-EPI sequences. The calculation of $F_{decay}$ assumed that the TE spoilers were applied at 90% of the maximum gradient value for 2 ms on all three axes since such spoilers had been found to work in practice. A mean diffusivity for white matter of $0.7 \times 10^{-3}$ $mm^2s^{-1}$ [163] was assumed.

The flip angle for Nolte's sequence was taken as 11°, which Nolte et al found by optimisation for a PE PSF with a FWHM of 2.5 mm even though the nominal PE resolution of their images was 2 mm. A higher flip angle would give a greater SNR but greater blurring and conversely, a lower flip angle would result in a lower image SNR but a narrower PSF. For the calculations here, Nolte's equation relating the FWHM of the PSF to the flip angle for the FLASH acquisition was used to calculate a flip angle $\alpha$ based on the interpulse time 'TR':

$$FWHM = \frac{2.FOV_{PE}}{\pi}\left(\frac{'TR'}{T_1} - \ln\cos\alpha\right)$$

**Equation 85**

Since a resolution of 1 mm was desired, the upper limit of the FWHM was set to 1.25 mm, which gave a flip angle of 4.8° for the 'TR' with the selected sequence parameters. The SNR was also calculated for a flip angle of 11° although this flip angle would give a blurring of almost 3 mm (FWHM PSF).

The EPI-based sequences will also have a finite PSF due to the $T_2$ and $T_2$'-based decay during the readout of the SE-EPI and STEAM-EPI echo signals. As stated above, the PSF can be estimated by simply Fourier transforming the signal decay envelope. Simulations assuming a $T_2$ of 60 ms and a $T_2$' of 20 ms (corresponding to $\gamma\Delta B_0 = 50$ Hz (See Equation 15 and Equation 36) and leading to a $T_2$* of 15 ms) demonstrated that the FWHM of the PSF would be no greater than 1.4 mm for the EPI-based sequences in Table 9. As described, this $T_2$* value corresponds to regions in which susceptibility artifacts are likely to be severe (see Chapter 5) so in the majority of the brain the FWHM of the PSF will be close to $\Delta y$.

Based on the parameters described, the sequence factors were calculated for each type of sequence. The overall SNR was then calculated by multiplying the base image SNR with the sequence-dependent factor as in Equation 78. It should be noted that the SNR calculated here is quoted without units and is a relative value, assuming no diffusion weighting and for comparison only. Since the voxel volumes were not exactly equal, the SNR was divided by the voxel volume to give a normalised single measure that would be directly comparable between sequences.

#### 4.3.4.2.4 Minimum Imaging Time and Gradient Duty Cycle Calculations

Initial calculations simply assumed that images could be acquired as fast as the $TE_{min}$ and other minimum sequence timings permitted (Table 9). However this is not feasible in practice since there are limitations on how quickly the gradient coils can be pulsed. This is because passing large currents repeatedly through the gradient coils, to produce the DW and imaging gradients, dissipates heat in the coils which could cause damaging temperature rises. The rate at which the gradient coils can be pulsed is increased in many modern MR systems, including the 4.7 T system used here, by passing cooled water through pipes in sufficient thermal contact with the gradient coils to transfer the heat out of the gradients. Even with such a gradient cooling system, manufacturers still

recommend limits to the gradient pulse rates. These maximum pulse rates dictate the duty cycle defined in Equations 86, 87 and 88.

| Relative current | | | Duty cycle (%) | | | Approximate Power Dissipation (kW) | | | |
|---|---|---|---|---|---|---|---|---|---|
| X | Y | Z | X | Y | Z | X | Y | Z | Total |
| 1 | 0.3 | 0.3 | 38.4 | 11.6 | 11.6 | 1.38 | 0.13 | 0.13 | 1.63 |
| 0.3 | 1 | 0.3 | 15.6 | 52.0 | 15.6 | 0.23 | 2.54 | 0.23 | 2.99 |
| 0.3 | 0.3 | 1 | 8.8 | 8.8 | 29.6 | 0.07 | 0.07 | 0.82 | 0.97 |
| 1 | 1 | 0.3 | 33.6 | 33.6 | 10.0 | 1.06 | 1.06 | 0.09 | 2.21 |
| 1 | 0.3 | 1 | 24.8 | 7.2 | 24.8 | 0.58 | 0.05 | 0.58 | 1.20 |
| 0.3 | 1 | 1 | 8.0 | 27.2 | 27.2 | 0.06 | 0.69 | 0.69 | 1.45 |
| 1 | 1 | 1 | 23.2 | 23.2 | 23.2 | 0.50 | 0.50 | 0.50 | 1.51 |

**Table 8 Manufacturer's Duty Cycle Limits**
These limits are the 'safe operating conditions' given by the manufacturer for the *Magnex SGRAD III 595/379* head gradient system inside the 4.7 T magnet. The duty cycle limits are percentages calculated using Equation 86 and assuming a peak current of 250A. The figures are based on restricting the temperature rise to <40K and allow a worst case power dissipation of 3kW. The power dissipation was calculated for a nominal resistance of 0.15 Ohms.

In order to investigate the effects of the manufacturer's duty cycle limits on the minimum sequence acquisition times it was necessary to obtain these limits. These are given in Table 8 along with an estimate of the heat dissipated in each relative current or gradient regime. The duty cycle limits are defined as percentages calculated using Equation 86 on each gradient axis:

$$Duty\ cycle\ (\%) = 100 \times \frac{RMS\ current}{Peak\ current}$$

**Equation 86**

In order to determine how fast the sequences could be repeated without violating the duty cycle limits, it was necessary to convert these limits into percentages based on gradient values for each sequence. For this conversion the basic assumption was that the gradient in a given coil is directly proportional to the current flowing through the coil.

Based on this assumption it was then possible to express Equation 86 in terms of gradients:

$$Duty\ cycle\ (\%) = 100 \times \frac{RMS\ gradient}{Peak\ gradient}$$

**Equation 87**

where the RMS gradient was defined as

$$RMS\ gradient = \sqrt{\frac{\sum_{sequence} \int_0^{\tau} G^2 dt}{T_{sequence}}}$$

**Equation 88**

where G is the magnitude of a particular gradient pulse and the integral is performed over the gradient pulse duration $\tau$ before summing all such integrals for the entire sequence. $T_{sequence}$ is the total sequence duration. Integrals were performed both for the trapezoidal gradient pulses that formed the majority in most sequences and for the sinusoidal EPI read gradients.

Using Equation 86, Equation 87 and Equation 88 the duty cycle (%) was calculated for each logical gradient axis (slice, read and phase) for each sequence. The calculation was done for two potential worst-case scenarios: with the maximal DW gradient on the read axis (which is the EPI imaging axis with the greatest gradients) and with equal DW gradients on all three axes. In the latter case the DW gradients have a magnitude such that the net DW gradient vector has an identical magnitude to the DW gradient in the first scenario.

Once the duty cycle for each axis had been calculated in this way, the maximum duty cycle limit corresponding to each particular gradient regime was selected. Since duty cycle limits were only available for seven different gradient regimes (Table 8), it was necessary to interpolate between these to find the duty cycle limits for the calculated gradient regimes. A linear interpolation between the 7 regimes in Table 8 was carried out using Matlab. The minimum total sequence time was then calculated using Equation 87 and Equation 88 for the axis with the greatest RMS gradient integral and using the maximum interpolated duty cycle limit for the sequence's relative gradient regime.

The duty cycle calculations and minimum imaging times were calculated assuming that every sequence was being used to acquire 10 slices. This number of slices was chosen since the SNR decay factor for the STEAM sequences indicated that the signal for the $10^{th}$ slice would have dropped to no less than one third of the initial SNR. If greater slice coverage were required, the STEAM sequence could be used to collect several cubes, each of 10 slices (see section 4.3.5.6). In this case the duty cycle calculations

could simply be multiplied up for blocks of 10 slices. It may then be necessary to add some extra time to allow full ($T_1$) relaxation of the region outside the first cube affected by the RF pulses of the volume selective DW-STEAM-EPI sequence before subsequent cubes are excited.

#### 4.3.4.2.5 SNR Efficiency per Unit Volume

Since both imaging time and SNR are important measures of a sequence's performance, it was decided to combine these two measures to give a measure of the SNR efficiency of each sequence, dividing by voxel volume to take into account the effect of the slightly different voxel dimensions:

$$SNR\ efficiency = \frac{SNR}{\Delta x.\Delta y.\Delta z\sqrt{T_{tot}}}$$

**Equation 89**

#### 4.3.4.2.6 Additional Sequences

With partial Fourier acquisitions it is possible to acquire the remaining sector (half) of k-space in further shots so that the whole of k-space is filled with real data before reconstruction thereby eliminating the need to synthesise raw data for the unfilled half of k-space. This is not expected to give any advantage over a single-shot technique in terms of distortion since $\Delta k_{PE}$ is the same as in the single-shot full Fourier case. However the multi-shot 'partial Fourier' acquisition will have a shorter echo time and therefore less SNR loss due to $T_2$ decay. The shorter echo time may also result in a faster total imaging time and it is therefore possible that filling the whole of k-space via a two-shot partial Fourier acquisition may be more efficient than a standard single-shot full Fourier acquisition. For this reason some two-shot 'partial Fourier' acquisitions were included in the calculations.

The main argument in favour of a single-shot technique in section 4.3.2 was that it does not require the extra acquisition time (and more complicated reconstruction) associated with using navigator echoes to overcome motion artifacts. Since the volume selective STEAM-EPI sequence is theoretically insensitive to motion, it should be possible to reduce distortion further (and possibly increase SNR efficiency) by implementing multi-shot versions of the volume selective STEAM-EPI technique. Unfortunately, a multi-shot volume selective STEAM-EPI sequence with the resolution and FOV specified

here would not be practicable. This is because the required PE blip gradient amplitudes would be at least double those for the single-shot sequence, causing the slew rates to exceed the maximum achievable by the scanner within a 50 μs blip ramp time. The blip ramp times could be increased to overcome this limitation but to avoid sampling during the blips it would then be necessary to extend the total acquisition time, resulting in a greater than expected level of distortion.

If the $FOV_{PE}$ were increased to overcome the slew rate limit and allow multi-shot acquisition, the STEAM-EPI technique would no longer remain volume selective. The distortion may still be reduced compared with a single shot technique but is no longer decreased by virtue of a reduced FOV. It may still be worth considering the merits of such a technique because the fact that a whole stack of slices only requires a single preparation (as compared with the SE-EPI sequence in which DW preparation must be applied before every slice) may make the sequence more time efficient than an equivalent SE-EPI sequence. To investigate this, two-shot and four-shot non-zoomed STEAM-EPI sequences were included in the calculations.

#### *4.3.4.3 Results*

Table 9 summarises the results of the calculations described above. As a first step it is interesting to note which sequences can achieve the minimum resolution. The next column shows the relative PE distortion and allows selection of sequences that are able to achieve a level of distortion less than that of the standard single shot SE-EPI sequence. It is then useful to compare the sequences on the basis of the relative SNR efficiency per pixel volume as this measure includes the effects of both the SNR and minimum (duty-cycle limited) imaging time. The $10^{th}$ slice decay factor is given for the STEAM-EPI sequences.

## Table 9 Summary of the Results of a Quantitative Comparison of Different Candidate DTI Sequences

| Single / Multi Shot | Partial or Full Fourier | Sequence | $N_{FE}$ final | $N_{PE}$ | $N_{PE}$ final | $BW_{total}$ (kHz) | $FOV_{FE}$ (mm) | $FOV_{PE}$ (mm) | **Read res (mm)** | **PE res (mm)** | **Relative EPI PE distortion (mm.ms)** | Relative Basic Image SNR without sequence factor ($mm^3.kHz^{-1/2}$) | Relative SNR including sequence factors ($mm^3.kHz^{-1/2}$) | Relative SNR / pixel volume ($kHz^{-1/2}$) | Fastest Possible Imaging Time for 10 slices (ms) | **$TR_{min}$ (ms) to be within duty cycle limit on worst axis - For 10 slices with max DW gradient on read axis** | **Relative SNR efficiency /pixel volume** | Estimated Decay Factor for 10th slice of STEAM-EPI sequences |
|---|---|---|---|---|---|---|---|---|---|---|---|---|---|---|---|---|---|---|
| Single Shot | Full Fourier | volume selective STEAM-EPI | 128 | 64 | 64 | 250 | 161 | 64 | **1.26** | **1.00** | **51.2** | 9.00 | 0.35 | 0.27 | 727 | **1737** | **0.658** | 0.405 |
| | | | 128 | 64 | 64 | 200 | 129 | 64 | **1.01** | **1.00** | **64.0** | 8.06 | 0.24 | 0.24 | 862 | **1871** | **0.549** | 0.336 |
| Single Shot | Full Fourier | SE-EPI | 128 | 128 | 128 | 250 | 161 | 176 | **1.26** | **1.38** | **140.8** | 17.50 | 0.79 | 0.46 | 2058 | **3766** | **0.749** | |
| | | | 128 | 128 | 128 | 200 | 129 | 176 | **1.01** | **1.38** | **176.0** | 15.68 | 0.43 | 0.31 | 2442 | **4260** | **0.472** | |
| Single Shot | Partial Fourier | volume selective STEAM-EPI | 128 | 37 | 64 | 250 | 161 | 64 | **1.26** | **1.00** | **51.2** | 6.84 | 0.81 | 0.65 | 483 | **1425** | **1.714** | 0.553 |
| | | | 128 | 37 | 64 | 200 | 129 | 64 | **1.01** | **1.00** | **64.0** | 6.13 | 0.71 | 0.71 | 558 | **1515** | **1.822** | 0.497 |
| Single Shot | Partial Fourier | SE-EPI | 128 | 74 | 128 | 250 | 161 | 176 | **1.26** | **1.38** | **140.8** | 13.31 | 3.40 | 1.97 | 1194 | **3353** | **3.397** | |
| | | | 128 | 74 | 128 | 200 | 129 | 176 | **1.01** | **1.38** | **176.0** | 11.92 | 2.81 | 2.03 | 1362 | **3194** | **3.592** | |
| Two - Shot | 'Partial Fourier' | volume selective STEAM-EPI | 128 | 37 | 64 | 250 | 161 | 64 | **1.26** | **1.00** | **51.2** | 9.00 | 1.07 | 0.85 | 966 | **2850** | **1.594** | 0.553 |
| | | | 128 | 37 | 64 | 200 | 129 | 64 | **1.01** | **1.00** | **64.0** | 8.06 | 0.94 | 0.93 | 1115 | **3030** | **1.694** | 0.497 |
| Two - Shot | 'Partial Fourier' | SE-EPI | 128 | 74 | 128 | 250 | 161 | 176 | **1.26** | **1.38** | **140.8** | 17.50 | 4.47 | 2.59 | 2388 | **6706** | **3.159** | |
| | | | 128 | 74 | 128 | 200 | 129 | 176 | **1.01** | **1.38** | **176.0** | 15.68 | 3.70 | 2.67 | 2724 | **6387** | **3.341** | |
| Two - Shot | Full Fourier | STEAM-EPI (non-zoomed) | 128 | 64 | 128 | 250 | 161 | 176 | **1.26** | **1.38** | **70.4** | 17.50 | 0.67 | 0.39 | 1455 | **3473** | **0.658** | 0.405 |
| | | | 128 | 64 | 128 | 200 | 129 | 176 | **1.01** | **1.38** | **88.0** | 15.68 | 0.47 | 0.34 | 1724 | **3742** | **0.549** | 0.336 |
| Two - Shot | Full Fourier | SE-EPI | 128 | 64 | 128 | 250 | 161 | 176 | **1.26** | **1.38** | **70.4** | 17.50 | 2.21 | 1.28 | 2580 | **6522** | **1.584** | |
| | | | 128 | 64 | 128 | 200 | 129 | 176 | **1.01** | **1.38** | **88.0** | 15.68 | 1.53 | 1.11 | 2964 | **6145** | **1.413** | |
| Four-Shot | Full Fourier | STEAM-EPI (non-zoomed) | 128 | 32 | 128 | 250 | 161 | 176 | **1.26** | **1.38** | **35.2** | 17.50 | 1.12 | 0.65 | 1834 | **5495** | **0.873** | 0.586 |
| | | | 128 | 32 | 128 | 200 | 129 | 176 | **1.01** | **1.38** | **44.0** | 15.68 | 0.88 | 0.64 | 2103 | **7015** | **0.760** | 0.534 |
| Four-Shot | Full Fourier | SE-EPI | 128 | 32 | 128 | 250 | 161 | 176 | **1.26** | **1.38** | **35.2** | 17.50 | 3.69 | 2.13 | 3624 | **11972** | **1.951** | |
| | | | 128 | 32 | 128 | 200 | 129 | 176 | **1.01** | **1.38** | **44.0** | 15.68 | 2.91 | 2.10 | 4008 | **10176** | **2.082** | |
| | | | | | | | | | | | | | Flip angle | | | 10 slices - DW grads on all axes | | |
| Single | Full | Nolte et al | 161 | 176 | 176 | 50 | 161 | 176 | **1.00** | **1.00** | N/A | 23.81 | 4.8 | 0.26 | 14831 | **54464** | **0.110** | |
| Single | Full | Nolte et al | 161 | 176 | 176 | 50 | 161 | 176 | **1.00** | **1.00** | N/A | 23.81 | 11.0 | 0.59 | 14831 | **54464** | **0.253** | |
| Single | Partial | Nolte et al | 161 | 110 | 176 | 50 | 161 | 176 | **1.00** | **1.00** | N/A | 18.82 | 4.8 | 0.20 | 9538 | **28836** | **0.120** | |

### 4.3.4.4 Discussion

It is clear from Table 9 that the only EPI-based sequences capable of reaching the highest desired 1 x 1 x 1 mm resolution are the volume selective STEAM-EPI sequences. The Nolte sequence obviously suffers no distortion but, of the EPI-based sequences, it is the four-shot sequences and the volume selective STEAM-EPI sequences that suffer least from geometric distortion. The best SNR efficiency comes from the single shot partial Fourier SE-EPI sequence whilst Nolte's sequence has the poorest SNR efficiency.

After this cursory look at the results according to the different quantities calculated, the discussion that follows will assess each of the sequences according to its relative merits.

Starting with the non-EPI Nolte sequence it is clear from the calculations that despite having no distortion, the sequence is very SNR inefficient. This is for two reasons; partly because of the very low flip angle required for a sufficiently narrow PSF and also because the experiment takes a prohibitively long time to acquire compared with all the EPI-based sequences. The duty cycle of this sequence is surprisingly high because of the large slice-select gradients that must be repeated for every PE line. Acquiring a partial Fourier version improves the SNR efficiency slightly over the full Fourier version but not to a level comparable with any of the other sequences. A whole 10-slice volume would still take of the order of 10-30 seconds to acquire during which extensive patient motion could take place. From the table and these considerations we can reject the Nolte sequence as a serious candidate for achieving high resolution DTI in a reasonable scan time because its SNR penalties are so great.

It is useful to discuss the SE-EPI sequences with reference to the standard single shot, full Fourier version. Despite having the best SNR efficiency of all the sequences, the partial Fourier SE-EPI sequences (both single and double shot) both suffer from geometric distortion as severely as the single shot full Fourier sequence. For this reason these will not be useful for achieving the reduced distortion that is required for DTI at high resolution to be applicable.

The remaining SE-EPI candidate sequences are then the two and four-shot full Fourier versions and it is important to compare these with the STEAM-EPI sequences. It should

be borne in mind that these multi-shot sequences will require the acquisition of navigator echoes for motion correction as well as cardiac gating. The extra acquisition time involved (as well as any potential motion-induced reduction in the overall SNR) has not been included in the calculations. This means that these sequences appear more SNR efficient in these calculations than they would be in practice.

It is clear that the dominant sequence factor in the SNR is the $T_2$ decay. This means that the reduction in echo time when going from two to four shots results in an improvement in the SNR per pixel and the SNR efficiency.

The single shot full Fourier volume selective STEAM-EPI sequence has a poorer SNR efficiency when compared with the multishot full Fourier SE-EPI sequences especially when the slice decay factor is included. However it has a distortion intermediate between the two and four-shot (full Fourier) SE-EPI sequences and retains the motion insensitivity associated with being a single-shot technique.

The two-shot non-zoomed STEAM-EPI technique has the same SNR efficiency as the volume selective single shot version but does not achieve the same resolution or reduction in distortion. Therefore there is little to commend this sequence over the single shot volume selective STEAM-EPI technique. However the four-shot non-zoomed version gives greater SNR efficiency and a further reduction in distortion at the expense of a slight increase in PE voxel size. As explained before, the STEAM preparation should ensure that the sequence is insensitive to motion so there should be no need for acquisition of navigator echoes. As with any multi-shot sequence, the possibility of motion between shots remains but it may be worth considering using this sequence if achieving the best possible geometric fidelity is the overriding motivation.

If the level of distortion provided by the single-shot STEAM-EPI techniques is deemed acceptable then the partial Fourier versions come into play. These have the additional advantage of having the best SNR efficiency of all the STEAM-EPI sequences (again because of the dominance over the SNR of the $T_2$ decay during the echo time) and a slower slice-to-slice decay than the full Fourier version. Acquiring the partial Fourier version of the single shot volume selective STEAM-EPI sequence improves the SNR efficiency by a factor of ~2.6-3.3. Even if the remaining half of k-space is acquired in

the same experiment (two shots), the SNR efficiency remains almost as high. This is because $N_{PE}$ is now almost doubled, increasing the SNR by a factor of nearly $\sqrt{2}$, whilst the imaging time is doubled, reducing the SNR efficiency by a factor of approximately $\sqrt{2}$. Both these partial Fourier sequences have first-slice SNR efficiencies that are similar to those of the two and four-shot full Fourier SE-EPI sequences and without motion sensitivity.

There is a potential advantage to using the two shot 'partial Fourier' volume selective STEAM-EPI technique. Since the centre of k-space can be collected in each of the two shots, one acquisition going from +ve k to –ve k and the other going in the opposite direction, there is potential to use this information to correct any remaining distortions left in the EPI dataset. The method first proposed by Chang and Fitzpatrick [164], applied to EPI by Bowtell et al [165], [166] and recently implemented for DW-SE-EPI by Andersson et al [99] could be used to 'undistort' or 'rectify' the data. Since only the central portion of k-space is acquired in both PE directions, the correction may be relatively low-resolution unless a technique such as zero filling is used for interpolation. Using data acquired simultaneously with each scan to correct the scan is particularly advantageous since any eddy-current-induced distortion from different DW gradients could potentially be removed from each scan.

From the table and discussion above it is clear that the volume selective STEAM-EPI technique shows promise as a high-resolution technique with distortion superior to two-shot SE-EPI methods. The relatively low SNR efficiency of the full Fourier single shot version can be overcome if only part of k-space is acquired in a partial Fourier version that has greater SNR efficiency than the two-shot SE-EPI sequence. Despite suffering from a SNR that decays with increasing slice number, these volume selective STEAM-EPI techniques should have the additional advantage over the multi-shot SE-EPI techniques of motion insensitivity. It is worth implementing the proposed volume selective STEAM-EPI sequence to investigate its properties further.

This quantitative comparison could eventually be extended for one or two of the sequences to compare their performance over a whole DTI experiment. If this was done, time for acquisition of navigator echoes for multi-shot SE-EPI sequences could be included. It would then be useful to perform a full optimisation of the whole experiment

using Jones' framework [68] to obtain the optimum number of measurements, the ratio of high to low b-factor measurements and the high b-factor value given the sequence TE and other parameters. To improve the accuracy of the comparison, Jones' formula for the sequence $TE_{min}$ for a given $b_{max}$ could be used to ensure that the sequences had exactly the same b-factors (rather than simply fixing $\delta$).

Even though there is no $T_2$*-related signal drop-out in SE-EPI or STEAM-EPI, $T_2$*-related signal blurring still occurs (see section 2.12.3.3). There may therefore come a point at which increasing the resolution and thereby the echo train length may be counterproductive when the intrinsic resolution limit from $T_2$* blurring is greater than the nominal sequence resolution. The quantitative comparison here could therefore be extended in future by estimating the point-spread function (PSF) for each of the sequences given $T_2^*$ values measured in different brain regions.

There are several suggestions for mitigating the SNR loss associated with the slice-to-slice signal decay in the volume selective STEAM-EPI sequence. Experiments could be done to investigate the minimum usable magnitudes for the TE spoiler gradients. Reducing these TE spoiler gradients could reduce the slice-to-slice decay (see Equation 82). In addition, several averages could be acquired with successive experiments having the slice acquisition order reversed (see section 4.3.5.3.3).

It is important to note that this exponential decay during slice acquisition should be the same for every b-value associated with the DW preparation so the diffusion weighting applicable for DTI should remain unaffected. This is investigated further in section 4.3.5.4.

## 4.3.5 First Implementation of the Volume Selective DW-STEAM-EPI Technique

It is clear from the quantitative comparison in section 4.3.4 that the volume selective DW-STEAM-EPI sequence shows promise for fulfilling the requirements in section 4.3.1. Here, preliminary experiments are carried out with the aim of showing that volume selective DW-STEAM-EPI is feasible and gives accurate diffusion coefficients in comparison with a standard SE technique. DW-SE-EPI experiments were also acquired for comparison.

The first phantom to be used was an 8.5cm diameter glass sphere filled with n-dodecane. This alkane was chosen since it has $T_1$, $T_2$ and ADC values similar to those in normal white matter [163]. The dodecane $T_1$ and $T_2$ values measured at 4.7 T (with an inversion recovery Fast SE and variable-TE SE techniques respectively) were 1162 ± 8 ms and 165 ± 10 ms respectively. These values agree well with literature values $T_1$ = 1160 ms and $T_2$ = 163 ms measured at 1.5 T and are close to white matter values reported at 4 T ($T_1$ = 1070 ms ± 110 ms and $T_2$ = 62 ± 0.65 ms [167]) although the $T_2$ of dodecane is longer than the 4 T white matter value. The dodecane diffusion coefficient quoted in the literature [163] is 0.75 x $10^{-3}$ $mm^2s^{-1}$ at 17.5°C and corresponds to the mean diffusivity of white matter value (approximately 0.70 - 0.75 $10^{-3}$ $mm^2s^{-1}$).

Some later measurements were made on an 11 cm diameter spherical $MnCl_2$-doped water phantom with $T_1$ = 1100 ms ± 67 ms and $T_2$ = 86.7 ± 0.2 ms measured at 4.7 T using inversion-recovery FSE and variable-TE SE sequences respectively.

### *4.3.5.1 Slab-Selectivity of RF Pulses*

#### 4.3.5.1.1 Methods

For the volume-selective DW-STEAM-EPI sequence there are several possibilities regarding the slab-selectivity of the RF pulses. It would be possible to make all of the first three pulses slab-selective to fully select the cuboid prior to imaging a set of slices. The effect of selecting a slab in the imaging slice direction was investigated using a 15cm diameter sphere containing silicone oil which has a negligible diffusion coefficient [84]. The volume selective DW-STEAM-EPI sequence was applied with the first 90° pulse selective along the slice direction (slab thickness =100 mm), the 180° pulse selective along the read direction (slab thickness = 42 mm) and the second 90°

pulse selective along the PE direction (slab thickness = 30 mm). All the RF pulses were 5-lobed Sinc-shaped and 30 transverse image slices were acquired with slice thickness = 2 mm and slice centre-to-centre separation = 4 mm. The mean signal in a rectangular ROI was measured in each of the slices.

#### 4.3.5.1.2 Results

The effect of the Sinc RF pulse slab profile on the mean signal measured in slices selected along the same axis as the slab is shown in Figure 65.

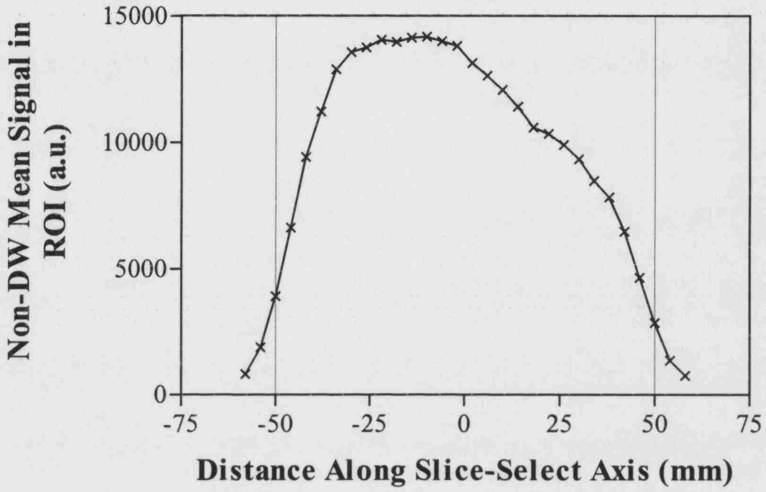


**Figure 65 The Effect of RF Pulse Slab-Selectivity on the Volume Selective STEAM-EPI Signal**
The graph shows the effect of RF pulse slab profile on the mean signal measured in slices selected along the same axis as the slab. The nominal thickness of the slab (dotted lines) was 100 mm.

The ideal slab profile would be expected to have a shape similar to the Sinc-SE profile in Figure 23.

#### 4.3.5.1.3 Discussion

From Figure 65 we can see that the mean signal within each slice is affected by the overall slab profile. This profile does seem to have a width similar to the nominal 100 mm width but is asymmetric (compared with the expected profile shape see Figure 23) due to the additional exponential slice-to-slice decay occurring in this sequence. To prevent the overall slab profile from affecting the signal in each imaging slice it was decided not to select a slab along the imaging slice axis and to leave one of the first three RF pulses non-selective in subsequent experiments. The effect of this can be

observed in Figure 69 and Figure 71 in each of which we see a pure exponential signal decay along the slice-select axis uncontaminated by any slab profile effects.

The non-slice-selective pulse can in theory be any of the first three in the sequence. We chose to make the 180° pulse non-selective (see Figure 64 and Figure 68) since the slice profile for this pulse will be poorer than for the 90° pulses. This is because the non-linearities in slice-selection become more significant at greater flip angles. Removing the 180° slice-select gradient also simplifies calculation of the b-factors in the DTI experiment by eliminating any cross-terms between the 180° slice select gradient and the DW gradients. In fact, some experiments were carried out with slab-selectivity in the phase encode direction only. This was because, as explained in section 4.3.4.2.2, there is no advantage to having a selective pulse in the read direction if the object is smaller than the minimum read FOV (which was the case for the phantoms used here).

### *4.3.5.2 Images*

#### 4.3.5.2.1 Methods and Results

Several acquisitions were carried out with the volume-selective DW-STEAM-EPI sequence using both phantoms and with a range of parameters. Some example images and profiles are shown in Figure 66 to illustrate cube selection inside the dodecane-filled sphere.

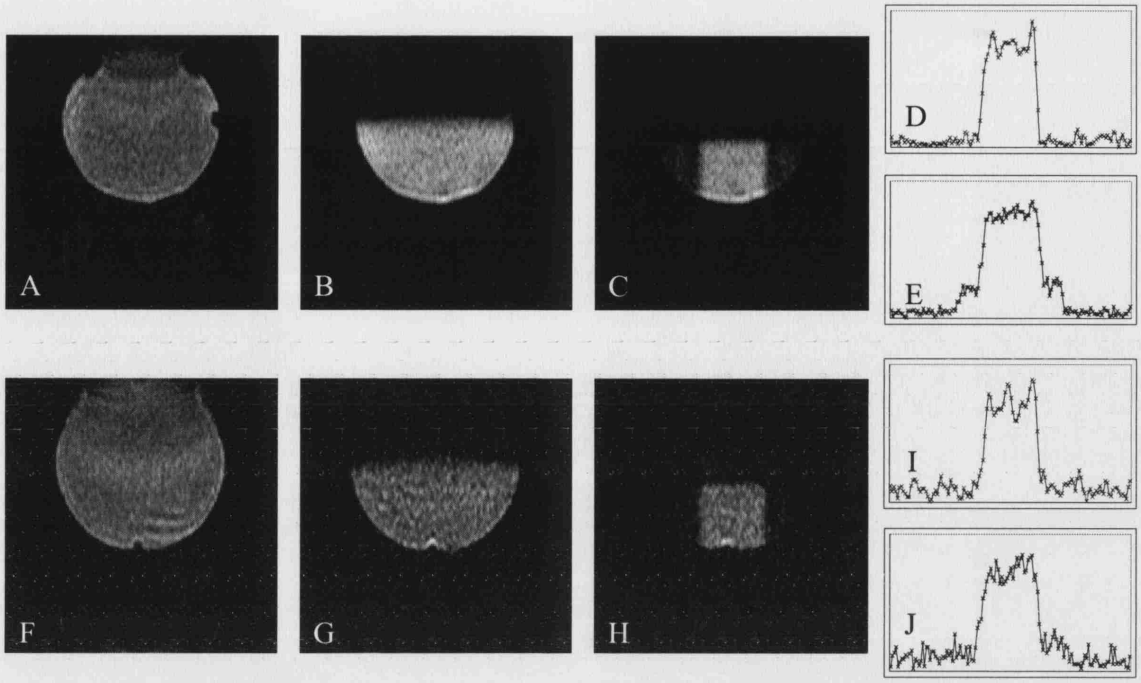


**Figure 66 STEAM EPI Images Illustrating Cuboid Selection**
The images are of the dodecane-filled spherical phantom. Images **A**, **B** and **C** are of the first slice and images **F** and **G** and **H** are of the 7$^{th}$ slice. Images **A** and **F** are the unprepared GE-EPI equivalents of the STEAM EPI images. Images **B** and **G** are non-diffusion-weighted STEAM-EPI images in which a 50 mm selective RF pulse has been applied in the vertical PE direction. Images **C** and **H** are non-diffusion-weighted volume selective STEAM-EPI images in which a 30 x 30 mm cube has been selected in both the PE and read directions. Each image intensity is scaled separately – in reality the prepared images **B**, **C**, **G** and **H** have much lower signal than the unprepared images. Profiles **D** and **E** are respectively vertical (PE) and horizontal (read) profiles through the centre of the cube in **C**. Profiles **I** and **J** are respectively vertical (PE) and horizontal (read) profiles through the centre of the cube in **H**. It should be noted that only the left-hand edges of profiles **D** and **I** reflect the selectivity of the RF pulse since the right-hand edges correspond to the edge of the spherical phantom. The images here were acquired with FOV = 129 x 129 mm FOV, matrix = 128 x 64 (read x PE) slice thickness = 1 mm, $TE_{SE}$ = 60 ms, TE = 85 ms, TM = 10 ms, TR = 3000 ms and spectral width = 200 kHz.

Figure 67 illustrates the effect, on dodecane images, of reducing the FOV, increasing the resolution to 1 x 1 x 1 mm and of increasing the number of averages.

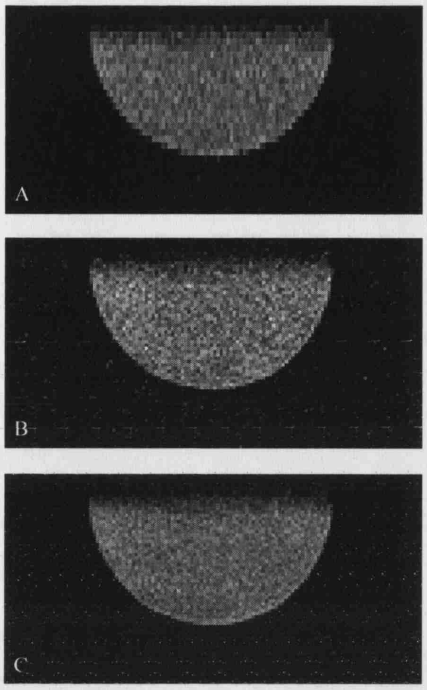


**Figure 67 High Resolution Reduced FOV Volume Selective STEAM-EPI Images**
These images of the dodecane-filled sphere were acquired with the same parameters as in Figure 66 but with a reduced FOV in the PE direction FOV = 129 x 64 mm (read x PE). Image **A** was acquired with 16 averages and matrix size = 128 x 32 (read x PE) resulting in a resolution of 1 x 2 x 1 mm. Images **B** and **C** were acquired with matrix size = 128 x 64 (read x PE) resulting in a resolution of 1 x 1 x 1 mm. **B** had 16 averages whilst **C** had 36 averages. The images are all shown on the same intensity scale.

#### 4.3.5.2.2 Discussion

The images in Figure 66 demonstrate that the volume selective DW-STEAM-EPI sequence successfully selects a cuboidal region. In the images in Figure 66C and Figure 66H as well as the corresponding profiles in Figure 66E and Figure 66J it is clear that some residual signal is left in the regions outside the selected slab in the read direction. This may be because of a relatively poor slice profile in this dimension although the profiles should be the same in both read and phase directions since the same RF pulse was used. The residual signal in the read direction may have been excited by the first read-selective 90° pulse, relaxed via longitudinal relaxation, been excited by the imaging 90° pulse and then failed to be completely spoiled by the final TE spoiler (or arrived via another coherence pathway).

The poor slice profile may have arisen because the RF pulse shape used was an unfiltered 5-lobe Sinc pulse and truncation of such a shape may result in side-lobes of the slice profile. The slice profiles could be improved by multiplying the Sinc function by a Gaussian or other smoothly decaying filter function. The profile edges could be

made sharper in this way or by designing the RF pulse shapes using Shinnar – Le Roux (SLR) methods [168]. The lower signal-to-noise in the images in Figure 66G and Figure 66H when compared with the images in Figure 66B and Figure 66C reflects the fact that the signal had decayed by the time the 7th slice was collected. By comparing the higher resolution image in Figure 67B with the lower resolution image in Figure 67A, it is clear that the noise speckle has a random pattern that is coarser when the voxels are larger. Increasing the number of averages decreases the noise and thereby improves the appearance of the image as can be seen when comparing image Figure 67C to Figure 67B.

Figure 67 also demonstrates that the volume selective DW-STEAM-EPI technique allows the PE FOV to be reduced without aliasing to yield images with the target 1 x 1 x 1 mm resolution. It would be useful to assess the distortion in such reduced field of view images to verify that it is reduced in comparison with SE-EPI images of similar resolution. This could be done using the phantom developed in Chapter 5 and eventually *in vivo*.

### *4.3.5.3 ADC values*

#### 4.3.5.3.1 Methods

The main aim of the acquisitions was to verify that the sequence was capable of producing DW images from which accurate ADC values could be calculated. With the dodecane phantom, a first experiment included the use of a standard Stejskal-Tanner diffusion-weighted spin-echo sequence to acquire single-slice diffusion-weighted images in order to compare the diffusion coefficients obtained with this simple 'gold-standard' sequence with the results from the volume selective DW-STEAM-EPI sequence. The standard DW-SE images were acquired at 10 b-values from 0 to 1102 $s.mm^{-2}$. Sequence parameters were: TR / TE = 1000 / 65 ms, $\delta$ = 20 ms, $\Delta$ = 37 ms, FOV = 128 x 128 mm, matrix size = 64 x 64, slice thickness = 2 mm and spectral width = 25 kHz. The experiment was repeated with the diffusion gradients in each of the X, Y and Z directions.

A similar DW-SE verification experiment was done with the water phantom but with 6 b-values from 0 to 410 $s.mm^{-2}$ (due to the higher diffusion coefficient of water with respect to dodecane) TE = 54 ms, $\delta$ = 13.7 ms, $\Delta$ = 32.9 ms.

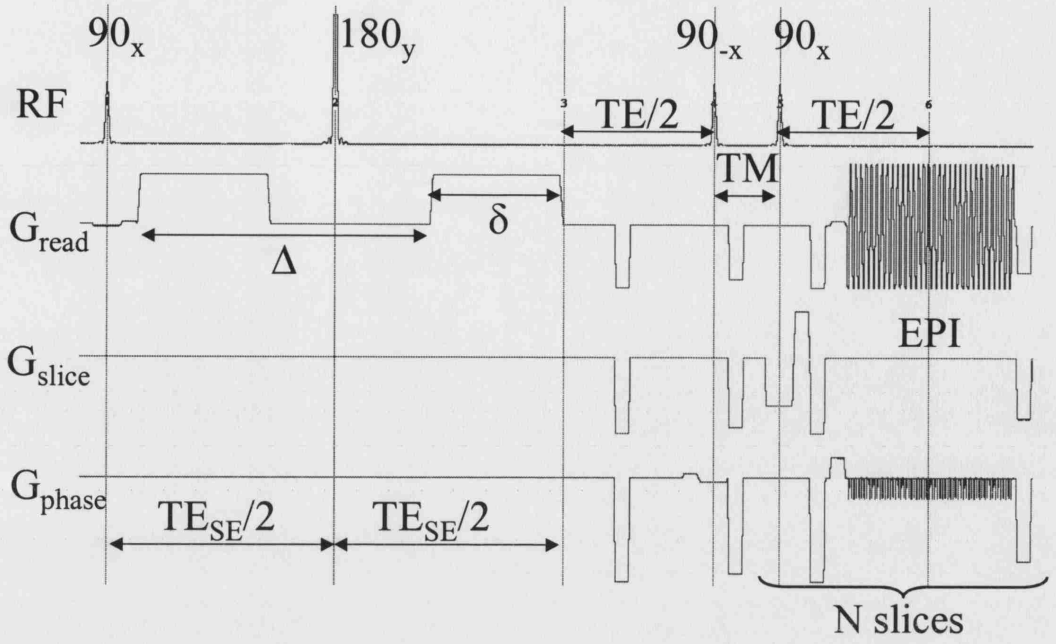


**Figure 68 RF and Gradient Outputs for the Volume Selective DW-STEAM-EPI Sequence**

This is a plot of the volume-selective DW-STEAM-EPI sequence measured using a data logger at the output of the gradient and RF amplifiers with accurate timescale and gradient values to scale on each axis. The parameters were those used to obtain the results shown in Figure 69 and Table 10.

For all experiments the temperature in the scanner room was measured with a mercury thermometer. A non-phase-encoded, non-diffusion-weighted, phase reference scan was acquired at the beginning of each volume selective DW-STEAM-EPI acquisition to allow phase correction to reduce Nyquist ghost intensity as explained in section 2.12.3.1.1. In all cases, the apparent diffusion coefficient (ADC) was calculated from a linear fit of the logarithm of the mean MR signal inside the rectangular ROI against b. In a heterogeneous sample, voxel-by-voxel fits would normally be carried out to calculate ADCs and eventually to estimate the diffusion tensor in each voxel. Since these phantoms were homogenous and isotropic, fits of ROI mean signals were carried out, with the ROI covering most of the selected cube. The b-values were calculated using the expression in Equation 67 with $\delta$ defined as the time between the initial rise of the trapezoidal diffusion weighting gradient pulse and the end of its plateau [66].

In some experiments, some standard DW-SE-EPI images were acquired to allow comparison of ADC values with the DW-STEAM-EPI images.

#### 4.3.5.3.2 Results

The ADC values from a multislice volume selective DW-STEAM-EPI experiment are plotted with the non-diffusion-weighted signal in the corresponding slices in Figure 69. Also shown for comparison is the single slice ADC from a single slice SE experiment with the diffusion weighting gradients in the same (Z) direction.

The experimental parameters for the volume selective DW-STEAM-EPI experiments whose results are shown in Figure 69 and Table 10 were $TE_{SE}$ = 70 ms, TE = 46 ms, TM = 10 ms, TR = 3000 ms, $\Delta$ = 44.88 ms, $\delta$ = 20 ms, spectral width = 250 kHz, FOV = 162 x 128 mm (read x phase) and matrix size = 64 x 64. Twelve slices could be prepared and acquired in 594 ms. The DW-STEAM-EPI images were acquired at 11 b-values from 0 to 1177 $s.mm^{-2}$ and only one experiment per b-value. Single-slice diffusion-weighted images of a 40 x 40 x 2 mm cuboid were acquired with diffusion gradients in the X and Y directions in separate experiments (Table 10). Multislice diffusion-weighted images (12 slices, 2mm slice thickness, 4 mm slice centre-centre separation, 40 x 40 x 46 mm cuboid) were acquired with diffusion weighting gradients in the Z direction (Figure 69). For the ADC values shown in Figure 69 and Table 10 the $r^2$ values for the ADC linear fits were greater than 0.95. The temperature in the scanner room was 17.5 ± 1 °C so that the ADC of dodecane should have been approximately equal to 0.748 x $10^{-3}$ $mm^2s^{-1}$ (linear interpolation from values in [163]).

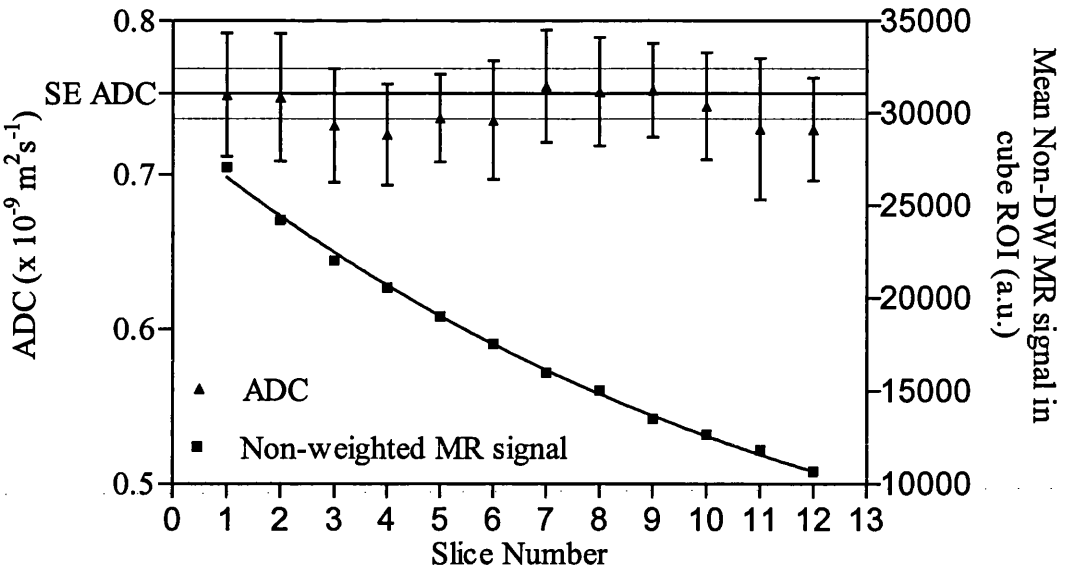


**Figure 69 Dodecane ADC Values and Non-Weighted Signal Variation with Slice Number for the Volume Selective DW-STEAM-EPI Technique**
ADC values (left-hand scale) measured with the multislice DW-STEAM-EPI technique (± SD) are compared to the ADC measured with the SE sequence (with 95% confidence interval – dotted lines) with the diffusion gradients in the same (Z) direction. The non-diffusion-weighted MR signal values (right-hand scale) for each DW-STEAM-EPI slice are also included, with an exponential curve fit. Since only one experiment was acquired per b-value, the error bars on the ADC values come from the standard errors on the linear fit coefficients.

Single slice ADC values with X and Y DW gradients are shown in Table 10.

| | ADC (x $10^{-3}$ $mm^2s^{-1}$) | |
|---|---|---|
| Sequence | DW Y Gradient | DW X Gradient |
| Standard DW-SE | 0.821 ± 0.014 | 0.781 ± 0.009 |
| DW-STEAM-EPI | 0.775 ± 0.012* | 0.754 ± 0.012 |

*** 16 averages**

**Table 10 Dodecane ADCs from the Volume Selective DW-STEAM-EPI Technique and a DW-SE Sequence**
Single Slice ADCs measured in regions of interest within the dodecane sphere acquired with both a standard DW-SE sequence and the volume selective DW-STEAM-EPI sequence. Since only one experiment was acquired per b-value, the ADCs are given ± the standard errors on the linear fit coefficients.

A comparison between multislice ADC values obtained using the DW-SE-EPI sequence and the volume selective DW-STEAM-EPI sequence with DW gradients applied simultaneously along all axes is shown in Figure 70. This experiment was carried out in the dodecane phantom and used the following parameters: volume selective DW-STEAM-EPI with $TE_{SE}$ = 62 ms, TE = 83 ms, TM = 10 ms, TR = 3000 ms, $\Delta$ = 34.88 ms, $\delta$ = 22 ms, spectral width = 200 kHz, FOV = 129 x 64 mm (read x phase), matrix size = 128 x 64, 36 averages and a 50 mm cube selected in the PE direction only and

DW-SE-EPI with TE = 170 ms, TR = 3000 ms, $\Delta$ = 85.5 ms, $\delta$ = 12.8 ms, spectral width = 200 kHz, FOV = 129 x 129 mm (read x phase), matrix size = 128 x 128 and 16 averages. Both sequences were used to collect 10 transverse slices with PE vertical, slice thickness = 1 mm and centre-to-centre separation = 2 mm. Both sequences were used to acquire images at almost the same 5 b-values from 0 to 1025 $s.mm^{-2}$ with equal gradients applied simultaneously on all axes. The $r^2$ values for the linear fits for the ADC values in Figure 70 were all greater than 0.98. The temperature in the scanner room was 18 ± 1 °C so that the ADC of dodecane should have been approximately equal to 0.756 x $10^{-3}$ $mm^2s^{-1}$ (linear interpolation from values in [163]).

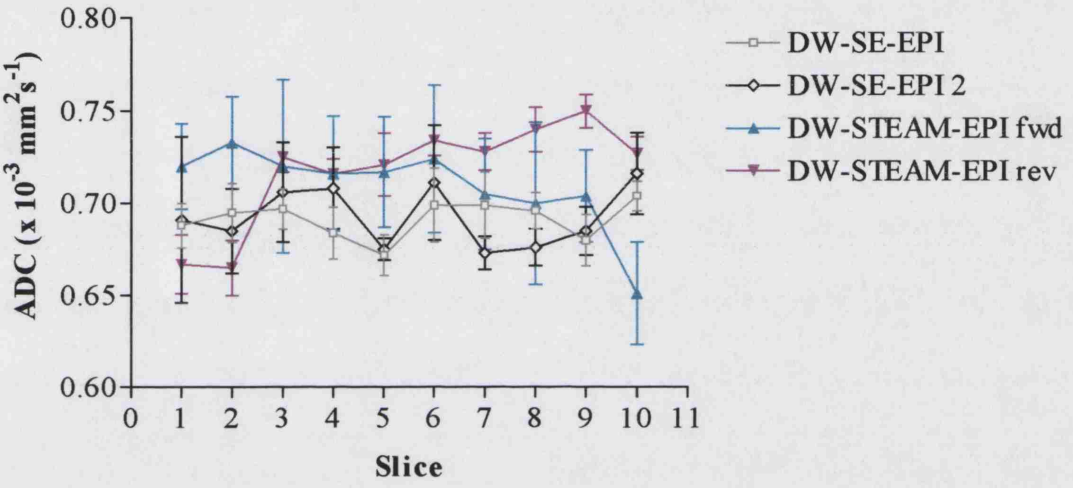


**Figure 70 Multislice Dodecane ADC Values for the Volume Selective DW-STEAM-EPI Technique and the DW-SE-EPI sequence**
DW-SE-EPI results are shown for two acquisitions of which the second was an identical repeat of the first but acquired after the phantom had been left in the scanner over night and had cooled. One DW-STEAM-EPI acquisition was made with the slices in the standard 'forward' order and another with slices acquired in the reverse order. Since only one experiment was acquired per b-value the error bars on the ADC values come from the standard errors on the linear fit coefficients. The mean ADC values across the slices for the four acquisitions shown here were 0.692 ± 0.010, 0.693 ± 0.016 x $10^{-3}$ $mm^2s^{-1}$ for DW-SE-EPI acquisitions 1 and 2 respectively and 0.709 ± 0.023 and 0.717 ± 0.029 x $10^{-3}$ $mm^2s^{-1}$ for forward and reverse DW-STEAM-EPI acquisitions respectively.

Results from similar experiments in the water phantom are shown in Figure 71 and Table 11. The experimental parameters were DW-STEAM-EPI with $TE_{SE}$ = 48 ms, TE = 35 ms, TM = 70 ms, TR = 6000 ms, $\Delta$ = 28.0 ms, $\delta$ = 15 ms, spectral width = 200 kHz, FOV = 129 x 64 mm (read x phase), matrix size = 64 x 32, 1 average, 10 repeats and a 50 mm cube selected in the PE direction only and DW-SE-EPI with TE = 71 ms, TR = 6000 ms, $\Delta$ = 34ms, $\delta$ = 13.25 ms, spectral width = 200 kHz, FOV = 129 x 129 mm (read x phase), matrix size = 64 x 64, 1 average and between 1 and 6 repeats. Both

sequences were used to collect 10 transverse slices with PE vertical, slice thickness = 2 mm and centre-to-centre separation = 3 mm. Both sequences were used to acquire images at almost the same 7 b-values from 0 to 400 $s.mm^{-2}$ with gradients applied on each axis in separate experiments. The $r^2$ values for the linear fits for the ADC values in Figure 71 were all greater than 0.98 and mostly very close to 1. The temperature in the scanner room was 17 ± 1 °C so that the ADC of water should have been approximately equal to $1.863 \times 10^{-3}$ $mm^2s^{-1}$ (linear interpolation from values in [163]).

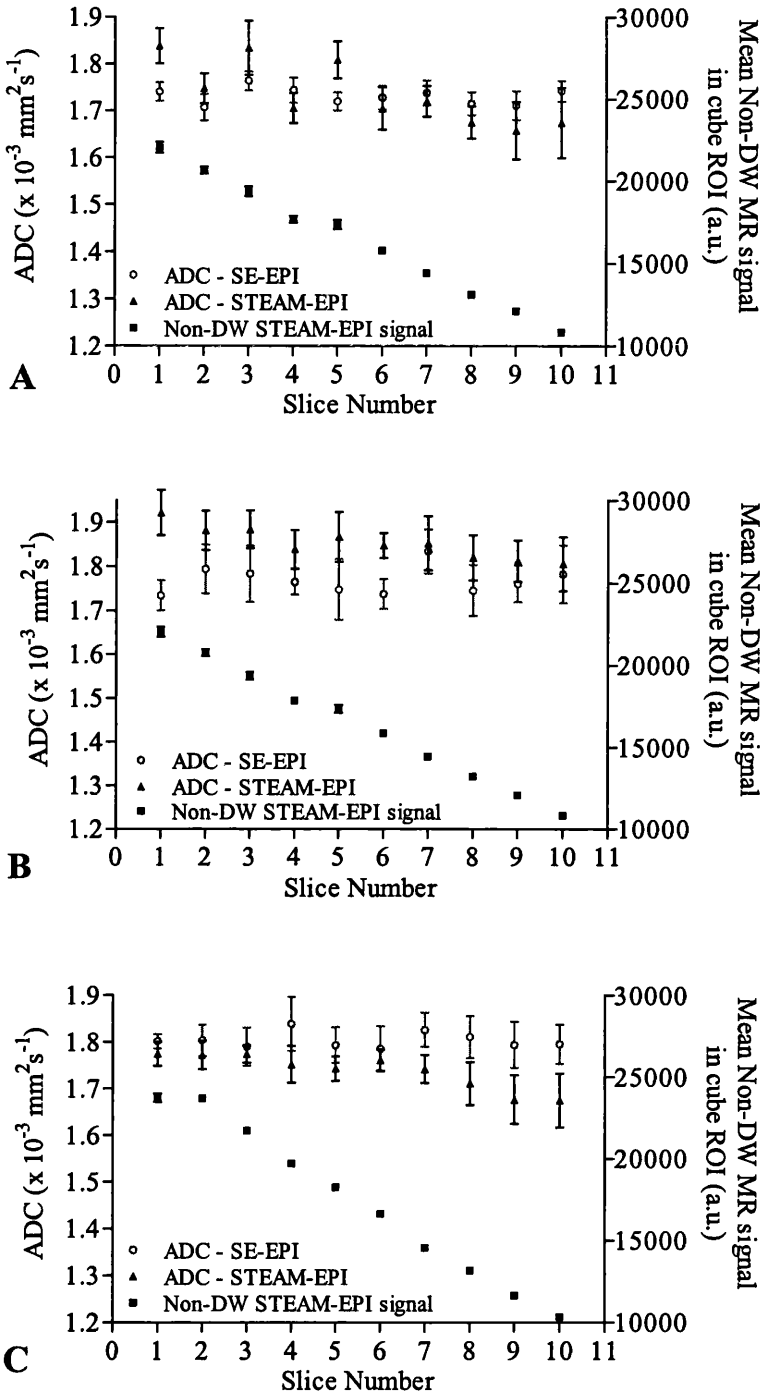


**Figure 71 Water ADC Values and Non-DW Signal using the Volume Selective DW-STEAM-EPI and DW-SE-EPI Sequences**

ADC values (± SD) measured with the multislice DW-STEAM-EPI and SE-EPI sequences are plotted (left-hand scale) on the same axes as the non-diffusion-weighted STEAM-EPI MR signal values (± SD) (right-hand scale). The DW gradients were along the X direction in **A** the Y direction in **B** and the Z direction in **C**. The error bars on the DW-STEAM-EPI ADC values and non-DW signal are the standard deviation of the results from each of the 10 repeats. The error bars on the DW-SE-EPI ADC values are the standard deviation of the results from 5 and 6 repeats for **A** and **C** respectively. In **B** the DW-SE-EPI ADC error bars are the standard error on the ADC linear fit for the single repeat acquired with the gradients in the Y direction.

The mean values across all slices from the above experiments are compared with those from a single slice 2DFT DW-SE experiment in the same phantom in Table 11.

| | ADC (x $10^{-3}$ $mm^2s^{-1}$) ± SD(ADC) | | |
|---|---|---|---|
| Sequence | DW X Gradient | DW Y Gradient | DW Z Gradient |
| Standard DW-SE | 1.786 ± 0.010 | 2.047 ± 0.041 | 1.877 ± 0.017 |
| DW-STEAM-EPI | 1.737 ± 0.068 | 1.853 ± 0.036 | 1.738 ± 0.038 |
| DW-SE-EPI | 1.731 ± 0.012 | 1.769 ± 0.031 | 1.804 ± 0.015 |

**Table 11 Water ADCs Measured Using Different Sequences**
The DW-STEAM-EPI and DW-SE-EPI values are means across all the slices of those shown in Figure 71. The DW-SE values are from single slice measurements. The errors on the DW-SE values are the standard errors on the linear fits since only one repeat was acquired.

#### 4.3.5.3.3 Discussion

Figure 69 and Table 10 demonstrate that the ADC values measured with the multislice and single-slice volume selective DW-STEAM-EPI sequence agree with those measured using the standard SE sequence as well as with the literature value for dodecane [163]. Similarly Figure 71 and Table 11 demonstrate that the ADC values measured with the multislice volume selective DW-STEAM-EPI sequence agree broadly with the literature value [163] for water in this temperature range. Evident in Figure 69, Figure 70, Figure 71, Table 10 and Table 11 are some small discrepancies between the ADC values measured using the standard DW-SE, the DW-SE-EPI and the DW-STEAM-EPI techniques, which could simply be attributed to temperature fluctuations in the scanner. Even assuming temperature changes, the water ADC obtained from the standard DW-SE sequence with the DW gradients in the Y direction seems particularly high compared with coefficients along the X and Z axes and the corresponding Y-axis values from both the DW-STEAM-EPI and DW-SE-EPI techniques (Table 10 and Table 11). This could have been because the DW-SE sequence used had the 90° pulse's slice-refocusing gradient lobe as an extension of the 180° pulse's slice-select gradient. This means that there would have been a relatively long gradient in between the DW gradient pulses on the slice-select (Y) axis, which would be expected to contribute to the diffusion weighting and increase the effective b-factor on this axis. Since this 'cross-term' was not taken into account in the calculation of the b-factor for the DW-SE sequence, the ADC measured with the DW-SE technique with the DW gradients in the Y direction may be higher than the true value and this is observed for both the phantoms. It should be noted that the 90° pulse slice refocusing in both the

DW-STEAM-EPI and DW-SE-EPI sequences was carried out immediately after the 90° pulse to minimise such cross-terms.

In future the accuracy of the ADC measurements could be improved by including such cross-terms, due to the interaction of the DW and imaging gradients on different axes, in the calculation of the b-factor, as demonstrated by Mattiello et al [169], [170]. It may be that the remaining small discrepancies between the ADC values measured by different techniques and with DW gradients along different axes can be explained by including cross-terms in the b-factor.

In Figure 69 there is no obvious variation in the DW-STEAM-EPI ADC with slice number despite the exponential signal decay with slice number. In fact the slope of a best-fit line to the ADC values in Figure 69 was found not to deviate significantly from zero. This data is in contrast to the trends observed in Figure 70 and Figure 71. In Figure 71 the DW-STEAM-EPI ADCs in all directions seem to decrease slightly with increasing slice number in contrast to the DW-SE-EPI values which remain relatively constant. This observation was corroborated by linear fits (not shown) to the graphs of ADC values against slice number in Figure 71: the small negative gradients of the DW-STEAM-EPI data were found to deviate significantly from zero whilst the slopes of the DW-SE-EPI data did not. This slight decrease in the ADC measured with the DW-STEAM-EPI data can be attributed to the decreased signal in the later slices. It has been found previously [171] that decreasing SNR at high diffusion weighting causes systematic decreases in calculated ADC values. It may be that the DW-STEAM-EPI signals in later slices are close to the noise level and therefore cause the calculated ADC to appear systematically lower than the true value.

In the experiment in Figure 69, the SNR may have been sufficiently high compared with the data in Figure 71 (due to the larger voxels and lower diffusion coefficient of dodecane compared with water) that the ADC values remained unbiased. Such a bias on the ADCs and other effects of noise on the diffusion tensor [172] might be expected for any high resolution DWI technique since the SNR is reduced by going to higher resolution (see Equation 78). However the volume selective DW-STEAM-EPI technique is unique in having an SNR that varies across the slices. This effect could be mitigated by acquiring slices in both the forward and reverse order and then averaging

the raw signals before fitting to obtain the ADC or diffusion tensor. Such an approach was followed for the data in Figure 70 and the results are shown in Figure 72.

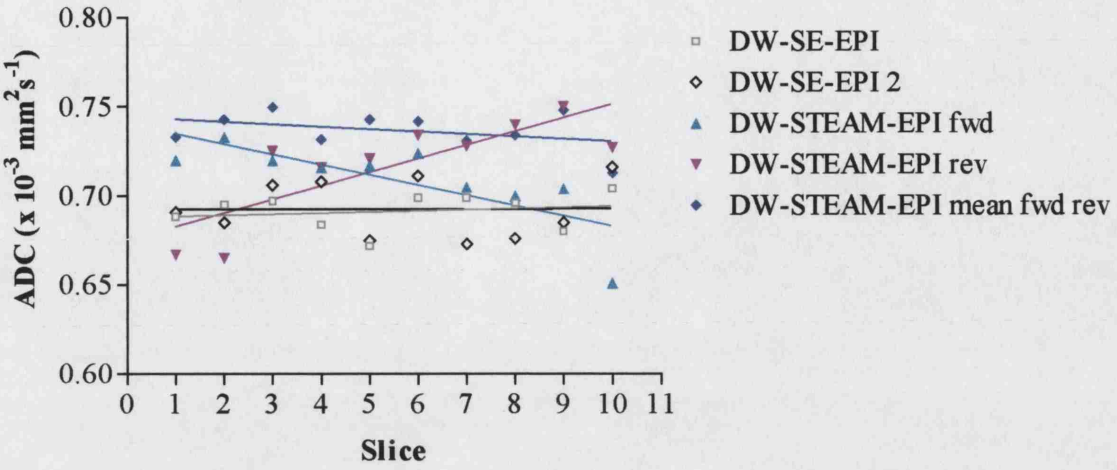


**Figure 72 The Effect of Averaging Forward and Reverse Acquisitions on multislice Volume Selective DW-STEAM-EPI ADC values compared with DW-SE-EPI ADCs**

This Figure is identical to Figure 70 except that best-fit lines from linear regression of the data sets have been added as has an additional DW-STEAM-EPI dataset formed by averaging the mean ROI signals from the forward and reverse DW-STEAM-EPI datasets before fitting to obtain the new ADC values for each slice.

Linear fits of the data yielded gradients not significantly different from zero for the two DW-SE-EPI acquisitions but a significantly non-zero negative gradient for the forward DW-STEAM-EPI acquisition and a significantly non-zero positive gradient for the reverse DW-STEAM-EPI acquisition. When the data from the forward and reverse acquisitions are combined, the linear fit of the ADC values has a slope that is not significantly different from zero. The new mean ADC value across the slices ($0.737 \pm 0.011 \times 10^{-3}$ $mm^2s^{-1}$) is higher than that from either the forward and reverse acquisitions separately and from the DW-SE-EPI acquisitions and is closer to the literature value. This suggests that such a strategy is easy to implement and can mitigate the ADC variation with slice number at low SNR levels.

In future it would be useful to measure the overall SNR of the technique *in vivo* to determine how many slices can be collected for different b-values and TE values before the ADC's become systematically decreased and other DT-based measures are corrupted.

Finally, there is a more general point to make about the errors on the ADC values given here: The errors on the ADCs calculated here are those on fits of ln(mean ROI data) against b value used to calculate ADC for single experiments, or the standard deviation of the ADCs from several repeat experiments. Alternatively the ADCs could be calculated by voxel-by-voxel fitting followed by region of interest analysis (treating each voxel as an independent measurement). If voxel-by-voxel fitting is carried out then the ADC values from the SE and DW-SE-EPI experiments could be plotted against those from the DW-STEAM-EPI experiment to look for any systematic differences. This would only be possible if the images were acquired with exactly the same FOV and resolution so that the same voxels were being interrogated by both techniques.

### *4.3.5.4 Slice Decay in Volume Selective DW-STEAM-EPI*

#### 4.3.5.4.1 Methods

In order to investigate whether the slice-to-slice decay could be explained by the model described in section 4.3.4.2.3, slice decay constants were predicted based on Equation 83 and compared with measured values. Measured slice decay constants were obtained from linear fits of the logarithm of the mean MR signal inside the ROI in each slice against the corresponding decay time for that slice ($\Delta_{slice}$ measured using a data logger see Figure 64). Separate linear fits were carried out for each b-value.

#### 4.3.5.4.2 Results

Figure 73 shows predicted and measured slice decay constants for the dodecane and water phantoms. The data in Figure 73A were acquired using the same parameters as the data in Figure 69. The data in Figure 73B were acquired with the same parameters as the data in Figure 71.

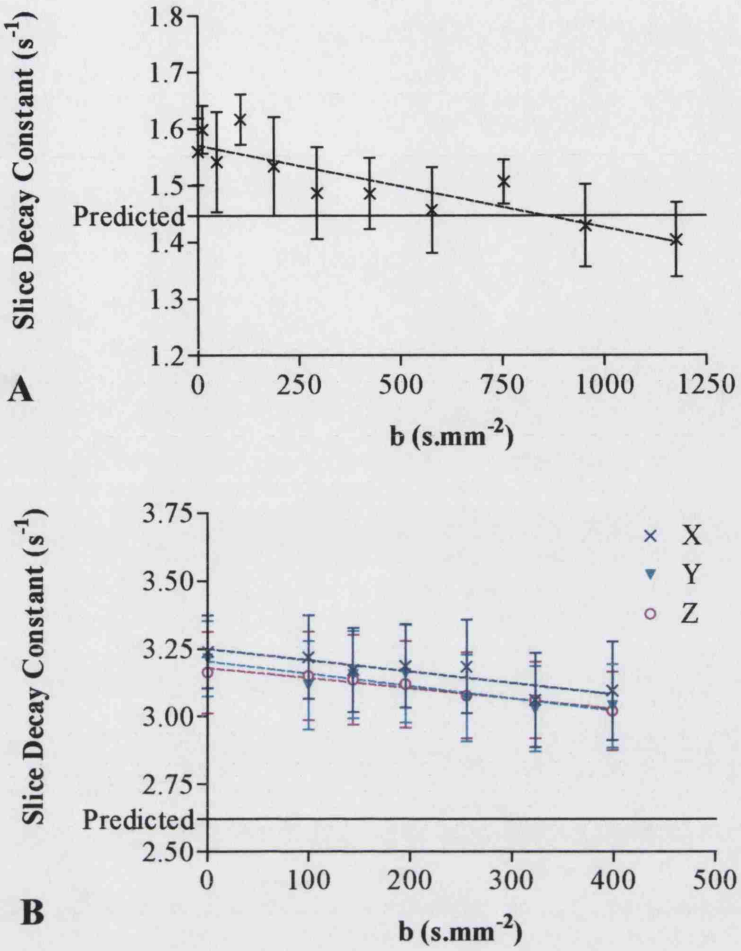


**Figure 73 Slice Decay Constants for the Volume Selective DW-STEAM-EPI Sequence**

The data in **A** are for the dodecane phantom with diffusion weighting gradients in the Z direction. The data in **B** are for the water phantom. In both cases the error bars are those from the linear fits of ln(mean signal in ROI) against $\Delta_{slice}$ used to obtain the slice decay constants. The best-fit lines for the measured data are dashed.

#### 4.3.5.4.3 Discussion

The predicted slice decay constant in Figure 73A is close to the measured values suggesting that the model explained in section 4.3.4.2.3 (Equation 82) can explain the slice decay. However in Figure 73B the predicted slice decay constant is lower than the observed values suggesting that there are processes causing the signal to decay faster than predicted. Such processes might include additional diffusion weighting due to the interaction between other imaging gradients (not just the TE spoilers) applied when the spins are in the transverse plane. The discrepancy between the predicted and measured slice constants may therefore be greater in the water phantom since its diffusion coefficient is greater than dodecane's so extra slice-to-slice diffusion weighting by imaging gradients might be expected to cause faster slice decay.

The initial hypothesis regarding the variation of the slice decay constant with b-value was that there would be none i.e. that the exponential signal decay is a function of the imaging module only and that there is no interaction between the SE-DW preparation (for which the b-value is calculated) and the rest of the sequence. However in both Figure 73A and B there is a slight decrease of the slice decay constants with increasing b-value. This may be because, at higher b-values, the signal is lower for later slices and comes close to the noise level, leading to an artificially decreased slice decay constant (in much the same way as decreased SNRs for high b-values in late slices leads to decreased ADC values). If there were severe cross terms due to interactions between the initial SE DW preparation and the imaging module then the opposite trend to that observed would be expected i.e. an increase of the slice decay constant with increasing b-value. The fact that this is not observed is good evidence that the SE DW preparation is highly independent of the imaging module in the volume selective DW-STEAM-EPI sequence.

### *4.3.5.5 Prepared v. Unprepared Signal Ratios in Volume Selective DW-STEAM-EPI*

#### 4.3.5.5.1 Methods

In order to check the EPI acquisition section of the sequence and to verify the STEAM signal-formation mechanism described in Equation 81, some unprepared equivalent GE-EPI images were acquired by simply switching off all the RF and gradient pulses in the diffusion preparation module (i.e. all the pulses outside the bracket in Figure 64). The ratio of the signal means in identical ROIs in the first slice of the non-DW STEAM-prepared and unprepared images was calculated. The measured ratio was compared with a predicted ratio calculated using Equation 81.

#### 4.3.5.5.2 Results

Table 12 shows the results of acquiring non–DW STEAM-prepared images with the volume selective DW-STEAM-EPI sequence as compared with the signal in unprepared images acquired with the same sequence but with all the preparation RF pulses and gradients switched off.

| Phantom | Mean ROI signal in STEAM-Prepared Image (a.u.) | Mean ROI signal in Unprepared Image (a.u.) | Ratio of Prepared / Unprepared signal | Predicted signal Ratio | Measured / Predicted signal ratio |
|---|---|---|---|---|---|
| Water | 4613 ± 802 | 52013 ± 5497 | 0.089 | 0.121 | 0.735 |
| Dodecane | 8526 ± 1105 | 26000 ± 3130 | 0.328 | 0.259 | 1.265 |

**Table 12 Prepared v Unprepared Signal Ratios in Volume Selective DW-STEAM-EPI**

These are 'first-slice' values. The first two columns contain ROI means with ± the standard deviation within the ROI. In the water phantom a cuboid was selected while in the dodecane the RF pulses were non-selective so the whole phantom appeared in the STEAM-prepared image. The dodecane images were acquired with the same parameters as in Figure 66 and the water images were acquired with $TE_{SE}$ = 62 ms, TE = 83 ms, TM = 70 ms, TR = 6000 ms, spectral width = 200 kHz, FOV = 129 x 129 mm (read x phase), matrix size = 128 x 64 and a 30 mm x 30 mm cube selected in the slice and PE directions.

#### 4.3.5.5.3 Discussion

The measured values are close to the predicted values which suggests that the model described in section 4.3.4.2.3 broadly explains the sequence relaxation factors that affect the STEAM-prepared images. However the measured ratio is less than predicted in the water phantom and greater than predicted in the dodecane phantom. The additional signal loss in the water phantom may arise from $B_1$-inhomogeneity effects – namely there is a dark region in the centre of the cube ROI in the STEAM-prepared image which is not present in the unprepared image. This dark region may represent the additive effect of $B_1$-inhomogeneity within the phantom due to the multiple non-uniform slab-selective RF pulses used for the STEAM-preparation. This effect does not seem to occur in the dodecane phantom because dodecane has a much lower dielectric constant than water. Further signal loss in the water phantom could also occur due to diffusion weighting from the interaction of imaging gradients and TE spoilers. In addition, the first slice was near the edge of the cuboid selected in the slice direction and may therefore have been affected by the poor slice profile as illustrated in Figure 65.

In contrast, the apparent excess of STEAM-prepared signal measured in the dodecane phantom as compared with the predicted value is most likely to reflect a lower-than-expected signal in the unprepared images. This may be because the signal decay in the (essentially gradient-echo) unprepared images is due to $T_2^*$ which may be much shorter than the $T_2$ value used to calculate the predicted ratio, particularly as there was a large air bubble in the dodecane phantom. Signal which drops out in the unprepared images

will be distorted in the STEAM-prepared images and may appear as a compressed region with increased signal intensity.

#### 4.3.5.6 Conclusions and Further Work

It has been shown in sections 4.3.5.2 and 4.3.5.3 that the volume-selective DW-STEAM-EPI technique can successfully select a reduced FOV region and gives reasonable ADC values in dodecane and water phantoms. Slice-to-slice signal decay was observed but the resulting small bias in the ADC values could be mitigated by averaging both forward and reverse acquisitions. It would be necessary to wait for full $T_1$ relaxation of the excited volume before acquiring it again with the slice order reversed. The sequence implemented here was a Full Fourier version but a partial Fourier version could be implemented in future to increase SNR efficiency. The increase in signal from the shorter TE may mitigate the ADC decrease with slice.

Throughout this work, a single non-phase-encoded reference scan was acquired prior to all the experiments and used to reduce the Nyquist ghosts throughout the whole dataset. In future, especially for DTI experiments, it may be desirable to acquire a reference scan or a minimum set of three central echoes for each different b-value and DW gradient direction, in case the diffusion preparation affects the ghosting in the EPI sequence via eddy currents for example.

It is important to evaluate the level of geometric distortion from this technique, which could be done using an anthropomorphic head phantom (see Chapter 5) and eventually *in vivo*. For example it would be useful to evaluate the amount of distortion when the cuboid is placed in regions of the brain (near air spaces) that normally suffer from severe susceptibility artifacts. It should be simple to apply localised shimming to the volume selected by the DW-STEAM-EPI technique to further reduce susceptibility-induced $B_0$ inhomogeneities and thereby geometric distortion and this could be investigated in further work.

It would be interesting to implement multi-shot DW-SE-EPI sequences and compare their performance, particularly with regard to motion sensitivity, with the volume selective DW-STEAM-EPI sequence. It may be possible to eliminate the need to

acquire separate navigator echoes in DW-SE-EPI if each shot is made self-navigating by acquiring the central 'keyhole' of k-space with increased density [124], [173].

As mentioned in section 4.3.4.2.4 multiple cubes could be collected to increase the spatial coverage of the volume selective DW-STEAM-EPI technique. A diagonal strategy for cube placement could be devised such that it would not be necessary to wait for full $T_1$ relaxation of the slabs excited outside the first cube before the next cube could be acquired. To select multiple cubes it would be necessary to make the 180° pulse slab-selective so that the whole sample volume would not be inverted. The profile of the 180° pulse could be improved by implementing the SLR methods suggested for the 90° pulses. Even with RF pulse profile optimisation there may be discernible discontinuities in composite images made by juxtaposing slices acquired in adjacent cubes. Unfortunately, since acquisition of one 10-slice image cube already requires additional dead-time to avoid exceeding the gradient duty cycle, it would not be possible to increase the SNR efficiency of the technique by rapidly acquiring multiple cubes.

Eventually the sequence could be used to acquire high-resolution Diffusion-Weighted STEAM-EPI images *in vivo*. The SNR of the technique could be assessed for a range of TE values and ADC measurements made to determine how many slices can be collected while retaining sufficient SNR for unbiased ADCs and Diffusion Tensor estimates.

The potential of the technique for Diffusion Tensor Imaging and fibre tracking would need to be evaluated along with its motion sensitivity in comparison with other methods such as multishot DW-SE-EPI. Cardiac gating may be desirable to minimise pulsatile cardiac motion artifacts. From the experimental results and theoretical assessment it seems that the volume selective DW-STEAM-EPI technique shows promise for reaching high isotropic resolution for efficient DTI at high field strength with reduced distortion.

# 5 DEVELOPMENT OF AN ANTHROPOMORPHIC HEAD PHANTOM TO TEST SUSCEPTIBILITY ARTIFACT REDUCTION TECHNIQUES

## 5.1 Introduction

Susceptibility artifacts such as geometric distortion and drop-out are worse at high field strengths (see section 2.12.3) and are especially problematic in the $T_2$*-weighted rapid imaging sequences commonly used for Blood Oxygentation Level Dependent (BOLD) contrast fMRI. High fields are advantageous for fMRI since they yield higher SNR and also greater sensitivity to BOLD contrast. $T_2$*-weighted GE-EPI is most commonly used to detect BOLD contrast but is also the most sensitive sequence to susceptibility artifacts due to its low bandwidth per pixel in the PE direction (see section 2.12.3.2). As seen in section 4.2, SE-EPI images often used for DTI are often affected by severe geometric distortions.

A plethora of different image acquisition methods have been proposed to mitigate some of the susceptibility artifacts in $T_2$*-weighted imaging sequences for fMRI [174] and other applications. Some of the techniques can be classified according to whether they help to reduce primarily geometric distortion or signal drop-out.

Examples of techniques whose main aim is to reduce signal drop-out include acquisition of several images with varying preparation gradients (usually but not exclusively [175] in the slice-select direction), also known as z-shimming [176], [177] and combining these images with either a Fourier transformation or a summation [178], [179], [180]. Alternatively the TE can be reduced but in GE-EPI this does not seem to be sufficient to recover the BOLD signal in regions affected by susceptibility artifacts [181] and reduces the overall BOLD sensitivity. Another simple technique for reducing drop-out due to through-slice susceptibility gradients is to reduce the slice thickness [18], [182]. Another option is to use tailored RF pulses [13], [183], [184] to excite a slice with a specific phase profile designed to compensate for intravoxel dephasing. This method requires individual design of the excitation pulse (often based on an acquired field map) prior to the experiment.

Some techniques developed primarily to mitigate signal drop-out should also result in reduced distortion since they are based on attaining the most homogenous $B_0$ field possible in the area of interest. Such methods are the use of optimised global shims [185] and local passive [186-188] and active [189], [190], [191] diamagnetic shimming although such shims have only been used for certain brain regions such as the inferior frontal cortex.

There are also a wide variety of methods for reducing distortions, many of which rely on some kind of field map acquisition (see section 5.5.4.2 below) followed by post-processing to 'unwarp' the distorted images [14], [97], [192], [193], [194], [99]. Other suggestions are the use of multi-shot (segmented or interleaved) EPI [195] to reduce the effective EPI acquisition time over which artifacts can develop. Other techniques to reduce this effective acquisition time include parallel imaging techniques such as sensitivity encoding [130] or reduced field of view methods [196], [126].

Of course it is possible to combine several complementary methods to achieve the best quality image for example by using a z-shimming-type acquisition to reduce drop-out and SENSE parallel imaging to reduce distortion [197].

Undoubtedly there is a need to systematically evaluate and compare the wide variety of techniques to establish the optimum procedure for each brain region and purpose. The rationale for building a head phantom is to enable systematic development, optimisation and comparison of susceptibility artifact reduction techniques at 4.7 T.

Previously, computational or numerical models [198], [199], [200], [201] have been used to simulate the main magnetic field distribution in the head. These have the advantages that they are not affected by $B_1$ inhomogeneity or signal drop-out and they could be performed for a particular subject's anatomy if based on a prior MRI or CT scan of an individual. However, in order to use such models for evaluating different imaging and artifact reduction techniques it would be necessary to be able to simulate the effects of whole sequences and the imaging process on these models. This would be computationally intensive (for example a memory limit of 1 GB and computation time limit of 10 hours restricted the resolution and extent of Truong et al's calculations [200]). It might also be difficult to include system-specific details such as the effects of eddy-currents and shims although Truong et al [200] argue that numerical simulations will be

especially useful for the assessment of active and passive shimming because they allow shim coil and passive shim configurations to be arbitrarily selected and optimised. For a particular imaging system though, it may be more convenient to simply use phantoms to test different techniques for susceptibility artifact reduction. For example a phantom should allow investigation of distortion and drop-out artifact reduction methods such as the use of tailored RF pulses.

In the past, investigations of MRI distortion have used very precise simple phantoms such as arrangements of water-and air- filled spheres or cylinders [202], [203], [204], [205] whose behaviour can be easily predicted using theory. However it can then be difficult to relate the results to the situation in a real head. Even so-called 'anthropomorphic' phantoms have consisted of little more than arrangements of spheres inside a larger sphere [206], [203] or fluid-filled whole-head-shaped phantoms [207], [208] containing some spherical objects so that they are only crude approximations of the real situation. Clearly it would be impractical to repeatedly scan the same person during comparison or development of different techniques. Furthermore, using several different subjects would introduce variation into the data due to different anatomy and physiology, which would confound comparison. A highly anthropomorphic head phantom which reproduces as accurately as possible the magnetic environment of the brain would provide a realistic and stable test object that could be scanned reproducibly, repeatedly and indefinitely. Using such a phantom would be quicker and cheaper than scanning several volunteers and safety concerns associated with scanning volunteers would be eliminated.

To ensure that it behaves in a similar way to the brain it is necessary to build a head phantom that reproduces as accurately as possible the magnetic environment of the brain. In order to allow quantitation of artifacts such as susceptibility-induced distortion and drop-out it is desirable that the optimum image of the phantom will be uniform in brain cavity and zero elsewhere. Computer simulations based on a 3-D, water and air, head model [199] have concluded that the global main ($B_0$) field distortion is primarily due to the geometrical configurations of tissue and air compartments so these need to be included in the phantom, which should also have realistic magnetic susceptibilities.

## 5.2 Properties to Simulate in the Phantom

As described above, the majority of the artifacts are caused by susceptibility differences between air and tissues so the primary head property to simulate in the phantom is the susceptibility of different tissues and their corresponding geometrical shapes and air cavities. For simplicity of construction we can segment the phantom into four regions on the basis of their tissue types and susceptibility: skull mimic, air cavities, soft tissue mimics and brain-mimicking fill.

The initial idea was to base the phantom around a plastic skull made for medical students (CS-20 Budget Skull, the Anatomical Chart Company, www.anatomical.com) (see Figure 74) to ensure that the anatomical brain dimensions were realistic. It was then necessary to investigate whether the material was suitable in terms of its magnetic susceptibility (see section 5.3.2). It was planned to retain existing air cavities and add those that were not present. The main air cavities to be included were (see Figure 75): frontal sinuses, ethmoid air cells, nasal cavity, sphenoid sinus, maxillary sinuses, mastoid air cells, auditory canals (internal and external auditory meatus (EAM)) and oropharynx.

**Figure 74 The Plastic Skull**
The CS-20 Budget Skull (the Anatomical Chart Company, www.anatomical.com) used as the basis for the anthropomorphic head phantom

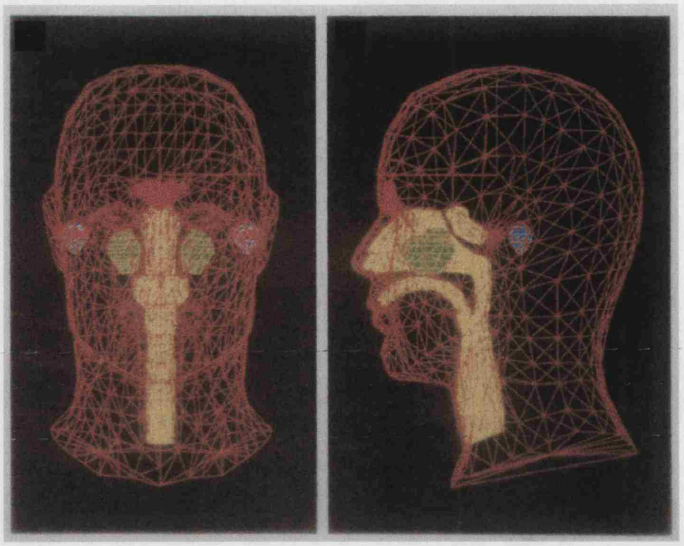

**Figure 75 Air Spaces in the Human Head**
An illustration of the air spaces for inclusion in the anthropomorphic head phantom. The Images [199] illustrate a computer model of the head used to calculate the magnetic field. The air spaces are clearly visible: frontal sinus, sphenoid sinus, maxillary sinuses, mastoid air cells, nasal and oral cavities.

The dimensions of these air spaces in real heads were estimated from a variety of sources including measurements made on MR images and CT scans. Table 13 summarises the results of these measurements.

| | Measurement Technique: | 3D CT | $T_1$-W MR | $T_2$-W MR | Female CT | Male CT |
|---|---|---|---|---|---|---|
| Airspace | Measurement description | Measurement (mm) | | | | |
| Frontal Sinus (treated as one big structure) | L-R max | 52 | 50-60 | 60-68 | 38 | 92 |
| | S-I max | 24 | | 22 | 21 | 54 |
| | A-P max | 28 | 5 | 14 | 9 | 14 |
| Sphenoidal Sinus | L-R max | 24 | | | 31 | 36 |
| | S-I max | 17 | | | 21 | 27 |
| | A-P max | 35 | | | 18 | 27 |
| Mastoid air cells &/ EAMs (one side) | L-R max (depth) | 32 | <= 30 | ~44 | ~30 | 36-46 |
| | S-I max (height/ diam) | 35 | <= 10 | ~30 | 39 | 39 |
| | A-P max (width at opening) | 27 | ~ 20 | ~ 44 | ~33 | 43 |
| Maxillary Sinuses (one side) | L-R max | | ~20 | 28 | 25 | 28 |
| | S-I max | | ~25 | | 42 | 48 |
| | A-P max | | ~25-30 | 32 | 36 | 39 |
| Nasopharynx/ Oropharynx | L-R diameter at opening to nose | 19 | | | | |
| | S-I diameter at opening to nose | 19 | | | | |
| | A-P diameter once tube is vertical | 10 | | | | |
| | L-R diameter once tube is vertical | 23 | | | | |
| | L-R diameter at join with mouth | 21 | | | | |
| | A-P diameter at join with mouth | 8 | | | | |

**Table 13 Airspace Measurements in Human Head Images**

The results of head airspace measurements made using a variety of datasets and measurement techniques are shown. The measurements were made in a variety of directions left to right (L-R), superior to inferior (S-I) and anterior to posterior (A-P). The **3D-CT** column includes measurements made on CT data from two volunteers supplied by the UCL medical graphics and imaging group using Dr Robin Richards' 3D Image rendering software (http://www.medphys.ucl.ac.uk/mgi/manual/3dintro.htm). The **$T_1$W-MR** column includes measurements made on a set of structural $T_1$-weighted MR images of a volunteer acquired ( with 1 x 1 x 1 mm resolution) on the 2 T scanner at the UCL Functional Imaging Laboratory. Distances were measured using the ruler facility in Adobe Photoshop software. The **$T_2$W-MR** column includes measurements made on a set of simulated $T_2$-weighted MR images from the Brainweb MR simulator (www.bic.mni.mcgill.ca/brainweb). The images have 1 x 1 x 1 mm resolution, 3% noise and 20% RF inhomogeneity. The measurements were made using the stereotactic coordinates provided in the simulator. The **Female CT** column includes measurements made on the visible human female reduced CT dataset (www-medrad.radiology.wisc.edu/vishum/index.html ) of resolution 1.8 x 1.8 x 3 mm using DispImage software (www.medphys.ucl.ac.uk/~dlp/dispim.htm). The **Male CT** column includes measurements made on the male reduced CT dataset from the visible human as for the Female CT column.

The soft tissues that need to be simulated in the phantom include the facial muscles, eyeballs, tongue and skin etc. Several materials such as paraffin wax, perspex, plasticine or wood were suggested as candidates to mimic the susceptibility of soft tissue, which is very slightly diamagnetic and has a susceptibility similar to water ($-0.9 \times 10^{-8}$ $m^3kg^{-1}$ [209]). These materials could then be built up in layers around the plastic skull perhaps using templates taken from MR images as a guide for the tissue thicknesses.

Finally, the substance filling the brain cavity should not only be MRI-visible and mimic the susceptibility of white and grey matter and CSF (which are similar to that of water and soft tissues) but also have a $T_2^*$ representative of values *in vivo*. This is because $T_2$*-weighted sequences are most sensitive to susceptibility artifacts. For a realistic $T_2^*$, both the susceptibility and the $T_2$ inside the brain cavity should be realistic because $T_2^*$ depends on these [198], [16], [161] (see Equation 15 and Equation 36):

$$\frac{1}{T_2^*} = \frac{1}{T_2} + \gamma \Delta B$$

**Equation 90**

where $\Delta B$ is the static field inhomogeneity in a particular region (strictly the average inhomogeneity across a voxel in a gradient-echo experiment) and $T_2$ and $\gamma$ are the transverse relaxation time and the gyromagnetic ratio.

# 5.3 Choice of Materials and Fill

## 5.3.1 CT Scan of the Plastic Skull

A Computed Tomography (CT) scan of the empty plastic skull was acquired to discover whether there were any existing air spaces or other inclusions that were not visible from the surface. It was carried out using the clinical scanner in the National Hospital for Neurology and Neurosurgery with a slice thickness of 5 mm. The resulting axial slice images were examined and any air spaces measured in Adobe Photoshop. The only hidden airspaces revealed were those in the position of the maxillary sinuses (see Figure 76), each of which was found to have maximum spatial dimensions of ~11 mm in the left-right and anterior-posterior directions and ~20 mm in the head-foot direction.

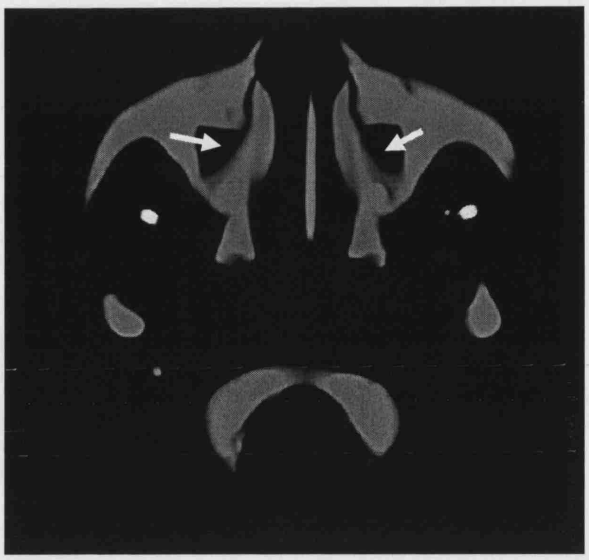

**Figure 76 CT Image of the Plastic Skull**
An image slice from a CT scan of the empty plastic skull that forms the basis of the anthropomorphic head phantom. This low transverse slice shows the maximum extent of the 'maxillary sinus' air spaces (white arrows) that were not visible from the surface of the phantom. The intense white dots are springs that originally joined the jaw-bone component to the rest of the skull. These were removed during construction of the phantom.

Despite being smaller than most real maxillary sinuses (see Table 13) the presence of these 'maxillary' air spaces in the phantom was desirable and they were retained.

## 5.3.2 SQUID Susceptibility Measurements

In order to decide which materials would be suitable tissue mimics, susceptibility measurements were made on a variety of candidate material samples using a Superconducting QUantum Interference Device (SQUID) magnetometer. A sample of the plastic skull was used to allow comparison of its susceptibility with that of a lamb bone sample to see if it was realistic. The susceptibilities of 'soft tissue' candidate materials were also compared with an existing sample of rat cortex to see which would be suitable soft tissue mimics. Silicone sealant was tested since it would prove useful for sealing the plastic skull.

### *5.3.2.1 SQUID Method*

These measurements were made with the help of Dimitri Hautot and Quentin Pankhurst in the Department of Physics and Astronomy, University College London using a Quantum Design MPM-7 SQUID magnetometer. The samples, of approximately 2-5 mm diameter and 3-5 mm height, were weighed before being placed in a gelatine

capsule that was mounted in a plastic straw that was then pierced and placed inside the SQUID probe. This had previously been found to be an optimal geometry for the SQUID measurements [210]. The magnetisation (M) of each sample was measured as a function of the applied magnetic field (H). The resulting plots were analysed by fitting a model that assumed superposition of the M-H characteristics i.e.

$$M = \frac{AH}{1+BH} + CH$$

**Equation 91**

where A and B are the constants pertaining to the ferromagnetic component and C is the required paramagnetic or diamagnetic susceptibility (C ≡ χ). In fact, the SQUID measurements were in the cgs system of units: magnetic moment in emu and field in Oe. In order to convert these to SI units to obtain mass susceptibilities ($\chi_\rho$) in $m^3kg^{-1}$ it was necessary to use the relationships [19]:

$1\ Oe = 10^3/(4\pi)\ A.m^{-1}$

**Equation 92**

$1\ emu = 10^{-3}\ A.m^2$

**Equation 93**

and also to divide the fit parameters (C) by the measured mass of the sample (kg).

### *5.3.2.2 SQUID Results*

Most of the substances were found to have a primarily diamagnetic susceptibility (see the example μ-H curve in Figure 77) except for teak and oak samples, which showed were strongly paramagnetic at low fields and diamagnetic at higher fields and were therefore rejected as appropriate soft tissue mimic materials. The diamagnetic susceptibilities of the rest of the samples are shown in Figure 78.

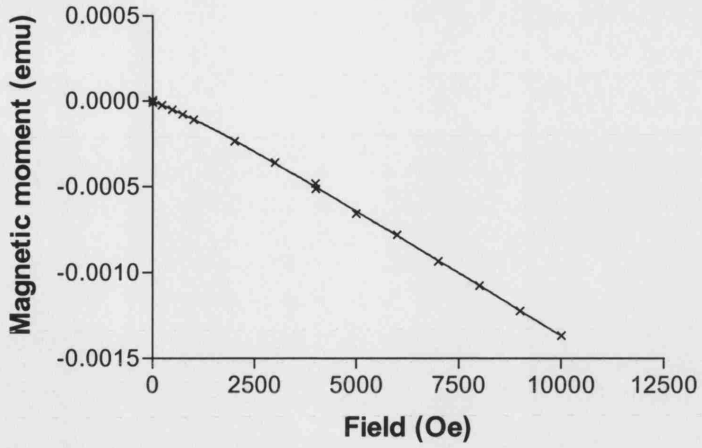


**Figure 77 SQUID Magnetisation Curve for Paraffin Wax**
Plot of the magnetic moment of a paraffin wax sample measured at different magnetic fields inside the SQUID magnetometer. The curve is the best fit to Equation 91. In order to obtain the mass susceptibility in SI units from the best fit 'C' parameter, it was multiplied by a conversion factor $4\pi \times 10^{-6}$ from Equation 92 and Equation 93 and divided by the sample mass ($0.174 \times 10^{-3}$ kg).

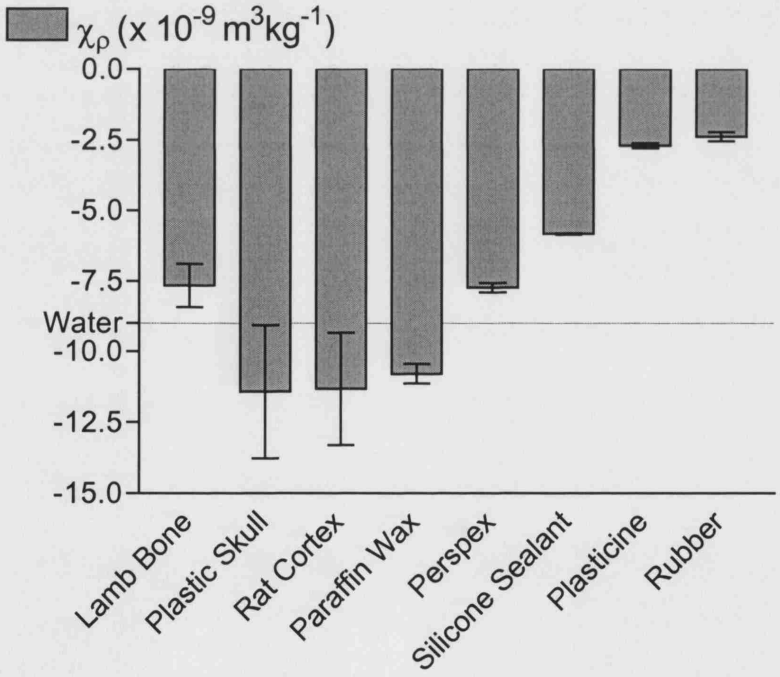


**Figure 78 Magnetic Susceptibilities of Various Materials Measured Using a SQUID**
The results of magnetic mass susceptibility measurements made with a SQUID magnetometer on a variety of samples. The error bars indicate the standard error on the best fit values from curve fits of magnetisation against applied field using a model (Equation 91) that assumes superposition of ferromagnetic, paramagnetic and diamagnetic characteristics.

### 5.3.2.3 Discussion and Conclusions

From Figure 78 we can see that the susceptibility of rat cortex was close to that of water (= -9.05 x $10^{-9}$ $m^3kg^{-1}$) as expected. This implies that water would be a good susceptibility substitute for the brain. Assuming that the susceptibilities of soft tissue and brain are similar we can conclude that paraffin wax would be the best soft tissue mimic since its susceptibility was closest to that of water and rat cortex. For this reason, paraffin wax was chosen as the best soft-tissue-mimicking material.

The magnitude of the susceptibility difference between water and the plastic skull is opposite to that between the rat cortex and lamb bone. At first glance this suggests that the direction of any susceptibility gradients between the water and plastic skull in the phantom will be opposite to those found in the real head. However this is not likely to be true since, after further investigation, the susceptibility measured for the cooked lamb bone sample seems not to be highly representative of the true *in vivo* skull bone susceptibility. There is evidence to suggest that the susceptibility of bone is more negative than that of water / soft tissue (–10.9 x $10^{-6}$ for human trabecular bone [211] compared with –9.0 x $10^{-6}$ for water) and this is the same as the relationship between the plastic skull and water. Therefore it was reasonable to use the water-filled plastic skull as the basis for the head phantom. If more accurate values for the susceptibility of human brain and skull were required, fresh ex vivo samples could be obtained and their susceptibilities measured using the SQUID as described above.

The susceptibilities of rubber and silicone sealant, although both weakly diamagnetic, were non-ideal compared to the susceptibilities of the plastic skull, wax, bone and rat cortex. However it was not found necessary to use large quantities of these substances in the phantom construction so they would not be likely to substantially affect the magnetic environment inside the phantom. In any case Li [199] found that the main factor determining susceptibility artifacts is the geometry of the air spaces within the head phantom.

## 5.3.3 Advantages and Disadvantages of Potential Fill Materials

Since the brain cavity must be visible in images and have a susceptibility similar to that of real brain it needs to be water-based. There are several fill materials that have been

used in previous phantoms. These are mostly aqueous solutions and gels doped with paramagnetic salts (such as $NiCl_2$) to give realistic $T_1$ and $T_2$ values.

Aqueous solutions are stable and easy to make and their $T_1$ and $T_2$ values can be easily predicted once relaxivity measurements have been made. However the advantage of using a gel (agarose [212], gelatine [206], polyacrylamide and TX-151 [213] have all been used in the past) is that the gel matrix material can further shorten $T_2$ giving a more realistic $T_1$ and $T_2$ at 4.7 T than can be obtained by simply doping water with paramagnetic salts. Conversely the $T_1$ and $T_2$ in a doped gel is not as easy to predict as in an aqueous solution since both the dopant and gel respectively contribute (somewhat independently [214]) to the $T_1$ and $T_2$.

For this reason it would be necessary to make up a variety of doped gel samples at a range of different gelling agent and dopant concentrations. Relaxation measurements would then need to be made to estimate the $T_1$ and $T_2$ of the different samples. These could then be used as a guideline to help decide on the concentration on gel and dopant for filling the brain cavity to obtain $T_1$ and $T_2$ values similar to those present in the brain at 4.7 T.

In fact there are almost no values in the literature for human brain relaxation times *in vivo* at 4.7 T so it would be desirable to make relaxation measurements to estimate the $T_1$ and $T_2$ of grey and white matter. Relaxation time values often depend on the measurement technique used to acquire them. To prevent the choice of technique from biasing the selection of gel and dopant concentrations with relaxation times similar to the brain, it would be desirable to use identical sequences and parameters to measure the relaxation times of both the range of gels and the human brain.

As explained in section 5.2, it was thought most important to simulate $T_2$ since it determines $T_2^*$, and $T_2^*$-weighted sequences suffer most from susceptibility artifacts. Because a highly realistic $T_1$ value was not vital for the utility of the phantom, it was decided to fill the phantom with $MnCl_2$-doped water. A liquid rather than a gel filling was also chosen for ease of filling and to reduce the number of concentration variables for relaxivity measurements (i.e. only the $MnCl_2$ concentration need be varied and optimised rather than both the dopant and gel concentrations).

A $MnCl_2$ concentration of 0.1mM was chosen based on $T_2$ measurements of several $MnCl_2$ concentrations at 4.7 T to try to simulate a mean $T_2$ of grey and white matter at 4.7 T. Literature $T_2$ values measured at 4 T (see Table 14) were used as a guide.

| Tissue | Measured $T_2$ (ms) | Measured $T_1$ (ms) | Field Strength (T) | Reference |
|---|---|---|---|---|
| Grey Matter | 63 ± 6.2 | 1724 ± 51 | 4 | 162 |
| White Matter | 49.8 ± 2.2 | 1043 ± 27 | 4 | |
| Grey Matter | 77 ± 0.8 | 1250 ± 130 | 4 | 167 |
| White Matter | 62 ± 0.65 | 1070 ± 110 | 4 | |
| Grey Matter | | 1354 ± 101 | 4 | 215 |
| White Matter | | 939 ± 35 | 4 | |
| Grey Matter | | 1630 ± 60 | 4.7 | 216 |
| White Matter | | 1070 ± 40 | 4.7 | |
| **Mean** | **63** | **1260** | | |

**Table 14 Literature Brain $T_2$ and $T_1$Values Measured at 4 and 4.7 Tesla**

## 5.3.4 Phantom Loading and $B_1$ distribution

In order to make the phantom easy to use it was decided to add NaCl to increase the conductivity of the water and thereby load the RF coil in a similar manner to a real head. Desired loading properties of phantoms are usually achieved by increasing their resistance to a similar value to that of the real head. This is necessary to ensure that the RF coil performs as well (in transmission and reception) as it would in the presence of a real head. In the absence of any coil loading, the power transmitted into the RF coil could be entirely reflected back into it with the risk of damage to coil components.

Since the phantom was to be filled with water, it would be expected that it would suffer to some degree from the field focusing effects and consequent $B_1$-inhomogeneity described in Chapter 3. This would not expected to strongly affect the $B_0$ field mapping but if images of the phantom were to be used to simulate those of the head, for example in sequence development, it may be desirable that the phantom images show similar $B_1$-inhomogeneity to those of the real head.

The initial approach to loading the coil might simply be to add a sufficient concentration of NaCl to mimic the conductivity of the brain at 200 MHz. However Yang et al [217] have shown that using a phantom with realistic conductivity does not necessarily produce a similar $B_1$ distribution to that in the real head. This is because the $B_1$ distribution also depends on the permittivity of the phantom and the permittivity of

water is not similar to that of the brain at high field strengths. It is possible to alter the permittivity of water using sucrose [218] but Yang et al have also shown that it is possible to reproduce a realistic $B_1$ distribution by altering only the conductivity of a water phantom (using NaCl) and its size such that both skin depths ($\delta$) and sample sizes (L) are scaled by the corresponding RF wavelength ($\lambda$) in the sample. The skin depth criterion can be fulfilled by altering the phantom conductivity $\sigma_p$ such that the following equation is satisfied:

$$\frac{\sigma_b}{\omega_b \varepsilon_b} = \frac{\sigma_p}{\omega_p \varepsilon_p}$$

**Equation 94**

where $\omega$ is the frequency and the subscripts b and p refer to the brain and phantom respectively.

Since, for simplicity, only NaCl was to be added to the phantom to load it, it was decided to use Equation 94 to try to achieve a more realistic $B_1$ distribution in the phantom. Conductivities and permittivities of grey and white matter at 200 MHz were obtained [219] and averaged to define the target brain ratio in Equation 94. The required conductivity to satisfy Equation 94 was calculated assuming a permittivity of 78.0 for water [217]. The required NaCl concentration (31mM) to achieve this conductivity was calculated from equations relating NaCl conductivity to concentration at 25°C [220]. The relevant conductivities, permittivities and ratio in Equation 94 are given in Table 15.

| | Conductivity $\sigma$ ($S.m^{-1}$) | Relative Permittivity $\varepsilon_r$ | $\sigma/\omega\varepsilon_0\varepsilon_r$ |
|---|---|---|---|
| Average Brain | 0.51 | 56.1 | 5.11 |
| Phantom Fill | 0.71 | 78.0 | 5.11 |

**Table 15 Conductivity and Permittivity of Brain Tissue and Phantom Fill at 4.7 T**
The equality of the quantity in the last column shows how the phantom fill conductivity was calculated to satisfy Equation 94. The brain data are the mean of published values for grey and white matter [219] and the permittivity of water was that used in Yang's work [217].

## 5.4 Phantom Construction and Filling

Firstly all the metal components of the plastic skull were removed (screws, latches and springs that had attached the jaw and the top of the skull to the rest of the skull). The jaw was then stuck to the skull with a small amount of cyanoacrylate adhesive. Next the skull's foramen magnum was plugged using a rubber bung of the appropriate diameter and sealed with silicone (bathroom) sealant. Subsequently the rest of the small holes in the skull around the brain cavity were filled with silicone sealant to ensure a waterproof brain cavity. A hole was drilled into the top of the skull, threaded and closed with a plastic screw and O-ring to allow filling (and emptying) of the brain cavity. The top part of the skull was then 'glued' to the bottom with silicone sealant.

Once the sealant was completely dry the brain cavity was filled with distilled water. To test whether the phantom was waterproof, water was used at first in preference to $MnCl_2$ solution which can be mildly toxic. Plugging the appropriate gaps with more silicone sealant alleviated leaks, before the phantom was topped-up with more distilled water and field maps were acquired.

Once the phantom had been verified as waterproof, it was emptied, left to dry and re-filled with the $MnCl_2$-doped water with added NaCl. An air bubble (Figure 82) was left when filling to simulate the frontal sinus with the phantom supine. Some paraffin wax was then melted, poured into the eye sockets and left to solidify (Figure 79). Field maps were again acquired before the next stage of phantom construction.

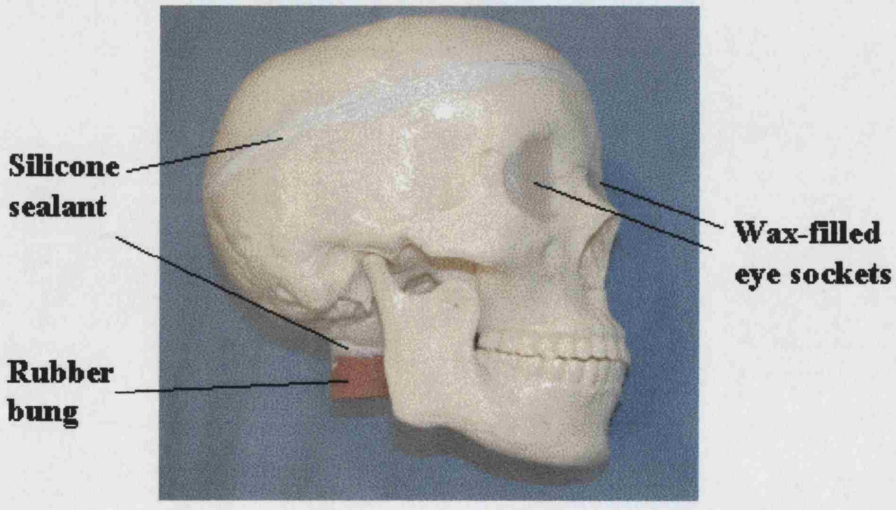


**Figure 79 The Plastic Skull at an Intermediate Stage of Phantom Construction**
The filled plastic skull is shown with silicon sealant, rubber bung plugging the foramen magnum and with wax-filled eye sockets.

Existing air spaces in the skull (such as the nasal cavity and maxillary sinuses (Figure 76 and Figure 82)) were retained and encased and additional ones were attached. The oral space was simulated by attaching half a ping-pong ball to the roof of the plastic skull's mouth. The nasopharynx was simulated by inserting two lengths of silicone rubber tubing into the base of the skull's nasal air space and the auditory canals and mastoid air cells were simulated by attaching two sealed lengths of the same tubing (Figure 82) to the base of the plastic skull. The dimensions of these air spaces were chosen to match those in Table 13 as closely as possible. They were fixed in place using small amounts of Milliput epoxy-putty (http://www.milliput.com).

To allow wax to be added around the plastic skull to mimic soft tissues outside the brain, a plastic (PETG – polyethylene terephthalate with glycol modifiers) head-shaped mould (Figure 80B) was made to fit around the plastic skull. In order to make the mould, a plaster cast of the skull (Figure 80A) was made and sawn in half sagittally. Plasticine was then added around each half to the approximate thickness of soft tissues to form a head and neck shape. Each plasticine and plaster-cast half-head was then placed in a vacuum-former under a sheet of heat-softened plastic, which was then vacuum-formed around the half-head. Excess plastic was cut away so that the two half-head moulds (see Figure 80B) could be stuck together around the skull to make a full head mould into which molten wax could be poured. The filled plastic skull plus air spaces was positioned inside the PETG mould using rubber spacers to keep it away from the sides of the mould. The two halves of the mould were then sealed around the plastic skull using Milliput epoxy putty, glass-repair tape and Duck tape to make a waterproof seal.

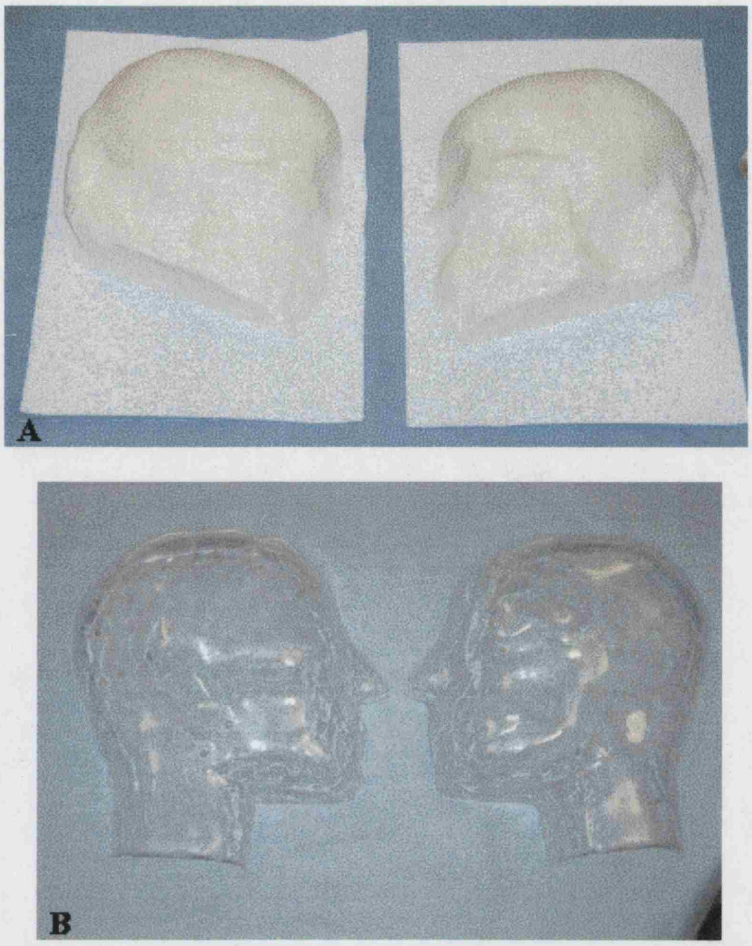


**Figure 80 Plaster Casts and Plastic Moulds Used in Phantom Construction**
The two halves of the plaster cast of the plastic skull (**A**) were used in forming the two 'half-head' plastic moulds (**B**).

Finally the mould and skull assembly was immersed 'head-first' in a bucket of warm water before filling with molten wax. Immersion was intended to warm the mould so that the wax would not solidify immediately on contact but would flow right to the bottom of the phantom (the top of the head). The wax was allowed to cool before removing the tape from the mould in case its glue had a large susceptibility, different from that of the phantom materials. The finished phantom is shown in Figure 81.

**Figure 81 The Finished Anthropomorphic Head Phantom**
Emerging from the phantom are the silicone rubber tubes that represent the pharyngeal airspaces. The white and yellow colours are present because two types of paraffin wax were used. The waxes both had the same magnetic susceptibility.

## 5.5 Phantom Evaluation

A variety of methods were used to evaluate the phantom and these are described in the following sections.

### 5.5.1 CT Scan of The Finished Phantom

The finished phantom was CT scanned in a similar manner to that described in section 5.3.1 to determine whether there were any spurious air bubbles and to check whether any molten wax had infiltrated into the nasal cavities or other air spaces. The scan was carried out using the clinical scanner in the National Hospital for Neurology and Neurosurgery with a slice thickness of 5 mm. Two representative transverse slices from the scan are shown in Figure 82.

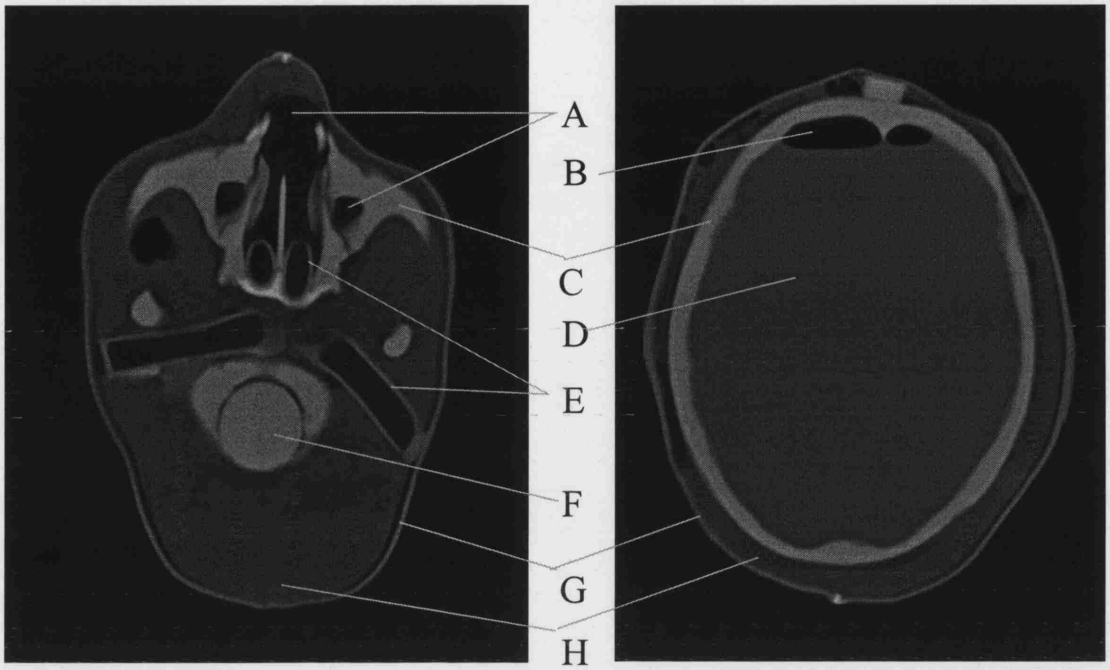


**Figure 82 Transverse CT Images of the Finished Phantom**
The labelled structures are the existing encased nasal cavity and maxillary sinuses (**A**), an air bubble (**B**) to simulate the frontal sinus with the phantom supine, the plastic skull (**C**), the $MnCl_2$-doped water fill (**D**), lengths of silicone tubing representing the nasopharynx and the auditory canals and mastoid air cells (**E**), the rubber bung plugging the brain cavity (**F**), the plastic (PETG) head-shaped mould (**G**) and the wax 'soft tissues' (**H**).

It is clear from Figure 82 and from inspecting all the CT scan slices that the molten wax did not infiltrate any of the major air spaces. There were a few small pockets of air between the wax and the plastic mould, especially at the very top of the head. The materials used in the phantom give good CT contrast suggesting that the phantom could also be a useful tool to test CT-MRI coregistration in the presence of susceptibility artifacts since the water-filled brain cavity is both CT and MR visible.

## 5.5.2 Phantom $T_1$ and $T_2$

The $T_1$ and $T_2$ of the phantom fill were estimated using sets of inversion-recovery FSE images with varying inversion time (TI) and standard SE images with varying TE respectively. The resulting phantom fill relaxation times were found to be $T_1 = 1116 \pm 49$ ms and $T_2 = 80.6 \pm 0.2$ ms (fit value ± S.D.). The phantom $T_2$ value is slightly longer than the $T_2$ values for grey and white matter at 4 T (see Table 14) but seems reasonably close.

The $T_1$ value seems closer to the value for white matter than that for grey matter at 4.7 T (see Table 14) but this still means that the phantom signal behaviour with sequence TR should be broadly representative of the behaviour of the real brain at 4.7 T.

## 5.5.3 Phantom $B_1$ Distribution

In order to assess how closely the $B_1$ distribution in the phantom matched that in the real head, $B_1$ maps of the phantom were acquired using De Vita's method [61], [7] (see section 3.5) and compared with similar (previously acquired) maps of a volunteer's head. The maps are displayed in Figure 83.

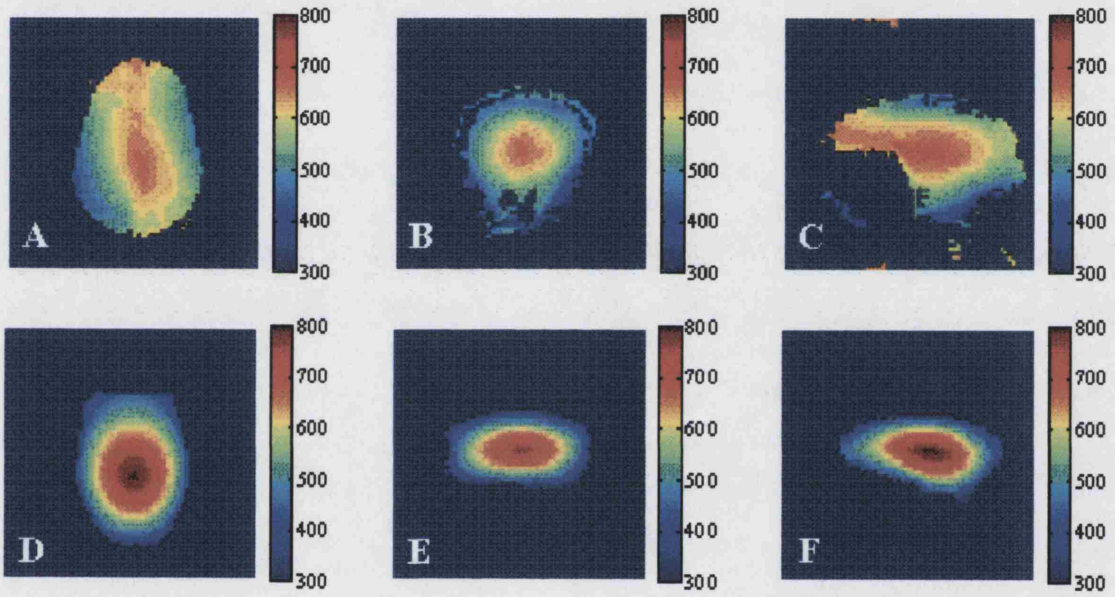


**Figure 83 $B_1$ maps of the Phantom and a Volunteer Head**
$B_1$ maps of a volunteer's head are shown in the transverse (**A**), coronal (**B**) and sagittal (**C**) orientations compared with $B_1$ maps of the phantom in transverse (**D**), coronal (**E**) and sagittal (**F**) orientations. All the maps are scaled between a $B_1$ of 300 Hz and 800 Hz.

Even though the general $B_1$ pattern in the phantom seems similar to that in the real head, with a central bright region of higher $B_1$, there are still significant differences in the $B_1$ distributions. Differences include the asymmetry of the pattern in Figure 83A and C compared with the symmetry in Figure 83D and F. Also there seems to be a greater overall $B_1$ variation in the phantom than in the real head. Differences are to be expected since the dimensions of the phantom were not scaled by the RF wavelength in the phantom as Yang et al recommend [217] therefore the wave behaviour will not be identical to that in the head.

## 5.5.4 Comparison of the Anthropomorphic Head Phantom with Real Heads: Field Mapping and Imaging

### *5.5.4.1 Aims*

Since regional variations of the magnetic susceptibility affect the homogeneity of the main magnetic field $B_0$, and $B_0$ differences cause drop-out and distortion artifacts, it would be useful to see how the $B_0$ varies in both the phantom and brain *in vivo* to see if the patterns are similar. If the phantom provides a similar magnetic environment for its brain cavity to that in brain *in vivo* then we can expect that the $B_0$ field maps will be similar. $B_0$ field maps of the phantom and volunteers' brains *in vivo* were therefore acquired to evaluate the phantom. As a final check, some images were also acquired of the phantom and a volunteer to assess the similarity of susceptibility artifacts arising from the magnetic field variations.

### *5.5.4.2 Field Mapping Methods*

The most commonly used and simplest method for field mapping is to acquire two images, one with a slightly longer TE than the other. The magnetic field difference $\Delta B_0$ (or deviation from $B_0$, the (200 MHz) main magnetic field at the magnet isocentre) as a function of position (x, y, z) can then be obtained from the phases of the two complex data sets using the following equations [192], [97]:

$$\Delta\phi(x,y,z) = \gamma\,\Delta B_0(x,y,z)\,\Delta TE$$

**Equation 95**

so

$$\Delta B_0(x,y,z)[Hz] = \frac{\Delta\phi(x,y,z)[rad]}{2\pi\,\Delta TE[s]}$$

**Equation 96**

where $\Delta\phi(x, y, z)$ is the phase difference, as a function of position, between the two images acquired with a TE difference of $\Delta$TE. The units are in square brackets.

It is possible to use several types of sequence to acquire the two images for field mapping and the advantages and disadvantages of some of these methods will now be discussed.

#### 5.5.4.2.1 Offset or Asymmetric Spin-Echo-Based Techniques

The offset- or asymmetric spin-echo technique [186], [221], [222] is simple to implement and understand. It involves the acquisition of a standard spin-echo image and a second spin-echo image with identical parameters except that the 180° pulse is offset in time relative to the centre of the read gradient. The offset time is equal to $\Delta TE/2$ in Equation 95 above.

The 3-point Dixon technique [223], [224], [225] is essentially the same as the basic offset- or asymmetric SE technique in terms of the sequence used but it requires the acquisition of three images (with particular time offsets to ensure $\pi$, 0 and $-\pi$ phases between fat and water in each image) because it was originally designed to obtain separate fat and water images. The image of $B_0$ is obtained almost as a by-product. Glover et al [223] developed an improved phase-unwrapping (see section 5.5.4.3 below) algorithm to overcome the failure of the original [225] technique in areas of high resonance offset or $B_0$ inhomogeneity. They also put the phase encode loop outside the 'resonance offset encode' loop in a bid to reduce the motion sensitivity of the technique.

#### 5.5.4.2.2 Gradient-Echo Techniques

In fact Glover et al suggest that the GRASS (gradient recalled acquisition in the steady state - a rewound gradient echo) sequence can be used with different TE values to obtain the same results as the offset-SE technique. Several investigators have collected two gradient-echo image volumes with echo times differing by $\Delta TE$ [226]. Cusack et al [14] advocate the use of such a 3D gradient-echo sequence over EPI because it gives a higher resolution field map and collects information in undistorted space so that there is maximum information available for any subsequent undistortion of EPI images.

There are also examples where, instead of collecting two separate image volumes, double or multiple-echo gradient-echo sequences have been used for field mapping [227], [97], [228]. This should reduce the total duration and motion-sensitivity of the technique and any $B_1$ phase errors will be eliminated because these will be constant for all the echoes and will cancel in the phase subtraction. Such techniques can also be used to estimate $T_2^*$ [228]. Further work could include writing a 3D double echo gradient-echo sequence for field mapping.

#### 5.5.4.2.3 EPI Technique

Hutton et al [192] used two EPI images acquired at different echo times (a ΔTE of 10 ms was found to be optimal for minimum field map / phase noise) and Reber et al used EPI-based field maps for distortion correction [194]. Advantages include the speed of acquisition and therefore reduced possibility of motion artifact as well as the high SNR. Also EPI has the same geometric characteristics as fMRI data if the field map is to be used for unwarping or distortion correction of such data. However data is lost if there is signal drop-out so EPI-based field maps cannot provide any information about regions in which there is severe drop-out or distortion.

#### 5.5.4.2.4 Double-DANTE Tagging Technique

A totally different technique that is not based on the phase difference methods described above is Double-DANTE-tagged imaging [229]. It uses two DANTE (Delays Alternating with Nutations for Tailored Excitation) pulse trains in the presence of orthogonal tagging gradients to label the sample with a grid of lines. The lines are displaced in the presence of field inhomogeneities giving a measure of absolute field shifts with a single image. Disadvantages of the technique are that the tag lines can be blurred where there are large field gradients and the sensitivity of the technique is limited to the change in $B_0$ field needed to shift a tag line by one pixel.

### *5.5.4.3 Field Map Acquisition*

For the purposes of determining the main magnetic field, particularly in areas where there are likely to be susceptibility artifacts, it would be counterproductive to use EPI acquisitions as these are the most vulnerable to such artifacts. For example, signal loss in EPI images would lead to a lack of information about the dropped-out regions in the field map. From this perspective it would seem that the sequence most insensitive to susceptibility artifacts (and therefore distortion and drop-out in the resultant field maps) would be the offset spin-echo sequence since the first non-offset image has no $T_2^*$ weighting at all (i.e. only pure $T_2$ weighting). However short-TE, low flip-angle gradient-echo sequences are still useful for field mapping since they do not suffer strongly from susceptibility artifacts (compared with EPI) and can be acquired much faster than the offset spin-echo images especially if implemented in 3D.

For these reasons the field map acquisitions here were made using a low flip-angle, short TE gradient-echo sequence. Since separate fat and water images were not required

here, images were acquired at two echo times. Some acquisitions were made using an offset spin-echo technique for comparison.

The phantom was put in the scanner in a realistic position. For the first acquisitions, made when the phantom did not contain any NaCl, it was placed inside a loading ring containing NaCl and doped with sufficient paramagnetic salt to shorten its $T_2$ sufficiently so that the ring did not appear in the images.

In all cases the phantom (or in later experiments the volunteer's head) was manually shimmed until the minimum linewidth was obtained. The full-width at half-maximum (FWHM) of each linewidth after shimming is shown in Table 16 and Table 17. The shims used were linear on all axes plus a quadratic shim along the scanner axis or 'z' direction.

The low flip-angle, short TE gradient-echo sequence had RF spoiling but no gradient spoiling. The flip angle was chosen empirically for approximately maximum signal given the (minimum) TR in each case. Since only the image phases are used to create the field map the actual image contrast weighting is not so important although both images are likely to have similar contrast since the only small difference between them is the TE.

The first image volume was acquired with the minimum possible echo time ($TE_1$) to ensure minimal drop-out and a good-quality image for use in masking the field map later on. The second image volume was acquired with identical parameters to the first except with echo time

$$TE_2 = TE_1 + \Delta TE$$

**Equation 97**

where $\Delta TE$ = an integer multiple of the fat-water chemical shift time = n × 1515 μs [97] assuming a differential fat-water chemical shift of 3.3 ppm at 4.7 T i.e. 1515 μs = 1/(3.3 ppm x 200 MHz). The reason for choosing $\Delta TE$ as an integer multiple of the fat-water chemical shift time is to ensure that the fat and water spins precess a whole number of $2\pi$ radians relative to each other. This means that the relative fat-water phase will be identical in both the short and long TE images. This should ensure that any phase

changes due to the chemical shift (particularly in voxels containing both fat and water) are not present as artifacts in the field map.

For the offset (asymmetric) spin-echo acquisition the first image volume was acquired with no offset (i.e. a regular spin echo) and the second image volume was acquired with identical parameters but with an offset time equal to ΔTE as described in Equation 97.

For both gradient-echo and offset-SE field mapping sequences, field maps were acquired with a few different $TE_1$ and ΔTE values. Most of the ΔTE values were shorter than the 10 ms recommended by Hutton et al [192] for GE-EPI-based field mapping and closer to the 4.34 ms [227] and 7.9 ms [228] values used previously with GE sequences. The ΔTE values were kept short to try to minimise signal drop-out in the long TE images.

The images (both phase and magnitude) were reconstructed in Matlab and an image equal to the phase difference map was saved. This phase difference was calculated from the phase of the division of the complex image data as these are equivalent:

$$\frac{e^{i\phi(TE_1)}}{e^{i\phi(TE_2)}} = e^{i[\phi(TE_1)-\phi(TE_2)]}$$

**Equation 98**

For all but the shortest choices of ΔTE the phase difference map, which forms the basis of the field map, will contain several phase wraps. This is because the phase can only take values between ± π but often evolves to far greater values than this during the ΔTE time. For this reason it is necessary to unwrap the phase in the phase difference map to create an accurate field map.

The latest 3D MR method of Jenkinson [62] called PRELUDE (Phase Region Expanding Labeller for Unwrapping Discrete Estimates from the FMRIB software library (FSL) [230], was chosen for unwrapping the phase maps.

At first the field maps were unwrapped using both PRELUDE and the method of Andersson [99] which is similar to that of Cusack [231] but later only PRELUDE was used since it was much faster (a few seconds running on a SUN UNIX machine compared with of the order of an hour running on a PC). The additional advantage of PRELUDE

(apart from computational speed) is that it uses the magnitude image as the basis for skull stripping [232] so that the field map is automatically masked to include only information from inside the brain cavity. Both mapping methods were shown to give almost identical results as corroborated by Andersson [99].

Once the field map was complete and scaled to be in units of Hertz, the maps were imported back into Matlab in order to collect statistics on the main magnetic field values inside the brain cavity (i.e. the region left after skull stripping or masking). The mean and standard deviation of the field ($\Delta B_0$) in the brain were calculated and 40-bin histograms from –400Hz to +400Hz of $\Delta B_0$ were plotted. Maps of the magnitude of the magnetic field gradient (MFG) [233] were calculated from the field maps using:

$$MFG = |\nabla B| = \sqrt{\left(\frac{\partial B}{\partial x}\right)^2 + \left(\frac{\partial B}{\partial y}\right)^2 + \left(\frac{\partial B}{\partial z}\right)^2}$$

**Equation 99**

This measure was used to summarise the likely signal loss artifacts since signal loss is dependent on the magnetic field gradients in all directions. It is similar to a $B_0$ homogeneity measure used by Wilson et al [185].

Field maps of four healthy volunteers were acquired and processed in the same way as the phantom field maps so that the field patterns could be compared.

Finally some GE-EPI images of the phantom and a volunteer were acquired with almost identical parameters to compare the susceptibility artifacts arising in each. The parameters, that were the same for both the phantom and volunteer scans, were: TE = 20 ms, FOV = 192 mm, matrix size = 64 x 64, bandwidth = 250 kHz, slice thickness = 2 mm and Nyquist ghost correction as described in section 2.12.3.1.1. These were the parameters used routinely for fMRI in this laboratory.

### *5.5.4.4 Results*

Statistics from field maps of the phantom and four volunteers are shown in Table 16 and Table 17 respectively.

| Phantom | | | | | (Hz) | | |
|---|---|---|---|---|---|---|---|
| Acquisition session | Shim: FWHM of Spectral Peak (Hz) | Sequence | $TE_1$ (μs) | ΔTE (μs) | Mean $\Delta B_0$ | Sdev $\Delta B_0$ | Comments |
| With empty eye sockets and water fill | | | | | | | |
| 1 | 14.2 | GE | 15000 | 1515 | 18.8 | 39.0 | |
| 1 | 14.2 | GE | 5800 | 1515 | 21.6 | 46.2 | See Figure 84A and D |
| 1 | 14.2 | GE | 5800 | 2000 | 20.3 | 46.3 | N.B. 2000μs ≠ fat-water separation time |
| 1 | 14.2 | GE | 5800 | 3030 | 17.0 | 45.7 | |
| 2 | 9.0 | GE | 5800 | 1515 | 8.8 | 44.4 | * GE map for subtraction – See Figure 85B and G |
| 2 | 9.0 | GE | 5800 | 6060 | 10.2 | 42.1 | |
| 2 | 9.0 | Offset SE | 15000 | 1515 | 14.9 | 48.1 | |
| 2 | 9.0 | Offset SE | 15000 | 1515 | 13.7 | 48.1 | |
| 2 | 9.0 | Offset SE | 15000 | 1515 | 15.6 | 48.5 | * SE map for subtraction – Figure 85A and F |
| 2 | 9.0 | Offset SE | 15000 | 3030 | 12.6 | 47.0 | |
| 2 | 9.0 | Offset SE | 15000 | 6060 | 10.9 | 43.0 | |
| | | Offset SE - GE | | | 4.4 | 22.8 | * SE map – GE map – Figure 85C and H |
| With wax in eye sockets and water fill | | | | | | | |
| 3 | 14.7 | GE | 5800 | 1515 | 9.3 | 38.4 | See Figure 84B and E |
| 3 | 14.7 | GE | 7315 | 1515 | 17.2 | 39.3 | |
| 3 | 14.7 | GE | 5800 | 3030 | 13.3 | 38.3 | |
| 4 | 22.8 | GE | 6300 | 4545 | -0.4 | 39.8 | |
| With all wax 'soft tissues', air spaces and $MnCl_2$-doped water fill with NaCl | | | | | | | |
| 5 | 15.4 | GE | 6500 | 4545 | 23.5 | 51.0 | Coronal Slices |
| 5 | 15.4 | GE | 6500 | 4545 | -4.8 | 51.7 | Transverse Slices See Figure 84C and F, See Figure 87A |
| 6 | 16.4 | GE | 5555 | 4545 | 0.0 | 49.6 | |
| 7 | 14.3 | GE | 4600 | 4545 | -3.3 | 48.0 | |

**Table 16 Field Map Statistics for the Phantom**

| Volunteers | | | | | (Hz) | | |
|---|---|---|---|---|---|---|---|
| Acquisition session and subject | Shim: FWHM of Spectral Peak (Hz) | Sequence | $TE_1$ (μs) | ΔTE (μs) | Mean $\Delta B_0$ | Sdev $\Delta B_0$ | Comments |
| 1A | 27.3 | GE | 6300 | 4545 | 3.7 | 47.5 | |
| 2A | 34.4 | GE | 6300 | 4545 | 1.2 | 49.4 | |
| 2A | NO SHIM | GE | 6300 | 4545 | -64.1 | 127.4 | No Shim - Figure 86A |
| 3B | 23.5 | GE | 5800 | 1515 | 9.3 | 62.2 | Figure 86B |
| 4C | 22.8 | GE | 5800 | 1515 | 21.2 | 42.6 | |
| 5C | 24.3 | GE | 5800 | 1515 | 0.0 | 41.0 | Figure 87B |
| 6D | 24.7 | GE | 5555 | 4545 | 0.0 | 54.2 | |

**Table 17 Field Map Statistics for Four Volunteers**

Example phantom and volunteer field maps and histograms are shown in the Figures below. All the field maps have the same intensity scale: white = +200Hz and black = -200Hz. The maps in each figure are shown in three orthogonal planes (transverse, coronal and sagittal) with slices in similar positions. All histograms shown have horizontal scales of –400Hz to +400Hz with bins of 20Hz width. The vertical scale is the number of voxels.

Example field maps of the phantom at different stages in its construction are shown in Figure 84. The effect of acquiring the phantom field map with the GE and SE techniques is illustrated in Figure 85. The effect of the manual shim on a volunteer field map is shown in Figure 86. The phantom field map is compared with that of a volunteer's brain in Figure 87 and the resulting MFG maps for the phantom and a volunteer are displayed in Figure 88. The GE-EPI images of the phantom and a volunteer are shown in Figure 89.

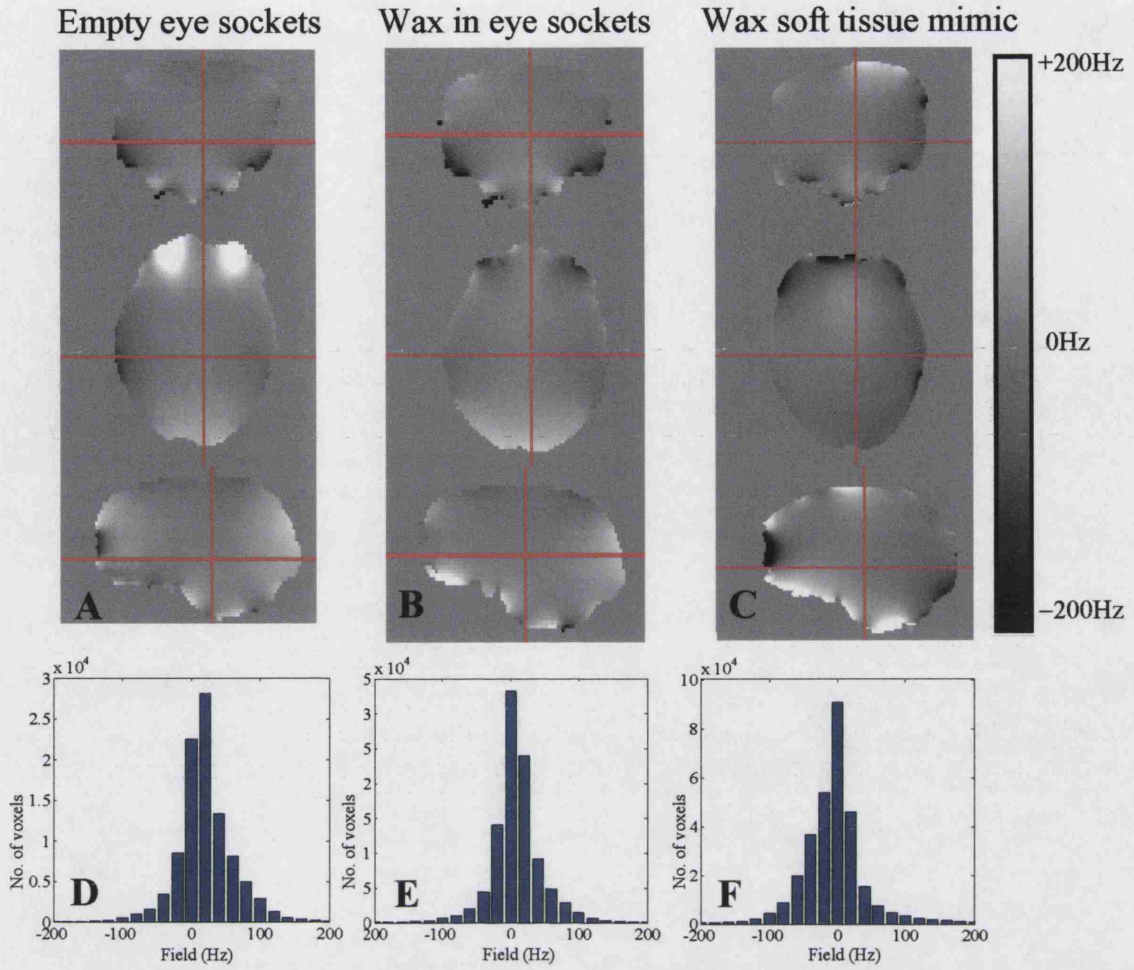


**Figure 84 Field Maps and Histograms of the Head Phantom at Different Stages in its Construction**

These maps were acquired with the parameters shown in Table 16, acquisition sessions 1, 3 and 5. Map **A** and histogram **D** show the phantom at the first stage with empty eye-sockets. The next stage of construction was to fill the eye sockets with wax and the effect of this is shown in map **B** and histogram **E**. The final phantom with soft tissues and doped and loaded fill is shown in map **C** and histogram **F**.

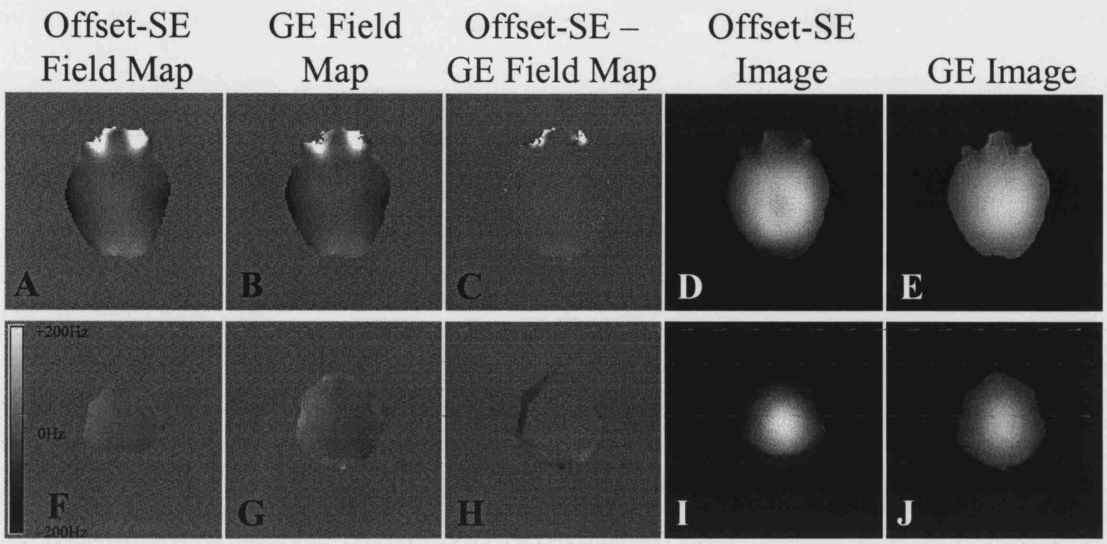


**Figure 85 Field Maps and Magnitude Images Acquired with GE and Offset SE Sequences**

These maps were acquired with the parameters shown in Table 16, acquisition session 2. The images were acquired when the phantom had empty eye sockets. The top row of images **A** to **E** are of a slice above the eye sockets and the bottom row of images **F** to **J** are of a slice near the top of the head. Images **A** and **F** are from a field map acquired using the offset SE sequence and **B** and **G** are from a field map acquired using the GE technique. Images **C** and **H** are from the subtraction of the GE map from the offset SE map i.e. **A** minus **B** and **F** minus **G** respectively. Images **D** and **I** are source (short TE) magnitude images acquired with the offset SE sequence and Images **E** and **J** are short-TE magnitude images acquired with the GE sequence.

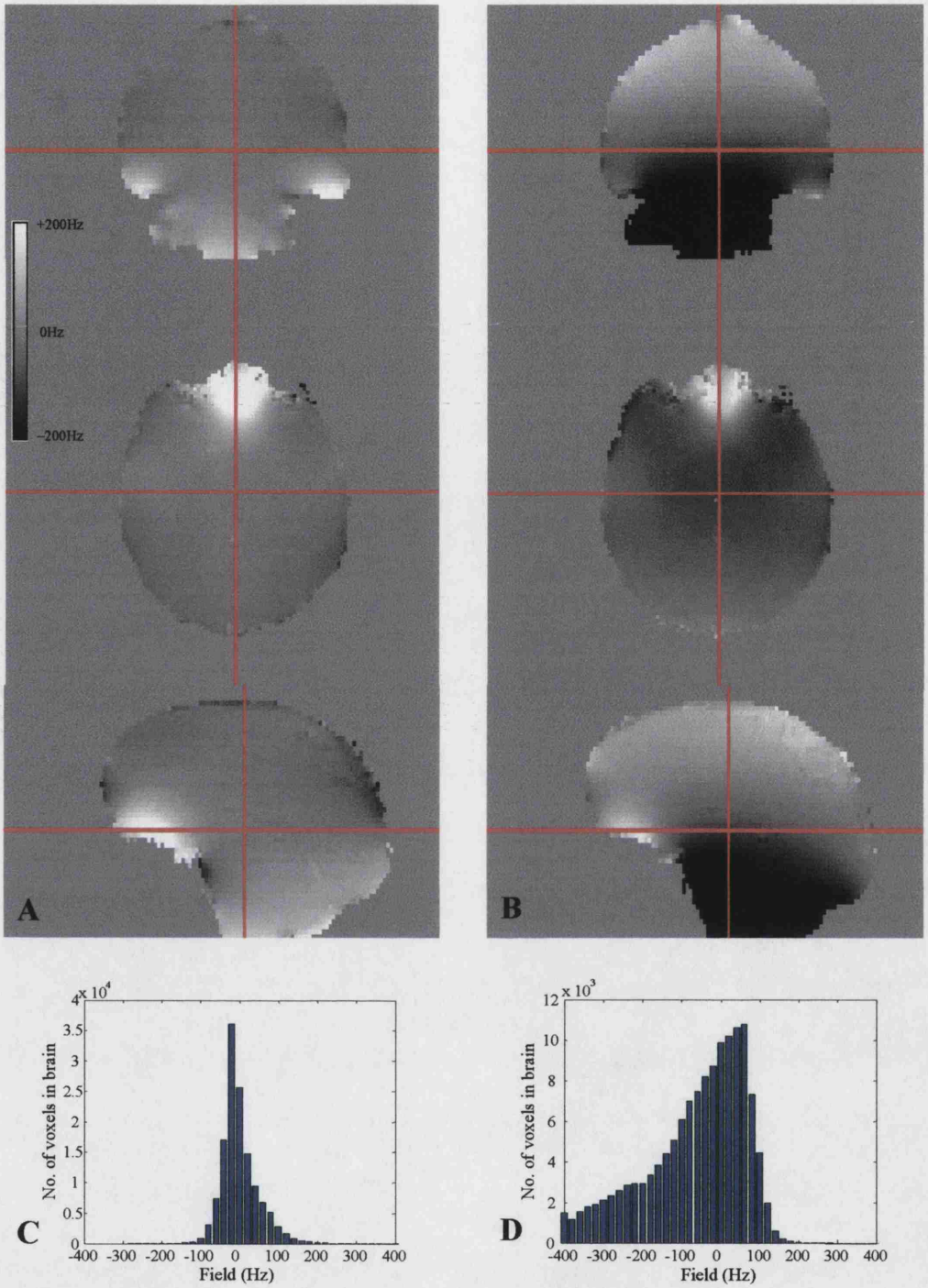


**Figure 86 Field Maps and Histograms of a Volunteer's Brain With and Without a Shim**

This map is of volunteer A and was acquired with the parameters shown in Table 17, acquisition session 2. The map in **A,** with its histogram in **C,** was acquired with a manual shim chosen to minimise the linewidth as described in section 5.5.4.3. The map in **B,** with its histogram in **D,** was acquired with no shim.

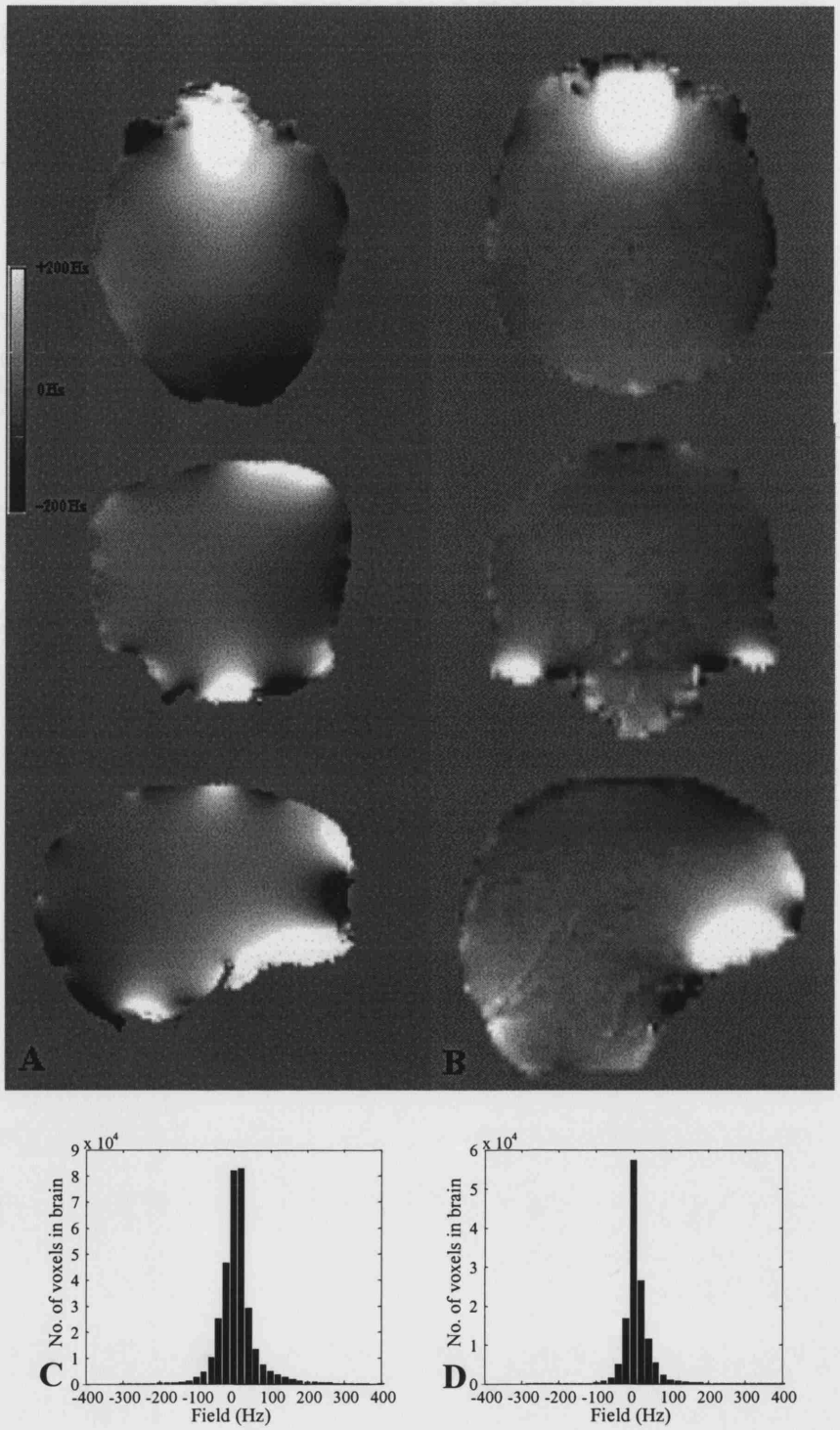


**Figure 87 Field Maps and Histograms for the Finished Phantom and a Volunteer's Brain**

The map in **A** with its histogram in **C** is of the phantom and is an average of two maps acquired in the same session, one with coronal slices and one with transverse slices. The phantom map was acquired with the parameters shown in Table 16, acquisition session 5. The map in **B** with its histogram in **D** is of volunteer C and was acquired with the parameters shown in Table 17. The volunteer map is an average of maps acquired in two different acquisition sessions (4 and 5) with one map being coregistered to the other before averaging using SPM2 software (http:// www.fil.ion.ucl.ac.uk/spm/).

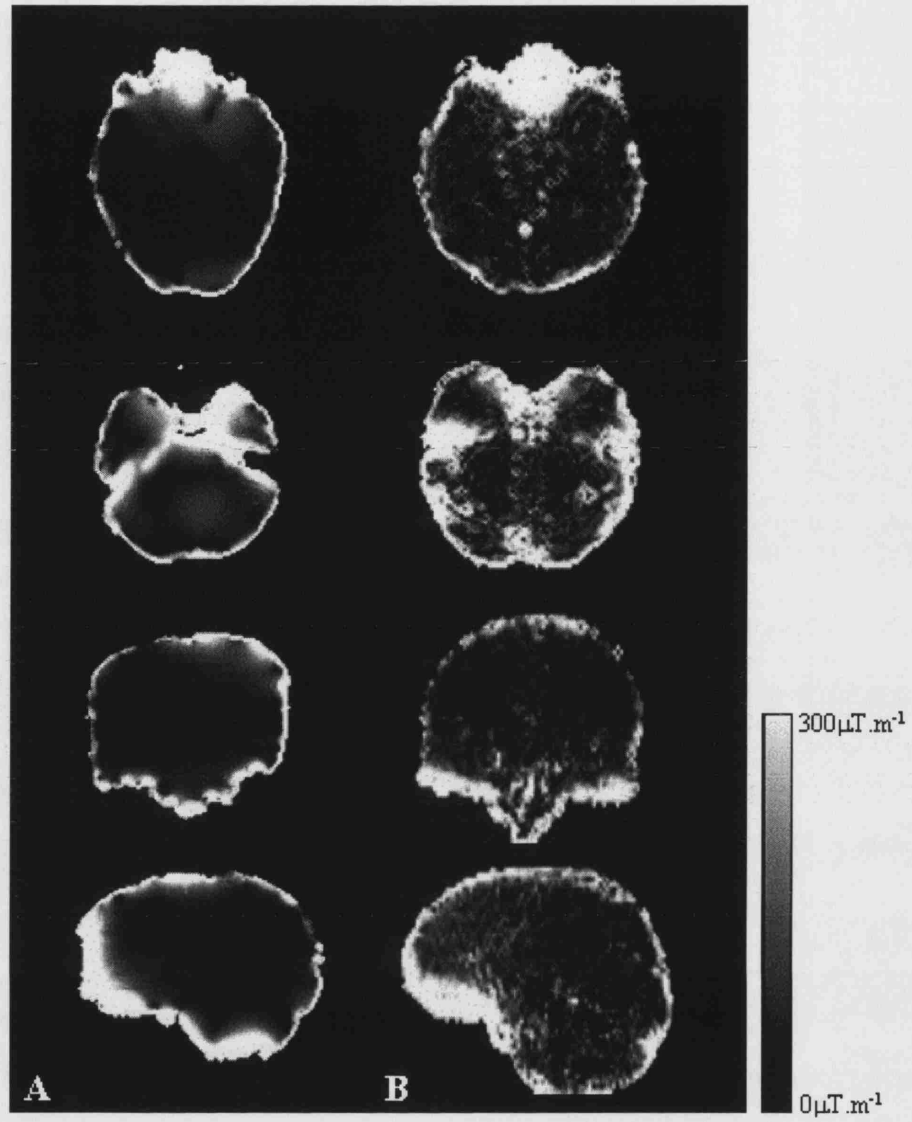


**Figure 88 Magnitude of the Magnetic Field Gradient in the Phantom and a Volunteer**

The maps were created from the field maps in Figure 87 using Equation 99. The phantom map is shown in **A** and the map in **B** is of volunteer C. The maps are scaled from 0 (black) to 300 $\mu T.m^{-1}$ (white).

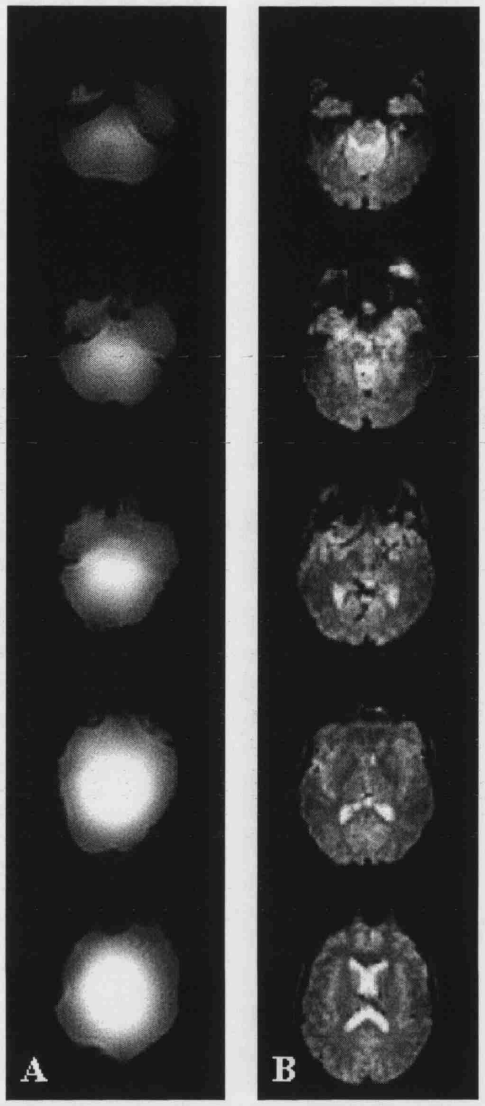


**Figure 89 GE-EPI Images of the Phantom and a Volunteer**
Some representative transverse slices from the GE-EPI scans of the phantom (**A**) and a volunteer (**B**) are shown.

## *5.5.4.5 Discussion*

### 5.5.4.5.1 Comparing Gradient-Echo and Offset-Spin-Echo Field Mapping Techniques

From Table 16 and Figure 85 we can conclude that both the gradient-echo and offset-SE techniques give reasonable, smooth and similar field maps. In addition, the subtracted field map shows that the two acquisition techniques give similar results since the mean $\Delta B_0$ is close to zero and there are few regional differences. The main cause of differences between the two methods in the phantom is the different masking (see Figure 85). The main mask differences occur near the top of the head (Figure 85F to J) because this is where the intensity drops off faster in the SE images (Figure 85I). This is because of greater $B_1$ inhomogeneity, probably due to the combined effects of two RF

pulses in the SE sequence rather than the single RF pulse in the GE sequence. This 'scraping off' of the top of the phantom's brain cavity could perhaps be alleviated by changing the masking threshold although this may lead to the inclusion of background noise voxels in some of the maps if the intensity drop-off is particularly severe.

It would be tempting to conclude that some of the differences between the SE and GE techniques in the phantom and the real head (e.g. near the eye sockets) (see Figure 85A to E) are due to signal drop-out and distortion occurring in the GE sequence but not in the SE sequence. This is partly true but some of these differences are again due to differences in the masks created from the magnitude images simply due to the difference in contrast between the two sequences (see Figure 85D compared to Figure 85E). We can therefore conclude that the offset SE sequence is most useful for collecting $\Delta B_0$ data in areas where distortion and drop-out are severe but care needs to be taken with masking because of $B_1$ inhomogeneity. The GE sequence was used for the majority of the phantom field map acquisitions and all of the volunteer acquisitions since it was so much faster than the offset SE sequence.

#### 5.5.4.5.2 Factors Affecting the Field Maps

It is clear from the maps and histograms in Figure 86 and Table 17 that the presence or absence of the manual shim has the largest effect of all on the field maps. The mean $\Delta B_0$ is negative and has a much greater magnitude and the field variation (SD $\Delta B_0$) is over two and a half times greater in the unshimmed map than with the shim. The measurements here were made in the presence of a shim since this is closest to the real situation: before acquiring images shimming is routinely used to remove the large, global field variations seen in Figure 86B. It is obvious from Figure 86A that shimming (at least with the low order shims used here) does not remove the magnetic field inhomogeneities resulting from the air spaces and hence these are responsible for most of the susceptibility artifacts commonly observed in images acquired with a shim (see Figure 49).

Since the shimming was performed manually it is possible that the shims were not particularly consistent or reproducible between sessions. In this way some of the differences between the field maps may have arisen due to shim differences but this is unlikely since the shim quality did not vary too greatly between sessions or subjects as

indicated by the relatively similar FWHM of the spectral peaks and by inspection of the field maps. As mentioned, even though the shims may have varied, they were only relatively low order (linear on all axes plus quadratic in the 'z' direction) and were therefore unlikely to be able to remove or affect the spatially localised $\Delta B_0$ patterns due to the air spaces as evidenced by Figure 86, Figure 84 and Figure 87. The shims obtained here do appear to be relatively consistent. However, an automated shimming technique (as is standard on most clinical scanners) would be useful to improve the precision and reproducibility of future field map acquisitions. An example of a technique for automated shimming is one based on a field map acquisition [185] followed by brain segmentation and automated $B_0$ optimisation.

In order to estimate the inherent variability associated with using the offset-SE acquisition technique we can compare field maps acquired with identical parameters (See Table 16). It seems that the standard deviation of $\Delta B_0$ over the brain cavity is the most reproducible global measure from the field map, followed by the mean $\Delta B_0$, which differs by less than 2 Hz or 0.01 ppm.

From studying phantom field maps and derived histograms and statistics there appears to be no strong effect of $\Delta TE$ on the offset-SE acquired maps. It is possible that increasing $\Delta TE$ from 1515 to 6060 μs leads to a slight decrease in the mean and standard deviation of $\Delta B_0$ but the changes are so small as to be negligible.

The field maps from phantom acquisitions 1 and 3 are mostly similar (Table 16) so there is no evidence for any strong effect of $\Delta TE$ on the gradient-echo data for the range of $\Delta TE$ used here. However Hutton et al [192] did show that (for their EPI-based field mapping technique) the signal-to-noise ratio in the acquired phase maps does increase with increasing echo-time difference or $\Delta TE$. They suggested an optimum of $\Delta TE = 10$ ms to increase SNR whilst minimising the unwrapping required. With gradient-echo-based field maps a compromise must be reached between minimal distortion and drop-out and maximum SNR in the field map.

The standard deviation of the field map acquired with a long $TE_1$ (Equation 97) of 15 ms is slightly decreased relative to the maps acquired with shorter $TE_1$ values and this

could be because of increased drop-out, leading to a slightly smaller map. It is worth emphasising that the map summary statistics included in Table 16 and Table 17 are not the most informative for assessing map similarity; as we have seen when comparing GE and SE field maps, it is necessary to compare the full 3D whole brain field maps to gain a full picture of any regional variations.

Since position and orientation within the magnet influences field maps, the phantom should ideally be placed in the same position and orientation when acquiring maps and testing various sequences. Reproducible phantom positioning could be ensured in future by placing fiducial marks on the phantom and the scanner head rest and aligning them each time the phantom is placed in the scanner.

#### 5.5.4.5.3 Comparing Field Maps of the Head Phantom with Volunteer Maps: How Realistic is the Phantom?

Now with confidence in the reliability of the field mapping technique, it is possible to discuss how well the phantom approximates the real head by comparing the field maps and statistics. Before comparing the final phantom with the volunteer maps, it is interesting to assess the effect of the various phantom components on its field map (Figure 84). It is clear from Figure 84A that the presence of the empty eye sockets leads to a large positive $\Delta B_0$ above them. Since these were not observed in volunteer field maps (Figure 87B) it was necessary to fill the eye sockets with wax. Figure 84B shows that this removed the bright high $\Delta B_0$ areas and made the phantom field map look more realistic in this area. However the main discrepancy between this intermediate phantom map and the volunteer field maps was the absence of large positive $\Delta B_0$ above the nasal cavity. This did start to appear in the phantom once the eye sockets had been filled but did not extend high or deep enough into the brain. This was probably due to the lack of soft tissue mimicking material below the brain. Figure 84C and Figure 87A show that the addition of soft-tissue-mimicking wax and the retention of air spaces in the final phantom introduced a realistic region of large positive $\Delta B_0$ above the nasal cavity.

Comparing Figure 84D, E and F, we see that the histograms for the phantom do not change dramatically as its construction progressed. This reflects the fact that even the initial phantom with the empty eye sockets had magnetic field inhomogeneities of a realistic magnitude and size but from Figure 84A, it is clear that they are not in anatomically realistic locations. From Figure 84 and Figure 87 we learn that the air

spaces need not only to be realistically shaped but also to be present in the correct locations within a matrix of diamagnetic tissue in order for the field pattern to begin to be similar to that of the head.

The field maps of the volunteers differed slightly (see Figure 86A and Figure 87B) probably due to differing anatomy and shims. However the volunteer maps showed many similar features that are well-known [187], [192]. These familiar features include a large positive $\Delta B_0$ area above the nasal air sinuses (including the sphenoidal and ethmoidal sinuses) in the region of the inferior frontal lobe of the brain. Further familiar field variations are the bright regions in the inferior temporal lobes corresponding to areas above the mastoid air cells and auditory canals. The frontal sinuses also cause small areas of low and then high field in their vicinity. Another feature volunteer maps have in common is the reduced field near the front of the head in lower slices in the region behind the nasopharyngeal air spaces.

Comparing the final phantom statistics in Table 16 with the volunteer field map statistics in Table 17 we can see that the phantom has a similar range of field values. However, as we have seen, the field map statistics are not sufficient measures of map similarity and it is important to compare the 3D whole-brain field maps (see Figure 87). Figure 87A and B show many similarities including a higher-field region above the nasal air spaces, a lower-field region behind the frontal sinuses and a similar field pattern near the auditory air spaces. However there remain some differences between the phantom and volunteer field maps. For example there is a higher-field region in the phantom at the base of the brain (Figure 87A and Figure 84C) above the large rubber bung due to the reduced susceptibility of rubber compared with wax. This bung could be replaced with wax in future versions of the phantom.

An additional difference between the phantom and volunteer maps in Figure 87 is the much larger relative extent of the bright and dark regions associated with the frontal sinus air space. This is because the bubble in the phantom brain cavity provided an air space that was much bigger than real frontal sinuses. The field pattern could be improved by adding more fill solution to the phantom. Alternatively future versions of the phantom could have a fixed air pocket (e.g. a sealed length of silicon tubing) stuck to the inside of the brain cavity before sealing to mimic the frontal sinus instead of a

bubble. As well as being more realistically sized and shaped, this would have the additional advantage of having a fixed position in the phantom, independent of the phantom's orientation. Figure 84 and Figure 87 show that the small amounts of silicone sealant and other materials used in the phantom construction did not have any significant effects on the field maps.

The similarity of the phantom and volunteer field maps suggests that they will suffer from similar susceptibility artifacts and further evidence for this is provided by the similarity of maps of the magnitude of the magnetic field gradients (MFG) in the phantom and a volunteer (see Figure 88). The MFG maps show the same sort of similarities and differences described for the field maps but the effect of the rubber bung is highlighted in the phantom MFG map. The volunteer MFG map appears more 'grainy' than the phantom map and this is probably because the volunteer field map was acquired with a much greater voxel size (2 x 2 x 3 mm) compared with 1.5 x 1.5 x 1.5 mm for the phantom field map. The real brain also contains many different tissue types and blood vessels, which can contribute small magnetic field gradients that are not present in the homogeneous phantom.

In fact from Figure 89 it appears that the GE-EPI images of the phantom and a volunteer do suffer from similar susceptibility artifacts. For example there are similar areas of signal drop-out in both the phantom and volunteer images around the nasal and auditory airspaces particularly in the lower slices of Figure 89. Similar distortions are also visible in the images. The distortions and areas of drop-out due to the large bubble in the phantom are larger than those due to the frontal sinus in the real brain as expected from the field maps.

## 5.5.5 Further Work

There is work that could be done in future to further evaluate the phantom and potentially improve it.

### *5.5.5.1 Phantom $T_1$ and $T_2$*

In future it could be useful to map $T_2^*$ [234] in the phantom and in volunteers to verify whether the combination of the $T_2$ and field inhomogeneities in the phantom lead to similar $T_2^*$ values to those *in vivo*.

If accurate $T_1$ and $T_2$ values are required, appropriate gel and dopant concentrations could be chosen for the phantom fill. It could be possible to create compartments of different contrast in future versions of the phantom.

### 5.5.5.2 Phantom $B_1$ distribution

In future, sucrose could be added as well as NaCl in an attempt to achieve identical permittivity and conductivity in the phantom and head. If $\sigma$, $\varepsilon$ and dimensions were matched [218] then the coil loading would be expected to be similar as well. In order to choose the appropriate concentrations of sucrose and NaCl it would be necessary to make many empirical measurements over a range of combined concentrations since the effects of the two substances on $\sigma$ and $\varepsilon$ are not independent [218].

In fact, it may be more useful in future not to try to mimic the $B_1$ distribution in the real head since image inhomogeneity due to $B_1$ effects may confound the assessment of susceptibility-induced artifacts, which after all was the main aim here. Future phantoms could be constructed with the aim of creating as uniform a $B_1$ distribution in the phantom as possible to ensure that any image non-uniformities arise only from the susceptibility effects. One way of creating a highly uniform $B_1$ field is to use silicone oil (polydimethylsiloxane – PDMS) to fill the phantom [60], [235] although the $T_1$ and $T_2$ would then need to be varied by altering the viscosity rather than by doping with paramagnetic salts. Silicone oil would be appropriate since it has a very low dielectric constant (approximately 2.8 [236]) and a magnetic susceptibility ( $-8.27 \times 10^{-9}$ $m^3.kg^{-1}$ [236]) not dissimilar from that of water.

### 5.5.5.3 Field mapping and Assessment of Susceptibility Artifacts

In future field mapping experiments it could be possible to differentiate the intrinsic $B_0$ inhomogeneity of the system from the susceptibility effects of the sample. To do this it would be necessary to acquire additional field maps in the presence of large, highly homogenous phantoms. However the $B_0$ inhomogeneity of the system is always present and is negligible when compared with the sample-geometry and susceptibility-dependent effects of interest here.

It would be desirable to acquire field maps for more volunteers to look at the effect of anatomical variation as well as position within the magnet and shim. It is well established that position makes a difference to field map; for example Truong [200] and Heberlein [237] found that tilting the head back reduced the field differences above the nasal cavities. It may be possible to coregister the magnitude images of different volunteers (using SPM (http://www.fil.ion.ucl.ac.uk/spm/) software used to coregister structural and functional scans in fMRI) and use the resulting transforms to coregister the field maps. This may make it easier to compare field maps and may even make it possible to calculate a 'mean' field map over several volunteers perhaps by coregistering all the maps [238].

The MFG maps help to highlight regions in which distortions and signal loss artifacts are likely to be severe as seen in the GE-EPI images. It would also be useful to acquire images with a range of TE values and slice thicknesses and with different sequences such as SE-EPI, which, unlike GE-EPI, is expected to suffer from distortion only.

In order to extend the qualitative comparison between the phantom and volunteer images performed here it could be possible to quantify the extent and severity of distortion and drop-out artifacts. Examples of such quantitation methods include those of Wilson et al [186] who made regional measures of the mean and standard deviation of $\Delta B_0$ in field maps inside a mask of the inferior frontal cortex. The mask was created by calculating the region inside which voxels experienced a signal loss greater than 25%. To calculate the signal loss inside dropped-out regions of EPI images, an 'ideal' tissue-segmented image was derived from each subject's $T_1$-weighted structural scan. Alternatively, Ojemann [239] quantified the severity and extent of signal loss artifacts by normalising all the EPI images to have a signal mode of 1000 and then calculating signal loss in percentage units as 1/10 the difference between the normalised pixel value and 1000.

### *5.5.5.4 Modifications of the Phantom*

Modifying the phantom slightly could broaden its utility beyond the applications suggested so far. For example, metabolites could be added in known concentrations so that the effect of susceptibility and various shimming techniques could be assessed in MR spectroscopy. A variable-current-carrying wire could be added to the phantom to

generate small magnetic field changes of a similar magnitude to those measured in fMRI experiments so that fMRI techniques could be compared.

## 5.6 Conclusions

An anthropomorphic head phantom has been successfully designed and constructed using materials of appropriate magnetic susceptibility and air spaces of realistic dimensions. As well as having a similar range of field values, $B_0$ field maps of the phantom and the brains of volunteers show many similarities including a higher-field region above the nasal air spaces, a lower-field region behind the frontal sinuses and a similar field pattern near the auditory air spaces. There remain some minor differences between the phantom and volunteer field maps, which could be reduced by improved phantom design.

Since it has a similar magnetic field pattern, the phantom suffers from similar susceptibility artifacts to real heads and will therefore be useful for evaluating and comparing different susceptibility artifact reduction techniques (see section 6 below). The phantom has relaxation times that are similar to those of brain grey and white matter at this field strength, making it useful for testing sequences before they are applied *in vivo*.

Because the materials in the phantom were selected on the basis of their magnetic susceptibilities, the phantom could in principle be used at any field strength to provide anatomically realistic field inhomogeneities and susceptibility artifacts (see Equation 35). The only factor that may need modification for different field strengths is the fill material since the variation with field strength of brain relaxation times is likely to be different from that of the phantom fill materials.

The phantom could also be a useful tool to test CT-MRI coregistration in the presence of susceptibility artifacts since the water-filled brain cavity is both CT and MR visible.

# 6 USING THE ANTHROPOMORPHIC HEAD PHANTOM TO EVALUATE DROP-OUT REDUCTION IN GRADIENT-ECHO IMAGING WITH HYPERBOLIC SECANT EXCITATION PULSES

Once the anthropomorphic phantom had been developed and evaluated, it was used to test a drop-out reduction technique based on using Hyperbolic Secant (HS) Pulses for excitation in gradient-echo imaging.

## 6.1 Background Theory and Simulations

Previous work [240] (and see Chapter 3) has shown that HS pulses applied for slice-selective 90° excitation (and 180° refocusing) lead to a quadratic phase variation through the slice. This property can be harnessed to help retrieve signal that has dropped-out due to through-slice susceptibility gradient dephasing (see section 2.12.3.3) in gradient-echo images.

Cho and Ro [13] first suggested the use of an RF pulse tailored to provide a quadratic phase distribution in the selected slice to recover 'dropped-out' signal. Both the functional form and design method of the pulse were undefined in their original paper [13]. However they described the principle of signal recovery, which is illustrated in Figure 90.

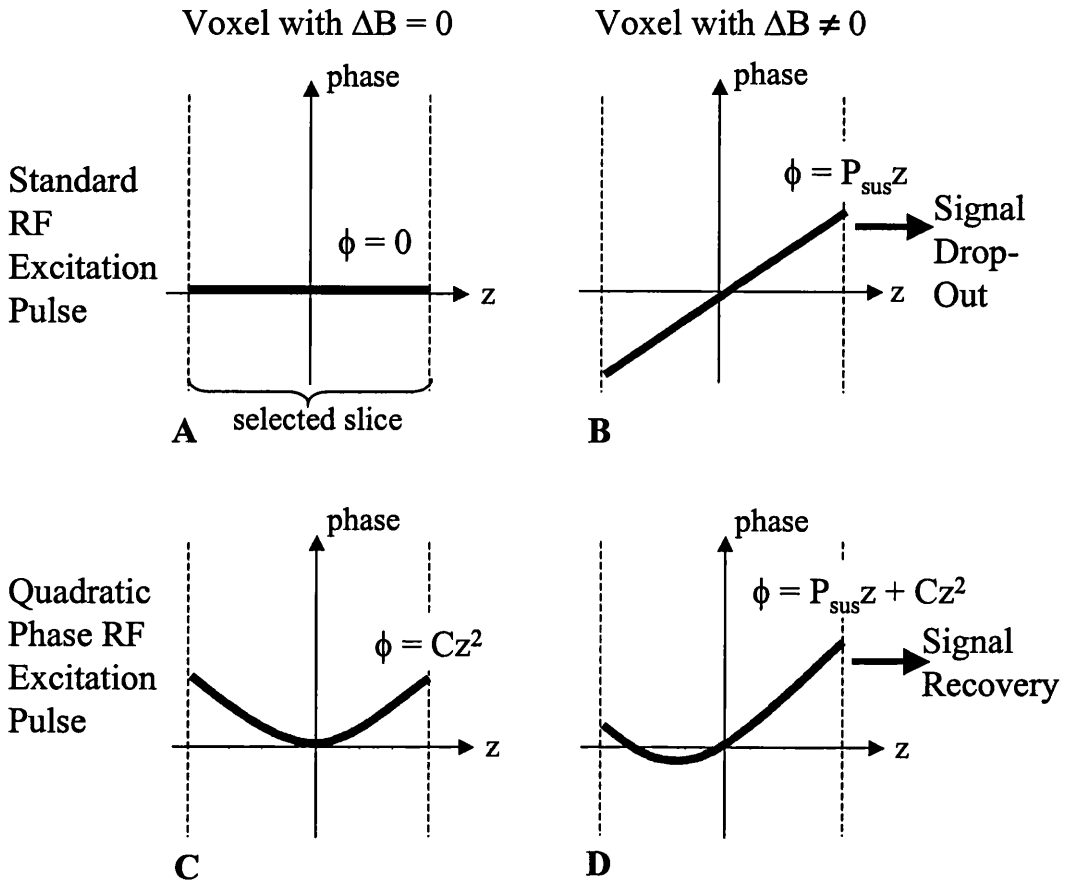


**Figure 90 Schematic Illustration of Signal Drop-Out and Recovery with a Quadratic Phase RF pulse**

The phase distribution of the spins in a voxel is shown in the ideal case in which there is no $B_0$ inhomogeneity (**A**) and when a strong susceptibility-induced field gradient exists (**B**). The phase distribution of the spins in a voxel is shown when a quadratic phase RF pulse is added onto a voxel with a homogenous field (**C**) and when this quadratic phase distribution from the RF pulse is superimposed onto a voxel where there is a strong linear field gradient due to susceptibility differences (**D**). In each case the phase ($\phi$) is related to the susceptibility phase gradient ($P_{sus}$) and the RF pulse quadratic phase coefficient (C).

Ordinarily, any through-slice $B_0$ field gradient, which may arise due to susceptibility differences and is assumed linear in this case, will cause signal loss because it results in phase dispersion across the voxel (Figure 90B). The idea of this signal recovery technique (Figure 90D) is that the quadratic phase distribution from the HS RF pulse approximately cancels the phase variation induced by susceptibility differences in at least part of the slice. Therefore the signal in one side of the slice has very little net phase dispersion so that the signal from the voxel is no longer completely dephased and does not drop out entirely. This method assumes that the phase dispersion within the slice is linearly proportional to the position along the slice thickness direction and that

there are no susceptibility differences causing phase dispersion in any other direction apart from the slice select direction.

The effect of the relative size of the susceptibility phase gradient ($P_{sus}$) and the RF pulse quadratic phase coefficient (C) on the signal in the voxel (S) can be obtained if the total signal is described as the sum of the real (R) and imaginary (I) components of the magnetisation in a voxel:

$$S = \sqrt{R^2 + I^2}$$

**Equation 100**

The phase dispersion modulates both real and imaginary components and is a function of slice thickness ($z_0$) so R and I can be written:

$$R = \int_{-\frac{z_0}{2}}^{\frac{z_0}{2}} M_0 \cos\phi(z) dz$$

**Equation 101**

$$I = \int_{-\frac{z_0}{2}}^{\frac{z_0}{2}} M_0 \sin\phi(z) dz$$

**Equation 102**

where $\phi$ is the phase as a function of position within the slice (z). In Figure 90D there is an equation for the phase distribution $\phi(z)$, which we can combine with Equation 100, Equation 101 and Equation 102 to yield a final expression for the total signal in terms of $P_{sus}$ and C:

$$S = \sqrt{\left\{\int_{\frac{-z_0}{2}}^{\frac{z_0}{2}} M_0 \cos\left(Cz^2 + P_{sus} z\right) dz\right\}^2 + \left\{\int_{\frac{-z_0}{2}}^{\frac{z_0}{2}} M_0 \sin\left(Cz^2 + P_{sus} z\right) dz\right\}^2}$$

**Equation 103**

The idea here was to use a scaled-down Hyperbolic Secant (HS) full passage RF pulse for 90° excitation, to produce the desired quadratic phase variation across the slice. It has been shown (Chapter 3) that the quadratic phase coefficient C can be selected by choosing the HS pulse parameters such as $\mu$.

Simulations using Equation 103 were carried out to investigate the expected degree of signal recovery for pulses with different quadratic phase coefficients and the results are illustrated in Figure 91.

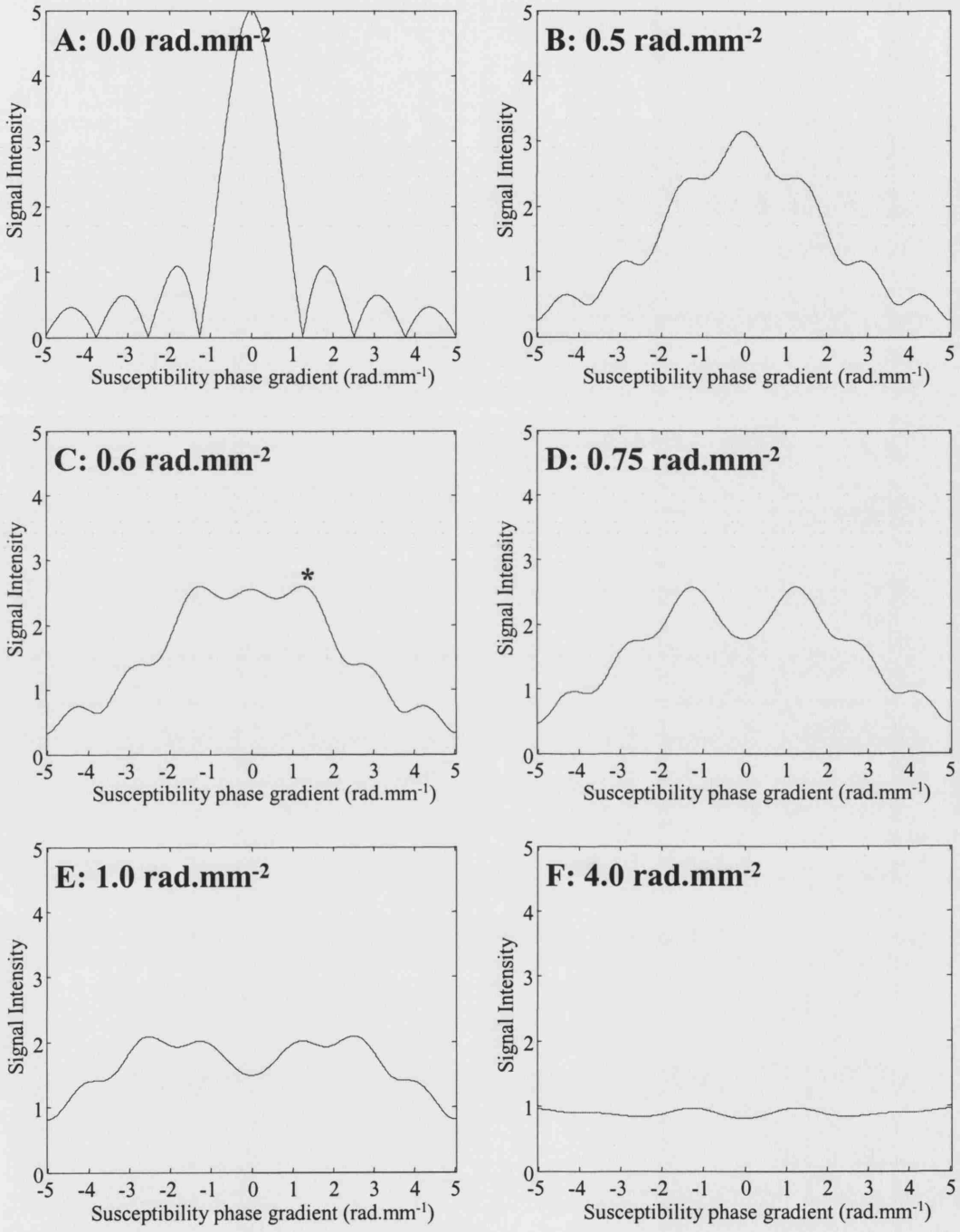


**Figure 91 Results of Simulations of Signal Intensity as a Function of Susceptibility Phase Gradient for Different RF Pulse Quadratic Phase Coefficients**

The graphs show signal intensity (a maximum of 5 for a slice thickness of 5 mm) as a function of susceptibility phase gradient ($P_{sus}$) obtained using Equation 103 with RF pulse quadratic phase coefficients (C in rad.mm$^{-2}$) of 0 (**A**), 0.5 (**B**), 0.6 (**C**), 0.75 (**D**), 1.0 (**E**) and 4.0 (**F**). The $P_{sus} = 0$ point in **A** has a phase distribution as shown in Figure 90A. Other points in **A** have phase distributions as in Figure 90B. The $P_{sus} = 0$ point in **B** to **F** has a phase distribution as shown in Figure 90C. Other points such as the point marked with a * in C will have a phase distribution as illustrated in Figure 90D.

Figure 91 illustrates the degree of signal recovery to be expected for different values of $P_{sus}$ and C. As an illustration of the principle, consider the point marked with a * in Figure 91C and the corresponding point with an equal $P_{sus}$ in Figure 91A. In Figure 91C there is much more signal at * than in Figure 91A where the signal is zero because the susceptibility phase gradient is sufficient to cause a $2\pi$ phase dispersion across the voxel, leading to total destructive interference or signal drop-out. It is clear from Figure 91 that the signal recovery comes at the expense of overall signal in regions where $P_{sus} = 0$. Figure 91 also shows that, as the quadratic phase coefficient increases, so does the breadth of the signal curve. However the signal intensity at $P_{sus} = 0$ decreases with increasing quadratic phase coefficient and is not always the maximum value. This means that there will be a trade-off between the range of susceptibility gradients for which signal can be retrieved and the signal intensity (SNR) in areas where there is little field inhomogeneity. Figure 91C is most similar to the graph in Cho and Ro's original paper [13].

Further simulations with different slice thicknesses showed that the quadratic phase coefficient required for the same level and range of signal retrieval is directly proportional to $1/z_0^2$ where $z_0$ is the slice thickness. This means that the thinner the slice, the greater the quadratic phase coefficient required for a given level of signal retrieval (for the same range of $P_{sus}$).

For a gradient-echo sequence of echo time TE, the through-slice phase difference $\Delta\phi$ accumulated across a voxel of slice thickness $z_0$ is given by

$$\Delta\phi = \gamma z_0 \frac{\partial B_z}{\partial z} TE$$

**Equation 104**

where $\partial B_z/\partial z$ is the partial derivative of the magnetic field in the slice-select direction. This means that $P_{sus}$ is given by

$$P_{sus} = \gamma \frac{\partial B_z}{\partial z} TE$$

**Equation 105**

and should in theory allow the relative signal in every voxel to be predicted for a given TE and C given the $B_0$ field map of an object using Equation 103 and Equation 105.

## 6.2 Methods

### 6.2.1 Preliminary experiments with GE sequences

The anthropomorphic head phantom (at the first stage of construction with empty eye sockets) was scanned with a standard short TE GE imaging sequence (flip angle = 48°, TE = 4.7 ms, TR = 950 ms, slice thickness = 2 mm, slice separation = 3 mm, RF spoiling only, in-plane voxel size = 1.5 mm x 1.5 mm). This image was acquired as a reference with minimal drop-out due to the thin slice and short TE. The phantom was then scanned with a long-TR and long TE gradient-echo technique so that a full 90° pulse could be used without compromising the signal and to increase the drop-out observed (flip angle = 90°, TE = 30 ms, TR = 5000 ms, slice thickness and separation = 3 mm, RF spoiling only, in-plane voxel size = 2 x 2 mm). The slice thickness was also increased from those in the original short TE image so that substantial regions of signal loss appeared in the long-TR gradient-echo image. An increase in slice thickness for a given TE is expected to lead to greater signal loss because there is more probability that the through-plane field inhomogeneities will be strong enough to lead to total dephasing within the thicker slice.

Firstly a standard 5-lobe (4 ms, 1.5 kHz bandwidth) Sinc-shaped pulse was used for 90° excitation. Images were then acquired with identical parameters but using two different Hyperbolic Secant (HS) 90° pulses both with duration = 8.8 ms and bandwidth = 4 kHz. The two HS pulses had $\mu = 8$ and $C = 1.96$ rad.mm$^{-2}$ and $\mu = 16$ and $C = 3.92$ rad.mm$^{-2}$ and had been calibrated for 90° excitation using the method described in section 3.3.1.2.

### 6.2.2 Signal Recovery in GE-EPI sequences

To investigate how this method for signal recovery fared in the presence of both drop-out and distortion in GE-EPI sequences such as those commonly used for fMRI acquisitions, GE-EPI images were acquired with both standard Sinc-90° RF pulses and a variety of HS-90° pulses. SE images were acquired, with the same slices, FOV and resolution as the GE-EPI images, as reference images of the completed phantom with no susceptibility-induced drop-out or distortion. The HS90° pulse parameters and corresponding echo times (TE) are given in Table 18. Remaining GE-EPI parameters were: TR = 6 s, FOV = 192 mm, matrix size = 64 x 64, bandwidth = 250 kHz, slice thickness and separation = 3 mm and Nyquist ghost correction as described in section

2.12.3.1.1. A field map was also acquired as described in section 5.5.4.3 with parameters for acquisition no. 7 in Table 16. The field map had the same FOV, resolution and slices as the SE and GE-EPI images so that all the image data sets could be co-registered.

The field map was then used with Equation 103 and Equation 105 implemented in Matlab to predict the relative signal intensities in the HS-90° images compared with the standard (C=0) images. Measured and simulated ratio maps were created to evaluate the extent of signal recovery (and loss) by dividing the HS90° images by the standard (Sinc-90°) images. A region of interest (ROI) was drawn on the same slice of the measured and simulated ratio maps (see Figure 92) and the resulting measured and simulated ROI mean signal ratios were compared.

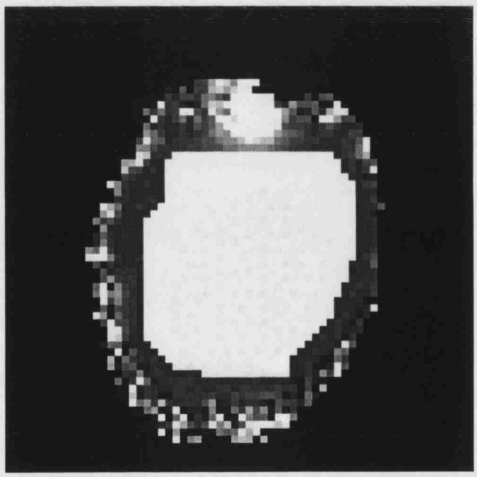

**Figure 92 ROI on A Transverse Slice of A HS90°/Sinc90° GE-EPI Signal Ratio Map**
The region of interest (white) (ROI) placed in an area of almost homogenous magnetic field on a transverse slice of the signal ratio map formed by dividing a GE-EPI image acquired with a HS90° pulse by a standard GE-EPI image acquired with a sinc90° pulse. The underlying ratio map was formed from a GE-EPI image acquired with the HS pulse with C = 3.75 rad.mm$^{-2}$. The mean values from the same ROI placed on a range of ratio maps are shown in Table 18.

## 6.3 Results

### 6.3.1 Preliminary experiments with GE sequences

The resulting images are shown in Figure 93. In Figure 93B to D the image intensities are all on the same scale whilst in Figure 93F to H they have been altered to emphasise the regions of drop-out.

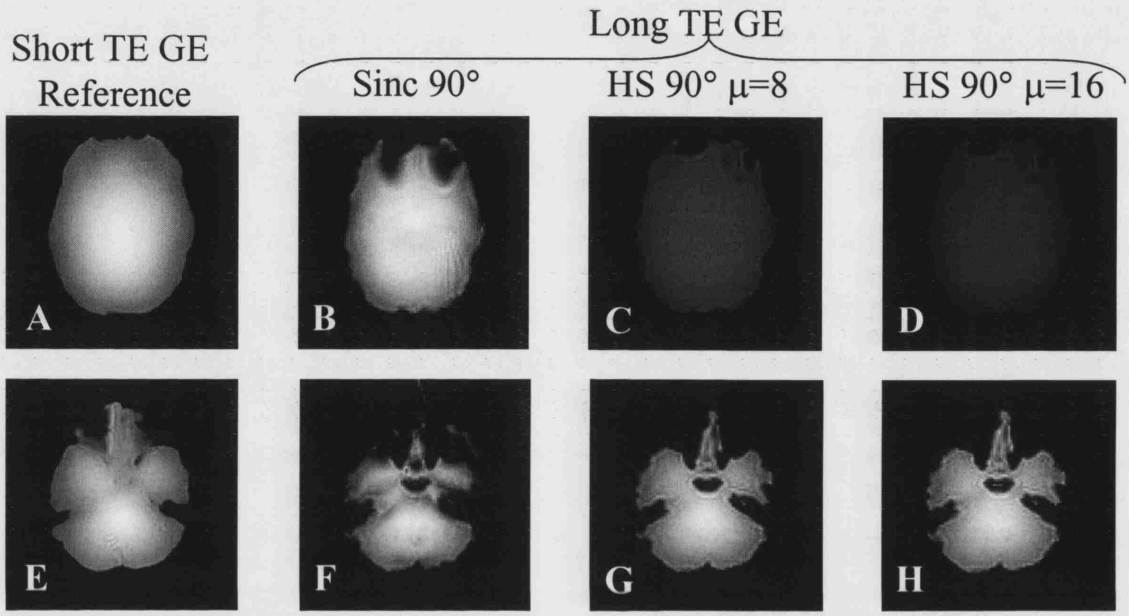


**Figure 93 GE Images of the Head Phantom Showing Signal Drop-Out Correction**
Transverse images of an upper slice (**A** to **D**) and a lower slice (**E** to **H**) in the anthropomorphic head phantom are shown. Images **A** and **E** were acquired with the short TE GE sequence as a reference with minimal drop-out and the rest of the images were acquired with the long TE gradient-echo sequence, with the conventional Sinc pulse (**B** and **F**), the HS-90° pulse ($\mu$=8, C = 1.96 rad.mm$^{-2}$) (**C** and **G**) and the HS-90° pulse ($\mu$=16, C = 3.92 rad.mm$^{-2}$) (**D** and **H**). The intensities of the long TE images in the top row (**B** to **D**) are on the same intensity scale to show the reduction in overall SNR associated with using the HS excitation pulses. The intensities of the corresponding images on the bottom row (**F** to **H**) have been adjusted independently to make all the images appear with similar brightness. The phantom was at an early stage in its construction with empty eye sockets and no soft-tissue-mimicking material.

## 6.3.2 Signal Recovery in GE-EPI sequences

The results of the experiments are shown in Figure 94, Figure 95 and Table 18.

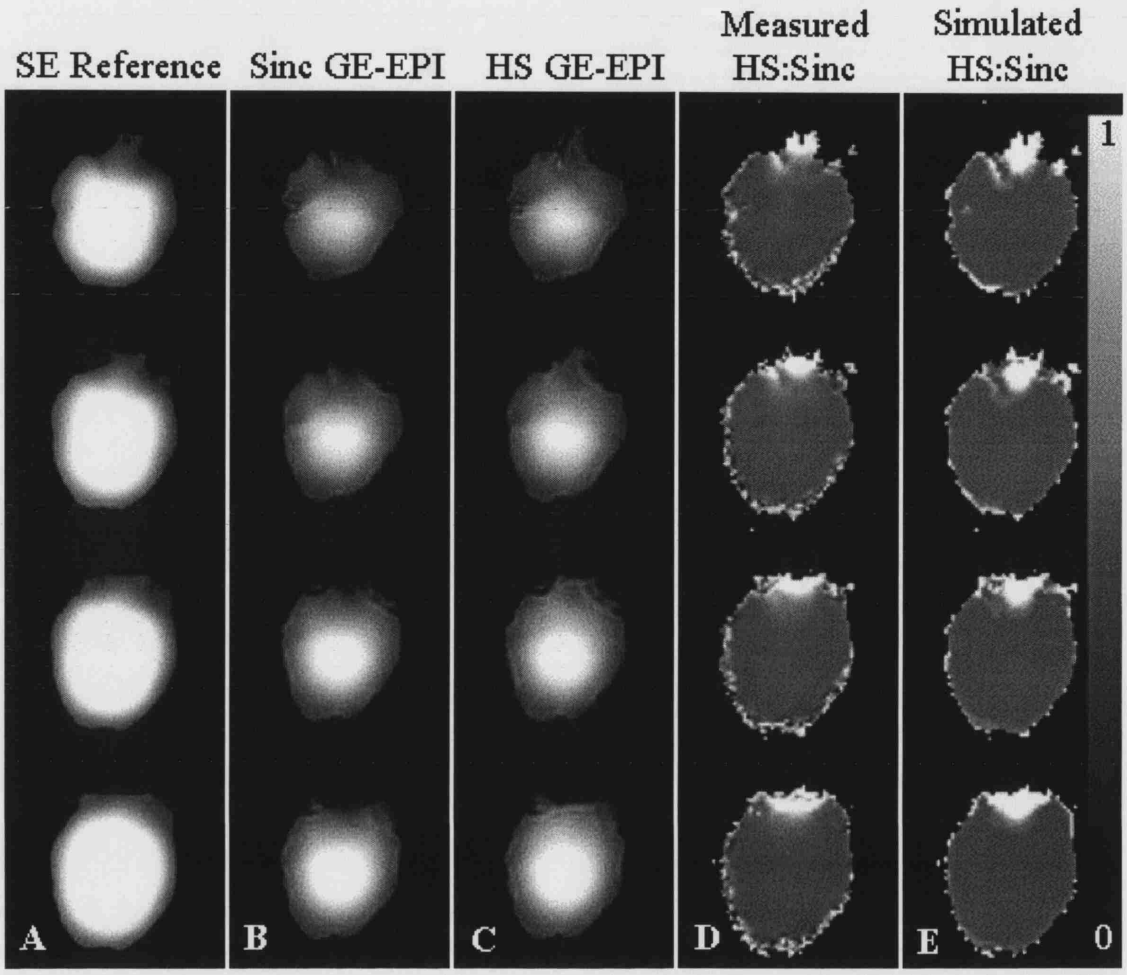


**Figure 94 Measured and Simulated Results for GE-EPI Signal Recovery with C = 1.67 rad.mm$^{-2}$**

Transverse images of four contiguous slices of the anthropomorphic head phantom are shown. The first column (**A**) shows SE reference images with no distortion or drop-out. The second column (**B**) shows standard GE-EPI images and the third column (**C**) shows GE-EPI images acquired with a HS90° excitation pulse to recover signal. These two columns of images have their intensities scaled independently to emphasise the signal recovery. The fourth column (**D**) is the ratio of images **C** to **B** masked with the short-TE GE image used for the field map. The fifth column (**E**) is the ratio of HS90° to standard simulated signals predicted from the field map using Equation 103 and Equation 105 and masked with the short-TE field map GE image. Columns **D** and **E** have intensities scaled between zero (black) and 1 (white). The HS90° pulse used to acquire the images in column **C** had a quadratic phase coefficient of 1.67 rad.mm$^{-2}$ (see Table 18).

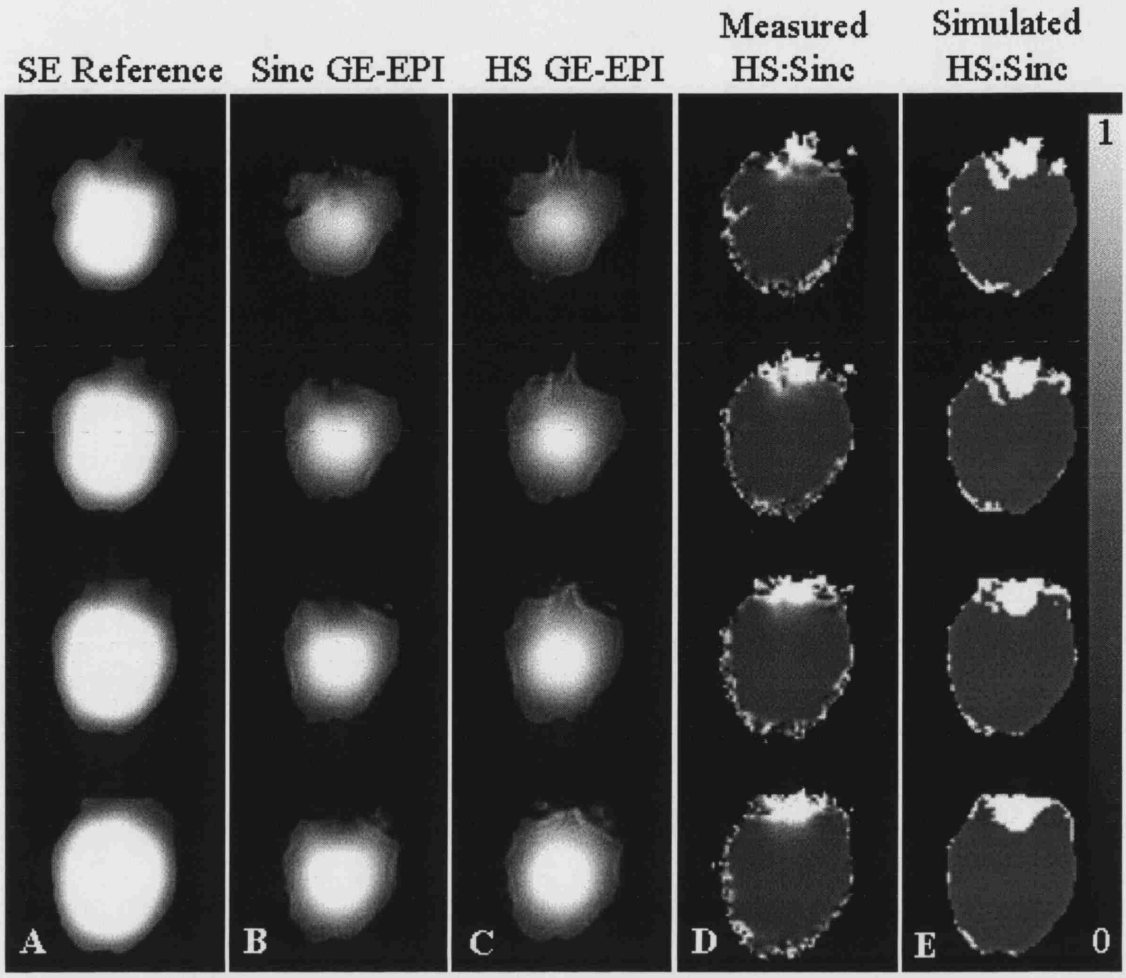


**Figure 95 Measured and Simulated Results for GE-EPI Signal Recovery with C = 2.45 rad.mm$^{-2}$**

Transverse images of four contiguous slices of the anthropomorphic head phantom are shown. The first column (**A**) shows SE reference images with no distortion or drop-out. The second column (**B**) shows standard GE-EPI images and the third column (**C**) shows GE-EPI images acquired with a HS90° excitation pulse to recover signal. These two columns of images have their intensities scaled independently to emphasise the signal recovery. The fourth column (**D**) is the ratio of images **C** to **B** masked with the short-TE GE image used for the field map. The fifth column (**E**) is the ratio of HS90° to standard simulated signals predicted from the field map using Equation 103 and Equation 105 and masked with the short-TE field map GE image. Columns **D** and **E** have intensities scaled between zero (black) and 1 (white). The HS90° pulse used to acquire the images in column **C** had a quadratic phase coefficient of 2.45 rad.mm$^{-2}$ (see Table 18).

| HS90° Pulse | | | | | TE (ms) | Measured HS90°/standard GE-EPI signal ratio (ROI mean) | Simulated HS90°/standard GE-EPI signal ratio (ROI mean) |
|---|---|---|---|---|---|---|---|
| Quadratic phase coefficient C (rad.mm$^{-2}$) | μ | Bandwidth (kHz) | Duration (ms) | Cut-off (%) | | | |
| 0.25 | 1.0 | 1.5 | 4.0 | 0.02 | 18 | 1.41 | 0.99 |
| 1.22 | 5.0 | 1.5 | 20.0 | 0.02 | 34 | 0.62 | 0.91 |
| 1.67 | 6.8 | 3.0 | 6.6 | 2.02 | 21 | 0.53 | 0.52 |
| 2.45 | 10.0 | 1.5 | 20.0 | 1.80 | 34 | 0.45 | 0.47 |
| 3.75 | 15.3 | 3.0 | 14.9 | 2.02 | 29 | 0.36 | 0.30 |

**Table 18 HS90°/standard Sinc GE-EPI Signal Ratios**
The table contains measured and simulated signal ratios collected using the ROI shown in Figure 92 on ratio maps created by dividing magnitude GE-EPI images acquired using the HS90° pulses with the parameters in the table by GE-EPI images acquired with a standard Sinc 90° pulse and the same TE. The corresponding simulated maps were created from field maps and using Equation 103 and Equation 105. Cut-off is the amplitude at the start and end of the HS pulse as a percentage of the maximum amplitude (see section 3.1.1.2.2.1.2).

# 6.4 Discussion

## 6.4.1 Preliminary experiments with GE sequences

From Figure 93 there is evidence of signal retrieval in the images acquired using the HS-90° excitation pulses in several areas of susceptibility-induced drop-out. The regions of drop-out are highlighted by comparing the short-TE images (Figure 93A and E) with the standard Sinc long-TE gradient-echo images (Figure 93B and F). Both HS90° pulses seem to perform equally well in terms of retrieving signal although comparing Figure 93H with G suggests that the pulse with C = 3.92 rad.mm$^{-2}$ may retrieve signal in slightly more areas than the pulse with C = 1.96 rad.mm$^{-2}$. There do not appear to be any areas where drop-out is worse in the HS-images than the Sinc-images.

The obvious disadvantage of the method is the overall reduction in signal-to-noise ratio (SNR) associated with using an excitation pulse that imposes a quadratic phase profile through the slice. Cho and Ro stated that the signal strength using their tailored RF pulse is reduced by a factor of 2. There is signal loss in regions free from drop-out because the RF (HS) pulses leave a quadratic phase across the slice in the absence of susceptibility differences so the spins within the voxel are not totally in phase and the resultant signal magnitude is decreased. The SNRs measured here in regions free from drop-out, were 727 in the Sinc image, 377 in the image acquired with the HS pulse with

C = 1.96 rad.mm$^{-2}$ and 261 in the image acquired with the HS pulse with C = 3.92 rad.mm$^{-2}$. In other words the HS images had an SNR that was 0.53 or 0.37 of the Sinc image SNR. These relative ratios are as expected from the quadratic phase coefficients of the pulses (Equation 103).

## 6.4.2 Signal Recovery in GE-EPI sequences

The main difference between the GE-EPI and GE images is that there is not only drop-out, to a greater extent than in the GE images, but also distortion. The effects of geometric distortion can be appreciated by comparing the GE-EPI images in Figure 94B and C with the SE reference image in Figure 94A. The distortion is also evident in Figure 94D and Figure 95D where there is a bright rim of noise around the GE-EPI signal ratio maps since they have been masked with the short-TE magnitude image used to acquire the field map. The phantom brain cavity appears distorted in the GE-EPI images so the boundaries do not match up.

From comparing Figure 94C with B and Figure 95C with B it is clear that these two HS90° pulses lead to signal recovery, particularly in the area just above and anterior to the nasal sinuses that would correspond in the real brain to the inferior frontal cortex. The areas in which there is signal recovery are also highlighted as white regions in Figure 94D (and Figure 95D) where the signal ratio of the images in Figure 94C divided by those in Figure 94B is greater than 1. All the pulses used here lead to signal recovery in similar areas to those highlighted in Figure 94 and Figure 95 except for the pulse with C = 0.25 rad.mm$^{-2}$ which gave almost no signal recovery. The fact that the quadratic phases of the HS90° pulses lead to signal reduction in areas of homogenous magnetic field is emphasised by the dark grey level (corresponding to a signal ratio <1) of most of the signal ratio maps in Figure 94D and E and Figure 95D and E.

The similarity of Figure 94E to D and Figure 95E to D shows that the pattern of signal recovery observed in practice is generally well predicted by simulations based on an acquired field map and Equation 103 and Equation 105. The signal ratio in the region in Figure 92 was also mostly well-predicted by simulations (see Table 18). This demonstrates that the technique is working as expected and that the model used to explain it (Figure 90 and Equation 100 to Equation 105) is useful. However there are differences between the measured and predicted ratios for the HS pulses with C = 0.25

and 1.22 rad.mm$^{-2}$ (Table 18). These may have arisen because of the different slice profiles of the Sinc and HS90° pulses (see 3.3.2.3) that were not taken into account in the simulations. Specifically, the C = 0.25 rad.mm$^{-2}$ pulse may have a measured ratio greater than 1 because the slice selected with this low-μ-value pulse is thicker than the standard Sinc-selected slice so there is correspondingly more signal in the HS90° image.

Such differences in the ROI mean ratios and slight differences in the patterns of the measured and simulated ratio maps may also have arisen due to the effect of geometric distortion which was not included in the simulations. Differences between the measured and simulated results could also have arisen in any areas in the phantom where the field pattern inside the voxels was non-linear. Future simulations could include the effects of distortion [97] and slice profile effects. However the differences between the measured and simulated data emphasise the utility of the phantom for comparing real imaging sequences since all the physical and experimental effects that will affect *in vivo* acquisitions are automatically present in the phantom acquisitions without having to be 'taken into account' in increasingly complicated simulations.

From inspecting the images and signal recovery ratio maps for all the pulses in Table 18, it is not immediately clear which pulse is the best for signal recovery in this phantom. What is clear from the measured signal ratios in Table 18 is that increasing the HS90° quadratic phase coefficient leads to a reduction in the signal in areas where the field is mostly homogenous, as first demonstrated by the simulations in Figure 91. It seems that a HS90° pulse with a C between 1.22 and 2.45 rad.mm$^{-2}$ would result in the best compromise between overall signal reduction in areas of homogenous field and signal recovery in inhomogeneous regions. Certainly a quadratic phase coefficient of 0.25 rad.mm$^{-2}$ was insufficient for signal recovery in this phantom with a voxel size of 3 mm.

As has been observed *in vivo* and in the phantom, the through-slice gradient varies across any particular slice. With reference to Figure 90, it can be deduced that the effective slice thickness (defined as that voxel thickness containing negligible phase variation, such that the spins from this region are coherent and add constructively to produce signal) in the HS90° sequence will also vary across the slice with the through-

slice gradient. It also follows that the position of the effective slice (which will always be narrower than the nominal slice thickness) will vary within the nominal slice thickness. The resulting signal localisation error in the slice direction will be smaller than the nominal slice thickness and may also be smaller than any in-plane geometric distortions. Therefore the decrease in signal in areas of homogenous magnetic field may not be as severe as indicated in these experiments if the comparison were to be made with the signal from a Sinc90° slice with a thickness closer to the narrower HS90° 'effective' slice thickness.

## 6.5 Conclusions and Further Work

The experiments in Chapter 6 demonstrate that the phantom shows suitable regions of drop-out to allow testing of a drop-out signal recovery technique. Tests on the phantom allowed optimisation of HS pulse parameters for signal recovery in GE-EPI so that the technique could be applied *in vivo* in future with knowledge of the appropriate parameters to achieve a reasonable compromise between signal reduction and drop-out recovery.

The technique could be developed further using the phantom to investigate whether some weighted combination of images acquired with HS90° pulses with several different quadratic phase coefficients could improve the images by optimising the trade-off between signal reduction and recovery. This would be analogous to the z-shimming type of approaches in which several images acquired with different preparation gradients are combined to form the final image (see section 5.1).

The technique could also be compared with other drop-out reduction methods such as z-shimming and intra-oral passive and active shims using the phantom. However, the phantom would need to be sawn open to allow access to the mouth cavity for testing of intra-oral shims. Future phantoms could perhaps be designed in two pieces to come apart at the level of the mouth to allow insertion of intra-oral shims.

# 7 CONCLUSIONS AND FURTHER WORK

In this chapter the most important findings arising from the work in this thesis are summarised and suggestions for further work are made.

## 7.1 Radio Frequency Pulse Sequence Development for Reduction of $B_1$ Inhomogeneity

In Chapter 3 a new spin-echo pulse sequence was developed which was intended to be less sensitive to $B_1$ variations across the head than previously proposed sequences. The sequence is based on the hyperbolic secant (HS) pulse which is insensitive to $B_1$ variations when used for adiabatic inversion. The aim was to use the HS pulse for refocusing to take advantage its $B_1$-insensitivity. However, when used for refocusing, the pulse introduces a quadratic phase coefficient across the imaging slice and the idea was to compensate for this by using a scaled-down full passage HS90° pulse for slice excitation.

Simulations and experiments were carried out to investigate and exploit the principle of quadratic phase compensation in the HS90°-HS180° sequence. The performance of this new sequence was compared with that of three pre-existing sequences: the conventional Sinc90°-Sinc180° spin-echo sequence, a linearly-frequency-modulated (LFM) LFM90°-LFM180° sequence and a Sinc90°-HS90°-HS180° sequence. Slice profiles showed that the new sequence gave a sharper slice than the standard Sinc SE sequence without the slice narrowing caused by using two HS refocusing pulses and the large (residual) phase variation in the LFM SE sequence.

The effect of HS pulse parameter $\mu$ on slice profiles and images was then investigated. A linear relationship between the HS quadratic phase coefficient and pulse $\mu$ was found (for a fixed bandwidth and pulse duration) for both excitation and refocusing pulses. It would be useful to investigate the effect of HS pulse bandwidth and duration on the quadratic phase coefficients to inform HS90°-HS180° sequence design in future.

A series of experiments was then performed to investigate the robustness of the HS90°-HS180° sequence to changes in $B_1$. Varying the HS180° pulse amplitude produced slight decreases in signal in images and profiles due to an unexpected increase in the

HS180° quadratic phase coefficient at high amplitudes caused by a compression of the HS180° pulse shape by the RF amplifier's non-linear behaviour. These signal decreases were shown to be negligible compared with the signal variation caused by varying both the HS90° pulse amplitude and HS180° pulse amplitudes simultaneously.

The HS90°-HS180° sequence resulted in a spatial phase variation in a water phantom due to the $B_1$ inhomogeneity. This variation, predicted by theory (and absent from the Sinc90°-HS180°-HS180° images), was not found to cause any image intensity reduction or additional non-uniformity. The phase variation could potentially be harnessed to yield a map of the $B_1$ distribution in the sample as a side-product of imaging with the HS90°-HS180° sequence.

A simplistic approach to comparing the uniformity of images acquired using the four different sequences by looking at a single set of images acquired with 'calibrated' pulse values was found to be inconclusive. Plots of overall image signal and uniformity with varying pulse amplitude multiplying factors clearly demonstrated the advantage of the adiabatic HS180° over the non-adiabatic LFM180° pulse and showed that the standard Sinc SE sequence was least robust to changes in $B_1$ and gave the least uniform images. It was, however, necessary to plot signal range maps to distinguish between the three other sequences which all showed similar maximum image uniformities and had varying image uniformities since none of them is fully adiabatic.

The signal range map for the HS90°-HS180° sequence seemed the most uniform, the sequence achieving relatively low signal ranges fairly consistently throughout the phantom. The Sinc90°-HS180°-HS180° sequence was extremely robust to $B_1$ changes in one region of the phantom but not in the centre of the phantom. These two sequences gave the most uniform images and were the most robust to $B_1$ inhomogeneity but the major advantage of the HS90°-HS180° sequence over the Sinc90°-HS180°-HS180° sequence is that it is shorter, using one less RF pulse and therefore having a lower SAR.

Despite the excellent performance of the HS90°-HS180° sequence relative to the others, it does not completely remove the effect of $B_1$-inhomogeneity on image uniformity since the HS90° pulse is non-adiabatic and the RF coil has receive inhomogeneity.

Further work could involve investigation of post-processing methods to remove the remaining image non-uniformity.

The HS90°-HS180° sequence performance remains to be investigated *in vivo* where its performance could be compared with other $B_1$-inhomogeneity reduction methods for applications such as DW-SE-EPI or SE-EPI for functional imaging.

## 7.2 Towards High Resolution Diffusion Tensor Imaging With Reduced Distortion at High Field Strength

In Chapter 4 a volume selective DW-STEAM-EPI sequence was developed to reduce the geometric distortion associated with the conventional single-shot SE-EPI technique and utilise the higher signal strength available at 4.7 T to achieve higher spatial resolution.

A first attempt at *in vivo* DTI at this field strength was made by applying the commonly used single shot DW-SE-EPI technique. Trace maps, FA maps and colour maps of the diffusion tensor were produced and trace values were measured in regions of grey matter, white matter and CSF in the maps. The base images were severely distorted and these geometric distortions were visible artifacts in the tensor-derived maps. There was no evidence for motion or eddy-current-induced distortions greater than the size of a voxel despite the lack of any form of motion or eddy current correction schemes. Trace values corresponded to those in the DWI literature and some familiar structures appeared in the FA and colour maps.

This basic DW-SE-EPI acquisition could be refined in future by acquiring several averages, acquiring non-phase-encoded reference data prior to every DW direction for Nyquist ghost removal and by using cardiac gating. In addition, the b-value and number of directions could be optimised for the particular SNR at 4.7 T using the approach of Jones et al [68].

A literature search was carried out to look for a sequence with high spatially isotropic resolution that would fulfil the requirements for high field DTI, which include reduced

distortion, good SNR efficiency and robustness to both motion and $B_1$ inhomogeneity. On this basis a new volume selective DW-STEAM-EPI sequence was proposed and developed (with the aim of fulfilling these requirements). The volume selective DW-STEAM-EPI sequence is able to reduce distortion and achieve higher resolution because it selects a cuboid, allowing reduction of the EPI field of view (FOV). It is robust to motion since the stimulated echo formation relies on introducing (and then unwinding) a large phase variation across the sample.

A quantitative comparison of the volume selective DW-STEAM-EPI technique with single and multishot DW-SE-EPI and a DW-STEAM-FLASH sequence was then carried out. Based on this comparison the DW-STEAM-FLASH sequence was rejected since despite being relatively free from distortion, it has a very low SNR efficiency compared with the other techniques. The comparison also demonstrated the promise of the volume selective DW-STEAM-EPI technique for achieving 1 x 1 x 1 mm resolution with distortion superior to two-shot SE-EPI methods. A partial Fourier version was also shown to yield greater SNR efficiency than the two-shot SE-EPI sequence. In the course of the comparison it was shown that the DW-STEAM-EPI technique would suffer from a decay in SNR with slice number although it was suggested that acquiring slices in both forward and reverse order could mitigate this.

To investigate further its properties and potential, the DW-STEAM-EPI sequence was implemented and tested on both dodecane and doped water phantoms. The new sequence successfully selected a reduced FOV region although the pulse profiles could perhaps be improved by applying SLR methods. Measured ADC values were compared with those from 2DFT SE and SE-EPI techniques and found to be in reasonable agreement. The expected slice-to-slice signal decay was observed but averaging both forward and reverse acquisitions removed the resulting small bias in the ADC values. The lack of a strong trend in slice decay constant with increasing b-value emphasised that the SE DW preparation is highly independent of the imaging module in the volume selective DW-STEAM-EPI sequence.

This first implementation of the volume selective DW-STEAM-EPI sequence showed that it could achieve high-resolution images and accurate ADC values. The experimental results together with the theoretical assessment suggest that this technique

will be capable of reaching high isotropic resolution for efficient DTI at high field strength with reduced distortion but limited spatial coverage.

It would be useful to extend the experiments in future to investigate further aspects of the technique before applying it *in vivo*. For example the partial Fourier version could be implemented to increase the SNR efficiency and its overall SNR could be measured *in vivo* to determine how many slices can be collected for different b and TE values. Multiple cube acquisition could be implemented to extend the spatial coverage of the technique. The level of geometric distortion could be evaluated using the anthropomorphic head phantom (Chapter 5) and *in vivo* with localised shimming applied to the selected cube.

The volume selective DW-STEAM-EPI sequence could be compared with multishot DW-SE-EPI methods *in vivo* in terms of their motion sensitivity, geometric distortion and their usefulness for tractography. It would be interesting to investigate whether the higher resolution and reduced distortion of the new sequence improve the accuracy of tractography.

In future a Gradient and Spin Echo (GRASE) readout [241] could be substituted for the EPI used here and may offer the potential for further reducing geometric distortion by decreasing the number of phase encoding steps over which the susceptibility gradients have an effect. This might reduce the gradient duty cycle and allow a corresponding improvement in SNR efficiency but at the expense of increased SAR.

## 7.3 Development of an Anthropomorphic Head Phantom to Test Susceptibility Artifact Reduction Techniques

In Chapter 5 the design, construction and use of an anthropomorphic head phantom was described. The motivation was to use the phantom as a tool for the comparison, development and optimisation of techniques for susceptibility artifact reduction. Measurements were made of the magnetic susceptibilities of a range of materials to allow selection of those most appropriate for mimicking the brain, bone and soft tissues in the phantom. The plastic skull that formed the basis of the phantom was found to

have a susceptibility not dissimilar to bone and paraffin wax turned out to be the best soft tissue mimic. The phantom was constructed based on a sealed plastic skull with the brain cavity filled with $MnCl_2$-doped water and retaining existing air spaces of realistic dimensions. A mimic for the soft tissues was added by pouring molten wax into a custom-made head-shaped mould.

As part of the evaluation of the phantom, main magnetic field maps were acquired in order to compare the magnetic fields in the phantom with those in the brains of volunteers. It was found that the field maps showed many similarities and some small differences. The range of field values in $B_0$ field maps of the phantom and the brains of volunteers was similar as was the field pattern with both showing characteristic features such as a higher-field region above the nasal air spaces, a lower-field region behind the frontal sinuses and higher-field areas near the auditory air spaces. Maps of the magnitude of the magnetic field gradients in the phantom and volunteer brain were also similar, indicating that the phantom would be likely to suffer from similar susceptibility artifacts to real brains. The main differences between the phantom and volunteer field maps arose due to the presence of a large rubber bung in the phantom and a bubble (to represent the frontal sinus air space) that was too large.

Improved phantom design, for example by using wax rather than rubber to plug the plastic skull and a fixed 'frontal sinus' airspace, could make the phantom field map and susceptibility artifacts even more realistic. Adding fiducial marks to the phantom (and RF coil or patient-positioning devices) could ensure reproducible phantom positioning.

The phantom was also evaluated in terms of its relaxation times and $B_1$ distribution. The relaxation times were found to be in the region of those expected for brain grey and white matter at 4.7 T. It would, however, be useful to perform brain relaxivity measurements *in vivo* at this field strength since there is a scarcity of published $T_2$ (and $T_1$) values for 4.7 T. Armed with these relaxation times, appropriate gel and dopant concentrations could be selected for the phantom fill. If further detail were required, for example for evaluating the contrast of structural imaging sequences, compartments with different $T_1$ and $T_2$ values could be created inside the phantom's brain cavity.

The $B_1$ variation in the phantom was found to be greater than that in the head but the overall $B_1$ pattern, with a bright region in the centre of the brain, was reproduced in the phantom. To remove the confounding effect of $B_1$-inhomogeneity on the assessment of susceptibility artifacts, it could be useful to fill the phantom with silicone oil since its low dielectric constant would yield a relatively homogenous $B_1$ field.

CT scans of the finished phantom were also acquired as part of its evaluation. The different elements of the phantom were clearly CT-visible, making it a potentially useful tool to test CT-MRI image coregistration in the presence of susceptibility artifacts. CT-MRI image registration has applications for neurosurgery and in radiotherapy treatment planning.

Since the phantom was built on the principle of reproducing magnetic susceptibilities and anatomically realistic airspaces, it should be useful in MRI scanners at any field strength. In future, it could be evaluated in scanners at 3 T or even 7 T using the methods applied in this work. If necessary the fill could be modified to yield relaxation times appropriate to the particular field strength.

The evaluation of the phantom could be improved and the magnetic fields and susceptibility artifacts in volunteers could be characterised further. To characterise the magnetic fields and susceptibility artifacts in the human head more fully it would be desirable to acquire many more field maps of different volunteers and perhaps coregister them into a standard space to calculate an average field map. This field map, and those acquired in phantoms as well as other images, could be further processed to predict and quantify the resulting susceptibility artifacts.

## 7.4 Using the Anthropomorphic Head Phantom to Evaluate Drop-Out Reduction in Gradient-Echo Imaging with Hyperbolic Secant Excitation Pulses

All the evidence from the phantom evaluation in Chapter 5 suggests that the phantom will be very useful for comparing and developing some of the large range of susceptibility artifact reduction techniques introduced in section 5.1 (although slight alterations in its design may be required if intra-oral shims are to be inserted). The utility of the phantom is demonstrated practically in Chapter 6 in which the phantom was used to test a signal drop-out recovery technique. HS excitation pulses were able to retrieve signal in both standard gradient-echo images and those acquired with the widely used GE-EPI sequence but at the expense of overall signal levels in both cases. Use of the phantom allowed multiple trials to be performed with a range of HS pulse parameters so that the technique could be optimised to achieve the best balance between signal recovery and overall signal reduction before application *in vivo*.

In general, simulations based on field maps seemed to predict the pattern of signal recovery and degree of signal reduction. However, the fact that maps of HS90°-GE-EPI to Sinc90°-GE-EPI signal ratio did not match simulated maps exactly in every case, emphasises the advantages of the phantom over computer simulations.

This particular technique could be developed further using the phantom to investigate whether using a weighted combination of images acquired with different HS90° pulses could optimise the trade-off between signal reduction and recovery.

Three main areas have been explored in this thesis, namely, the reduction of $B_1$ inhomogeneity, diffusion tensor imaging with reduced distortion, and the development and use of an anthropomorphic head phantom to test susceptibility artifact reduction techniques. This work has addressed some of the main problems associated with high field strength MRI but more work must be done to fully optimise the techniques for imaging the human brain.

# REFERENCES


1. Wang, L., McCarthy, G., Song, A. W., & Labar, K. S., Amygdala Activation to Sad Pictures During High-Field (4 Tesla) Functional Magnetic Resonance Imaging, *Emotion.* **2005**, Vol. 5, No. 1, pp. 12-22

2. Hagiwara, Y., Hatori, M., Abe, A., Tanaka, K., & Kokubun, S., Periosteal Chondroma of the Fifth Toe--a Case Report, *Ups.J.Med.Sci.* **2004**, Vol. 109, No. 1, pp. 65-70

3. Marzola, P., Osculati, F., & Sbarbati, A., High Field MRI in Preclinical Research, *European Journal of Radiology* **2003**, Vol. 48, No. 2, pp. 165-170

4. McRobbie, D. W., Moore, E. A., Graves, M. J., & Prince, M. R., *MRI From Picture to Proton*, **2003** Cambridge University Press

5. http://www.beyonddiscovery.org/content/view.article.asp?a=129

6. http://www.emrf.org/FAQs%20MRI%20History.html

7. De Vita, E., *Development and Optimisation of High-Field MRI Techniques,* **2003** Doctor of Philosophy, Department of Medical Physics and Bioengineering, University College London, University of London

8. Hu, X. P. & Norris, D. G., Advances in High-Field Magnetic Resonance Imaging, *Annual Review of Biomedical Engineering* **2004**, Vol. 6, pp. 157-184

9. Norris, D. G., High Field Human Imaging, *Journal of Magnetic Resonance Imaging* **2003**, Vol. 18, No. 5, pp. 519-529

10. Wiesinger, F., Van De Moortele, P. F., Adriany, G., De Zanche, N., Ugurbil, K., & Pruessmann, K. P., Parallel Imaging Performance As a Function of Field Strength - An Experimental Investigation Using Electrodynamic Scaling, *Magnetic Resonance in Medicine* **2004**, Vol. 52, No. 5, pp. 953-964

11. Vaughan, J. T., Garwood, M., Collins, C. M., Liu, W., DelaBarre, L., Adriany, G., Andersen, P., Merkle, H., Goebel, R., Smith, M. B., & Ugurbil, K., 7T Vs. 4T: RF Power, Homogeneity, and Signal-to-Noise Comparison in Head Images, *Magnetic Resonance in Medicine* **2001**, Vol. 46, No. 1, pp. 24-30

12. Ibrahim, T. S., Lee, R., Baertlein, B. A., Abduljalil, A. M., Zhu, H., & Robitaille, P. M. L., Effect of RF Coil Excitation on Field Inhomogeneity at Ultra High Fields: A Field Optimized TEM Resonator, *Magnetic Resonance Imaging* **2001**, Vol. 19, No. 10, pp. 1339-1347

13. Cho, Z. H. & Ro, Y. M., Reduction of Susceptibility Artifact in Gradient-Echo Imaging, *Magnetic Resonance in Medicine* **1992**, Vol. 23, No. 1, pp. 193-200

14. Cusack, R., Brett, M., & Osswald, K., An Evaluation of the Use of Magnetic Field Maps to Undistort Echo-Planar Images, *Neuroimage* **2003**, Vol. 18, No. 1, pp. 127-142

15. Edelstein, W. A., Bottomley, P. A., & Pfeifer, L. M., A Signal-to-Noise Calibration Procedure for NMR Imaging Systems, *Medical Physics* **1984**, Vol. 11, No. 2, pp. 180-185

16. Yablonskiy, D. A. & Haacke, E. M., Theory of NMR Signal Behavior in Magnetically Inhomogeneous Tissues: the Static Dephasing Regime, *Magnetic Resonance in Medicine* **1994**, Vol. 32, No. 6, pp. 749-763

17. Yablonskiy, D. A., Quantitation of Intrinsic Magnetic Susceptibility-Related Effects in a Tissue Matrix. Phantom Study, *Magnetic Resonance in Medicine* **1998**, Vol. 39, No. 3, pp. 417-428

18. Reichenbach, J. R., Venkatesan, R., Yablonskiy, D. A., Thompson, M. R., Lai, S., & Haacke, E. M., Theory and Application of Static Field Inhomogeneity Effects in Gradient-Echo Imaging, *Jmri-Journal of Magnetic Resonance Imaging* **1997**, Vol. 7, No. 2, pp. 266-279

19. Haacke, E. M., Brown, R. D., III, Thompson, M. R., & Venkatesan, R., *Magnetic Resonance Imaging: Physical Principles and Sequence Design*, 1st edn, **1999** Wiley-Liss

20. Collins, C. M., Li, S. Z., & Smith, M. B., SAR and B-1 Field Distributions in a Heterogeneous Human Head Model Within a Birdcage Coil, *Magnetic Resonance in Medicine* **1998**, Vol. 40, No. 6, pp. 847-856

21. Jin, J. M., Chen, J., Chew, W. C., Gan, H., Magin, R. L., & Dimbylow, P. J., Computation of Electromagnetic Fields for High-Frequency Magnetic Resonance Imaging Applications, *Phys.Med.Biol.* **1996**, Vol. 41, No. 12, pp. 2719-2738

22. Alecci, M., Collins, C. M., Smith, M. B., & Jezzard, P., Radio Frequency Magnetic Field Mapping of a 3 Tesla Birdcage Coil: Experimental and Theoretical Dependence on Sample Properties, *Magnetic Resonance in Medicine* **2001**, Vol. 46, No. 2, pp. 379-385

23. Ibrahim, T. S., Abduljalil, A. M., Baertlein, B. A., Lee, R., & Robitaille, P. M. L., Analysis of B-1 Field Profiles and SAR Values for Multi-Strut Transverse Electromagnetic RF Coils in High Field MRI Applications, *Physics in Medicine and Biology* **2001**, Vol. 46, No. 10, pp. 2545-2555

24. Simmons, A., Tofts, P. S., Barker, G. J., & Arridge, S. R., Sources of Intensity Nonuniformity in Spin Echo Images at 1.5 T, *Magnetic Resonance in Medicine* **1994**, Vol. 32, No. 1, pp. 121-128

25. Roschmann, P., Radiofrequency Penetration and Absorption in the Human Body: Limitations to High-Field Whole-Body Nuclear Magnetic Resonance Imaging, *Medical Physics* **1987**, Vol. 14, No. 6, pp. 922-931

26. Hoult, D. I., Sensitivity and Power Deposition in a High-Field Imaging Experiment, *Journal of Magnetic Resonance Imaging* **2000**, Vol. 12, No. 1, pp. 46-67

27. Roschmann, P., Role of B1-Eigenfields of Dielectric Objects in High-Field MRI, *Proceedings of the International Society for Magnetic Resonance in Medicine* Vol. 8, **2000**, p. 151

28. Collins, C. M., Schreiber, W., Yang, Q. X., & Smith, M. B., Central Brightening Due to Constructive Interference Despite Dielectric Resonance With Central Magnetic Field Minimum, *Proceedings of the International Society for Magnetic Resonance in Medicine* Vol. 11, **2003**, p. 2391

29. Kangarlu, A., Baertlein, B. A., Lee, R., Ibrahirm, T., Yang, L. N., Abduljalil, A. M., & Robitaille, E. M. L., Dielectric Resonance Phenomena in Ultra High Field MRI, *Journal of Computer Assisted Tomography* **1999**, Vol. 23, No. 6, pp. 821-831

30. Yang, Q. X., Wang, J. H., Zhang, X., Smith, M. B., Adriany, G., Zhu, H., Ugurbil, K., & Chen, W., Phantom Design in the Presence of Wave Behavior of the Radiofrequency Field, *Proceedings of the International Society for Magnetic Resonance in Medicine* Vol. 10, **2002**, p. 913

31. Barker, G. J., Simmons, A., Arridge, S. R., & Tofts, P. S., A Simple Method for Investigating the Effects of Non-Uniformity of Radiofrequency Transmission and Radiofrequency Reception in MRI, *British Journal of Radiology* **1998**, Vol. 71, No. 841, pp. 59-67

32. Yang, Q. X., Smith, M. B., Liu, H., Zhang, X., Wang, J. H., Ugurbil, K., & Chen, W., Manipulation of Signal Intensity Distribution With Dielectric Loading at 7.0T, *Proceedings of the International Society for Magnetic Resonance in Medicine* Vol. 9, **2001**, p. 1096

33. Ledden, P., Transmit Homogeneity at High Fields: Computational Effects of "B1 Shimming" With an Eight Element Volume Coil, *Proceedings of the International Society for Magnetic Resonance in Medicine* Vol. 11, **2003**, p. 2390

34. Ibrahim, T. S., Lee, R., Baertlein, B. A., Kangarlu, A., & Robitaille, P. M. L., Application of Finite Difference Time Domain Method for the Design of Birdcage RF Head Coils Using Multi-Port Excitations, *Magnetic Resonance Imaging* **2000**, Vol. 18, No. 6, pp. 733-742

35. Clare, S., Alecci, M., & Jezzard, P., Compensating for B-1 Inhomogeneity Using Active Transmit Power Modulation, *Magnetic Resonance Imaging* **2001**, Vol. 19, No. 10, pp. 1349-1352

36. Deichmann, R., Good, C. D., & Turner, R., RF Inhomogeneity Compensation in Structural Brain Imaging, *Magnetic Resonance in Medicine* **2002**, Vol. 47, No. 2, pp. 398-402

37. Saekho, S., Boada, F. E., Noll, D. C., & Stenger, V. A., B1 Inhomogeneity Compensation Using 3D Tailored RF Pulses, *Proceedings of the International Society for Magnetic Resonance in Medicine* Vol. 11, **2003**, p. 717

38. Thesen, S., Krueger, G., & Mueller, E., Compensation of Dielectric Resonance Effects by Means of Composite Excitation Pulses, *Proceedings of the International Society for Magnetic Resonance in Medicine* Vol. 11, **2003**, p. 715

39. Silver, M. S., Joseph, R. I., & Hoult, D. I., Selective Spin Inversion in Nuclear Magnetic Resonance and Coherent Optics Through an Exact Solution of the Bloch-Riccati Equation, *Physical Review A* **1985**, Vol. 31, No. 4, pp. 2573-2755

40. Silver, M. S., Joseph, R. I., & Hoult, D. I., Highly Selective Pi/2 and Pi-Pulse Generation, *Journal of Magnetic Resonance* **1984**, Vol. 59, No. 2, pp. 347-351

41. Baum, J., Tycko, R., & Pines, A., Broad-Band and Adiabatic Inversion of a 2-Level System by Phase-Modulated Pulses, *Physical Review A* **1985**, Vol. 32, No. 6, pp. 3435-3447

42. Garwood, M. & DelaBarre, L., The Return of the Frequency Sweep: Designing Adiabatic Pulses for Contemporary NMR, *Journal of Magnetic Resonance* **2001**, Vol. 153, No. 2, pp. 155-177

43. Tyszka, J. M. & Mamelak, A. N., Quantification of B-0 Homogeneity Variation With Head Pitch by Registered Three-Dimensional Field Mapping, *Journal of Magnetic Resonance* **2002**, Vol. 159, No. 2, pp. 213-218

44. Conolly, S., Nishimura, D., & Macovski, A., Sweep-Diagram Analysis of Selective Adiabatic Pulses, *Journal of Magnetic Resonance* **1989**, Vol. 83, No. 3, pp. 549-564

45. Payne, G. S. & Leach, M. O., Implementation and Evaluation of Frequency Offset Corrected Inversion (FOCI) Pulses on a Clinical MR System, *Magnetic Resonance in Medicine* **1997**, Vol. 38, No. 5, pp. 828-833

46. De Graaf, R. A. & Nicolay, K., Adiabatic Water Suppression Using Frequency Selective Excitation, *Magnetic Resonance in Medicine* **1998**, Vol. 40, No. 5, pp. 690-696

47. Conolly, S., Glover, G., Nishimura, D., & Macovski, A., A Reduced Power Selective Adiabatic Spin-Echo Pulse Sequence, *Magnetic Resonance in Medicine* **1991**, Vol. 18, No. 1, pp. 28-38

48. Kunz, D., Frequency-Modulated Radiofrequency Pulses in Spin-Echo and Stimulated-Echo Experiments, *Magnetic Resonance in Medicine* **1987**, Vol. 4, No. 2, pp. 129-136

49. Kunz, D., Use of Frequency-Modulated Radiofrequency Pulses in MR Imaging Experiments, *Magnetic Resonance in Medicine* **1986**, Vol. 3, No. 3, pp. 377-384

50. Pipe, J. G., Spatial Encoding and Reconstruction in MRI With Quadratic Phase Profiles, *Magnetic Resonance in Medicine* **1995**, Vol. 33, No. 1, pp. 24-33

51. De Graaf, R. A. & Nicolay, K., Adiabatic RF Pulses: Applications into In Vivo NMR, *Concepts in Magnetic Resonance* **1997**, Vol. 9, pp. 247-268

52. Ugurbil, K., Garwood, M., Rath, A. R., & Bendall, M. R., Amplitude-Modulated and Frequency Phase-Modulated Refocusing Pulses That Induce Plane Rotations Even in the Presence of Inhomogeneous B1 Fields, *Journal of Magnetic Resonance* **1988**, Vol. 78, No. 3, pp. 472-497

53. Garwood, M. & Ugurbil, K., B1 Insensitive Adiabatic RF Pulses, pp. 109-147 in *NMR Basic Principles and Progress*, vol. 26, **1992** Springer-Verlag

54. Tannus, A. & Garwood, M., Adiabatic Pulses, *Nmr in Biomedicine* **1997**, Vol. 10, No. 8, pp. 423-434

55. De Graaf, R. A., *Adiabatic RF Pulses in In Vivo NMR Spectroscopy,* **1998** Doctorate, University of Utrecht

56. Norris, D. G., Adiabatic Radiofrequency Pulse Forms in Biomedical Nuclear Magnetic Resonance, *Concepts in Magnetic Resonance* **2002**, Vol. 14, No. 2, pp. 89-101

57. De Graaf, R. A., Nicolay, K., & Garwood, M., Single-Shot, B-1-Insensitive Slice Selection With a Gradient- Modulated Adiabatic Pulse, BISS-8, *Magnetic Resonance in Medicine* **1996**, Vol. 35, No. 5, pp. 652-657

58. Mansfield, P. & Morris, P. G., *NMR Imaging in Biomedicine*, 1st edn, **1982** Academic Press, Inc.

59. Park, J.-Y. & Garwood, M., Imaging Pseudo-Echoes Produced by a Frequency-Swept Pulse, *Proceedings of the International Society for Magnetic Resonance in Medicine* Vol. 12, **2004**, p. 534

60. Tofts, P. S., Barker, G. J., Dean, T. L., Gallagher, H., Gregory, A. P., & Clarke, R. N., A Low Dielectric Constant Customized Phantom Design to Measure RF Coil Nonuniformity, *Magnetic Resonance Imaging* **1997**, Vol. 15, No. 1, pp. 69-75

61. De Vita, E., Thomas, D. L., Deichmann, R., Turner, R., & Ordidge, R. J., Fast B1 Mapping With EPI, *Proceedings of the International Society for Magnetic Resonance in Medicine* Vol. 12, **2004**, p. 2090

62. Jenkinson, M., Fast, Automated, N-Dimensional Phase-Unwrapping Algorithm, *Magnetic Resonance in Medicine* **2003**, Vol. 49, No. 1, pp. 193-197

63. Lerski, R. A., De Wilde, J. , Boyce, D., & Ridgway, J., *Quality Control in Magnetic Resonance Imaging*, Second edn, **2002** Institute of Physics and Engineering in Medicine

64. Conolly, S., Nishimura, D., & Macovski, A., A Selective Adiabatic Spin-Echo Pulse, *Journal of Magnetic Resonance* **1989**, Vol. 83, No. 2, pp. 324-334

65. Stejskal, E. O. & Tanner, J. E., Spin Diffusion Measurements - Spin Echoes in the Presence of a Time-Dependent Field Gradient, *Journal of Chemical Physics* **1965**, Vol. 42, No. 1, pp. 288-292

66. Le Bihan, D., *Diffusion and Perfusion Magnetic Resonance Imaging: Applications to Functional MRI*, **1995**, Le Bihan, D., Raven Press

67. Basser, P. J., Mattiello, J., & LeBihan, D., Estimation of the Effective Self-Diffusion Tensor From the NMR Spin-Echo, *Journal of Magnetic Resonance Series B* **1994**, Vol. 103, No. 3, pp. 247-254

68. Jones, D. K., Horsfield, M. A., & Simmons, A., Optimal Strategies for Measuring Diffusion in Anisotropic Systems by Magnetic Resonance Imaging, *Magnetic Resonance in Medicine* **1999**, Vol. 42, No. 3, pp. 515-525

69. Pierpaoli, C., Jezzard, P., Basser, P. J., Barnett, A., & DiChiro, G., Diffusion Tensor MR Imaging of the Human Brain, *Radiology* **1996**, Vol. 201, No. 3, pp. 637-648

70. Basser, P. J. & Jones, D. K., Diffusion-Tensor MRI: Theory, Experimental Design and Data Analysis - a Technical Review, *Nmr in Biomedicine* **2002**, Vol. 15, No. 7-8, pp. 456-467

71. Mori, S. & van Zijl, P. C. M., Diffusion Weighting by the Trace Fo the Diffusion Tensor Within a Single Scan, *Magnetic Resonance in Medicine* **1995**, Vol. 33, No. 1, pp. 41-52

72. Wong, E. C., Cox, R. W., & Song, A. W., Optimized Isotropic Diffusion Weighting, *Magnetic Resonance in Medicine* **1995**, Vol. 34, No. 2, pp. 139-143

73. Sotak, C. H., The Role of Diffusion Tensor Imaging in the Evaluation of Ischemic Brain Injury - a Review, *NMR Biomed.* **2002**, Vol. 15, No. 7-8, pp. 561-569

74. Le Bihan, D., Mangin, J. F., Poupon, C., Clark, C. A., Pappata, S., Molko, N., & Chabriat, H., Diffusion Tensor Imaging: Concepts and Applications, *Journal of Magnetic Resonance Imaging* **2001**, Vol. 13, No. 4, pp. 534-546

75. Beaulieu, C., The Basis of Anisotropic Water Diffusion in the Nervous System - a Technical Review, *NMR Biomed.* **2002**, Vol. 15, No. 7-8, pp. 435-455

76. van Zijl, P. C. M. & Le Bihan, D., Diffusion Tensor Imaging and Axonal Mapping - State of the Art, *NMR Biomed.* **2002**, Vol. 15, No. 7-8, pp. 431-601

77. Mori, S. & van Zijl, P. C., Fiber Tracking: Principles and Strategies - a Technical Review, *NMR Biomed.* **2002**, Vol. 15, No. 7-8, pp. 468-480

78. Song, A. W., Harshbarger, T., Li, T., Kim, K., Mori, S., & Kim, D., Functional Activation Using ADC Contrast Allows Better Spatial Localization to the Neuronal Activity: Evicence Using DTI Fiber Tracking, *Proceedings of the International Society for Magnetic Resonance in Medicine* Vol. 11, **2003**, p. 396

79. Nimsky, C., Ganslandt, O., Hastreiter, P., Wang, R., Benner, T., Sorensen, A. G., & Fahlbusch, R., Preoperative and Intraoperative Diffusion Tensor Imaging-Based Fiber Tracking in Glioma Surgery, *Neurosurgery* **2005**, Vol. 56, No. 1, pp. 130-137

80. Nimsky, C., Ganslandt, O., Hastreiter, P., Wang, R., Benner, T., Sorensen, A. G., & Fahlbusch, R., Intraoperative Diffusion-Tensor MR Imaging: Shifting of White Matter Tracts During Neurosurgical Procedures--Initial Experience, *Radiology* **2005**, Vol. 234, No. 1, pp. 218-225

81. Tournier, J.-D., *Diffusion Tensor Magnetic Resonance Imaging and Fibre Tractography in the Brain,* **2003** Ph.D., University of London

82. Skare, S., Hedehus, M., Moseley, M. E., & Li, T. Q., Condition Number As a Measure of Noise Performance of Diffusion Tensor Data Acquisition Schemes With MRI, *Journal of Magnetic Resonance* **2000**, Vol. 147, No. 2, pp. 340-352

83. Thomas, D. L., De Vita, E., Deichmann, R., Turner, R., & Ordidge, R. J., Can Two Wrongs Make a Right? B1-Insensitive T1-Weighted Imaging of the Human Brain at 4.7T Using 3D MDEFT With a Standard Non-Adiabatic Preparation Pulse, *Proceedings of the International Society for Magnetic Resonance in Medicine* Vol. 12, **2004**, p. 84

84. Il'yasov, K. A. & Zhilkin, P., On Correction of Eddy Current Induced Distortions in Diffusion Weighted Echo Planar Images With a Calibration on a Reference Phantom, *Proceedings of the International Society for Magnetic Resonance in Medicine* Vol. 11, **2003**, p. 2116

85. http://www.fil.ion.ucl.ac.uk/spm/software/spm2/

86. http://www.dtiatlas.org/

87. Redpath, T. W. & Wayte, S. C., Fat Suppressed Magnetic Resonance Imaging at 0.5 T Using Binomial Radiofrequency Pulses, *Br.J.Radiol.* **1993**, Vol. 66, No. 790, pp. 886-891

88. Reese, T. G., Heid, O., Weisskoff, R. M., & Wedeen, V. J., Reduction of Eddy-Current-Induced Distortion in Diffusion MRI Using a Twice-Refocused Spin Echo, *Magnetic Resonance in Medicine* **2003**, Vol. 49, No. 1, pp. 177-182

89. Jezzard, P., Barnett, A. S., & Pierpaoli, C., Characterization of and Correction for Eddy Current Artifacts in Echo Planar Diffusion Imaging, *Magnetic Resonance in Medicine* **1998**, Vol. 39, No. 5, pp. 801-812

90. Bodammer, N., Kaufmann, J., Kanowski, M., & Tempelmann, C., Eddy Current Correction in Diffusion-Weighted Imaging Using Pairs of Images Acquired With Opposite Diffusion Gradient Polarity, *Magnetic Resonance in Medicine* **2004**, Vol. 51, No. 1, pp. 188-193

91. Jones, D. K., Williams, S. C. R., Gasston, D., Horsfield, M. A., Simmons, A., & Howard, R., Isotropic Resolution Diffusion Tensor Imaging With Whole Brain Acquisition in a Clinically Acceptable Time, *Human Brain Mapping* **2002**, Vol. 15, No. 4, pp. 216-230

92. Lehnert, A., Machann, J., Helms, G., Claussen, C. D., & Schick, F., Diffusion Characteristics of Large Molecules Assessed by Proton MRS on a Whole-Body MR System, *Magnetic Resonance Imaging* **2004**, Vol. 22, No. 1, pp. 39-46

93. Chun, T., Ulug, A. M., & van Zijl, P. C. M., Single-Shot Diffusion-Weighted Trace Imaging on a Clinical Scanner, *Magnetic Resonance in Medicine* **1998**, Vol. 40, No. 4, pp. 622-628

94. Wakana, S., Jiang, H., Nagae-Poetscher, L. M., van Zijl, P. C., & Mori, S., Fiber Tract-Based Atlas of Human White Matter Anatomy, *Radiology* **2004**, Vol. 230, No. 1, pp. 77-87

95. Andersson, J. L. R., Richter, M., Richter, W., Skare, S., Nunes, R., Robson, M. D., & Behrens, T. E., Effects of Susceptibility Distortions on Tractography, *Proceedings of the International Society for Magnetic Resonance in Medicine* Vol. 12, **2004**, p. 87

96. Gui, M., Lazar, M., & Arfanakis, K., A Comparison of White Matter Fiber-Tracking Results Using PROPELLER and SE-EPI Datasets, *Proceedings of the International Society for Magnetic Resonance in Medicine* Vol. 12, **2004**, p. 1283

97. Jezzard, P. & Balaban, R. S., Correction for Geometric Distortion in Echo-Planar Images From B-0 Field Variations, *Magnetic Resonance in Medicine* **1995**, Vol. 34, No. 1, pp. 65-73

98. Cercignani, M., Symms, M. R., Boulby, P., & Barker, G. J., Errors in Diffusion Tensor Data Following B0 Field Map Correction, *10th Annual Meeting of the British Chapter of the ISMRM* **2004**, p. P4

99. Andersson, J. L. R., Skare, S., & Ashburner, J., How to Correct Susceptibility Distortions in Spin-Echo Echo- Planar Images: Application to Diffusion Tensor Imaging, *Neuroimage* **2003**, Vol. 20, No. 2, pp. 870-888

100. Alexander, A. L., Hasan, K. M., Lazar, M., Tsuruda, J. S., & Parker, D. L., Analysis of Partial Volume Effects in Diffusion-Tensor MRI, *Magnetic Resonance in Medicine* **2001**, Vol. 45, No. 5, pp. 770-780

101. Nunes, R., Jezzard, P., Behrens, T. E., & Clare, S., The Impact of Increased Spatial Resolution in Anisotropy Measurements, *10th Annual Meeting of the British Chapter of the ISMRM* **2004**, p. L6

102. Tournier, J.-D., Calamante, F., Gadian, D. G., & Connelly, A., Direct Estimation of Fibre Orientations in Partial Volume Contaminated Regions Using Spherical Deconvolution, *Proceedings of the International Society for Magnetic Resonance in Medicine* Vol. 12, **2004**, p. 88

103. Conturo, T. E., Lori, N. F., Cull, T. S., Akbudak, E., Snyder, A. Z., Shimony, J. S., McKinstry, R. C., Burton, H., & Raichle, M. E., Tracking Neuronal Fiber Pathways in the Living Human Brain, *Proc.Natl.Acad.Sci.U.S.A* **1999**, Vol. 96, No. 18, pp. 10422-10427

104. Milman, R. & Zhou, X. J., Improved Correlation Between Diffusion Parameters and Cell Volume Fraction in High-Resolution Diffusion-Weighted Images, *Proceedings of the International Society for Magnetic Resonance in Medicine* Vol. 11, **2003**, p. 2136

105. Golay, X., Jiang, H., van Zijl, P. C. M., & Mori, S., High-Resolution Isotropic 3D Diffusion Tensor Imaging of the Human Brain, *Magnetic Resonance in Medicine* **2002**, Vol. 47, No. 5, pp. 837-843

106. Deoni, S. C. L., Peters, T. M., & Rutt, B. K., Quantitative Diffusion Imaging With Steady-State Free Precession, *Magnetic Resonance in Medicine* **2004**, Vol. 51, No. 2, pp. 428-433

107. Delalande, C., de Zwart, J. A., Trillaud, H., Grenier, N., & Moonen, C. T., An Echo-Shifted Gradient-Echo MRI Method for Efficient Diffusion Weighting, *Magnetic Resonance in Medicine* **1999**, Vol. 41, No. 5, pp. 1000-1008

108. Merboldt, K. D., Hanicke, W., & Frahm, J., Self-Diffusion NMR Imaging Using Stimulated Echoes, *Journal of Magnetic Resonance* **1985**, Vol. 64, No. 3, pp. 479-486

109. Jeong, E. K., Kim, S. E., & Parker, D. L., High-Resolution Diffusion-Weighted 3D MRI, Using Diffusion-Weighted Driven-Equilibrium (DW-DE) and Multishot Segmented 3D-SSFP Without Navigator Echoes, *Magnetic Resonance in Medicine* **2003**, Vol. 50, No. 4, pp. 821-829

110. Thomas, D. L., Pell, G. S., Lythgoe, M. F., Gadian, D. G., & Ordidge, R. J., A Quantitative Method for Fast Diffusion Imaging Using Magnetization-Prepared TurboFLASH, *Magnetic Resonance in Medicine* **1998**, Vol. 39, No. 6, pp. 950-960

111. Frank, L. R., Wong, E. C., Liu, T. T., & Buxton, R. B., Increased Diffusion Sensitivity With Hyperechos, *Magnetic Resonance in Medicine* **2003**, Vol. 49, No. 6, pp. 1098-1105

112. Coremans, J., Spanoghe, M., Budinsky, L., Sterckx, J., Luypaert, R., Eisendrath, H., & Osteaux, M., A Comparison Between Different Imaging Strategies for Diffusion Measurements With the Centric Phase-Encoded TurboFLASH Sequence, *Journal of Magnetic Resonance* **1997**, Vol. 124, No. 2, pp. 323-342

113. Gudbjartsson, H., Maier, S. E., Mulkern, R. V., Morocz, I. A., Patz, S., & Jolesz, F. A., Line Scan Diffusion Imaging, *Magnetic Resonance in Medicine* **1996**, Vol. 36, No. 4, pp. 509-519

114. Pipe, J. G., Farthing, V. G., & Forbes, K. P., Multishot Diffusion-Weighted FSE Using PROPELLER MRI, *Magnetic Resonance in Medicine* **2002**, Vol. 47, No. 1, pp. 42-52

115. Trouard, T. P., Theilmann, R. J., Altbach, M. I., & Gmitro, A. F., High-Resolution Diffusion Imaging With DIFRAD-FSE (Diffusion- Weighted Radial Acquisition of Data With Fast Spin-Echo) MRI, *Magnetic Resonance in Medicine* **1999**, Vol. 42, No. 1, pp. 11-18

116. Bastin, M. E. & Le Roux, P., On the Application of a Non-CPMG Single-Shot Fast Spin-Echo Sequence to Diffusion Tensor MRI of the Human Brain, *Magnetic Resonance in Medicine* **2002**, Vol. 48, No. 1, pp. 6-14

117. Williams, C. F., Redpath, T. W., & Norris, D. G., A Novel Fast Split-Echo Multi-Shot Diffusion-Weighted MRI Method Using Navigator Echoes, *Magnetic Resonance in Medicine* **1999**, Vol. 41, No. 4, pp. 734-742

118. Liu, C. L., Bammer, R., Kim, D. H., & Moseley, M. E., Self-Navigated Interleaved Spiral (SNAILS): Application to High-Resolution Diffusion Tensor Imaging, *Magnetic Resonance in Medicine* **2004**, Vol. 52, No. 6, pp. 1388-1396

119. Bammer, R., Stollberger, R., Augustin, M., Simbrunner, J., Offenbacher, H., Kooijman, H., Ropele, S., Kapeller, P., Wach, P., Ebner, F., & Fazekas, F., Diffusion-Weighted Imaging With Navigated Interleaved Echo-Planar Imaging and a Conventional Gradient System, *Radiology* **1999**, Vol. 211, No. 3, pp. 799-806

120. Atkinson, D., Porter, D. A., Hill, D. L. G., Calamante, F., & Connelly, A., Sampling and Reconstruction Effects Due to Motion in Diffusion- Weighted Interleaved Echo Planar Imaging, *Magnetic Resonance in Medicine* **2000**, Vol. 44, No. 1, pp. 101-109

121. Norris, D. G., Implications of Bulk Motion for Diffusion-Weighted Imaging Experiments: Effects, Mechanisms, and Solutions, *Journal of Magnetic Resonance Imaging* **2001**, Vol. 13, No. 4, pp. 486-495

122. Bammer, R., Basic Principles of Diffusion-Weighted Imaging, *European Journal of Radiology* **2003**, Vol. 45, No. 3, pp. 169-184

123. Ordidge, R. J., Helpern, J. A., Qing, Z. X., Knight, R. A., & Nagesh, V., Correction of Motional Artifacts in Diffusion-Weighted MR-Images Using Navigator Echoes, *Magnetic Resonance Imaging* **1994**, Vol. 12, No. 3, pp. 455-460

124. Nunes, R., Jezzard, P., Johansen-Berg, B., Behrens, T. E., & Clare, S., An EPIK Navigation Towards High-Resolution Diffusion-Weighted Imaging, *Proceedings of the International Society for Magnetic Resonance in Medicine* Vol. 12, **2004**, p. 2467

125. Porter, D. & Mueller, E., Multi-Shot Diffusion-Weighted EPI With Readout Mosaic Segmentation and 2D Navigator Correction, *Proceedings of the International Society for Magnetic Resonance in Medicine* Vol. 12, **2004**, p. 442

126. Wang, J. J., Deichmann, R., Turner, R., & Ordidge, R., 3D DT-MRI Using a Reduced-FOV Approach and Saturation Pulses, *Magnetic Resonance in Medicine* **2004**, Vol. 51, No. 4, pp. 853-857

127. Symms, M. R., Wheeler-Kingshott, C. A., Parker, G. J. M., & Barker, G. J., ZOnally-Magnified Oblique Multislice (ZOOM) EPI, *Proceedings of the International Society for Magnetic Resonance in Medicine* Vol. 8, **2000**, p. 160

128. Wheeler-Kingshott, C. A. M., Parker, G. J. M., Symms, M. R., Hickman, S. J., Tofts, P. S., Miller, D. H., & Barker, G. J., ADC Mapping of the Human Optic Nerve: Increased Resolution, Coverage, and Reliability With CSF-Suppressed ZOOM-EPI, *Magnetic Resonance in Medicine* **2002**, Vol. 47, No. 1, pp. 24-31

129. Wheeler-Kingshott, C. A. M., Hickman, S. J., Parker, G. J. M., Ciccarelli, O., Symms, M. R., Miller, D. H., & Barker, G. J., Investigating Cervical Spinal Cord Structure Using Axial Diffusion Tensor Imaging, *Neuroimage* **2002**, Vol. 16, No. 1, pp. 93-102

130. Pruessmann, K. P., Weiger, M., Scheidegger, M. B., & Boesiger, P., SENSE: Sensitivity Encoding for Fast MRI, *Magnetic Resonance in Medicine* **1999**, Vol. 42, No. 5, pp. 952-962

131. Jaermann, T., Crelier, G., Pruessmann, K. P., Golay, X., Netsch, T., van Muiswinkel, A. M. C., Mori, S., van Zijl, P. C. M., Valavanis, A., Kollias, S., & Boesiger, P., SENSE-DTI at 3 T, *Magnetic Resonance in Medicine* **2004**, Vol. 51, No. 2, pp. 230-236

132. Nagae-Poetscher, L. M., Jiang, H. Y., Wakana, S., Golay, X., van Zijl, P. C. M., & Mori, S., High-Resolution Diffusion Tensor Imaging of the Brain Stem at 3 T, *American Journal of Neuroradiology* **2004**, Vol. 25, No. 8, pp. 1325-1330

133. Naganawa, S., Koshikawa, T., Kawai, H., Fukatsu, H., Ishigaki, T., Maruyama, K., & Takizawa, O., Optimization of Diffusion-Tensor MR Imaging Data Acquisition Parameters for Brain Fiber Tracking Using Parallel Imaging at 3 T, *European Radiology* **2004**, Vol. 14, No. 2, pp. 234-238

134. Ordidge, R., Carmichael, D., Chhina, N., Cooper, M., De Vita, E., & Randell, C., High Resolution Imaging at 4.7 T Using Four Irregularly-Shaped Receiver Coils, *Proceedings of the International Society for Magnetic Resonance in Medicine* Vol. 12, **2004**, p. 1557

135. Schar, M., Kozerke, S., Fischer, S. E., & Boesiger, P., Cardiac SSFP Imaging at 3 Tesla, *Magnetic Resonance in Medicine* **2004**, Vol. 51, No. 4, pp. 799-806

136. Nolte, U. G., Finsterbusch, J., & Frahm, J., Rapid Isotropic Diffusion Mapping Without Susceptibility Artifacts: Whole Brain Studies Using Diffusion-Weighted Single- Shot STEAM MR Imaging, *Magnetic Resonance in Medicine* **2000**, Vol. 44, No. 5, pp. 731-736

137. Beaulieu, C. F., Zhou, X. H., Cofer, G. P., & Johnson, G. A., Diffusion-Weighted MR Microscopy With Fast Spin-Echo, *Magnetic Resonance in Medicine* **1993**, Vol. 30, No. 2, pp. 201-206

138. Norris, D. G., Bornert, P., Reese, T., & Leibfritz, D., On the Application of Ultra-Fast RARE Experiments, *Magnetic Resonance in Medicine* **1992**, Vol. 27, No. 1, pp. 142-164

139. Alsop, D. C., Phase Insensitive Preparation of Single-Shot RARE: Application to Diffusion Imaging in Humans, *Magnetic Resonance in Medicine* **1997**, Vol. 38, No. 4, pp. 527-533

140. Schick, F., SPLICE: Sub-Second Diffusion-Sensitive MR Imaging Using a Modified Fast Spin-Echo Acquisition Made, *Magnetic Resonance in Medicine* **1997**, Vol. 38, No. 4, pp. 638-644

141. Alexander, A. L., Ma, X., Zong, X., & Pipe, J. G., Diffusion-Weighted PROPELLER Imaging of the Human Brain at 3 Tesla, *Proceedings of the International Society for Magnetic Resonance in Medicine* Vol. 10, **2002**, p. 436

142. Pipe, J. G., Han, E. T., & Busse, R. F., SAR Reduction for PROPELLER DWI at 3T, *Proceedings of the International Society for Magnetic Resonance in Medicine* Vol. 11, **2003**, p. 2127

143. Pipe, J. G., Turboprop - an Improved PROPELLER Sequence for Diffusion Weighted MRI, *Proceedings of the International Society for Magnetic Resonance in Medicine* Vol. 10, **2002**, p. 435

144. Pipe, J. G., Mixed-CPMG FSE, *Proceedings of the International Society for Magnetic Resonance in Medicine* Vol. 9, **2001**, p. 162

145. Roberts, T., Liu, F., & Sussman, M., Diffusion Weigthed Imaging Near the Base of the Brain: Reducing Magnetic Susceptibility Effects Using Parallel Imaging EPI Vs. PROPELLER FSE, *Proceedings of the International Society for Magnetic Resonance in Medicine* Vol. 12, **2004**, p. 1182

146. Roberts, T. & Haider, M., Diffusion Weighted Imaging of the Prostate Gland in the Face of Magnetic Susceptibility Differences - Parallel EPI and PROPELLER FSE Approaches, *Proceedings of the International Society for Magnetic Resonance in Medicine* Vol. 12, **2004**, p. 946

147. Pipe, J. G., The Use of Parallel Imaging With PROPELLER DWI, *Proceedings of the International Society for Magnetic Resonance in Medicine* Vol. 11, **2003**, p. 66

148. Lee, S.-K., Mori, S., Kim, J., Lee, Y., & Kim, D., Diffusion Tensor MRI and Fibre Tractography in Malformations of Cortical Development, *Proceedings of the International Society for Magnetic Resonance in Medicine* Vol. 12, **2004**, p. 1263

149. Lazar, M., Thottakara, P., Field, A. S., Laundre, B., Badie, B., Jellison, B., & Alexander, A. L., A White Matter Tractography Study of White Matter Reorganization After Surgical Resection of Brain Neoplasms, *Proceedings of the International Society for Magnetic Resonance in Medicine* Vol. 12, **2004**, p. 1259

150. Frahm, J., Haase, A., Matthaei, D., Merboldt, K. D., & Hanicke, W., Rapid NMR Imaging Using Stimulated Echoes, *Journal of Magnetic Resonance* **1985**, Vol. 65, No. 1, pp. 130-135

151. Finsterbusch, J. & Frahm, J., Half-Fourier Single-Shot STEAM MRI, *Magnetic Resonance in Medicine* **2002**, Vol. 47, No. 3, pp. 611-615

152. Merboldt, K. D., Hanicke, W., & Frahm, J., Diffusion Imaging Using Stimulated Echoes, *Magnetic Resonance in Medicine* **1991**, Vol. 19, No. 2, pp. 233-239

153. Merboldt, K. D., Hanicke, W., Bruhn, H., Gyngell, M. L., & Frahm, J., Diffusion Imaging of the Human Brain in Vivo Using High-Speed STEAM MRI, *Magnetic Resonance in Medicine* **1992**, Vol. 23, No. 1, pp. 179-192

154. Moonen, C. T., Pekar, J., Devleeschouwer, M. H. M., van Gelderen, P., van Zijl, P. C. M., & Despres, D., Restricted and Anisotropic Displacement of Water in Healthy Cat Brain and in Stroke Studied by NMR Diffusion Imaging, *Magnetic Resonance in Medicine* **1991**, Vol. 19, No. 2, pp. 327-332

155. van Zijl, P. C. M., Moonen, C. T., Alger, J. R., Cohen, J. S., & Chesnick, S. A., High Field Localized Proton Spectroscopy in Small Volumes: Greatly Improved Localization and Shimming Using Shielded Strong Gradients, *Magnetic Resonance in Medicine* **1989**, Vol. 10, No. 2, pp. 256-265

156. Yongbi, M. N., Ding, S. J., & Dunn, J. F., A Modified Sub-Second Fast-STEAM Sequence Incorporating Bipolar Gradients for in Vivo Diffusion Imaging, *Magnetic Resonance in Medicine* **1996**, Vol. 35, No. 6, pp. 911-916

157. Turner, R., von Kienlin, M., Moonen, C. T., & van Zijl, P. C. M., Single-Shot Localized Echo-Planar Imaging (STEAM-EPI) at 4.7 Tesla, *Magnetic Resonance in Medicine* **1990**, Vol. 14, No. 2, pp. 401-408

158. Muller, M. F., Prasad, P., Siewert, B., Nissenbaum, M. A., Raptopoulos, V., & Edelman, R. R., Abdominal Diffusion Mapping With Use of a Whole-Body Echo-Planar System, *Radiology* **1994**, Vol. 190, No. 2, pp. 475-478

159. Heiland, S., Dietrich, O., & Sartor, K., Diffusion-Weighted Imaging of the Brain: Comparison of Stimulated- and Spin-Echo Echo-Planar Sequences, *Neuroradiology* **2001**, Vol. 43, No. 6, pp. 442-447

160. Wielopolski, P. A., Schmitt, F., & Stehling, M. K., Echo-Planar Imaging Pulse Sequences, pp. 65-139 in *Echo-Planar Imaging: Theory, Technique and Application: Magnetic Resonance Imaging in a Fraction of a Second*, edn 1, **1998**, F. Schmitt, M. K. Stehling, & R. Turner, eds., Springer-Verlag

161. Schmitt, F., Stehling, M. K., & Turner, R., *Echo-Planar Imaging Theory, Technique and Application*, **1998** Springer-Verlag

162. Jezzard, P., Duewell, S., & Balaban, R. S., MR Relaxation Times in Human Brain: Measurement at 4 T, *Radiology* **1996**, Vol. 199, No. 3, pp. 773-779

163. Tofts, P. S., Lloyd, D., Clark, C. A., Barker, G. J., Parker, G. J. M., McConville, P., Baldock, C., & Pope, J. M., Test Liquids for Quantitative MRI Measurements of Self- Diffusion Coefficient in Vivo, *Magnetic Resonance in Medicine* **2000**, Vol. 43, No. 3, pp. 368-374

164. Chang, H. & Fitzpatrick, J. M., A Technique for Accurate Magnetic Resonance Imaging in the Presence of Field Inhomogeneities, *IEEE Transactions on Medical Imaging* **1992**, Vol. 11, No. 3, pp. 319-329

165. Bowtell, R., McIntyre, D. J. O., Commandre, M.-J., Glover, P. M., & Mansfield, P., Correction of Geometric Distortion in Echo Planar Images, *Proceedings of the Second Meeting of the Society for Magnetic Resonance* **1994**, p. 411

166. Morgan, P. S., Bowtell, R. W., McIntyre, D. J. O., & Worthington, B. S., Correction of Spatial Distortion in EPI Due to Inhomogeneous Static Magnetic Fields Using the Reversed Gradient Method, *Journal of Magnetic Resonance Imaging* **2004**, Vol. 19, No. 4, pp. 499-507

167. Barfuss, H., Fischer, H., Hentschel, D., Ladebeck, R., & Vetter, J., Whole-Body MR Imaging and Spectroscopy With a 4-T System, *Radiology* **1988**, Vol. 169, No. 3, pp. 811-816

168. Pauly, J. M., Le Roux, P., Nishimura, D., & Macovski, A., Parameter Relations for the Shinnar-Le Roux Selective Excitation Pulse Design Algorithm, *IEEE Transactions on Medical Imaging* **1991**, Vol. 10, No. 1, pp. 53-65

169. Mattiello, J., Basser, P. J., & LeBihan, D., The b Matrix in Diffusion Tensor Echo-Planar Imaging, *Magnetic Resonance in Medicine* **1997**, Vol. 37, No. 2, pp. 292-300

170. Mattiello, J., Basser, P. J., & LeBihan, D., Analytical Expressions for the B-Matrix in NMR Diffusion Imaging and Spectroscopy, *Journal of Magnetic Resonance Series A* **1994**, Vol. 108, No. 2, pp. 131-141

171. Dietrich, O., Heiland, S., & Sartor, K., Noise Correction for the Exact Determination of Apparent Diffusion Coefficients at Low SNR, *Magnetic Resonance in Medicine* **2001**, Vol. 45, No. 3, pp. 448-453

172. Jones, D. K. & Basser, P. J., "Squashing Peanuts and Smashing Pumpkins": How Noise Distorts Diffusion-Weighted MR Data, *Magnetic Resonance in Medicine* **2004**, Vol. 52, No. 5, pp. 979-993

173. Zaitsev, M., Zilles, K., & Shah, N. J., Shared K-Space Echo Planar Imaging With Keyhole, *Magnetic Resonance in Medicine* **2001**, Vol. 45, No. 1, pp. 109-117

174. Turner, R. & Ordidge, R. J., Technical Challenges of Functional Magnetic Resonance Imaging, *IEEE Eng Med.Biol.Mag.* **2000**, Vol. 19, No. 5, pp. 42-54

175. Deichmann, R., Josephs, O., Hutton, C., Corfield, D. R., & Turner, R., Compensation of Susceptibility-Induced BOLD Sensitivity Losses in Echo-Planar FMRI Imaging, *Neuroimage* **2002**, Vol. 15, No. 1, pp. 120-135

176. Frahm, J., Merboldt, K. D., & Hanicke, W., Direct FLASH MR Imaging of Magnetic-Field Inhomogeneities by Gradient Compensation, *Magnetic Resonance in Medicine* **1988**, Vol. 6, No. 4, pp. 474-480

177. Ordidge, R. J., Gorell, J. M., Deniau, J. C., Knight, R. A., & Helpern, J. A., Assessment of Relative Brain Iron Concentrations Using T2-Weighted and T2*-Weighted MRI at 3-Tesla, *Magnetic Resonance in Medicine* **1994**, Vol. 32, No. 3, pp. 335-341

178. Yang, Q. X., Williams, G. D., Demeure, R. J., Mosher, T. J., & Smith, M. B., Removal of Local Field Gradient Artifacts in T-2*-Weighted Images at High Fields by Gradient-Echo Slice Excitation Profile Imaging, *Magnetic Resonance in Medicine* **1998**, Vol. 39, No. 3, pp. 402-409

179. Constable, R. T. & Spencer, D. D., Composite Image Formation in Z-Shimmed Functional MR Imaging, *Magnetic Resonance in Medicine* **1999**, Vol. 42, No. 1, pp. 110-117

180. Glover, G. H., 3D Z-Shim Method for Reduction of Susceptibility Effects in BOLD FMRI, *Magnetic Resonance in Medicine* **1999**, Vol. 42, No. 2, pp. 290-299

181. Gorno-Tempini, M. L., Hutton, C., Josephs, O., Deichmann, R., Price, C., & Turner, R., Echo Time Dependence of BOLD Contrast and Susceptibility Artifacts, *Neuroimage* **2002**, Vol. 15, No. 1, pp. 136-142

182. Merboldt, K. D., Finsterbusch, J., & Frahm, J., Reducing Inhomogeneity Artifacts in Functional MRI of Human Brain Activation-Thin Sections Vs Gradient Compensation, *J.Magn Reson.* **2000**, Vol. 145, No. 2, pp. 184-191

183. Stenger, V. A., Boada, F. E., & Noll, D. C., Three-Dimensional Tailored RF Pulses for the Reduction of Susceptibility Artifacts in T-2*-Weighted Functional MRI, *Magnetic Resonance in Medicine* **2000**, Vol. 44, No. 4, pp. 525-531

184. Chen, N. K. & Wyrwicz, A. M., Removal of Intravoxel Dephasing Artifact in Gradient-Echo Images Using a Field-Map Based RF Refocusing Technique, *Magnetic Resonance in Medicine* **1999**, Vol. 42, No. 4, pp. 807-812

185. Wilson, J. L., Jenkinson, M., de Araujo, I., Kringelbach, M. L., Rolls, E. T., & Jezzard, P., Fast, Fully Automated Global and Local Magnetic Field Optimization for FMRI of the Human Brain, *Neuroimage* **2002**, Vol. 17, No. 2, pp. 967-976

186. Wilson, J. L., Jenkinson, M., & Jezzard, P., Optimization of Static Field Homogeneity in Human Brain Using Diamagnetic Passive Shims, *Magnetic Resonance in Medicine* **2002**, Vol. 48, No. 5, pp. 906-914

187. Wilson, J. L. & Jezzard, P., Utilization of an Intra-Oral Diamagnetic Passive Shim in Functional MRI of the Inferior Frontal Cortex, *Magnetic Resonance in Medicine* **2003** , Vol. 50, No. 5, pp. 1089-1094

188. Wilson, J. L., Jenkinson, M., & Jezzard, P., Protocol to Determine the Optimal Intraoral Passive Shim for Minimisation of Susceptibility Artifact in Human Inferior Frontal Cortex, *Neuroimage* **2003**, Vol. 19, No. 4, pp. 1802-1811

189. Hsu, J.-J. & Glover, G. H., Mitigation of Susceptibility-Induced Signal Loss in Neuroimaging Using Localized Shim Coils, *Proceedings of the International Society for Magnetic Resonance in Medicine* Vol. 11, **2003**, p. 734

190. Wong, E. C. & Mazaheri, Y., Shimming of the Inferior Frontal Cortex Using an External Local Shim Coil, *Proceedings of the International Society for Magnetic Resonance in Medicine* Vol. 12, **2004**, p. 520

191. Hsu, J.-J. & Glover, G. H., Localized Active Shimming for FMRI Signal Recovery, *Proceedings of the International Society for Magnetic Resonance in Medicine* Vol. 12, **2004**, p. 994

192. Hutton, C., Bork, A., Josephs, O., Deichmann, R., Ashburner, J., & Turner, R., Image Distortion Correction in FMRI: A Quantitative Evaluation, *Neuroimage* **2002**, Vol. 16, No. 1, pp. 217-240

193. Roopchansingh, V., Cox, R. W., Jesmanowicz, A., Ward, B. D., & Hyde, J. S., Single-Shot Magnetic Field Mapping Embedded in Echo-Planar Time-Course Imaging, *Magnetic Resonance in Medicine* **2003**, Vol. 50, No. 4, pp. 839-843

194. Reber, P. J., Wong, E. C., Buxton, R. B., & Frank, L. R., Correction of Off Resonance-Related Distortion in Echo-Planar Imaging Using EPI-Based Field Maps, *Magnetic Resonance in Medicine* **1998**, Vol. 39, No. 2, pp. 328-330

195. Menon, R. S., Thomas, C. G., & Gati, J. S., Investigation of BOLD Contrast in FMRI Using Multi-Shot EPI, *NMR Biomed.* **1997**, Vol. 10, No. 4-5, pp. 179-182

196. Rieseberg, S., Frahm, J., & Finsterbusch, J., Two-Dimensional Spatially Selective RF Excitation Pulses in Echo-Planar Imaging, *Proceedings of the International Society for Magnetic Resonance in Medicine* Vol. 10, **2002**, p. 2339

197. Yang, Q. X., Wang, J., Smith, M. B., Meadowcroft, M., Sun, X., Eslinger, P. J., & Golay, X., Reduction of Magnetic Field Inhomogeneity Artifacts in Echo Planar Imaging With SENSE and GESEPI at High Field, *Magnetic Resonance in Medicine* **2004**, Vol. 52, No. 6, pp. 1418-1423

198. Li, S., Williams, G. D., Frisk, T. A., Arnold, B. W., & Smith, M. B., A Computer Simulation of the Static Magnetic Field Distribution in the Human Head, *Magnetic Resonance in Medicine* **1995**, Vol. 34, No. 2, pp. 268-275

199. Li, S., Dardzinski, B. J., Collins, C. M., Yang, Q. X., & Smith, M. B., Three-Dimensional Mapping of the Static Magnetic Field Inside the Human Head, *Magnetic Resonance in Medicine* **1996**, Vol. 36, No. 5, pp. 705-714

200. Truong, T. K., Clymer, B. D., Chakeres, D. W., & Schmalbrock, P., Three-Dimensional Numerical Simulations of Susceptibility- Induced Magnetic Field Inhomogeneities in the Human Head, *Magnetic Resonance Imaging* **2002**, Vol. 20, No. 10, pp. 759-770

201. Yang, B., Collins, C. M., & Song, H. K., Calculation of Static Magnetic Field Distribution in a Multi-Tissue Human Head Model for MRI, *Proceedings of the International Society for Magnetic Resonance in Medicine* Vol. 9, **2001**, p. 616

202. Abduljalil, A. M., Kangarlu, A., Yu, Y., & Robitaille, P. M., Macroscopic Susceptibility in Ultra High Field MRI. II: Acquisition of Spin Echo Images From the Human Head, *J.Comput.Assist.Tomogr.* **1999**, Vol. 23, No. 6, pp. 832-841

203. Orth, R. C., Sinha, P., Madsen, E. L., Frank, G., Korosec, F. R., Mackie, T. R., & Mehta, M. P., Development of a Unique Phantom to Assess the Geometric Accuracy of Magnetic Resonance Imaging for Stereotactic Localization, *Neurosurgery* **1999**, Vol. 45, No. 6, pp. 1423-1429

204. Karger, C. P., Hipp, P., Henze, M., Echner, G., Hoss, A., Schad, L., & Hartmann, G. H., Stereotactic Imaging for Radiotherapy: Accuracy of CT, MRI, PET and SPECT, *Phys.Med.Biol.* **2003**, Vol. 48, No. 2, pp. 211-221

205. Daisne, J. F., Sibomana, M., Bol, A., Cosnard, G., Lonneux, M., & Gregoire, V., Evaluation of a Multimodality Image (CT, MRI and PET) Coregistration Procedure on Phantom and Head and Neck Cancer Patients: Accuracy, Reproducibility and Consistency, *Radiother.Oncol.* **2003**, Vol. 69, No. 3, pp. 237-245

206. Rice, J. R., Milbrandt, R. H., Madsen, E. L., Frank, G. R., Boote, E. J., & Blechinger, J. C., Anthropomorphic 1H MRS Head Phantom, *Medical Physics* **1998**, Vol. 25, No. 7 Pt 1, pp. 1145-1156

207. Drzymala, R. E. & Mutic, S., Stereotactic Imaging Quality Assurance Using an Anthropomorphic Phantom, *Comput.Aided Surg.* **1999**, Vol. 4, No. 5, pp. 248-255

208. Bednarz, G., Downes, M. B., Corn, B. W., Curran, W. J., & Goldman, H. W., Evaluation of the Spatial Accuracy of Magnetic Resonance Imaging-Based Stereotactic Target Localization for Gamma Knife Radiosurgery of Functional Disorders, *Neurosurgery* **1999**, Vol. 45, No. 5, pp. 1156-1161

209. Kaye, G. W. C., *Tables of Physical and Chemical Constants*, 16 edn, **1995** Longman

210. Hautot, D., Pankhurst, Q. A., Khan, N., & Dobson, J., Preliminary Evaluation of Nanoscale Biogenic Magnetite in Alzheimer's Disease Brain Tissue, *Proceedings of the Royal Society of London Series B-Biological Sciences* **2003**, Vol. 270, p. S62-S64

211. Hwang, S. N. & Wehrli, F. W., Experimental Evaluation of a Surface Charge Method for Computing the Induced Magnetic Field in Trabecular Bone, *J.Magn Reson.* **1999**, Vol. 139, No. 1, pp. 35-45

212. Walker, P. M., Balmer, C., Ablett, S., & Lerski, R. A., A Test Material for Tissue Characterisation and System Calibration in MRI, *Phys.Med.Biol.* **1989**, Vol. 34, No. 1, pp. 5-22

213. Mazzara, G. P., Briggs, R. W., Wu, Z., & Steinbach, B. G., Use of a Modified Polysaccharide Gel in Developing a Realistic Breast Phantom for MRI, *Magnetic Resonance Imaging* **1996**, Vol. 14, No. 6, pp. 639-648

214. Cochlin, L., Blamire, A. M., & Styles, P., Dependence of T1 and T2 on High Field Strengths in Doped Agarose Gels; Facilitating Selection of Composition for Specific T1/T2 at Relevant Field, *Proceedings of the International Society for Magnetic Resonance in Medicine* Vol. 11, **2003**, p. 885

215. Kim, S. G., Hu, X., & Ugurbil, K., Accurate T1 Determination From Inversion Recovery Images: Application to Human Brain at 4 Tesla, *Magnetic Resonance in Medicine* **1994**, Vol. 31, No. 4, pp. 445-449

216. Takaya, N., Watanabe, H., & Mitsumori, F., Elongated T1 Values in Human Brain and the Optimization of MDEFT Measurements at 4.7 T, *Proceedings of the International Society for Magnetic Resonance in Medicine* Vol. 12, **2004**, p. 2339

217. Yang, Q. X., Wang, J. H., Collins, C. M., Smith, M. B., Zhang, X. L., Ugurbil, K., & Chen, W., Phantom Design Method for High-Field MRI Human Systems, *Magnetic Resonance in Medicine* **2004**, Vol. 52, No. 5, pp. 1016-1020

218. Beck, B. L., Jenkins, K. A., Rocca, J. R., & Fitzsimmons, J. R., Tissue-Equivalent Phantoms for High Frequencies, *Concepts in Magnetic Resonance Part B-Magnetic Resonance Engineering* **2004**, Vol. 20B, No. 1, pp. 30-33

219. http://www.fcc.gov/fcc-bin/dielec.sh

220. Neelakanta, S. P., *Handbook of Electromagnetic Materials: Monolithic and Composite Versions and Their Applications*, **1995** CRC Press

221. Jenkinson, M., Improved Unwarping of EPI Images Using Regularised B0 Maps, *Neuroimage* Vol. 13, **2001**, p. S165

222. Park, H. W., Ro, Y. M., & Cho, Z. H., Measurement of the Magnetic-Susceptibility Effect in High-Field NMR Imaging, *Physics in Medicine and Biology* **1988**, Vol. 33, No. 3, pp. 339-349

223. Glover, G. H. & Schneider, E., Three-Point Dixon Technique for True Water/Fat Decomposition With B0 Inhomogeneity Correction, *Magnetic Resonance in Medicine* **1991**, Vol. 18, No. 2, pp. 371-383

224. Yeung, H. N. & Kormos, D. W., Separation of True Fat and Water Images by Correcting Magnetic Field Inhomogeneity in Situ, *Radiology* **1986**, Vol. 159, No. 3, pp. 783-786

225. Lodes, C. C., Felmlee, J. P., Ehman, R. L., Sehgal, C. M., Greenleaf, J. F., Glover, G. H., & Gray, J. E., Proton MR Chemical Shift Imaging Using Double and Triple Phase Contrast Acquisition Methods, *Journal of Computer Assisted Tomography* **1989**, Vol. 13, No. 5, pp. 855-861

226. Young, I. R., Khenia, S., Thomas, D. G. T., Davis, C. H., Gadian, D. G., Cox, I. J., Ross, B. D., & Bydder, G. M., Clinical Magnetic Susceptibility Mapping of the the Brain, *Journal of Computer Assisted Tomography* **1987**, Vol. 11, No. 1, pp. 2-6

227. Tyszka, J. M. & Mamelak, A. N., Quantification of B-0 Homogeneity Variation With Head Pitch by Registered Three-Dimensional Field Mapping, *Journal of Magnetic Resonance* **2002**, Vol. 159, No. 2, pp. 213-218

228. Bonny, J. M., Laurent, W., & Renou, J. P., Detection of Susceptibility Effects Using Simultaneous T2* and Magnetic Field Mapping, *Magnetic Resonance Imaging* **2000**, Vol. 18, No. 9, pp. 1125-1128

229. Mosher, T. J. & Smith, M. B., Magnetic Susceptibility Measurement Using a Double-DANTE Tagging (DDT) Sequence, *Magnetic Resonance in Medicine* **1991**, Vol. 18, No. 1, pp. 251-255

230. http://www.fmrib.ox.ac.uk/fsl/

231. Cusack, R. & Papadakis, N., New Robust 3-D Phase Unwrapping Algorithms: Application to Magnetic Field Mapping and Undistorting Echoplanar Images, *Neuroimage* **2002**, Vol. 16, No. 3, pp. 754-764

232. Smith, S. M., Fast Robust Automated Brain Extraction, *Hum.Brain Mapp.* **2002**, Vol. 17, No. 3, pp. 143-155

233. Cusack, R., Russell, B., Cox, S. M. L., De Panfilis, C., Schwarzbauer, C., & Ansorge, R., An Evaluation of the Use of Passive Shimming to Improve Frontal Sensitivity in FMRI, *Neuroimage* **2005**, Vol. 24, No. 1, pp. 82-91

234. Thomas, D. L., Lythgoe, M. F., Gadian, D. G., & Ordidge, R. J., Rapid Simultaneous Mapping of T2 and T2* by Multiple Acquisition of Spin and Gradient Echoes Using Interleaved Echo Planar Imaging (MASAGE-IEPI), *Neuroimage* **2002**, Vol. 15, No. 4, pp. 992-1002

235. Parker, G. J. M., Rowland, I., Collins, D. J., & Leach, M. O., Investigation of Factors Affecting Uniformity in Test Objects and the Advantages of Using Polydimethylsiloxane (PDMS), *Proceedings of the Second Meeting of the Society for Magnetic Resonance* **1994**, p. 203

236. Kuo, A. C. M., Polydimethylsiloxane, pp. 411-435 in *Polymer Data Handbook*, **1999** Oxford University Press

237. Heberlein, K. & Hu, X., Improved Shim by Subject Head Positioning, *Proceedings of the International Society for Magnetic Resonance in Medicine* Vol. 9, **2001**, p. 1157

238. Ashburner, J., Andersson, J. L., & Friston, K. J., Image Registration Using a Symmetric Prior--in Three Dimensions, *Hum.Brain Mapp.* **2000**, Vol. 9, No. 4, pp. 212-225

239. Ojemann, J. G., Akbudak, E., Snyder, A. Z., McKinstry, R. C., Raichle, M. E., & Conturo, T. E., Anatomic Localization and Quantitative Analysis of Gradient Refocused Echo-Planar FMRI Susceptibility Artifacts, *Neuroimage.* **1997**, Vol. 6, No. 3, pp. 156-167

240. Shmueli, K., Thomas, D. L., & Ordidge, R. J., Slice-Selective Spin-Echo Formation Using Hyperbolic Secant RF Pulses, *Proceedings of the International Society for Magnetic Resonance in Medicine* Vol. 11, **2003**, p. 961

241. Feinberg, D. A., Gradient and Spin-Echo (GRASE) Imaging, pp. 605-631 in *Echo-Planar Imaging: Theory, Technique and Application: Magnetic Resonance Imaging in a Fraction of a Second*, edn 1, **1998**, F. Schmitt, M. K. Stehling, & R. Turner, eds., Springer-Verlag